Title
Understanding the Morphological Effects of Self-Assembly and Molecular Doping in Semiconducting Polymers

Author
Yee, Patrick

Publication Date
2019

Peer reviewed|Thesis/dissertation

UNIVERSITY OF CALIFORNIA

Los Angeles

Understanding the Morphological Effects of Self-Assembly and Molecular Doping in Semiconducting Polymers

A dissertation submitted in partial satisfaction of the requirements for the degree Doctor of Philosophy in Chemistry

by

Patrick Yi Yen Yee

2019

ABSTRACT OF THE DISSERTATION

Understanding the Morphological Effects of Self-Assembly and Molecular Doping in Semiconducting Polymers

by

Patrick Yi Yen Yee

Doctor of Philosophy in Chemistry

University of California, Los Angeles, 2019

Professor Sarah H. Tolbert, Chair

Semiconducting polymers are a versatile class of materials used for a variety of electronic applications. They are a cheap source of material relative to their inorganic counterparts, are flexible, and with solution processing, are easily scalable However, they are intrinsically poor conductors, which can result in low device efficiencies and shorter carrier lifetimes. The conductivity can be improved using a variety of methods, including controlling the morphology to improve carrier transport or introducing charge carriers using chemical dopants. In this dissertation, we describe experiments that use a combination of X-ray and

neutron scattering techniques to understand how we can use morphology in semiconducting polymers to improve their charge transport properties.

The first part of this dissertation focuses on the design of an amphiphilic conjugated polyelectrolyte model system to control the aggregation of polymer chains in solution, with the goal of straightening chains to reduce carrier trap sites caused by kinks that disrupt the π-conjugation. After showing good control of the nanoscale morphology in a well-defined, ideal system in solution, we then look at the controllably improving the electron transfer process in an actual organic photovoltaic (OPV) device. We then look to control and improve the electron transfer process in full organic photovoltaic devices. We show that using sequential processing, where the polymer and fullerene are deposited in two separate steps, we can control the device level mixing of polymer and fullerene.

We end with a discussion of studies focused on the morphological effects of molecular doping of semiconducting polymers. Using small molecule dopants, we show that with SqP, the polymer morphology is maintained as compared to conventional blend casting (BC) method. This allows more dopant to incorporate into thin films, further increasing the conductivity. Thereafter, we focus on how SqP provides the opportunity to tune the polymer morphology prior to doping and investigate how controlling the polymer crystallinity affects the optical and electronic properties in its doped state. Using statistical copolymers, we investigate the effect of polymer crystallinity and energy level offset between polymer and dopant. Finally, we conclude with a study on how the interplay between polymer chain ordering and the location of the dopant counterion in the lattice controls polymer conductivity. Overall, these results emphasize the importance of understanding and controlling the morphology of semiconducting polymers on multiple length-scales.

This dissertation of Patrick Yi Yen Yee is approved.

Yu Huang

Daniel Neuhauser

Sarah H. Tolbert, Committee Chair

University of California, Los Angeles

2019

CONTENTS

LIST OF FIGURES

and 50:50 (blue) and (b) PSDTTT:$PC_{61}BM$ with the $PC_{61}BM$ deposited from a co-solvent blend of Tol:2-CP with ratios of 35:65 (red), 50:50 (green), and 65:35 (blue).

Figure 3.2. 2D diffractograms on films of (a) pure PTB7, (b) pure PSDTTT, (c) PTB7:$PC_{61}BM$, and (d) PSDTT:$PC_{61}BM$ showing both polymers are face-on oriented with a prominent (010) π-stacking peak in the out-of-plane direction.

Figure 3.3. (a) Full integrations of GIWAXS diffractograms for the PTB7:$PC_{61}BM$ system: pure PTB7 (black), 40:60 2CP:1-BuOH (red), and 50:50 2CP:1-BuOH (blue). The in- (b) and out-of-plane (c) scattering is shown to confirm the edge-on orientation for PTB7 with strong (010) scattering in the out-of-plane direction. Further examination of the (010) peak is facilitated by subtraction of all isotropic scattering (mainly fullerene scattering). The difference patterns (d) show a (010) peak only in the out-of-plane direction (light curves), indicating that any non-isotropic polymer has a face-on orientation with respect to the substrate, even after SqP processing.

Figure 3.4. (a) Full integration of GIWAXS diffractograms for the PSDTTT:$PC_{61}BM$ system: pure PSDTTT (black), 35:65 Tol:2CP (red), 50:50 Tol:2CP (green) and 65:35 Tol:2CP (blue). The (b) in- and (c) out-of-plane integrations are shown to confirm edge-on orientation for PSDTTT with strong (010) scattering in the out-of-plane direction. Further examination of this (010) peak is facilitated by subtraction of all isotropic scattering (mainly fullerene scattering), showing that this SqP process is not altering the polymer orientation: (010) peak in the out-of-plane direction (light curves) rather than the in-plane (dark curves).

Figure 3.5. SLD vertical phase profiles for PTB7:$PC_{61}BM$ BHJ films using fullerene solvent blends of (a) 40:60 2CP:1-BuOH (red curve) and (b) 50:50 2CP:1-BuOH (blue curve). The data show the molecular distribution of polymer-rich regions (blue), mixed regions (yellow), and fullerene-

Figure 4.4. Comparison of the conductivity of P3HT thin films doped with F_4TCNQ by (a) traditional blend-casting method, data taken from Ref. 1, and (b) our SqP method. The sequentially processed films were prepared by spinning various concentrations of F4TCNQ onto P3HT films at 4000 rpm. Thicknesses of the different sequentially processed films are given in Table 4.1. The horizontal axis for the two panels are different because of the differences in processing method; the doping level in panel (a) is given in units of mole fraction F_4TCNQ in the blended solution, while the horizontal axis for panel (b) is in units of mg/mL F_4TCNQ in the solution used for SqP.

Figure 4.5. Thickness-normalized absorbance as a function of increasing F4TCNQ casting concentration for P3HT films doped by the SqP method. The upper right inset shows an energy level diagram of the various polaron transitions, while the upper left inset shows a plot of how the peak absorbance of the P1 transition at 0.5 eV and mobility change with free-carrier concentration as measured by the AC B-field Hall Effect (Table 4.2).

Chapter 5

Figure 5.1. Integrated (a) out-of-plane and (b) in-plane x-ray diffraction patterns for chloroform (CF)-cast (blue dashed curves), *o*-dichlorobenzene (*o*-DCB)-cast (green dashed curves), and 100% RR P3HT ODCB-cast polymer films (red dashed curves), as well as the same films after doping by SqP with 1 mg/mL of F_4TCNQ in dichloromethane (DCM; solid curves of the same colors, respectively). The inset in (a) shows the region around the P3HT out-of-plane (010) peak on an expanded scale. The combination of in-plane and out-of-plane data for both the (100) and (010) diffraction can be used to conclude that for the pristine films, both the relative crystallinity and degree of edge-on crystallite orientation increases in the order CF-cast, *o*-DCB-

cast, 100% RR. Moreover, the data make clear that this order is maintained following doping with F_4TCNQ by SqP. We also used GIWAXS to follow the doping process by examining films with progressively higher doping levels, as seen in integrated and normalized (c) out-of-plane and (d) in-plane x-ray diffraction peaks for P3HT films cast from *o*-DCB at 1000 rpm for 60 s (red curves), followed by doping via SqP with different concentrations of F_4TCNQ in DCM (various colored curves). Increasing doping levels causes a shift of the (100) diffraction peak to lower q, the appearance of a new (010) diffraction peak at higher q, and a complete loss of the (001) diffraction peak, indicative of the dopant residing in the lamellar regions of the sample but not the P3HT crystalline π-stacks, as suggested in Fig. 5.2.

Figure 5.2. Cartoon consistent with the GIWAXS data illustrating how F_4TCNQ anions could incorporate into the lamellar regions of the crystallites as well as the amorphous regions of the film. The presence of the anion causes the side chains to shift in order to incorporate the new F_4TCNQ volume, which in turn causes the increase in spacing in the lamellar direction and the loss of along-the-chain registry. Polarons can also delocalize between chains in the π-stacking direction, leading to a decrease in the π–π stacking distance (not shown).

Figure 5.3. (a) UV-vis absorption data for pristine CF-cast P3HT (blue curve), *o*-DCB-cast P3HT (green curve), and 100% RR P3HT (red curve) films. (b) Combined FTIR (0.05 to 0.5 eV) and UV-Vis (0.5-3.0 eV) absorption spectra for the same P3HT films after doping via SqP with 1 mg/mL F_4TCNQ in DCM. The data are normalized to the peak intensity of the P1 absorption band in the 0.3-0.5 eV region. Clearly the polaron P1 band redshifts, the relative absorption intensity below 0.18 eV increases, and the overall P1 absorption cross-section increases with increasing polymer crystallinity. The inset in panel (a) shows a representative energy level diagram for the P1 and P2 transitions of the polaron.

Figure 5.4. (a) Experimental absorption spectra of the P1 polaron transition for CF-cast (blue curve), *o*-DCB-cast (green curve), and 100% RR (red curve) P3HT doped via SqP with 1 mg/mL F_4TCNQ in DCM. (b) Simulated P1 absorption band with a negative point charge representing the anion placed 0.36 nm (blue curve), 0.5 nm (light blue curve), 0.6 nm (green curve), 0.7 nm (yellow curve), 0.8 nm (orange curve), and infinitely far away (red dashed curve) from a 10 × 2 P3HT chain array. Spectra were obtained by averaging over 1000 configurations of random site disorder; see the Supporting Information. (c) Simulated P1 absorption band obtained by further averaging over different anion distances ranging from 0.6-0.8 nm, giving good general agreement with the spectral shape and peak position seen experimentally in (a). The inset in panel (c) is a cartoon representation of the simulation. The fact that the experimental spectra are not strongly blue-shifted or narrowed suggests that anions do not lie within 5 Å of the polymer, reinforcing the conclusion that the F_4TCNQ anion does not π-stack with crystalline P3HT.

Figure 5.5. Logarithmic derivative plot of the conductivity of different P3HT films doped via SqP with 1 mg/mL F_4TCNQ in DCM versus temperature: (a) 100% RR P3HT (red circles), (b) *o*-DCB-cast (green circles), and (c) CF-cast (blue circles). The dashed and dotted lines are linear fits with the corresponding slopes listed in the legend. The arrows mark the temperature at which the behavior deviates from traditional variable-range-hopping transport.

Chapter 6

Figure 6.1. (a) Chemical structure of P37S-*stat*-P3HT copolymers; (b) optical image of P37S-*stat*-P3HT films ranging in composition from 0 to 100% P37S in 25% increments, showing three films of each composition; (c) cartoon schematic of the estimated change in valence and

conduction band levels (consistent with the measured optical bandgap) of the copolymers as a function of P37S composition; (d) UV-Visible absorbance of P37S-*stat*-P3HT copolymer films, normalized to the absorption maximum. The inset shows an energy level diagram indicating the allowed polaron transitions upon chemical doping; (e) UV-Visible-NIR absorbance of P37S-*stat*-P3HT copolymer films that were doped by SqP with 1 mg/mL F_4TCNQ in DCM, normalized to the intensity of the P1 polaron absorption near 0.5 eV; (f) chemical structure of F_4TCNQ. The arrows in panel (e) show the trends in doped-film absorption with increasing selenophene content.

Figure 6.2. Absorbance of the P1 polaron peak in P37S-stat-P3HT copolymer films doped by SqP with 1 mg/mL F4TCNQ in DCM; the spectra are normalized by the height of the peak near ~0.45 eV for ease of comparison. All the spectra, including the IR active vibration peaks, have been smoothed to allow for better visualization of relative peak locations and heights; the raw unsmoothed data are available in the Supporting Information. (b) Plots quantifying the depletion of the neutral absorbance intensity (black crosses) and the interchain to intrachain polaron peak ratio (green plus signs, from the data in panel (a)).

Figure 6.3. Radially integrated GIWAXS data for (a) the undoped copolymers and (b) the same polymer films after SqP doping with 1 mg/mL F_4TCNQ in DCM. The (100) peak of the undoped films shifts monotonically to larger d-spacing as the selenophene content is increased, as expected for the larger Se atom and longer side chains of the P37S monomer compared to P3HT, except for 100% P37S, as discussed in the text. The (100) peak of the doped films shifts to even larger *d*-spacing after F_4TCNQ has been incorporated. The peak positions and areas are summarized in Table 1; see the text for details. (c) DSC melting enthalpy (normalized per monomer unit) and integrated (100) peak area from GIWAXS and DSC as a function of increasing selenophene content. The good correlation indicates that GIWAXS does provide a good measure of relative crystallinity in each sample.

Figure 6.4. Percent change in film thickness due to swelling caused by exposure to DCM vapors as measured by ellipsometry (black bars) for the P37S-*stat*-P3HT copolymer series. Also plotted is the change in relative crystallinity as quantified by the ratio of the SqP doped film (100) peak area to the undoped film (100) peak area for each P37S-*stat*-P3HT copolymer in the series (orange stars).

Figure 6.5. Semilogarithmic plots of (a) electrical conductivity, (b) doped:undoped (100) peak area ratio, (c) carrier density, extracted from AC Hall effect measurements, and (d) carrier mobility, calculated from the ratio of the conductivity and carrier density, all as a function of selenophene content across the copolymer series. All of the electrical measurements were for films doped by SqP with 1 mg/mL F_4TCNQ in DCM.

Chapter 7

Figure 7.1: (a) Molecular structures of P3HT, F_4TCNQ, and TCNQ and (b) UV-Vis absorbance of a thin film of RRa-P3HT (blue), and similar films infiltrated by SqP with F_4TCNQ (red), $FeCl_3$ (pink), and TCNQ (green), showing successful incorporation of each of the small molecules. The new bands centered near 1.55 eV and 0.65 eV result from the production of polarons, indicating doping has occurred with F_4TCNQ and $FeCl_3$. The thermally dedoped film (black) confirms successful removal of dopant in the films. The inset shows the normalized low-energy P1 absorption for the F_4TCNQ- and $FeCl_3$-doped films; the relative blueshift of the $FeCl_3$-doped P1 absorption is indicative of more trapped charge carriers.

Figure 7.2. (a) Radially-integrated diffraction of undoped RRa-P3HT (blue), 0.003M F_4TCNQ-Doped RRa-P3HT (red), RRa-P3HT with TCNQ (green), and dedoped RRa-P3HT and (b) in-plane (solid) and out-of-plane integrations (dashed) with the inset zoomed in on the lamellar

overtones and π-stacking region. Doping with F_4TCNQ shows a clear increase in molecular order/overall crystallinity as well as the introduction of a strong preference for edge-on orientation. In contrast, infiltration with the structurally similar TCNQ has little effect on the RRa-P3HT structure, indicating that simple space filling is not responsible for the increased ordering upon doping.

Figure 7.3. (a) Radially-integrated diffraction of undoped RRa-P3HT (blue), 0.01M $FeCl_3$-doped RRa-P3HT (pink), 0.003M-doped RRa-P3HT (purple), and dedoped RRa-P3HT (black) and (b) in-plane (solid) and out-of-plane integrations (dashed) with the inset zoomed in on the lamellar overtones and π-stacking regions. The similar dopant-induced ordering (increase of (100) intensity, appearance of lamellar overtones and increased edge-on orientation) to what is seen with F_4TCNQ indicates that the structural changes are due to primarily to the polarons created by the doping process.

LIST OF TABLES/SCHEMES

Chapter 2

Chapter 3

Chapter 4

Chapter 5

ACKNOWLEDGMENTS

To say that this adventure of pursuing a Ph.D. has been a life-changing experience would be an understatement. While the goal has always been to further my knowledge and contribute to the scientific community, none of it would have been possible without a number of people. First and foremost, I would like to thank my advisor, Professor Sarah Tolbert, for first giving me an opportunity for exploring scientific research as an undergraduate and then for allowing me to continue to grow as a scientist and person in her research group. Without her support and guidance, I would not be where I am today. She was always willing to provide advice while still allowing me the space to discover myself as scientific researcher on my own, especially when it came to numerous synchrotron runs. I also want to thank Professor Ben Schwartz, who, at times, has been like a co-advisor to me. He pushed me to learn the device physics side of my experiments so that I could stay grounded in the applications instead of simply zeroing in on the details of my structural studies. He treated me as if one of his own and provided a secondary research home, wherein I probably spent more time in his labs than my own. I also want to express gratitude to my committee: Professor Yu Huang, Professor Danny Neuhauser, and Professor Alex Spokoyny. Thank you for challenging me to improve my presentation skills so that I can better communicate my science to a variety of audiences and for providing insight and discussion on my research.

I am very proud to have been part of the Tolbert group and be one of the Tolbies. Being a part of this research group provided an uncountable number of conversations that flawlessly or not so flawlessly flowed between scientific discussion, social event planning, random factoids, and even fantastical imaginations. Everyone in the group has always been fun and supportive in many ways outside of just science. I want to thank my mentor Dr. Rachel Huber who showed me during my undergraduate studies that pursuing a Ph.D. was not just about

research and publishing, but also about creating memories and experiences that I will never forget. To all of my collaborators, and particularly Dr. Tyler Scholes, none of this research would have been possible without you.

I am very fortunate to have developed a number of long-lasting friendships throughout this journey, providing a release valve outside of just research. This journey would not have been possible without my friends and family who provided much needed emotional support as I went through every trial and tribulation pursuing this degree. Thank you to everyone who has provided me support and encouragement throughout my pursuit, and to those who I do not mention, please know that I appreciate every single conversation and encounter we have had together. To my family, who definitely assume I am smarter than I actually am, thank you for your never-ending support, despite not necessarily understanding exactly what I do. To my roommate and best friend Ben Harris (who has dealt with all of my nonsense since we were Freshmen at UCLA), Dr. Terri Lin and Ty Karaba (who always managed to transform listening to me endlessly complain about life into an adventure filled with joy and laughter since they became fellow Tolbies), Collin Grant (who has been my number one drinking buddy and fellow beer/Scotch enthusiast), K.J. Winchell (who has been instrumental to nearly every part of this thesis from scientific conversation and collaboration to emotional support, in addition to requiring me to have an extremely organized social calendar), Rafal Dziedzic, Tori Basile, Sophia King, Dan Baumann, and many, many more, I cannot thank you enough for partaking in this journey with me. Finally, I would like to thank my partner, Donn Hoffman. Your endless encouragement and support throughout this pursuit has been a constant source of inspiration to continue to grow as a person. You are the love of my life, and I am truly grateful to have the opportunity to enjoy life with you.

Previous Publications and Contributions of Co-Authors

Chapter 2 and **Appendix A** are versions of Winchell, K.J.-†, Yee, P.Y.†, Li, Y., Thompson, R.J., Rubin, Y., and Tolbert, S.H. "Design Rule for Straightening Conjugated Polymer Electrolyte Chains for OPV Applications." K.J. and I contributed equally in writing the manuscript as well as collecting/analyzing the solution SAXS data. Yolanda and Rob synthesized the PCT material. The PIs and/or project directors were: Yves Rubin and Sarah Tolbert. The manuscript will be submitted for publication shortly after filing this dissertation.

Chapter 3 and **Appendix B** are versions of Yee, P.Y., Fontana, M.T., Huber, R.C., Aguirre, J.C., Jenekhe, S.A., Schwartz, B.J., and Tolbert, S.H. "Controlling Fullerene:Polymer Vertical Phase Segregation Using Sequential Processing and Solvent Swelling in Organic Photovoltaics." I wrote the manuscript and collected/analyzed the GIWAXS and NR data. Matt and Jordan prepared samples for GIWAXS and NR measurements and collected the JV data. Rachel helped collect and analyze the NR data. The PIs and/or project directors were: Benjamin Schwartz and Sarah Tolbert. The manuscript will be submitted for publication shortly after filing this dissertation.

Chapter 4 and **Appendix C** are versions of Scholes, D. T.; Hawks, S. A.; Yee, P. Y.; Wu, H.; Lindemuth, J. R.; Tolbert, S. H.; Schwartz, B. J. "Overcoming Film Quality Issues for Conjugated Polymers Doped with F4TCNQ by Solution Sequential Processing: Hall Effect, Structural, and Optical Measurements." Tyler wrote the manuscript and collected the device and optical data. Steve helped with the electrical measurements and optical spectroscopy. I collected/analyzed the GIWAXS data. Hao Wu helped with DC Hall effect measurements. Jeff Lindemuth performed all of the AC Hall effect measurements. The PIs and/or project directors were: Sarah Tolbert and Benjamin Schwartz.

Chapter 5 and **Appendix D** are versions of Scholes, D. T., Yee, P. Y., Lindemuth, J. R., Kang, H., Onorato, J., Ghosh, R., Luscombe, C. K., Spano, F. C., Tolbert, S. H., and Schwartz, B. J. "The Effects of Crystallinity on Charge Transport and the Structure of Sequentially Processed F4TCNQ-Doped Conjugated Polymer Films." Tyler wrote the manuscript and collected the device and optical data. I collected/analyzed the GIWAXS data and helped edit/write the manuscript. Jeff Lindemuth performed the AC Hall measurements and the temperature dependent conductivity measurements. Hyeyeon Kang performed the ellipsometry/porosimetry measurements and fitting. Jonathan Onorato synthesized the highly regioregular P3HT. Raja Ghosh performed the optical modeling of the P3HT polaron absorbance. The PIs and/or project directors were: Christine Luscombe, Frank Spano, Sarah Tolbert, and Benjamin Schwartz.

Chapter 6 and **Appendix E** are versions of Scholes, D. T., Yee, P. Y., McKeown, G. R., Li, S., Kang, H., Lindemuth, J. R., Xia, X., King, S. C., Seferos, D. S., Tolbert, S. H., and Schwartz, B. J. "Designing Conjugated Polymers for Molecular Doping: The Roles of Crystallinity, Swelling, and Conductivity in Sequentially-Doped Selenophene-Based Copolymers." Tyler wrote the manuscript and collected the device and optical data. I collected/analyzed the GIWAXS data and helped edit/write the manuscript. George McKeown synthesized the statistical copolymers and the P37S polymer as well as characterized it. Hyeyeon Kang performed the ellipsometry/porosimetry measurements and fitting. Jeff Lindemuth performed the AC Hall measurements. Xia Xun assisted with sample prep and electrical measurements. Sophia helped me collect the DSC measurements. The PIs and/or project directors were: Dwight Seferos, Sarah Tolbert, and Benjamin Schwartz.

Chapter 7 and **Appendix F** are versions of Yee, P.Y., Scholes, D.T., Schwartz, B.J., and Tolbert, S.H. "Dopant-Induced Ordering of Amorphous Regions in Regiorandom P3HT." I collected/analyzed the GIWAXS measurements and wrote the manuscript. Tyler collected the

device and optical data as well as helped edit the manuscript. The PIs and/or project directors were: Benjamin Schwartz and Sarah Tolbert. The manuscript will be submitted for publication shortly after filing this dissertation.

VITA

2013	B.S. *in Chemistry*
	University of California, Los Angeles
2013-2015	*M.S. in Chemistry with a focus on Materials Chemistry*
	University of California, Los Angeles

Publications

Winchell, K.J.[†], **Yee, P.Y.**[†], Li, Y., Thompson, R.J., Rubin, Y., and Tolbert, S.H. "Design Rule for Straightening Conjugated Polymer Electrolyte Chains for OPV Applications" *Chemistry of Materials*, In Preparation.

Yee, P.Y., Scholes, D.T., Schwartz, B.J., and Tolbert, S.H. "Dopant-Induced Ordering of Amorphous Regions in Regiorandom P3HT" *The Journal of Physical Chemistry Letters*, In Preparation.

Yee, P.Y., Fontana, M.T., Huber, R.C., Aguirre, J.C., Jenekhe, S.A., Schwartz, B.J., and Tolbert, S.H. "Controlling Fullerene:Polymer Vertical Phase Segregation Using Sequential Processing and Solvent Swelling in Organic Photovoltaics" *ACS Applied Materials and Interfaces*, In Preparation.

Zhang, G., Huang, S., **Yee, P.Y.**, Fontana, M.T., Huber, R.C., Ferreira, A.S., Knutson, N., Tolbert, S.H., and Schwartz, B.J. "Vertical Phase Segregation and Surface Recombination in Polymer:Fullerene BHJ Solar Cells: The Role of Surface Energy" *Journal of Materials Chemistry A*, In Preparation.

Kynaston, E.L., Winchell, K.J., **Yee, P.Y.**, Manion, J.G., Hendsbee, A.D., Li, Y., Huettner, S., Tolbert, S.H., Seferos, D.S. "Poly(3-alkylthiophene)-*block*-polymer(3-alkylselenophene)s: Conjugated Diblock Co-polymers with Atypical Self-Assembly Behavior" *ACS Applied Materials and Interfaces* 11 (7), (2019): 7174-7183

Scholes, D. T., **Yee, P. Y.**, McKeown, G. R., Li, S., Kang, H., Lindemuth, J. R., Xia, X., King, S. C., Seferos, D. S., Tolbert, S. H., and Schwartz, B. J. "Designing Conjugated Polymers for

Molecular Doping: The Roles of Crystallinity, Swelling, and Conductivity in Sequentially-Doped Selenophene-Based Copolymers" *Chemistry of Materials* 31, (2018): 73–82

Aubry, T. J., Ferreira, A. S., **Yee, P. Y.**, Aguirre, J. C., Hawks, S. A., Fontana, M. T., Schwartz, B. J., and Tolbert, S. H. "Processing Methods for Obtaining a Face-On Crystalline Domain Orientation in Conjugated Polymer-Based Photovoltaics" *The Journal of Physical Chemistry C* 122, (2018): 15078–15089

Fontana, M. T., Kang, H., **Yee, P. Y.**, Fan, Z., Hawks, S. A., Schelhas, L. T., Subramaniyan, S., Hwang, Y., Jenekhe, S. A., Tolbert, S. H., and Schwartz, B. J. "Low-Vapor-Pressure Solvent Additives Function as Polymer Swelling Agents in Bulk Heterojunction Organic Photovoltaics" *The Journal of Physical Chemistry C* 122, (2018): 16574–16588

Scholes, D. T., **Yee, P. Y.**, Lindemuth, J. R., Kang, H., Onorato, J., Ghosh, R., Luscombe, C. K., Spano, F. C., Tolbert, S. H., and Schwartz, B. J. "The Effects of Crystallinity on Charge Transport and the Structure of Sequentially Processed F4TCNQ-Doped Conjugated Polymer Films" *Advanced Functional Materials* 27, no. 44 (2017): 1–13

Scholes, D. T., Hawks, S. A., **Yee, P. Y.**, Wu, H., Lindemuth, J. R., Tolbert, S. H., and Schwartz, B. J. "Overcoming Film Quality Issues for Conjugated Polymers Doped with F4TCNQ by Solution Sequential Processing: Hall Effect, Structural, and Optical Measurements" *Journal of Physical Chemistry Letters* 6, no. 23 (2015): 4786–4793

Aguirre, J. C., Hawks, S. A., Ferreira, A. S., **Yee, P.**, Subramaniyan, S., Jenekhe, S. A., Tolbert, S. H., and Schwartz, B. J. "Sequential Processing for Organic Photovoltaics: Design Rules for Morphology Control by Tailored Semi-Orthogonal Solvent Blends" *Advanced Energy Materials* 5, no. 11 (2015): 1402020

Presentations

Yee, P.Y., Scholes, D.T., Lindemuth, J.R., Kang, H., Onorato, J., Ghosh, R., Luscombe, C.K., Spano, F.C., Tolbert, S.H., Schwartz, B.J. "The Effects of Crystallinity and Charge Transport and the Structure of Sequentially Processed F_4TCNQ-Doped Conjugated Polymer Films." *MRS Spring Meeting and Exhibit*, Oral Presentation, Phoenix, AZ, April 2018.

Yee, P.Y., Fontana, M.T., Huber, R.C., Aguirre, J.C., Jenekhe, S.A., Schwartz, B.J., Tolbert, S.H. "Controlling Vertical Phase Segregation in Organic Photovoltaics: Relating Device Performance to Film Morphology." *American Chemical Society National Meeting*, Oral Presentation, San Francisco, CA, April 2017.

Patents

Tolbert, S.H., Thomas, A., Dunn, B.S., Fischer, S., Roeser, J., Lin, T.C., DeBlock, R.H., Lau, J., **Yee, P.Y.** Novel Microporous Aluminate Polymers and Their Application as Solid Electrolytes and Conductive Binders for Lithium-Ion Batteries. *2019*.

Chapter 1. Introduction

Semiconducting polymers are a versatile class of materials with a variety of (opto)electronic applications. Structurally, they are comprised of carbon and earth abundant elements that keep synthetic costs low and their solubility is tunable such that they are solution processable, making device fabrication and scale-up relatively inexpensive to their inorganic counterparts.[1-7] Synthetically, the polymer backbone can be designed and modified to tune the optical and electronic properties, leading to significant advances in the performance of organic photovoltaics (OPVs), organic light emitting diodes (OLEDS), and transistors.[8-16] However, semiconducting polymers suffer intrinsically from their inherent disordered nature, wherein kinks and bends along the polymer chains disrupt the π-system and result in low conductivities, especially when compared to the inorganic materials predominantly used in commercial technologies. The effects of this inherent disorder are apparent in resulting devices, as the device performance is highly sensitive to the self-assembly of the semiconducting polymers and resultant thin film morphologies. Fortunately, there has a been a large effort in the literature to understand and improve the relationship between optical, electronic, and structural properties in semiconducting polymers.[17-24]

This nanoscale morphology is highly complex, with a multitude of factors affecting the self-assembly and corresponding electronic properties across various length scales. On a more global level, there are both crystalline and amorphous domains, where the charge transport properties are more optimal in the crystalline regions.[20,25,26] For the amorphous regions where the polymer chains are inherently disordered with bends and kinks in the chains, charge transport is much less efficient. Synthetic methods for controlling the amount and size of crystalline regions have been developed, wherein the degree of regioregularity (polymer head-to-tail ratio) or the molecular weight (MW) is tuned. Increasing the regioregularity results in a

decrease in amorphous content due to the larger driving force for large crystal formation and packing,[19,27,28] while increasing the MW increases the amount of long-chained polymers that can connect multiple crystallites via "tie-chains".[20,29] Film processing conditions can also adjust the relative crystallinity just by choosing different casting solvents, where the longer it takes for a film to dry, the more time it allows for crystallite formation.[30,31]

Within the crystalline and amorphous regions, polymer chains can self-assemble into π-stacks of different orientations with respect to the substrate as seen in Figure 1.1.[32] This orientation inherently affects the dominant charge transport direction, as charges conduct best

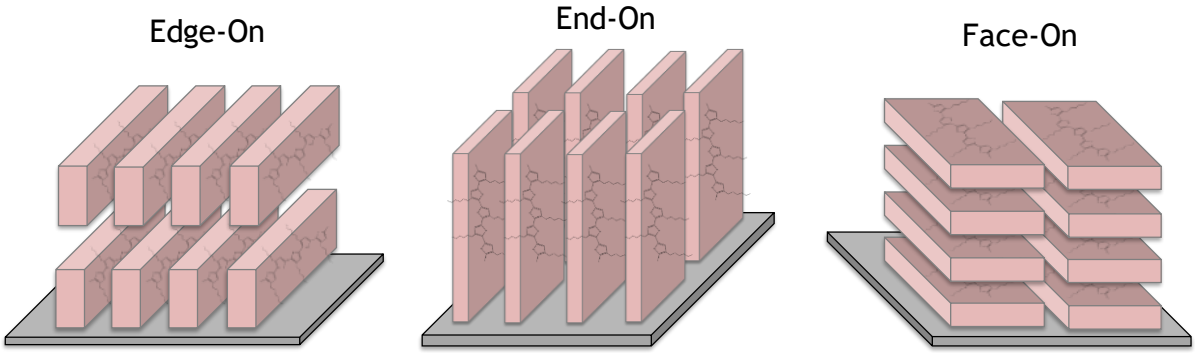

Figure 1.1. Cartoon illustrating the potential polymer stacking orientations in organic electronic devices

along the polymer backbone, followed by conduction between chains in the π-stacking direction, and least well between chains in the side chain direction. Thus, for horizontal conduction pathways such as in field-effect transistors (FETs), the preferred polymer orientation would be edge-on, where the polymer side chains align perpendicular to the substrate allowing for along chain and through the π-system transport between electrodes.[33-36] Alternatively, for top-to-bottom electrode configurations like in OPVs, the preferred, but less likely orientation would be end-on, where the polymer chains align with the polymer end perpendicular to the substrate. Instead, a face-on orientation where the polymer π-stacks are oriented perpendicular to the substrate allowing for charge carriers to move through the π-conjugation network.[37-39] On the molecular level, in addition to modifying the backbone to tune

the base optical and electronic properties, the side chains can be engineered to affect and control how the individual polymer chains will interact with each other, and thus influence the morphology throughout the thin films[40-42].

Understanding the correlation between semiconducting polymer self-assembly and the resulting optical and electronic properties is imperative for the rational design and improvement of organic electronics. This thesis focuses on controlling the self-assembly and resulting nanoscale morphology in order to better understand the structure-function relationship in these organic materials. The work presented here can be represented in three overarching parts: the first part (Chapter 2) focuses on controlling the local assembly of amphiphilic conjugated polyelectrolytes (CPEs) in water to straighten polymer chains for improved charge transport; the second part (Chapter 3) examines how to form an ideal bulk heterojunction (BHJ) by controlling the global mixing in polymer:fullerene solar cells; the final part (Chapters 4-7) investigates the structural effects upon small molecule doping of semiconducting polymers.

The first part of this thesis (Chapter 2) addresses the problem of the intrinsic disorder and resulting carrier trap sites by using self-assembly to straighten polymer chains. Amphiphilic CPEs can self-assemble into a variety of structures due to their charged side chains, wherein the assembly is driven by the kinetics of the polymer aggregation in solution.[43] A design rule to drive the formation of cylindrical micelles in water was developed with the synthesis of an alternating copolymer, poly(fluorene-alt-thiophene) (PFT), consisting of a rigid hydrophobic backbone and charged hydrophilic side chains that are all on the same side of the polymer chain.[43-45] This design rule is expanded with the design and synthesis of poly(cyclopentadithiophene-alt-thiophene) (PCT) to further straighten the polymer chain and resulting micelle formation. The cyclopentadithiophene subunit moiety has a more similar bond

angle to the thiophene moiety, resulting in a straighter polymer backbone. Upon self-assembly, this straighter backbone should result in straighter, more compact micelles as previously seen in the PFT system. In addition to straightening the polymer chains, cyclopentadithiophene absorbs in visible spectrum, making PCT particularly interesting for OPV applications, as it is capable of utilizing visible light for carrier excitation. We confirm the expansion of our design rule for straight cylinder CPE self-assembly in water using a combination of cryo-electron microscopy (cryoEM), solution small-angle X-ray scattering (SAXS), and Dammin bead modeling of the SAXS scattering data. By confirming the expansion of this amphiphilic self-assembly design rule for straightening polymer chains with the synthesis of PCT, we open up the possibilities for the incorporation of appropriate acceptors to study charge transfer properties both in solution and solid-state.

The second part of this thesis looks to control the formation of an ideal BHJ in polymer:fullerene OPVs. In order to achieve a high power conversion efficiency (PCE), these BHJs must comprise of an ideal nanoscale morphology: the donor (polymer) and acceptor (fullerene derivative) must be mixed well enough (< 20 nm) to prevent exciton recombination prior to charge separation[46] but also have separated domains for efficient charge collection.[47,48] Traditionally, this morphology has been achieved through blend-casting (BC), wherein the polymer and fullerene are codissolved in solution and deposited onto a substrate. This process, however, relies on the polymer and fullerene demixing in order to form an ideal BHJ, which is often aided by the use of solvent additives[31,49–51] or post-treatments steps such as thermal and solvent annealing[52–55]. An alternative method, sequential processing (SqP), has been more recently developed in order to more controllably form ideal [39,56–63]. With SqP, the polymer is first deposited and out of a semi-orthogonal solvent or solvent blend, as to not dissolve the underlying polymer layer, the fullerene is intercalated into the pre-existing polymer matrix.

This provides the ability to tune and control the polymer morphology first, resulting in more reproducible devices, especially when scaling up to larger devices[56].

We look to take advantage of the control provided with SqP in conjunction with tuning the fullerene casting solvent, where amorphous regions of the polymer layer are swelled by a semi-orthogonal solvent blend, to regulate the vertical mixing and incorporation of fullerenes for ideal BHJ formation. Specifically in Chapter 3, we look to control the polymer:fullerene mixing using two high-performance polymers that have different degrees of crystallinity and solubility: semi-crystalline poly[(4,8-bis[(ethylhexyl)oxy]benzo[1,2-*b*:4,5-*b*']dithiophene-2,6-diyl)(3-fluoro-2-[(2-ethylhexyl)carbonyl]thieno[3,4-*b*]thiophenediyl)] (PTB7)[64] and amorphous poly[(4,8-di(2-butyloctyl)oxybenzo[1,2-*b*:4,5-*b*']dithiophene-2,6-diyl)-alt-(2,5-bis(4,4'-bis(2-octyl)dithieno[3,2-*b*:2'3'-*d*]silole-2,6-diyl)thiazolo[5,4-*d*]thiazole)] (PSDTTT).[65] We show that by tuning the fullerene co-solvent blend, we can tune the device efficiencies for each polymer system. Using a combination of 2D-grazing-incidence wide-angle X-ray scattering (GIWAXS) and neutron reflectometry (NR), we probe both the local and global morphology as a function of increasing swelling solvent for each polymer. By controlling how effectively the solvent swells the polymer matrix, we are able to control polymer:fullerene mixing profiles within the device. These morphological changes directly correlate with improved device performances upon the addition of increased swelling solvent.

The last part of this dissertation investigates the structure-function relationship in molecular doped polymers. Alternative to controlling the self-assembly of semiconducting polymers to counteract the inherent disorder and poor conductivities, the electronic properties of these materials is readily tunable via small molecule doping.[66–74] Typical dopants are strong electron or hole acceptors that can undergo electron transfer with the polymer by either adding an electron (*n*-doping) or more commonly removing an electron (*p*-doping). At low dopant

concentrations the introduction of doped carriers can fill intrinsic trap sites[75] whereas large dopant concentrations can improve the overall conductivity and carrier mobility.[76–79] While a lot of work has been done to investigate the optical, electronic, and structural properties of doped semiconducting polymer, the polymer-dopant interactions and doping mechanism are still not well understood.[80–88] The following chapters (Chapters 4-7) aim to provide insights on the structure-function relationship upon molecular doping, particularly using SqP as a way to control and understand how the polymer morphology is affected by the addition of dopant.

In Chapter 4, we look at the immediate advantages of SqP relative to the more traditional BC technique when infiltrating the molecular dopant 2,3,5,6-tetrafluoro-7,7,8,8-tetracyanoquinodimethane (F_4TCNQ) into pure poly(3-hexylthiophene-2,5-diyl) (P3HT) thin films. Using profilometry measurements, optical microscopy, and GIWAXS, we find that with SqP the P3HT film quality and underlying morphology is preserved, allowing more dopant to be intercalated into the P3HT matrix. Contrarily, in BC-doped films P3HT and F_4TCNQ form aggregates in solution prior to casting, resulting in poor quality films and disruption of the P3HT crystallite sizes and orientation. Expanding on the benefits and morphological preservation of SqP for polymer doping, we further investigate the structural effects of doping by systematically tuning the initial polymer crystallinity. Chapter 5 again uses SqP to intercalate F_4TCNQ into P3HT films whose crystallinities have been varied using different processing techniques. GIWAXS data suggests that the F_4TCNQ anions primarily reside in the lamellar regions of the P3HT crystallites or in the amorphous regions of the film, and do not form π-stacked $P3HT^+$:F_4TCNQ^- co-crystals. Optical spectroscopy shows that increasing the crystallinity results in red-shifted polaron absorption, indicative of more mobile charge carriers that correspond to the increase in overall conductivity. Theoretical modeling of the optical spectroscopy corroborates the GIWAXS data, predicting the dopant anions to reside 6-8 Å from the polymer backbone, a distance too large for π-stacking and more in line with changes in the lamellar stacking

distances. This suggests that the increased polymer crystallinity is attributing to delocalizing the polaron by keeping the F_4TCNQ anion further away in the lamellar regions rather than in the π-stacks.

Chapter 6 utilizes a series of statistical copolymers of P3HT and poly(3-heptylselenophene-2,5-diyl) (P37S) to create a series of materials with controllably tuned gradients in bandgap, HOMO energy levels, and crystallinity. Upon SqP doping with F_4TCNQ, we determine that the copolymer's HOMO energy level relative to the F_4TNCQ LUMO energy level dominates the copolymer's ability to effectively dope. Using GIWAXS and ellipsometric porosimetry, we conclude that the final doped polymer crystallinity correlates best with increased conductivity, which in turn is dependent on the pure copolymer crystallinity, its swellability, and its ability to restructure and allow for dopant intercalation. We end our discussion of small molecule doping in Chapter 7, wherein we investigate the structural effect of doping on the amorphous regions in polymer thin films. Using regiorandom (RRa) P3HT as our model amorphous system, we use GIWAXS to monitor any structural changes upon the incorporation of a small molecule that energetically cannot dope P3HT, tetracyanoquinodimethane (TCNQ), a small molecule that cannot π-stack with P3HT upon doping, iron (III) chloride ($FeCl_3$), and the π-stackable F_4TCNQ. We determine that the act of doping, regardless of the ability to π-stack, induces a structural ordering and crystal structure change similar to that of regioregular (RR) P3HT in order to separate the dopant anion and polaron and create more mobile charge carriers.

1.1. References

(1) Bao, Z.; Rogers, J. a.; Katz, H. E. Printable Organic and Polymeric Semiconducting Materials and Devices. *J. Mater. Chem.* **1999**, *9* (9), 1895–1904.

(2) Woo, E. P.; Sirringhaus, H.; Inbasekaran, M.; Friend, R. H.; Kawase, T.; Shimoda, T.; Wu, W. High-Resolution Inkjet Printing of All-Polymer Transistor Circuits. *Science (80-.).* **2000**, *290* (5499), 2123–2126.

(3) Krebs, F. C. Fabrication and Processing of Polymer Solar Cells: A Review of Printing and Coating Techniques. *Sol. Energy Mater. Sol. Cells* **2009**, *93* (4), 394–412.

(4) Søndergaard, R. R.; Hösel, M.; Krebs, F. C. Roll-to-Roll Fabrication of Large Area Functional Organic Materials. *J. Polym. Sci. Part B Polym. Phys.* **2013**, *51* (1), 16–34.

(5) Forrest, S. R. The Path to Ubiquitous and Low-Cost Organic Electronic Appliances on Plastic. *Nature* **2014**, *428*, 911–918.

(6) Khan, S.; Lorenzelli, L.; Dahiya, R. S. Technologies for Printing Sensors and Electronics over Large Flexible Substrates: A Review. *IEEE Sens. J.* **2015**, *15* (6), 3164–3185.

(7) Arias, A. C.; MacKenzie, J. D.; McCulloch, I.; Rivnay, J.; Salleo, A. Materials and Applications for Large Area Electronics: Solution-Based Approaches. *Chem. Rev.* **2010**, *110* (1), 3–24.

(8) Hoppe, H.; Sariciftci, N. Organic Solar Cells: An Overview. *J. Mater. Res.* **2004**, *19* (07), 1924–1945.

(9) Gunes, S.; Neugebauer, H.; Sariciftci, N. S. Conjugated Polymer-Based Organic Solar Cells. *Chem. Rev.* **2007**, *107* (4), 1324–1338.

(10) Dimitrakopoulos, C. D.; Malenfant, P. R. L. Organic Thin Film Transistors for Large Area Electronics. **2002**, *14* (2), 99–117.

(11) Braun, D.; Heeger, A. J. Visible Light Emission from Semiconducting Polymer Diodes. *Appl. Phys. Lett.* **1991**, *58* (18), 1982–1984.

(12) Sirringhaus, H.; Tessler, N.; Friend, R. H. Integrated Optoelectronic Devices Based on Conjugated Polymers. *Sci. (80-.).* **1998**, *280* (5370), 1741–1744.

(13) Yu, G.; Gao, J.; Hummelen, J. C.; Wudl, F.; Heeger, A. J. Polymer Photovoltaic Cells: Enhanced Efficiencies via a Network of Internal Donor-Acceptor Heterojunctions. *Science (80-.).* **1995**, *270* (5243), 1789–1791.

(14) Burroughes, J. H.; Bradley, D. D. C.; Brown, A. R.; Marks, R. N.; Mackay, K.; Friend, R. H.; Burns, P. L.; Holmes, A. B. Light-Emitting Diodes Based on Conjugated Polymers. *Nature* **1990**, *347* (6293), 539–541.

(15) Duan, C.; Huang, F.; Cao, Y. Recent Development of Push–Pull Conjugated Polymers for Bulk-Heterojunction Photovoltaics: Rational Design and Fine Tailoring of Molecular Structures. *J. Mater. Chem.* **2012**, *22* (21), 10416.

(16) Deibel, C.; Dyakonov, V. Polymer–Fullerene Bulk Heterojunction Solar Cells. *Rep. Prog. Phys.* **2010**, *73* (9), 1–39.

(17) Liang, Z.; Reese, M. O.; Gregg, B. A. Chemically Treating Poly(3-Hexylthiophene) Defects to Improve Bulk Heterojunction Photovoltaics. *ACS Appl. Mater. Interfaces* **2011**, *3* (6), 2042–2050.

(18) Xin, H.; Reid, O. G.; Ren, G.; Kim, F. S.; Ginger, D. S.; Jenekhe, S. A. Polymer Nanowire/Fullerene Bulk Heterojunction Solar Cells: How Nanostructure Determines Photovoltaic Properties. *ACS Nano* **2010**, *4* (4), 1861–1872.

(19) Mazzio, K. A.; Rice, A. H.; Durban, M. M.; Luscombe, C. K. Effect of Regioregularity on Charge Transport and Structural and Excitonic Coherence in Poly(3-Hexylthiophene) Nanowires. *J. Phys. Chem. C* **2015**, *119* (27), 14911–14918.

(20) Noriega, R.; Rivnay, J.; Vandewal, K.; Koch, F. P. V; Stingelin, N.; Smith, P.; Toney, M. F.; Salleo, A. A General Relationship between Disorder, Aggregation and Charge Transport in Conjugated Polymers. *Nat. Mater.* **2013**, *12* (8), 1–7.

(21) Rogers, J. T.; Schmidt, K.; Toney, M. F.; Kramer, E. J.; Bazan, G. C. Structural Order in Bulk Heterojunction Films Prepared with Solvent Additives. *Adv. Mater.* **2011**, *23* (20), 2284–2288.

(22) Porzio, W.; Scavia, G.; Barba, L.; Arrighetti, G.; Milita, S. Depth-Resolved Molecular Structure and Orientation of Polymer Thin Films by Synchrotron X-Ray Diffraction. *Eur. Polym. J.* **2011**, *47* (3), 273–283.

(23) Woo, C. H.; Piliego, C.; Holcombe, T. W.; Toney, M. F.; Fre, J. M. J. A Quantitative Correlation between the Mobility and Crystallinity of Photo-Cross-Linkable P3HT. **2012**.

(24) Rivnay, J.; Salleo, a; Mannsfeld, S.; Miller, C.; Toney, M. Determination of Organic Semiconductor Microstructure from the Molecular to Device Scale with Quantitative X-Ray Scattering and Absorption Analyses. *Chem. Rev.* **2012**, *112*, 5488–5519.

(25) Kline, R. J.; McGehee, M. D. Morphology and Charge Transport in Conjugated Polymers. *Polym. Rev.* **2006**, *46* (1), 27–45.

(26) Mollinger, S. A.; Salleo, A.; Spakowitz, A. J. Anomalous Charge Transport in Conjugated Polymers Reveals Underlying Mechanisms of Trapping and Percolation. *ACS Cent. Sci.* **2016**, *2* (12), 910–915.

(27) Bolinger, J. C.; Traub, M. C.; Brazard, J.; Adachi, T.; Barbara, P. F.; Vanden Bout, D. A. Conformation and Energy Transfer in Single Conjugated Polymers. *Acc. Chem. Res.* **2012**, *45* (11), 1992–2001.

(28) Poelking, C.; Andrienko, D. Effect of Polymorphism, Regioregularity and Paracrystallinity on Charge Transport in Poly(3-Hexylthiophene) [P3HT] Nanofibers. *Macromolecules* **2013**, *46* (22), 8941–8956.

(29) Mollinger, S. A.; Krajina, B. A.; Noriega, R.; Salleo, A.; Spakowitz, A. J. Percolation, Tie-Molecules, and the Microstructural Determinants of Charge Transport in Semicrystalline Conjugated Polymers. *ACS Macro Lett.* **2015**, *4* (7), 708–712.

(30) Chang, J. F.; Sun, B.; Breiby, D. W.; Nielsen, M. M.; Sölling, T. I.; Giles, M.; McCulloch, I.; Sirringhaus, H. Enhanced Mobility of Poly(3-Hexylthiophene) Transistors by Spin-Coating from High-Boiling-Point Solvents. *Chem. Mater.* **2004**, *16* (23), 4772–4776.

(31) Kwon, S.; Kang, H.; Lee, J. H.; Lee, J.; Hong, S.; Kim, H.; Lee, K. Effect of Processing Additives on Organic Photovoltaics: Recent Progress and Future Prospects. *Adv. Energy Mater.* **2017**, *7* (10).

(32) Chabinyc, M. L. *X-Ray Scattering from Films of Semiconducting Polymers*; 2008; Vol. 48.

(33) Sirringhaus, H.; Brown, P. J.; Friend, R. H.; Nielsen, M. M.; Bechgaard, K.; Langeveld-Voss, B. M. W.; Spiering, a. J. H.; Janssen, R. a. J.; Meijer, E. W.; Herwig, P.; et al. Two-Dimensional Charge Transport in Self-Organized, High-Mobility Conjugated Polymers. *Nature* **1999**, *401* (6754), 685–688.

(34) Kline, R. J.; McGehee, M. D.; Kadnikova, E. N.; Liu, J.; Fréchet, J. M. J.; Toney, M. F. Dependence of Regioregular Poly(3-Hexylthiophene) Film Morphology and Field-Effect Mobility on Molecular Weight. *Macromolecules* **2005**, *38* (8), 3312–3319.

(35) Heil, H.; Finnberg, T.; Von Malm, N.; Schmechel, R.; Von Seggern, H. The Influence of Mechanical Rubbing on the Field-Effect Mobility in Polyhexylthiophene. *J. Appl. Phys.* **2003**, *93* (3), 1636–1641.

(36) Horowitz, G. Organic Field-Effect Transistors. *Adv. Mater.* **1998**, *10* (5), 365–377.

(37) Ma, J.; Hashimoto, K.; Koganezawa, T.; Tajima, K. End-on Orientation of Semiconducting Polymers in Thin Films Induced by Surface Segregation of Fluoroalkyl Chains. *J. Am. Chem. Soc.* **2013**, *135* (26), 9644–9647.

(38) Saeki, A.; Koizumi, Y.; Aida, T.; Seki, S. Comprehensive Approach to Intrinsic Charge Carrier Mobility in Conjugated Organic Molecules, Macromolecules, and Supramolecular Architectures. *Acc. Chem. Res.* **2012**, *45* (8), 1193–1202.

(39) Aubry, T. J.; Ferreira, A. S.; Yee, P. Y.; Aguirre, J. C.; Hawks, S. A.; Fontana, M. T.; Schwartz, B. J.; Tolbert, S. H. Processing Methods for Obtaining a Face-On Crystalline Domain Orientation in Conjugated Polymer-Based Photovoltaics. *J. Phys. Chem. C* **2018**, *122*, 15078–15089.

(40) Beaujuge, P. M.; Fréchet, J. M. J.; Toney, M. F.; Lee, O. P.; Yiu, A. T.; Woo, C. H. Side-Chain Tunability of Furan-Containing Low-Band-Gap Polymers Provides Control of

Structural Order in Efficient Solar Cells. *J. Am. Chem. Soc.* **2011**, *134* (4), 2180–2185.

(41) Strzalka, J.; Guo, J.; Chen, L. X.; Xu, T.; Yu, L.; Rolczynski, B. S.; Marks, T. J.; Loser, S.; Lee, B.; Liang, Y.; et al. When Function Follows Form: Effects of Donor Copolymer Side Chains on Film Morphology and BHJ Solar Cell Performance. *Adv. Mater.* **2010**, *22* (48), 5468–5472.

(42) Mei, J.; Bao, Z. Side Chain Engineering in Solution-Processable Conjugated Polymers. *Chem. Mater.* **2014**, *26* (1), 604–615.

(43) Clark, A. P.-Z.; Shi, C.; Ng, B. C.; Wilking, J. N.; Ayzner, A. L.; Stieg, A. Z.; Schwartz, B. J.; Mason, T. G.; Rubin, Y.; Tolbert, S. H. Self-Assembling Semiconducting Polymers—Rods and Gels from Electronic Materials. *ACS Nano* **2013**, *7* (2), 962–977.

(44) Huber, R. C.; Ferreira, A. S.; Thompson, R.; Kilbride, D.; Knutson, N. S.; Devi, L. S.; Toso, D. B.; Challa, J. R.; Zhou, Z. H.; Rubin, Y.; et al. Long-Lived Photoinduced Polaron Formation in Conjugated Polyelectrolyte-Fullerene Assemblies. *Science (80-.).* **2015**, *348* (6241), 1340–1343.

(45) Huber, R. C.; Ferreira, A. S.; Aguirre, J. C.; Kilbride, D.; Toso, D. B.; Mayoral, K.; Zhou, Z. H.; Kopidakis, N.; Rubin, Y.; Schwartz, B. J.; et al. Structure and Conductivity of Semiconducting Polymer Hydrogels. *J. Phys. Chem. B* **2016**, *120* (26), 6215–6224.

(46) Shaw, P. E.; Ruseckas, A.; Samuel, I. D. W. Exciton Diffusion Measurements in Poly(3-Hexylthiophene). *Adv. Mater.* **2008**, *20* (18), 3516–3520.

(47) Halls, J. J. M.; Walsh, C. A.; Greenham, N.; Marseglia, E. A.; Friend, R.; Moratti, S. C.; Holmes, A. Efficient Photodiodes from Interpenetrating Polymer Networks. *Nature* **1995**, *376* (6540), 498–500.

(48) Shaheen, S. E.; Brabec, C. J.; Sariciftci, N. S.; Padinger, F.; Fromherz, T.; Hummelen, J. C. 2.5% Efficient Organic Plastic Solar Cells. *Appl. Phys. Lett.* **2001**, *78* (6), 841–843.

(49) Peet, J.; Kim, J. Y.; Coates, N. E.; Ma, W. L.; Moses, D.; Heeger, A. J.; Bazan, G. C. Efficiency Enhancement in Low-Bandgap Polymer Solar Cells by Processing with Alkane Dithiols. *Nat Mater* **2007**, *6* (7), 497–500.

(50) Lee, J. K.; Ma, W. L.; Brabec, C. J.; Yuen, J.; Moon, J. S.; Kim, J. Y.; Lee, K.; Bazan, G. C.; Heeger, A. J. Processing Additives for Improved Efficiency from Bulk Heterojunction Solar Cells. *J. Am. Chem. Soc.* **2008**, *130* (11), 3619–3623.

(51) Zhao, Y.; Xie, Z.; Qu, Y.; Geng, Y.; Wang, L. Solvent-Vapor Treatment Induced Performance Enhancement of Poly(3-Hexylthiophene):Methanofullerene Bulk-Heterojunction Photovoltaic Cells. *Appl. Phys. Lett.* **2007**, *90* (4), 43503–43504.

(52) Ma, W.; Yang, C.; Gong, X.; Lee, K.; Heeger, A. J. Thermally Stable, Efficient Polymer Solar Cells with Nanoscale Control of the Interpenetrating Network Morphology. *Adv. Funct. Mater.* **2005**, *15* (10), 1617–1622.

(53) Huttner, S.; Sommer, M.; Chiche, A.; Krausch, G.; Steiner, U.; Thelakkat, M. Controlled Solvent Vapour Annealing for Polymer Electronics. *Soft Matter* **2009**, *5* (21), 4206–4211.

(54) Verploegen, E.; Miller, C. E.; Schmidt, K.; Bao, Z.; Toney, M. F. Manipulating the Morphology of P3HT–PCBM Bulk Heterojunction Blends with Solvent Vapor Annealing. *Chem. Mater.* **2012**, *24* (20), 3923–3931.

(55) Ayzner, A. L.; Wanger, D. D.; Tassone, C. J.; Tolbert, S. H.; Schwartz, B. J. Room to Improve Conjugated Polymer-Based Solar Cells: Understanding How Thermal Annealing Affects the Fullerene Component of a Bulk Heterojunction Photovoltaic Device. *J. Phys. Chem. C* **2008**, *112* (48), 18711–18716.

(56) Hawks, S. A.; Aguirre, J. C.; Schelhas, L. T.; Thompson, R. J.; Huber, R. C.; Ferreira, A. S.; Zhang, G.; Herzing, A. A.; Tolbert, S. H.; Schwartz, B. J. Comparing Matched Polymer:Fullerene Solar Cells Made by Solution-Sequential Processing and Traditional Blend Casting: Nanoscale Structure and Device Performance. *J. Phys. Chem. C* **2014**, *118* (31), 17413–17425.

(57) Fontana, M. T.; Kang, H.; Yee, P. Y.; Fan, Z.; Hawks, S. A.; Schelhas, L. T.; Subramaniyan, S.; Hwang, Y.; Jenekhe, S. A.; Tolbert, S. H.; et al. Low-Vapor-Pressure Solvent Additives Function as Polymer Swelling Agents in Bulk Heterojunction Organic Photovoltaics. *J. Phys. Chem. C* **2018**, *122*, 16574–16588.

(58) Aguirre, J. C.; Hawks, S. A.; Ferreira, A. S.; Yee, P.; Subramaniyan, S.; Jenekhe, S. A.; Tolbert, S. H.; Schwartz, B. J. Sequential Processing for Organic Photovoltaics: Design Rules for Morphology Control by Tailored Semi-Orthogonal Solvent Blends. *Adv. Energy Mater.* **2015**, *5* (11), doi: 10.1002/aenm.201402020.

(59) Ayzner, A. L.; Tassone, C. J.; Tolbert, S. H.; Schwartz, B. J. Reappraising the Need for Bulk Heterojunctions in Polymer−Fullerene Photovoltaics: The Role of Carrier Transport in All-Solution-Processed P3HT/PCBM Bilayer Solar Cells. *J. Phys. Chem. C* **2009**, *113* (46), 20050–20060.

(60) Gevaerts, V. S.; Koster, L. J. A.; Wienk, M. M.; Janssen, R. A. J. Discriminating between Bilayer and Bulk Heterojunction Polymer:Fullerene Solar Cells Using the External Quantum Efficiency. *ACS Appl. Mater. Interfaces* **2011**, *3* (9), 3252–3255.

(61) Cheng, P.; Hou, J.; Li, Y.; Zhan, X. Layer-by-Layer Solution-Processed Low-Bandgap Polymer-PC 61 BM Solar Cells with High Efficiency. *Adv. Energy Mater.* **2014**, *4* (9), 1301349.

(62) Zhang, G.; Huber, R. C.; Ferreira, A. S.; Boyd, S. D.; Luscombe, C. K.; Tolbert, S. H.; Schwartz, B. J. Crystallinity Effects in Sequentially Processed and Blend-Cast Bulk-Heterojunction Polymer/Fullerene Photovoltaics. *J. Phys. Chem. C* **2014**, *118* (32), 18424–18435.

(63) Ferreira, A. S.; Aguirre, J. C.; Subramaniyan, S.; Jenekhe, S. A.; Tolbert, S. H.; Schwartz, B. J. Understanding How Polymer Properties Control OPV Device Performance: Regioregularity, Swelling, and Morphology Optimization Using Random

Poly(3-Butylthiophene-Co-3-Octylthiophene) Polymers. *J. Phys. Chem. C* **2016**, *120* (39), 22115–22125.

(64) Liang, Y.; Xu, Z.; Xia, J.; Tsai, S. T.; Wu, Y.; Li, G.; Ray, C.; Yu, L. For the Bright Future-Bulk Heterojunction Polymer Solar Cells with Power Conversion Efficiency of 7.4%. *Adv. Mater.* **2010**, *22* (20).

(65) Subramaniyan, S.; Xin, H.; Kim, F. S.; Shoaee, S.; Durrant, J. R.; Jenekhe, S. A. Effects of Side Chains on Thiazolothiazole-Based Copolymer Semiconductors for High Performance Solar Cells. *Adv. Energy Mater.* **2011**, *1* (5), 854–860.

(66) Gao, Z. Q.; Mi, B. X.; Xu, G. Z.; Wan, Y. Q.; Gong, M. L.; Cheah, K. W.; Chen, C. H. An Organic P-Type Dopant with High Thermal Stability for an Organic Semiconductor. *Chem. Commun. (Camb).* **2008**, No. 1, 117–119.

(67) Yamamoto, J.; Furukawa, Y. Electronic and Vibrational Spectra of Positive Polarons and Bipolarons in Regioregular Poly(3-Hexylthiophene) Doped with Ferric Chloride. *J. Phys. Chem. B* **2015**, *119* (13), 4788–4794.

(68) Scholes, D. T.; Hawks, S. A.; Yee, P. Y.; Wu, H.; Lindemuth, J. R.; Tolbert, S. H.; Schwartz, B. J. Overcoming Film Quality Issues for Conjugated Polymers Doped with F4TCNQ by Solution Sequential Processing: Hall Effect, Structural, and Optical Measurements. *J. Phys. Chem. Lett.* **2015**, *6* (23), 4786–4793.

(69) Jacobs, I. E.; Aasen, E. W.; Oliveira, J. L.; Fonseca, T. N.; Roehling, J. D.; Li, J.; Zhang, G.; Augustine, M. P.; Mascal, M.; Moulé, A. J. Comparison of Solution-Mixed and Sequentially Processed P3HT:F4TCNQ Films: Effect of Doping-Induced Aggregation on Film Morphology. *J. Mater. Chem. C* **2016**, *4* (16), 3454–3466.

(70) Méndez, H.; Heimel, G.; Winkler, S.; Frisch, J.; Opitz, A.; Sauer, K.; Wegner, B.; Oehzelt, M.; Röthel, C.; Duhm, S.; et al. Charge-Transfer Crystallites as Molecular Electrical Dopants. *Nat. Commun.* **2015**, *6*, 8560.

(71) Fincher, Jr., C. R.; Ozaki, M.; Tanak, M.; Peebles, D.; Lauchlan, L.; Heeger, A. J. Electronic Structure of Polyacetylene: Optical and Infrared Studies of Undoped Semiconducting (CH)x and Heavily Doped Metallic (CH)X. *Phys. Rev. B* **1979**, *20* (4).

(72) Seeger, K.; Gill, W. D.; Clarke, T. C.; Street, G. B. Conductivity and Hall Effect Measurements in Doped Polyacetylene. *Solid State Commun.* **1978**, *28* (10), 873–878.

(73) Karpov, Y.; Erdmann, T.; Raguzin, I.; Al-Hussein, M.; Binner, M.; Lappan, U.; Stamm, M.; Gerasimov, K. L.; Beryozkina, T.; Bakulev, V.; et al. High Conductivity in Molecularly P-Doped Diketopyrrolopyrrole-Based Polymer: The Impact of a High Dopant Strength and Good Structural Order. *Adv. Mater.* **2016**, 6003–6010.

(74) Gao, J.; Roehling, J. D.; Li, Y.; Guo, H.; Moulé, A. J.; Grey, J. K. The Effect of 2,3,5,6-Tetrafluoro-7,7,8,8-Tetracyanoquinodimethane Charge Transfer Dopants on the Conformation and Aggregation of Poly(3-Hexylthiophene). *J. Mater. Chem. C* **2013**, *1* (36), 5638.

(75) Yu, S.; Frisch, J.; Opitz, A.; Cohen, E.; Bendikov, M.; Koch, N.; Salzmann, I. Effect of Molecular Electrical Doping on Polyfuran Based Photovoltaic Cells. *Appl. Phys. Lett.* **2015**, *106* (20).

(76) Lu, G.; Blakesley, J.; Himmelberger, S.; Pingel, P.; Frisch, J.; Lieberwirth, I.; Salzmann, I.; Oehzelt, M.; Di Pietro, R.; Salleo, A.; et al. Moderate Doping Leads to High Performance of Semiconductor/Insulator Polymer Blend Transistors. *Nat. Commun.* **2013**, *4*, 1588.

(77) Wang, Z.; Zou, Y.; Chen, W.; Huang, Y.; Yao, C.; Zhang, Q. The Role of Weak Molecular Dopants in Enhancing the Performance of Solution-Processed Organic Field-Effect Transistors. *Adv. Electron. Mater.* **2018**, *1800547*, 1800547.

(78) Glaudell, A. M.; Cochran, J. E.; Patel, S. N.; Chabinyc, M. L. Impact of the Doping Method on Conductivity and Thermopower in Semiconducting Polythiophenes. *Adv. Energy Mater.* **2015**, *5* (4).

(79) Lim, E.; Peterson, K. A.; Su, G. M.; Chabinyc, M. L. Thermoelectric Properties of Poly(3-Hexylthiophene) (P3HT) Doped with 2,3,5,6-Tetrafluoro-7,7,8,8-Tetracyanoquinodimethane (F4TCNQ) by Vapor-Phase Infiltration. *Chem. Mater.* **2018**, *30* (3), 998–1010.

(80) Chew, A. R.; Ghosh, R.; Shang, Z.; Spano, F. C.; Salleo, A. Sequential Doping Reveals the Importance of Amorphous Chain Rigidity in Charge Transport of Semi-Crystalline Polymers. *J. Phys. Chem. Lett.* **2017**, 4974–4980.

(81) Hamidi-Sakr, A.; Biniek, L.; Bantignies, J. L.; Maurin, D.; Herrmann, L.; Leclerc, N.; Lévêque, P.; Vijayakumar, V.; Zimmermann, N.; Brinkmann, M. A Versatile Method to Fabricate Highly In-Plane Aligned Conducting Polymer Films with Anisotropic Charge Transport and Thermoelectric Properties: The Key Role of Alkyl Side Chain Layers on the Doping Mechanism. *Adv. Funct. Mater.* **2017**, *27* (25), 1–13.

(82) Jacobs, I. E.; Cendra, C.; Harrelson, T. F.; Bedolla Valdez, Z. I.; Faller, R.; Salleo, A.; Moulé, A. J. Polymorphism Controls the Degree of Charge Transfer in a Molecularly Doped Semiconducting Polymer. *Mater. Horizons* **2018**, 3–6.

(83) Thomas, E. M.; Brady, M. A.; Nakayama, H.; Popere, B. C.; Segalman, R. A.; Chabinyc, M. L. X-Ray Scattering Reveals Ion-Induced Microstructural Changes During Electrochemical Gating of Poly(3-Hexylthiophene). *Adv. Funct. Mater.* **2018**, *1803687*, 1–8.

(84) Tang, K.; McFarland, F.; Travis, S.; Lim, J.; Azoulay, J. D.; Guo, S. Aggregation of P3HT as a Preferred Pathway for Its Chemical Doping by F4-TCNQ. *Chem. Commun.* **2018**, *1* (c), 11925–11928.

(85) Hase, H.; O'Neill, K.; Frisch, J.; Opitz, A.; Koch, N.; Salzmann, I. Unraveling the Microstructure of Molecularly Doped Poly(3-Hexylthiophene) by Thermally Induced Dedoping. *J. Phys. Chem. C* **2018**, *122*, 25893–25899.

(86) Hynynen, J.; Kiefer, D.; Yu, L.; Kroon, R.; Munir, R.; Amassian, A.; Kemerink, M.; Müller, C. Enhanced Electrical Conductivity of Molecularly P-Doped Poly(3-Hexylthiophene) through Understanding the Correlation with Solid-State Order. *Macromolecules* **2017**, *50* (20), 8140–8148.

(87) Neelamraju, B.; Watts, K. E.; Pemberton, J. E.; Ratcliff, E. L. Correlation of Coexistent Charge Transfer States in F_4TCNQ-Doped P3HT with Microstructure. *J. Phys. Chem. Lett.* **2018**, 6871–6877.

(88) Liu, W.; Müller, L.; Ma, S.; Barlow, S.; Marder, S. R.; Kowalsky, W.; Köhn, A.; Lovrincic, R. The Origin of the π-π Spacing Change upon Doping of Semiconducting Polymers. *J. Phys. Chem. C* **2018**, *122* (49), 27983–27990.

Chapter 2. Design Rule for Straightening Conjugated Polymer Electrolyte Chains for OPV Applications

2.1. Introduction

Semiconducting conjugated polymers have a variety of applications due to their ease of processing, low-cost, and structural tunability.[1-5] In particular, the electronic tunability and ability to control polymer self-assembly provide logical routes to improve the device performance for organic photovoltaics (OPVs). However, semiconducting polymers suffer intrinsically from their inherent disorder. Any kink or bend along the polymer backbone breaks the π-conjugation, creating a carrier trap and thus decreases the polymer conductivity. Poor conductivity as a result of the inherent disorder directly affects device performance.

Recently, one method of improving polymer conductivity that has been studied extensively is of molecular doping.[6-11] At low dopant concentrations the introduction of doped carriers can fill intrinsic trap sites[12-14] whereas large dopant concentrations can improve the overall conductivity and carrier.[15-18] Alternatively, the intrinsic conductivity can be improved by controlling the polymer morphology to reduce the kinks and bends in the polymer chain and therefore decrease the number of carrier trap sites. Tuning the polymer side-chains to promote more tightly π-stacked domains has been shown to improve OPV device performance and carrier transport,[19-22] while controlling the polymer crystallinity and polymer π-stacking orientation has also been heavily investigated to improve OPV efficiencies.[23-26]

We aim to address the problem of the intrinsic disorder and resulting carrier trap sites by using amphiphilic self-assembly as a driving force to straighten the polymer chains. Other methods to improve the intrinsic carrier mobility by causing the polymer chains to be straighter has been previously investigated. By using inorganic host systems, semiconducting polymers

such as poly-(3-hexylthiophene-2,5-diyl) (P3HT) and poly[2-methoxy-5-(2'-ethylhexyloxy)-p-phenylene vinylene] (MEH-PPV) have been infiltrated into straight nanopores.[27-30] In particular, Coakley et al. showed using this method that the hole mobility of regioregular P3HT could be enhanced by a factor of 20.[29] However, the use of these inorganic host systems limit the application despite improving carrier mobility and charge transfer properties due to chain straightening.

To make straighter polymer chains while circumventing the host system strategy, we have taken advantage of the amphiphilic self-assembly of conjugated polyelectrolytes (CPEs).[31] CPEs are polymers that consist of a conjugated backbone with charged sidechains, allowing for processing in polar solvents and unique self-assembly properties. CPEs are particularly useful for optoelectronic properties because their bandgap and other electronic properties are dependent only on the conjugated back-bone, while the solvation of the charged side chains and anion can be used to drive the desired self-assembly.[32,33] In the past, we have extensively studied, poly(fluorene-alt-thiophene) (PFT), an alternating copolymer with a rigid hydrophobic

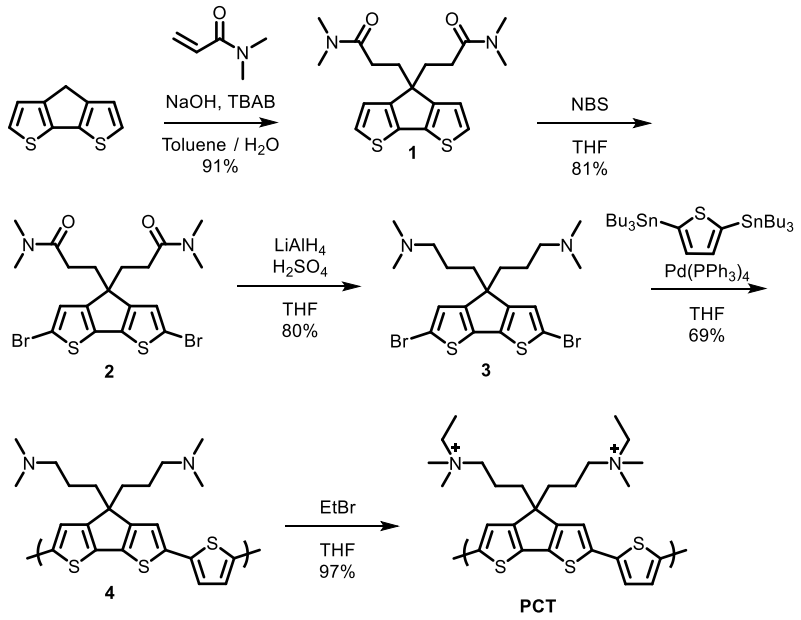

Scheme 2.1: Synthetic route for PCT.

conjugated backbone and charged hydrophilic side chains that are all on the same side of the polymer chain., This alternating copolymer CPEs structure creates a driving force for the formation of straight, cylindrical micelles.[31,34-36] Studies of the optical and structural properties of PFT, showed efficient charge transfer properties with acceptor molecules and straight cylindrical micelle assembly.

In this work, we expand on this alternating copolymer amphiphilic CPE design rule to a new polymer system. By exchanging the fluorene monomer subunit with cyclopentadithiophene, we synthesized poly(cyclopentadithiophene-alt-thiophene) (PCT), chemical structure shown in Scheme 2.1. We hypothesized that this new structure would demonstrate two advantages over the previously studied PFT. As compared to the fluorene unit in PFT, the cyclopentadithiophene subunit moiety has a more similar bond angle to the thiophene moiety, resulting in a straighter polymer backbone. Upon self-assembly, this straighter backbone should, in theory, result in straighter cylindrical micelles that what was previously seen in the PFT system. In addition to straightening the polymer chains, cyclopentadithiophene absorbs in the visible spectrum,[37] which should make this polymer more applicable for use in OPVs. We will study the expansion of our design rule for straight cylinder CPE self-assembly in water using a combination of cryo electron microscopy (cryoEM), solution small-angle X-ray scattering (SAXS), and Dam-min bead modeling of the SAXS scattering data. Overall, we aim to demonstrate that this amphiphilic polymer structure can be used as a design rule for making straight polymer chains.

2.2. Results and Discussion

The linear structure of amphiphilic PCT was achieved through choice of cyclopentadithiophene as one of the monomeric units and incorporation of hydrophilic terminal ammonium side chains. Installation of these side chains began via Michael addition at the sp^3

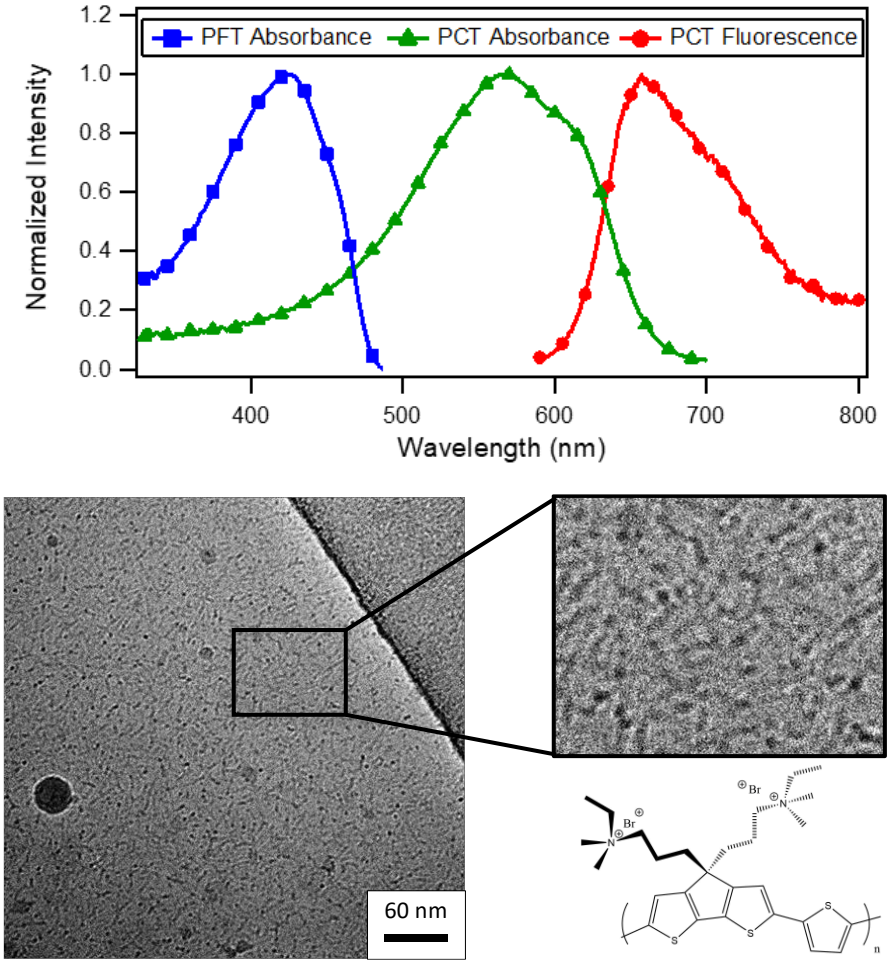

Figure 2.1: (a) optical characterization of PCT demonstrating visible-region band gap absorption. (b) cryoEM image of PCT solution showing micelle-like structures with average diameters of 2 nm, and a chemical structure of PCT.

carbon of the cyclopentadithiophene moiety. Subsequent bromination and later reduction of the amides to amines yielded the monomeric core of PCT, which could later be functionalized. After polymerization with 2,5-bis(tributylstannyl)thiophene, the final polymer is quaternized with ethylbromide to give hydrophilic terminal ammonium moieties. The versatility in this strategy easily allows for changes to the core or side chains and thus a potential library of amphiphilic polymers.

Optical characterization of PCT shown in Figure 1a demonstrates the large red-shift in the band gap as com-pared to PCT is caused only by exchanging the fluorine unit for

cyclopentadithiophene. As expected the emission spectrum is further red-shifted. These optical results demonstrate that the band gap of this polymer can easily be tuned with only slight changes in the atomic structure.

We performed preliminary structural characterization by observing dilute samples of PCT in water with cryoEM, as seen in Figure 2.1. The cryoEM samples are prepared by the standard method, producing thin-films of vitreous solution suspended across holey-carbon grids. The procedure produces a network of micelles with many individual micelles overlapping one another, and each micelle measuring about 2 nm in diameter. While the formation of a micellar-

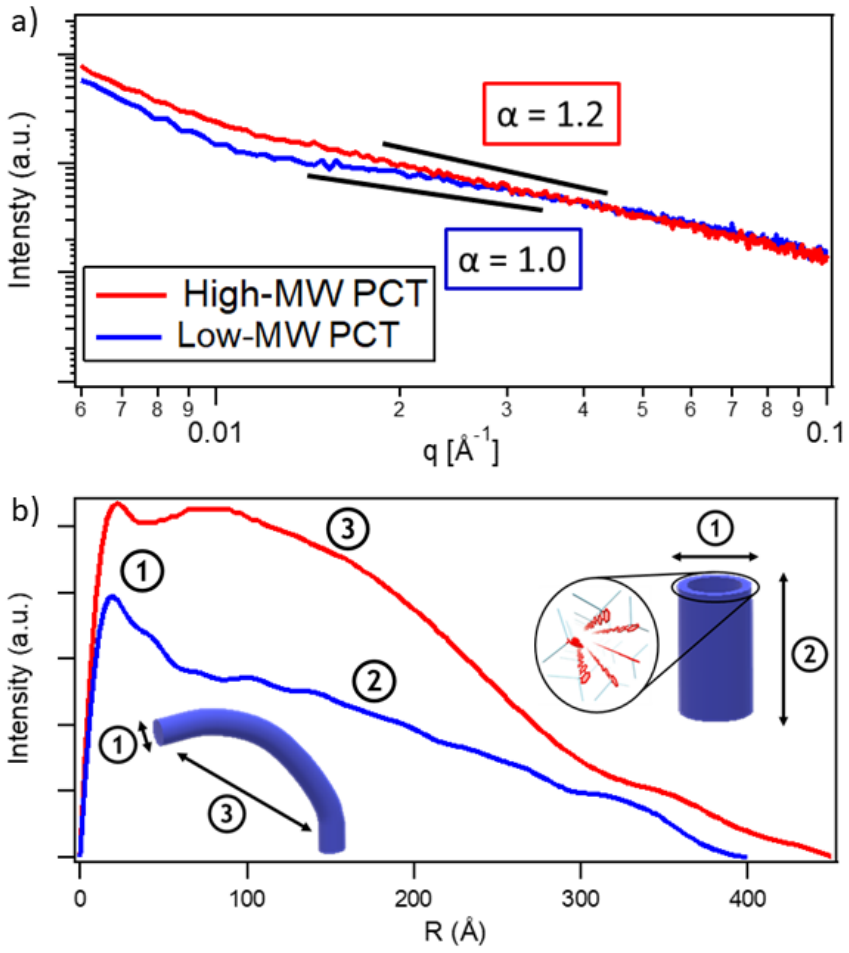

Figure 2.2: (a) radially averaged SAXS data with power-law fits and (b) P(r) transformations of the SAXS data confirming rod-like micelle structures for both high- (red) and low- (blue) MW PCT in water.

network makes distinguishing individual micelles difficult, we estimate that the average length of each micelle is roughly several-tens-of-nanometers. Most importantly, the cryoEM data provides clear evidence for PCT micelle formation.

To complement the images of our cylindrical micelles, we use solution SAXS which provides more quantitative information on the size and shape of self-assembly and aggregates in solution. All samples measured by solution SAXS underwent size-selective precipitation to separate high and low molecular weight. We expect low molecular weight polymer chains to demonstrate nearly ideal cylindrical self-assembly behavior while high molecular weight chains will give us insight as to the behavior that would be observed if these polymers were used in real OPV applications. The raw scattering data in Figure 2.2a of both high- and low-molecular weight (MW) samples (red and blue curves, respectively) are fairly featureless, which is expected for cylindrical micelles in solution.[31,38,39] The general shape of solution self-assembly can be determined by fitting to a Guinier/power law, wherein the power law slope is representative of the polymer fractal structure.[40] In essence, this power law slope is representative of the dimensionality of the average shapes in solution: slopes of 1, 2, and 3 correlate to rigid rod, flat disk, and spherical structures, respectively. Interactions between molecules, or branching/bending in the case of rigid rods, will result in deviations from a slope of 1. As can be seen in Figure 2.2a, both high- and low-MW scattering profiles have slopes near 1, with the low-MW scattering profile fitting exactly to 1. This confirms that using the cyclopentadithiophene unit to match the bond angle of the thiophene unit, indeed straightens the polymer chain and results in perfectly straight micelles at low-MW. For the high-MW sample, the deviation of the power law slope to 1.3 can be explained by the presence of longer chains that increase the odds of misaligned polymer chains during micelle formation resulting in slightly curved micelles.

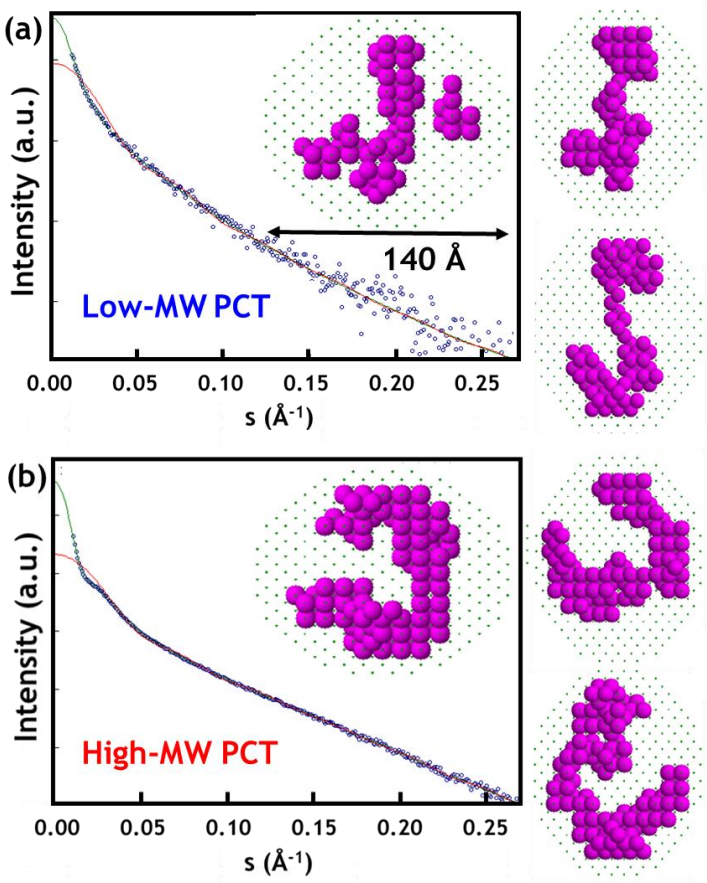

Figure 2.3: Dammin bead model fit and structure for (a) 1 mg/mL high-MW PCT and (b) 1 mg/mL low-MW PCT confirming rod-like micelle shapes; the curvature in the high-MW PCT is due to the broad correlation peak seen in the *P(r)* function from Figure 2.2c.

The radially averaged scattering data shown in Figure 2.2a can then be Fourier transformed to pair-distance distribution functions, *P(r)*, as seen in Figure 2.2b. These *P(r)* functions represent the radially averaged distribution of electron density correlations as a function of the separation distance, *r*, within a solution-phase aggregate.[38,41,42] We note that if the interparticle spacing is ordered, such as in liquid crystals or aligned systems, we would observe distinct peaks representing the corresponding average interparticle distance.[43,44] The *P(r)* functions of the SAXS data in part at in Figure 2.2b confirm the cylindrical scattering profile with a sharp peak corresponding to the diameter of the cylinder (region 1) followed by a linear decay (region 2) related to the long axis of the cylinder. For both high- and low-MW PCT samples (red and blue curves, respectively), there is a sharp peak at r=~20 Å. Particularly in the case of

low-MW, the P(r) demonstrates a shape nearly identical to that of a perfect rigid rod, further indicating that matching the bond angles between the alternating units of the copolymer is crucial for creating straight polymer chains. We also note that there is a broad peak centered at ~100 Å for the high-MW sample (red curve, region 3), suggesting some intra-particle correlation is possible at longer chain lengths due to curvature of the micelle, a phenomenon which will be discussed in more detail below.

In addition to the cryoEM, SAXS power-law analysis, and *P(r)* transformations, we perform Dammin bead modeling, a type of Monte Carlo simulation of our SAXS data, to conclusively prove expansion of our design rule for straightening polymer chains using amphiphilic CPEs with the synthesis of PCT. Before performing the simulation, the radially averaged SAXS is fit to a singular function (green, Figure 2.2) based on shape and size constraints. The Dammin bead model then uses this fit of the data to output a simulated structure in agreement with, and representative of, the scattering data.[42,45]

Low-MW 3D reconstruction results (Figure 2.3a) show straight-rod like chains that are in agreement with the Guinier-Porod fit and the *P(r)* function suggesting straight polymer micelles. The overall shape of the high-MW micelle simulations still represent cylinders but only at shorter length scales. As would be expected by the intra-particle correlation peak seen in the *P(r)* results, high-MW polymer chains are long enough to have a slight bend to them. The size limit of this integration is 140 nm, thus the electron density correlation peak at 100 nm falls well within the limits of the model. Overall, the comparison of high and low molecule weight Dammin bead models further demonstrate that PCT forms rod-like micelles with straight chains but, as expected, high molecular weight polymer chains have slight more disorder resulting in some curvature to the micelles. For both samples, more examples of bead models are shown in Figures S2 and S3.

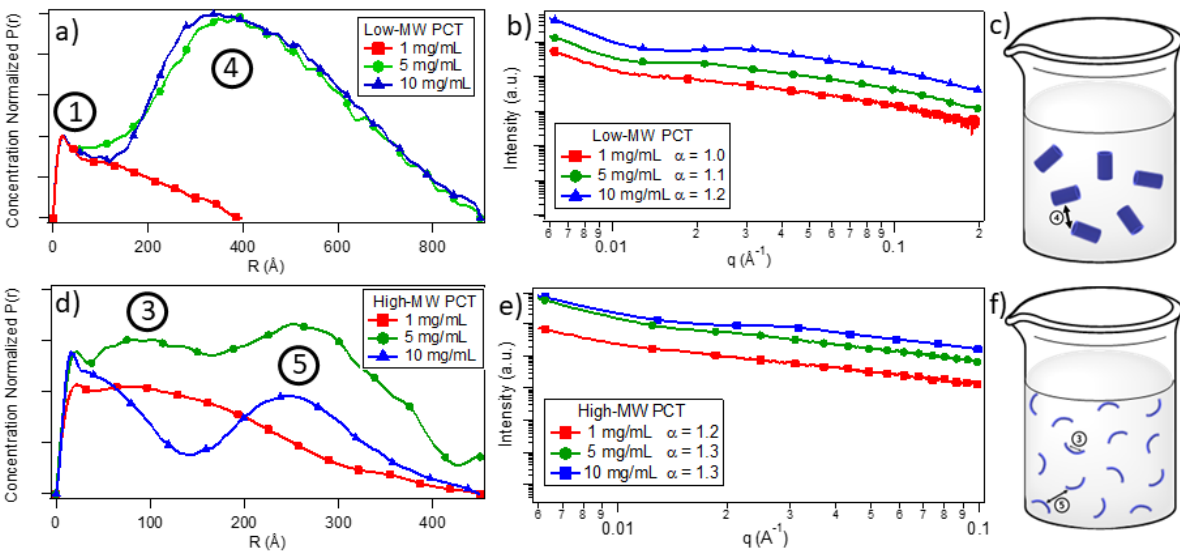

Figure 2.4: Concentration-dependent studies of low-MW PCT (a-c) and high-MW PCT (d-f) demonstrating that cylinder shape is maintained while micelles interact with each other in solution.

In order to ensure the previously discussed SAXS results are not due to aggregation effects and to observe the interaction of polymer chains in solution, we further examine both high- and low-MW samples at varying concentrations, as seen in Figure 2.4. In non-interacting systems the scattering profiles shapes stay the same, with only the scattering intensity increasing with increasing concentration.

Figure 2.4a shows concentration-normalized P(r) trans-formations for the low-MW fraction of PCT. The peak at 20 Å remains the same for all concentrations indicating that the rod-like shape of the individual micelles remains unchanged and that all measurements were per-formed above the critical micelle concentration.[46] However, as the concentration increases, a large peak appears at ~400 Å, corresponding to the electron density correlation of neighboring chains in solution. These changes are also reflected in the Guinier-Porod power law fits shown in Figure 2.4b. The increase in slope from 1.0 to 1.2, indicating a deviation from perfect linearity, can thus be explained because of the interaction between separate polymer

micelles. These interchain relationships observed in the SAXS data are represented (region 4) in the schematic shown in Figure 2.4c.

It can be seen in the *P(r)* results for high-MW (Figure 2.4d) that there are three distinct peaks at the different concentrations. The first peak at ~20 Å, as with the low-MW samples, corresponds to the cylinder diameter (region 1). The peak at ~100 Å (region 3), as previously dis-cussed, relates to the electron density correlation of intra-micelle interactions that only occur because of the increased length of the polymer chains. However, as the concentration increases, an additional peak at ~300 Å (region 5) appears. Similar to what has been seen for the low-MW PCT, this new peak occurs due to inter-micelle correlation because the distinct micelles are now closer to each other. Despite the changes in the *P(r)* function, the radially averaged data and corresponding Guinier-Porod fits seen in Figure 2.4e have very little change be-cause both correlation peaks represent a deviation from ideal-rod like behavior. It is also interesting to note that the inter-micelle correlation peak appears at longer distances for low-MW as compared to high-MW PCT. In the low-MW system, the polymer chains are short enough that that are able to minimize repulsive forces more effectively with increased distance between micelles. However, at higher-MW, there is too much disorder caused by the longer polymer chains to spatially separate each micelle as effectively.

2.3. Conclusions

In conclusion, we are able to confirm our ability to expand the design rule for straightening polymer chains by using self-assembling amphiphilic CPEs to form cylindrical micelles with the synthesis of PCT. We were able to move the band-gap ~150 nm into the visible region, making this polymer much better applicable for future OPV applications. CryoEM images indicate rod-like micelle self-assembly with dimension of ~20 Å. Solution SAXS profiles and the resulting *P(r)* transformations provide further proof of this cylindrical micelle

formation, with featureless raw scattering decays and a sharp peak at low distances representative of the cylinder diameter followed by a decay for correlations along the length of the cylinder, respectively. The radially averaged SAXS profiles are fit to the Guinier/power law to determine the straightness of the cylinders. With slope values of 1.2 and 1.0 for high- and low-MW PCT, respectively, in dilute solution, we corroborate the idea of straightening the polymer backbone with a more similar bond-angled cyclopentadithiophene relative to the thiophene moiety for straighter micelle formation. We prove our ability to design a straighter amphiphilic CPE for self-assembly into micelles with Dammin bead models of our SAXS data. For low-MW PCT samples, the bead models further suggest straight-chained micelle formation, while high-MW PCT samples produce curved micelles due the appropriation of the larger correlation peaks observed in the *P(r)* functions. We further explored the concentration-dependent effects of self-assembly and were able to show that while inter- and intra-micelle interactions change at varying concentrations, the core rigid rod-like assembly is unchanged no matter the molecular weight or concentration. By confirming the expansion of our amphiphilic self-assembly design rule for straightening polymer chains with the synthesis of PCT, we open up the possibilities for the incorporation of appropriate acceptors to study charge transfer properties both in solution and solid-state. Due to ease of structural tenability, other CPEs can be synthesized using this design rule to further rigidify the backbone for improved electronic properties or the incorporation of different monomer moieties to tailor the optical properties. In all, we have shown that by straightening the individual polymer chain backbone, we can control the self-assembly to form straight rod-like micelles in water for potential in OPV applications.

2.4. Experimental Methods

Polymer Synthesis. Synthetic procedures and characterization data can be found in the Supporting Information. T0 purify the PCT into high- and low-MW fractions, 250 mg of PCT was dissolved in 5 mL of DMSO. Once dissolved, ethyl acetate was added to the PCT in DMSO solution until the high-MW polymer fraction started to precipitate out of solution. The precipitate is then centrifuged to separate from the solution, which is poured off and the solid is dried to collect the high-MW fraction. More ethyl acetate is then added to the remaining solution and the rest of the polymer is precipitated to collect the low-MW fraction. All resulting studies were then performed on the size-separated PCT dissolved in water at various concentrations.

cryoEM Measurements. Cryo EM grids were prepared using a Vitrobot Mark IV cryo-sample plunger. Briefly, 2.5 µl of polymer sample at a concentration of 1 mg/ml was deposited onto a glow-discharged Quantifoil holey-carbon grid (SPI Quantifoil R3.5/1). The grid was then blotted dry and rapidly frozen by plunging the grid into a 2:1 mixture of liquid propane:liquid ethane cooled to liquid nitrogen temperatures, producing thin films of amorphous ice containing the sample in the holey carbon film. Grids were imaged on an FEI (Hillsboro, OR) Tecnai TF20 EM (Electron Imaging Center for Nanomachines, California Nanosystems Institute, Los Angeles, CA) at either 50 kX or 100 kX magnification with a defocus value of around 3 µm.

Solution SAXS Characterization. SAXS experiments were conducted at the Stanford Synchrotron Radiation Lightsource (SSRL) on beamline 4-2. Using a syringe, 50 µL of each sample was loaded into a quartz capillary held at 25°C. Scattered X-rays (12 keV) were collected on a Rayonix MX225-HE detector (sample-to-detector distance = 1.7 m). The 2-D data was radially averaged to obtain 1-D scattering profiles. The 1-D scattering profiles were fit and smoothed using Gnom,[42] and bead modeling was performed on the smoothed data using Dammin, a Monte Carlo type modeling software, to use beads and solvent for creating

shapes to replicated SAXS scattering representative of the experimental curves. Within Dammin, expert mode was used and the bead size radius was set to 5 Å, corresponding to the wide of a single polymer chain. The diameter of the volume space sphere was set to be 140 Å. Each data set was run at least 5 times to ensure trends/model structures were reproducible. Only a subset of the overall data is shown in the main text.

2.5. Supporting Information

Supporting Information is available in Appendix A.

2.6. References

(1) Friend, R. H.; Gymer, R. W.; Holmes, A. B.; Burroughes, J. H.; Marks, R. N.; Taliani, C.; Bradley, D. D. C.; Santos, D. A. Dos; Bredas, J. L.; Logdlund, M.; et al. Electroluminescence in Conjugated Polymers. *Nature* **1999**, 397 (6715), 121–128.

(2) McNeill, C. R.; Greenham, N. C. Conjugated-Polymer Blends for Optoelectronics. *Adv. Mater.* **2009**, 21 (38–39), 3840–3850.

(3) Sirringhaus, H.; Bird, M.; Richards, T.; Zhao, N. Charge Transport Physics of Conjugated Polymer Field-Effect Transistors. *Adv. Mater.* **2010**, 22 (34), 3893–3898.

(4) Hamid, M.; Abdulameer, D.; Faizul, M.; Sabri, M.; Binti, S.; Said, M.; Haji, M.; Bashir, M.; Bashir, A. A Review on Thermoelectric Renewable Energy : Principle Parameters That Affect Their Performance. *Renew. Sustain. Energy Rev.* **2014**, 30, 337–355.

(5) Burroughes, J. H.; Bradley, D. D. C.; Brown, A. R.; Marks, R. N.; Mackay, K.; Friend, R. H.; Burns, P. L.; Holmes, A. B. Light-Emitting Diodes Based on Conjugated Polymers. *Nature* **1990**, 347, 539–541.

(6) Scholes, D. T.; Hawks, S. A.; Yee, P. Y.; Wu, H.; Lindemuth, J. R.; Tolbert, S. H.; Schwartz, B. J. Overcoming Film Quality Issues for Conjugated Polymers Doped with F4TCNQ by Solution Sequential Processing: Hall Effect, Structural, and Optical Measurements. *J. Phys. Chem. Lett.* **2015**, 6 (23), 4786–4793.

(7) Scholes, D. T.; Yee, P. Y.; Lindemuth, J. R.; Kang, H.; Onorato, J.; Ghosh, R.; Luscombe, C. K.; Spano, F. C.; Tolbert, S. H.; Schwartz, B. J. The Effects of Crystallinity on Charge Transport and the Structure of Sequentially Processed F4TCNQ-Doped Conjugated Polymer Films. *Adv. Funct. Mater.* **2017**, 1702654.

(8) Aubry, T. J.; Axtell, J. C.; Basile, V. M.; Winchell, K. J.; Lindemuth, J. R.; Porter, T. M.; Liu, J. Y.; Alexandrova, A. N.; Kubiak, C. P.; Tolbert, S. H.; et al. Dodecaborane-Based Dopants Designed to Shield Anion Electrostatics Lead to Increased Carrier Mobility in a Doped Conjugated Polymer. *Adv. Mater.* **2019**, 31 (11), 1–8.

(9) Hynynen, J.; Kiefer, D.; Yu, L.; Kroon, R.; Munir, R.; Amassian, A.; Kemerink, M.; Müller, C. Enhanced Electrical Conductivity of Molecularly P-Doped Poly(3-Hexylthiophene) through Understanding the Correlation with Solid-State Order. *Macromolecules* **2017**, 50 (20), 8140–8148.

(10) Liang, Z.; Reese, M. O.; Gregg, B. A. Chemically Treating Poly(3-Hexylthiophene) Defects to Improve Bulk Heterojunction Photovoltaics. *ACS Appl. Mater. Interfaces* **2011**, 3 (6), 2042–2050.

(11) Gao, J.; Roehling, J. D.; Li, Y.; Guo, H.; Moulé, A. J.; Grey, J. K. The Effect of 2,3,5,6-Tetrafluoro-7,7,8,8-Tetracyanoquinodimethane Charge Transfer Dopants on the Conformation and Aggregation of Poly(3-Hexylthiophene). *J. Mater. Chem. C* **2013**, 1 (36), 5638.

(12) Yan, H.; Manion, J. G.; Yuan, M.; García de Arquer, F. P.; McKeown, G. R.; Beaupré, S.; Leclerc, M.; Sargent, E. H.; Seferos, D. S. Increasing Polymer Solar Cell Fill Factor by Trap-Filling with F4TCNQ at Parts Per Thousand Concentration. *Adv. Mater*. **2016**, 28 (30), 6491–6496.

(13) Yu, S.; Frisch, J.; Opitz, A.; Cohen, E.; Bendikov, M.; Koch, N.; Salzmann, I. Effect of Molecular Electrical Doping on Polyfuran Based Photovoltaic Cells. *Appl. Phys. Lett*. **2015**, 106 (20).

(14) Zhang, Y.; Zhou, H.; Seifter, J.; Ying, L.; Mikhailovsky, A.; Heeger, A. J.; Bazan, G. C.; Nguyen, T. Q. Molecular Doping Enhances Photoconductivity in Polymer Bulk Heterojunction Solar Cells. *Adv. Mater*. **2013**, 25 (48), 7038–7044.

(15) Lu, G.; Blakesley, J.; Himmelberger, S.; Pingel, P.; Frisch, J.; Lieberwirth, I.; Salzmann, I.; Oehzelt, M.; Di Pietro, R.; Salleo, A.; et al. Moderate Doping Leads to High Performance of Semiconductor/Insulator Polymer Blend Transistors. *Nat. Commun*. **2013**, 4, 1588.

(16) Lüssem, B.; Keum, C.-M.; Kasemann, D.; Naab, B.; Bao, Z.; Leo, K. Doped Organic Transistors. *Chem. Rev*. **2016**, 116 (22), 13714–13751.

(17) Glaudell, A. M.; Cochran, J. E.; Patel, S. N.; Chabinyc, M. L. Impact of the Doping Method on Conductivity and Thermopower in Semiconducting Polythiophenes. *Adv. Energy Mater*. **2015**, 5 (4).

(18) Patel, S. N.; Glaudell, A. M.; Kiefer, D.; Chabinyc, M. L. Increasing the Thermoelectric Power Factor of a Semiconducting Polymer by Doping from the Vapor Phase. *ACS Macro Lett*. **2016**, 5 (3), 268–272.

(19) Strzalka, J.; Guo, J.; Chen, L. X.; Xu, T.; Yu, L.; Rolczynski, B. S.; Marks, T. J.; Loser, S.; Lee, B.; Liang, Y.; et al. When Function Follows Form: Effects of Donor Copolymer Side Chains on Film Morphology and BHJ Solar Cell Performance. *Adv. Mater*. **2010**, 22 (48), 5468–5472.

(20) Beaujuge, P. M.; Fréchet, J. M. J.; Toney, M. F.; Lee, O. P.; Yiu, A. T.; Woo, C. H. Side-Chain Tunability of Furan-Containing Low-Band-Gap Polymers Provides Control of Structural Order in Efficient Solar Cells. *J. Am. Chem. Soc*. **2011**, 134 (4), 2180–2185.

(21) Yang, L.; Zhou, H.; You, W. Quantitatively Analyzing the Influence of Side Chains on Photovoltaic Properties of Polymer-Fullerene Solar Cells. *J. Phys. Chem. C* **2010**, 114 (39), 16793–16800.

(22) Yang, H. Y.; Kang, N. S.; Hong, J.-M.; Song, Y.-W.; Kim, T. W.; Lim, J. A. Efficient Bilayer Heterojunction Polymer Solar Cells with Bumpy Donor–Acceptor Interface Formed by Facile Polymer Blend. *Org. Electron*. **2012**, 13 (11), 2688–2695.

(23) Aubry, T. J.; Ferreira, A. S.; Yee, P. Y.; Aguirre, J. C.; Hawks, S. A.; Fontana, M. T.; Schwartz, B. J.; Tolbert, S. H. Processing Methods for Obtaining a Face-On Crystalline Domain Orientation in Conjugated Polymer-Based Photovoltaics. *J. Phys. Chem. C* **2018**, 122, 15078–15089.

(24) Aguirre, J. C.; Hawks, S. A.; Ferreira, A. S.; Yee, P.; Subramaniyan, S.; Jenekhe, S. A.; Tolbert, S. H.; Schwartz, B. J. Sequential Processing for Organic Photovoltaics: Design Rules for Morphology Control by Tailored Semi-Orthogonal Solvent Blends. *Adv. Energy Mater.* **2015**, 5 (11)

(25) Zhang, G.; Huber, R. C.; Ferreira, A. S.; Boyd, S. D.; Luscombe, C. K.; Tolbert, S. H.; Schwartz, B. J. Crystallinity Effects in Sequentially Processed and Blend-Cast Bulk-Heterojunction Polymer/Fullerene Photovoltaics. *J. Phys. Chem. C* **2014**, 118 (32), 18424–18435.

(26) Ferreira, A. S.; Aguirre, J. C.; Subramaniyan, S.; Jenekhe, S. A.; Tolbert, S. H.; Schwartz, B. J. Understanding How Polymer Properties Control OPV Device Performance: Regioregularity, Swelling, and Morphology Optimization Using Random Poly(3-Butylthiophene-Co-3-Octylthiophene) Polymers. *J. Phys. Chem. C* **2016**, 120 (39), 22115–22125.

(27) Tolbert, S. H.; Wu, J.; Gross, A. F.; Nguyen, T.-Q.; Schwartz, B. J. Directional Energy Migration in an Oriented Nanometer-Scale Host / Guest Composite : Semiconducting Polymers Threaded into Mesoporous Silica. *Microporous Mesoporous Mater.* **2001**, 45, 445–451.

(28) Cadby, A. J.; Tolbert, S. H. Controlling Optical Properties and Interchain Interactions in Semiconducting Polymers by Encapsulation in Periodic Nanoporous Silicas with Different Pore Sizes. *J. Phys. Chem. B* **2005**, 109 (38), 17879–17886.

(29) Coakley, K. M.; Srinivasan, B. S.; Ziebarth, J. M.; Goh, C.; Liu, Y.; McGehee, M. D. Enhanced Hole Mobility in Regioregular Polythiophene Infiltrated in Straight Nanopores. *Adv. Funct. Mater.* **2005**, 15 (12), 1927–1932.

(30) Molenkamp, W. C.; Watanabe, M.; Miyata, H.; Tolbert, S. H. Highly Polarized Luminescence from Optical Quality Films of a Semiconducting Polymer Aligned within Oriented Mesoporous Silica. *J. Am. Chem. Soc.* **2004**.

(31) Clark, A. P.-Z.; Shi, C.; Ng, B. C.; Wilking, J. N.; Ayzner, A. L.; Stieg, A. Z.; Schwartz, B. J.; Mason, T. G.; Rubin, Y.; Tolbert, S. H. Self-Assembling Semiconducting Polymers—Rods and Gels from Electronic Materials. *ACS Nano* **2013**, 7 (2), 962–977.

(32) Cui, Q.; Bazan, G. C. Narrow Band Gap Conjugated Polyelectrolytes. *Acc. Chem. Res.* **2018**, 51 (1), 202–211.

(33) Jiang, H.; Taranekar, P.; Reynolds, J. R.; Schanze, K. S. Conjugated Polyelectrolytes: Synthesis, Photophysics, and Applications. *Angewandte Chemie - International Edition*. **June 2, 2009**, pp 4300–4316.

(34) Huber, R. C.; Ferreira, A. S.; Thompson, R.; Kilbride, D.; Knutson, N. S.; Devi, L. S.; Toso, D. B.; Challa, J. R.; Zhou, Z. H.; Rubin, Y.; et al. Long-Lived Photoinduced Polaron Formation in Conjugated Polyelectrolyte-Fullerene Assemblies. *Science* (80-.). **2015**, 348 (6241), 1340–1343.

(35) Huber, R. C.; Ferreira, A. S.; Aguirre, J. C.; Kilbride, D.; Toso, D. B.; Mayoral, K.; Zhou, Z. H.; Kopidakis, N.; Rubin, Y.; Schwartz, B. J.; et al. Structure and Conductivity of Semiconducting Polymer Hydrogels. *J. Phys. Chem. B* **2016**, 120 (26), 6215–6224.

(36) Hu, J.; Clark, K. W.; Hayakawa, R.; Li, A.-P.; Wakayama, Y. Enhanced Electrical Conductivity in Poly(3-Hexylthiophene)/Fluorinated Tetracyanoquinodimethane Nanowires Grown with a Porous Alumina Template. *Langmuir* **2013**, 29 (24), 7266–7270.

(37) Willot, P.; Govaerts, S.; Koeckelberghs, G. The Controlled Polymerization of Poly(Cyclopentadithiophene)s and Their All-Conjugated Block Copolymers. *Macromolecules* **2013**, 46 (22), 8888–8895.

(38) Svergun, D. I.; Koch, M. H. J. Reports on Progress in Physics Related Content Small-Angle Scattering Studies of Biological Macromolecules in Solution Small-Angle Scattering Studies of Biological Macromolecules in Solution. *Reports Prog. Phys.* **2003**, No. 66, 1735.

(39) Putnam, D. K.; Lowe, E. W.; Meiler, J. Reconstruction of Saxs Profiles From Protein Structures. *Comput. Struct. Biotechnol. J.* **2013**, 8 (11), e201308006.

(40) Hammouda, B. A New Guinier-Porod Model. *J. Appl. Crystallogr.* **2010**, 43 (4), 716–719.

(41) Liu, H.; Zwart, P. H. Determining Pair Distance Distribution Function from SAXS Data Using Parametric Functionals. *J. Struct. Biol.* **2012**, 180 (1), 226–234.

(42) Svergun, D. I. Determination of the Regularization Parameter in Indirect-Transform Methods Using Perceptual Criteria. *J. Appl. Crystallogr.* **1992**, 25 (pt 4), 495–503.

(43) Xu, Z.; Gao, C. Graphene Chiral Liquid Crystals and Macroscopic Assembled Fibres. *Nat. Commun.* **2011**, 2 (1), 571–579.

(44) Wang, Z.; Liu, F.; Gao, Y.; Zhuang, W.; Xu, L.; Han, B.; Li, G.; Zhang, G. Hexagonal Liquid Crystalline Phases Formed in Ternary Systems of Brij 97-Water-Ionic Liquids. *Langmuir* **2005**, 21 (11), 4931–4937.

(45) Svergun, D. I. Restoring Low Resolution Structure of Biological Macromolecules from Solution Scattering Using Simulated Annealing. *Biophys. J.* **1999**, 76 (6), 2879–2886.

(46) Yu, D.; Huang, F.; Xu, H. Determination of Critical Concentrations by Synchronous Fluorescence Spectrometry. *Anal. Methods* **2012**, 4 (1), 47–49.

Chapter 3. Controlling Fullerene:Polymer Vertical Phase Segregation Using Sequential Processing and Solvent Swelling in Organic Photovoltaics

3.1. Introduction

Organic photovoltaics (OPVs) are of particular interest due to their low cost, ease of solution processing, and flexible properties[1]. These devices typically consist of a conjugated, semiconducting polymer that acts as the main photoabsorber and electron donor, and a fullerene derivative, typically phenyl-C61-butyric acid methyl ester (PCBM), as the primary electron acceptor. Together, the polymer and fullerene derivative form the active layer, which usually takes the form of a bulk heterojunction (BHJ), whose morphology plays an integral role in determining the device performance and efficiency.[2-6] An ideal BHJ morphology requires the polymer and fullerene to be mixed on small enough length scales (~20 nm) to prevent exciton recombination prior to charge separation, but also to have separated domains to enable efficient charge collection.[7-9]

Traditionally, this morphology has been achieved through blend-casting (BC), wherein the polymer and fullerene are codissolved in solution and deposited onto a substrate. This process, however, relies on the polymer and fullerene demixing in order to form an ideal BHJ, which is often aided by the use of solvent additives[10-13] or post-treatments steps such as thermal and solvent annealing.[14-17] Unfortunately, the spontaneous donor-acceptor phase separation that drives BHJ formation in blend-cast systems is hard to control, particularly in large scale devices.[18] An alternative method, sequential processing (SqP), allows for more structural control.[19-27] With SqP, the polymer is first deposited as a homogeneous film. Then, using a semi-orthogonal solvent or solvent blend that will swell but not dissolve the polymer layer, the fullerene is intercalated into the pre-existing polymer matrix. This provides the ability to tune

the polymer morphology first, resulting in more reproducible devices, especially when scaling up to larger areas.[20]

Inherent to SqP, BHJ formation relies on the mass action to drive fullerene into the already cast polymer matrix. While thermal annealing has been shown to help improve mixing for crystalline polymers such as the well-studied poly-3-hexylthiophene (P3HT),[28–32] it is not always applicable for more amorphous polymers. Alternatively, it has been shown that fullerene diffusion into the film can be aided by polymer swelling via solvent additives[13,21] or using solvent blends.[22,33–35] Indeed, we have previously shown that the fullerene casting solvent, or swelling solvent, can be rationally selected to swell but not dissolve the polymer film using its Flory-Huggins χ parameter, which in turn can be determined by performing ellipsometry on solvent-swollen polymer films.[22] Recently, this method has also been expanded to other applications, such as infiltrating molecular dopants into polymer thin films to produce highly conductive materials.[36–40]

In this paper, we expand on the solvent swelling SqP method, and show that we can control vertical fullerene distribution as well as local phase separation in SqP processed BHJ films simply by tuning the swelling solvent blend ratios. We demonstrate how this method can be applied to two high-performance polymers that have different degrees of crystallinity and solubility: semi-crystalline poly[(4,8-bis[(ethylhexyl)oxy]benzo[1,2-b:4,5-b']dithiophene-2,6-diyl)(3-fluoro-2-[(2-ethylhexyl)carbonyl]thieno[3,4-b¬]thiophenediyl)] (PTB7)[41] and amorphous poly[(4,8-di(2-butyloctyl)oxybenzo[1,2-b:4,5-b']dithiophene-2,6-diyl)-alt-(2,5-bis(4,4'-bis(2-octyl)dithieno[3,2-b:2'3'-d]silole-2,6-diyl)thiazolo[5,4-d]thiazole)] (PSDTTT).[42] We show that by increasing the amount of swelling solvent in the fullerene solvent blend (up to the point of polymer dissolution), we improve device efficiencies for each polymer system. Using a combination of 2D-grazing-incidence wide-angle X-ray scattering (GIWAXS) and neutron

reflectometry (NR), we probe both the local and global morphology as a function of increasing swelling solvent for each polymer. The GIWAXS data shows that we can introduce more fullerene into the polymer films using a solvent blend that more effectively swells the polymer matrix, and that this is accomplished without drastically altering the polymer morphology. Using NR, we can globally differentiate between polymer and fullerene, and are able to obtain vertical phase separation profiles for each system. By controlling how effectively the solvent swells the polymer matrix, we are able to control polymer:fullerene mixing profiles within the device. These morphological changes directly correlate with improved device performances upon the addition of increased swelling solvent.

3.2. Results and Discussion

Device Performance. We start by looking at the device performance of our polymer:fullerene solar cells. Using the Flory-Huggins x-parameter, it was determined that a 'good' SqP swelling co-solvent blend should have an effective x in the range $1.4 \leq \chi \leq 2.22$ For

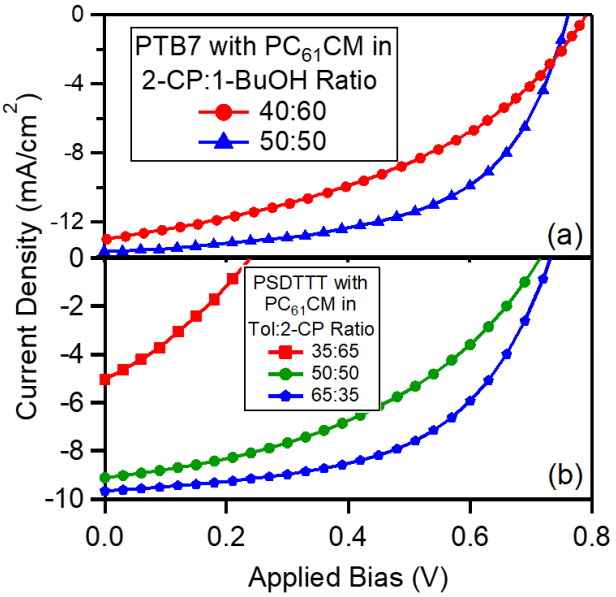

Figure 3.1. Photovoltaic device performance for SqP active layers containing (a) PTB7:$PC_{61}BM$ with the $PC_{61}BM$ deposited from a co-solvent blend of 2-CP:1-BuOH with ratios of 40:60 (red) and 50:50 (blue) and (b) PSDTTT:$PC_{61}BM$ with the $PC_{61}BM$ deposited from a co-solvent blend of Tol:2-CP with ratios of 35:65 (red), 50:50 (green), and 65:35 (blue).

these systems, we use 2-chlorophenol (2-CP) as the base fullerene solvent due to its high fullerene solubility and its low vapor pressure. PTB7 is fairly soluble in 2-CP ($\chi \leq 1$) and thus a co-solvent with a larger χ -parameter must be added to prevent PTB7 dissolution during the SqP process. Here, we choose 1-butanol (1-BuOH) as our co-solvent, which had previously been shown to act as effective non-solvent while maintaining the ability to wet and swell the polymer film.[22] By increasing the amount of 2-CP in our solvent blends, we induce more PTB7 swelling solvent and potentially provide more space for the PC61BM to intercalate into the polymer matrix.

The photovoltaic device performance for the PTB7:$PC_{61}BM$ devices with different 2-CP:1-BuOH ratios can be seen in Figure 3.1a. We indeed see an increase in device performance from 4.1% to 6.0% by increasing the 2-CP:1-BuOH ratio from 40:60 (red curve) to 50:50 (blue curve). We note that a 2-CP:1-BuOH ratio of 60:40 washed away part of the PTB7 film, indicating that we had reached the point of dissolution. From the solar cell performance data summarized in Table 3.1, we clearly see that increasing the amount of swelling solvent (2-CP) results in a higher short circuit current density (J_{sc}) and increased fill factor. This suggests that with more swelling solvent, there is better charge transfer and charge collection, presumably due to better fullerene intercalation. We also see a small decrease in the open-circuit voltage (V_{oc}) for

	V_{oc} (mV)	J_{sc} (mA/cm^2)	FF (%)	PCE (%)
PTB7:$PC_{61}BM$ 40:60 2CP:1-BuOH	0.79	12.97	42.0	4.1
PTB7:$PC_{61}BM$ 50:50 2CP:1-BuOH	0.76	13.70	60.2	6.0
PSDTTT:$PC_{61}BM$ 35:65 Tol:2CP	0.23	4.94	31.5	0.62
PSDTTT:$PC_{61}BM$ 50:50 Tol:2CP	0.71	9.11	42.4	2.7
PSDTTT:$PC_{61}BM$ 65:35 Tol:2CP	0.73	9.67	54.77	3.8

Table 3.1. Summary of photovoltaic device parameters and efficiencies for PTB7:$PC_{61}BM$ and PSDTTT:$PC_{61}BM$ devices with different co-solvent blend ratios.

the 50:50 2-CP:1-BuOH device, suggesting that there is more efficient charge extraction occurring, reducing the charge buildup upon photoexcitation.

PSDTTT, in contrast, has poor solubility in most organic solvents, and is completely insoluble in 2-CP ($\chi \geq 2.5$). Thus, for this polymer, we must add a good solvent for the polymer such as toluene (herein abbreviated as "tol") to the SqP solution to induce enough swelling to drive fullerene intercalation. Indeed we see in the J-V data in Figure 1b, that by increasing the amount of toluene in the solvent blend from 35:65 (red curve) to 50:50 (green curve) and finally to 65:35 (blue curve), the device characteristics monotonically improve. This improvement corresponds to an increase in efficiency from 0.6% to 3.8%. Similar to the PTB7 system, we also see an increase in Jsc and fill factor as we use more toluene in our co-solvent blends. This again suggests that with increased swelling of the polymer layer, there is better polymer:fullerene mixing, which in turn leads to improved charge transfer and charge collection.

GIWAXS Characterization of the Polymer:Fullerene Active Layers. To better understand the changes in the solar cell device performance for PTB7:$PC_{61}BM$ and

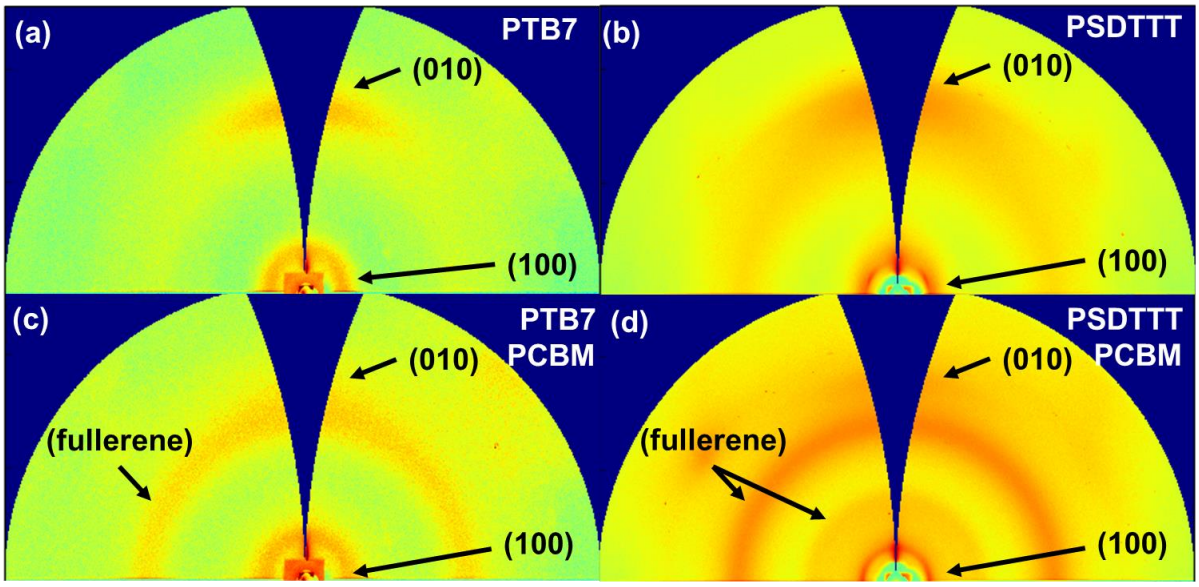

Figure 3.2. 2D diffractograms on films of (a) pure PTB7, (b) pure PSDTTT, (c) PTB7:$PC_{61}BM$, and (d) PSDTT:$PC_{61}BM$ showing both polymers are face-on oriented with a prominent (010) π-stacking peak in the out-of-plane direction.

PSDTTT:$PC_{61}BM$ active layers with changes in solvent composition during fullerene deposition, we first take a look at the molecular structure of our films using two-dimensional GIWAXS. This powerful technique allows us to study the changes in relative crystallinity for both polymer and fullerene, as well as any effect on the polymer orientation when tuning the fullerene co-solvent blends. The polymer orientation can be ascertained by comparing the intensity of the (100) lamellar stacking peak to that of the (010) π-stacking peak in both the in- and out-of-plane scattering directions. The in-plane scattering encompasses the diffraction planes oriented perpendicular to the plane of the substrate while the out-of-plane scattering consists of the diffraction planes oriented parallel to the plane of the substrate. The resulting 2D diffractograms of our pure polymers and SqP processed polymer:fullerene films are presented in Figure 3.2.

Looking at the diffractograms for pure PTB7 and PSDTTT films in Figures 3.2a,b, we clearly see that both polymers are face-on oriented with the lamellar stacking peak predominantly scattering in the in-plane direction and the π-stacking peak in the out-of-plane direction. Upon the addition of $PC_{61}BM$ (Figs. 3.2c,d), we see the appearance of broad isotropic peaks that largely obscure the π-stacking peak, arising from fullerene scattering. By selectively integrating over these diffractograms we can glean more quantitative information regarding the relative crystallinities (full integrations) and polymer orientation (in- and out-of-plane integrations).

We first look at the fully integrated scattering curves for our PTB7:$PC_{61}BM$ system, as shown in Figure 3.3a. Upon fullerene addition (red and blue curves), we notice that the (100) stacking peak intensity at q = 0.3 $Å^{-1}$ decreases relative to the pure PTB7 (100) peak intensity (black curve), suggesting that the fullerene is disrupting the polymer crystallinity to form a BHJ. Furthermore, we see the main fullerene scattering peak intensity centered at q = 1.35 $Å^{-}$

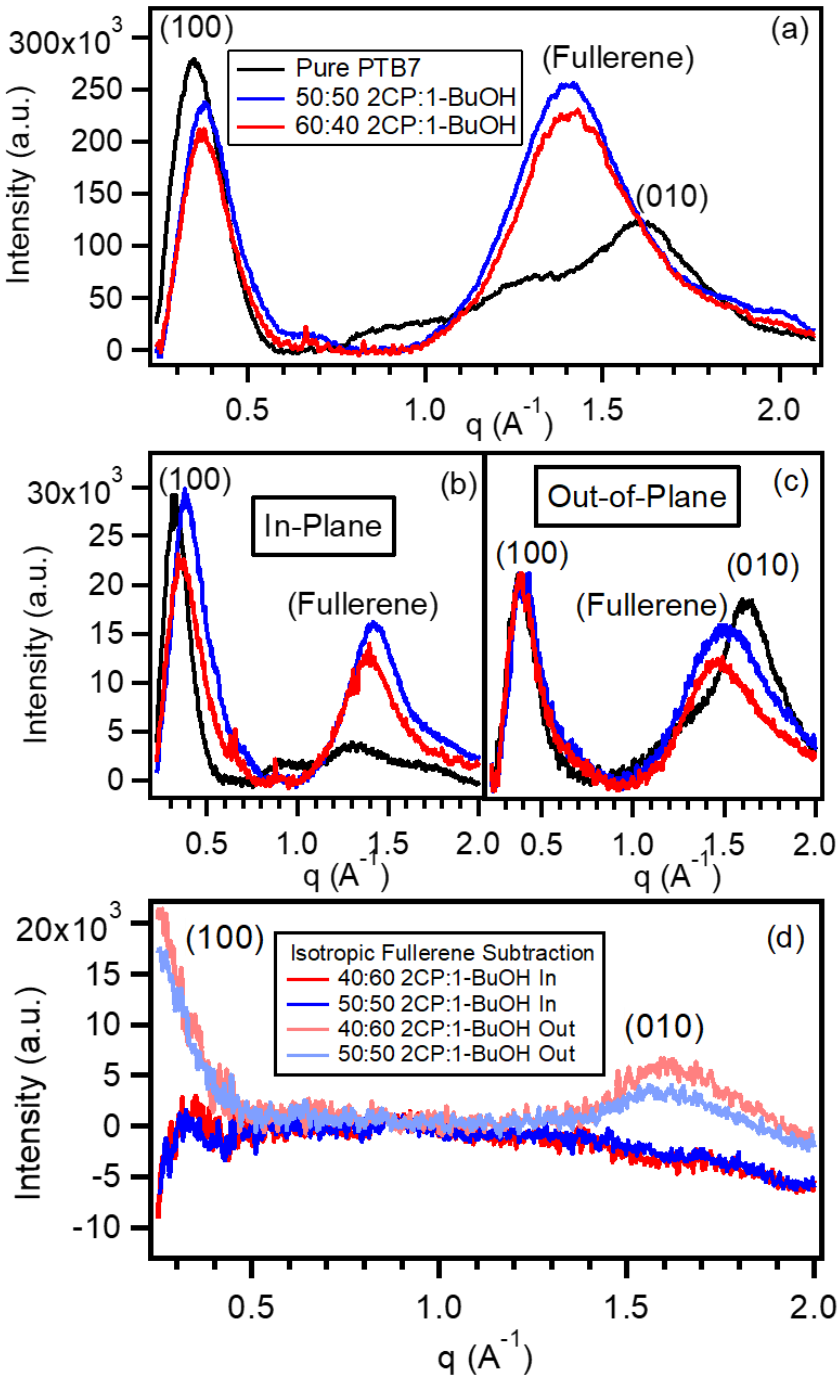

Figure 3.3: (a) Full integrations of GIWAXS diffractograms for the PTB7:$PC_{61}BM$ system: pure PTB7 (black), 40:60 2CP:1-BuOH (red), and 50:50 2CP:1-BuOH (blue). The in- (b) and out-of-plane (c) scattering is shown to confirm the edge-on orientation for PTB7 with strong (010) scattering in the out-of-plane direction. Further examination of the (010) peak is facilitated by subtraction of all isotropic scattering (mainly fullerene scattering). The difference patterns (d) show a (010) peak only in the out-of-plane direction (light curves) , indicating that any non-isotropic polymer has a face-on orientation with respect to the substrate, even after SqP processing.

[1] appear, an indication that there is fullerene within the polymer film. We note that if the $PC_{61}BM$ was deposited on top of the film, rather than infiltrating into the PTB7 matrix, we would see sharp diffraction peaks superimposed on this broad scattering due to the formation of larger fullerene crystallites. Delving further into our solvent blend system, we see that increasing the 2-CP:1-BuOH ratio from 40:60 (red curve) to 50:50 (blue curve) increases the fullerene intensity, confirming that with better swelling, we are able to incorporate more fullerene into PTB7 film.

In order to look at the PTB7 orientation in our pure polymer and BHJ films, we examine the in- and out-of-plane integrated diffraction, as plotted in Figure 3.3b,c, respectively. For pure PTB7 (black), we see that there are apparently two polymer populations with different orientation. The (100) intensity is roughly equivalent both the in- and out-of-plane, which could arise from a purely isotropic domain distribution. This possibility is excluded by the very different (010) or π-stacking peak position in the in- and out-of-plane directions, however. The in-plane data shows a prominent peaks at very large spacing of $q = 1.3$ Å^{-1}, a value that is usually associated with disordered π-stacking. By contrast, the out-of-plane data has a peak at a much more standard π-stacking value of $q = 1.6$ Å^{-1}. For complex polymers like these, it is often observed that that those domains that lie face-on to a flat surface show more ordered crystallinity and small π-stacking distances.[43]

For OPV applications, we are most interested in the closely stacked out-of-plane (010) peak, as this provides the needed conduction pathway for carriers traveling through the π-system perpendicular to the substrate between the device electrodes. For the BHJ films, however, the fullerene scattering peak largely obscures any π-stacking peak character. Due to the isotropic nature of the $PC_{61}BM$ scattering, we can subtract off a 10° radial segment of the diffractogram centered at 45° from both our in-plane and out-of-plane data to uncover any

information on oriented or non-isotropic domains, as seen in Figure 3.3d. We find is that when subtracting the isotropic scattering from the out-of-plane direction (light curves), we see a clear (010) peak; no oriented (010) diffraction remains in the in-plane direction (dark curves). This indicates that the swelling and fullerene intercalation process does not destroy the favorable face-on polymer orientation. We also notice that as we increase the amount of 2CP in our solvent blends from 40:60 (red) to 50:50 (blue), we see a slight decreasing the π-stacking scattering intensity, again confirming that we are disrupting the PTB7 crystallinity by intercalating more fullerene into our films.

Having shown that for a semi-crystalline polymer such as PTB7 we can controllably introduce more fullerene into BHJ films by tuning the nature of the co-solvent blend while preserving the face-on polymer orientation, we now turn to examination of local structure for the more amorphous, less soluble polymer in PSDTTT. The full integration scattering curves in Figure 3.4a show a clear (100) lamellar stacking peak centered at q = 0.3 $Å^{-1}$ and a very broad (010) π-stacking peak centered around q = 1.6 $Å^{-1}$ for pure PSDTTT (black curve). With the least swelling solvent, 35:65 Tol:2CP (red curve), we see minimal change in the (100) scattering intensity, but the (010) peak becomes obscured by PC61BM scattering centered around q = 1.35 $Å^{-1}$. The lack of change in the diffraction data agrees with the device performance shown in Figure 3.1, which suggests little fullerene is intercalating into the PSDTTT matrix. When we increase the amount of toluene in our solvent blends to 50:50 Tol:2CP (green curve) and 65:35 Tol:2CP (blue curve), there is a decrease in the (100) scattering intensity, similar to the results for PTB7:$PC_{61}BM$. This again indicates that with enough swelling, we are able to infiltrate fullerene into the film and disrupt the polymer crystallinity. The $PC_{61}BM$ scattering intensity also increases with increasing toluene concentration, proving that we are able to controllably intercalate fullerene into the film.

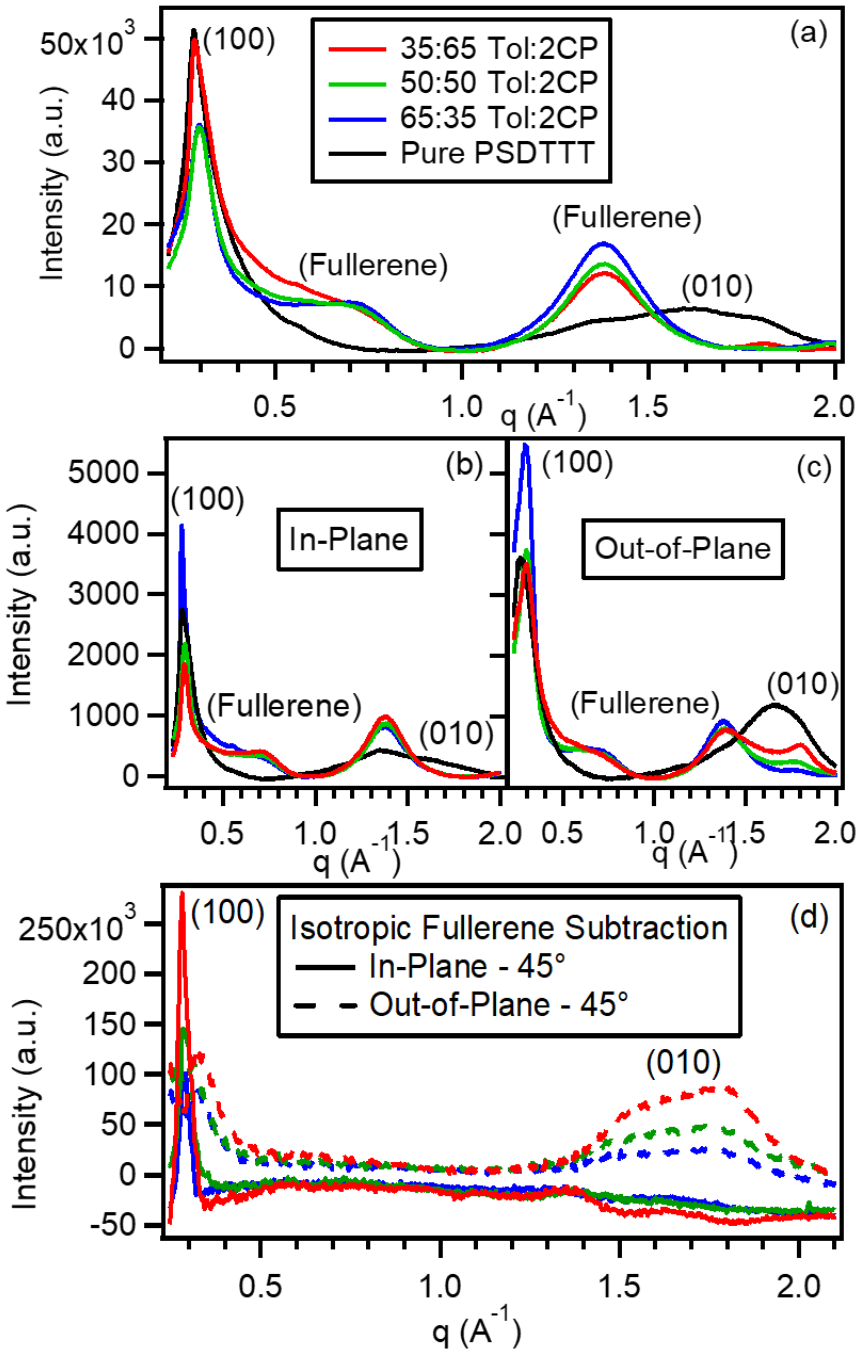

Figure 3.4: (a) Full integration of GIWAXS diffractograms for the PSDTTT:$PC_{61}BM$ system: pure PSDTTT (black), 35:65 Tol:2CP (red), 50:50 Tol:2CP (green) and 65:35 Tol:2CP (blue). The (b) in- and (c) out-of-plane integrations are shown to confirm edge-on orientation for PSDTTT with strong (010) scattering in the out-of-plane direction. Further examination of the of this (010) peak is facilitated by subtraction of all isotropic scattering (mainly fullerene scattering), showing that this SqP process is not altering the polymer orientation: (010) peak in the out-of-plane direction (light curves) rather than the in-plane (dark curves).

The PSDTTT orientation is more quantitatively examined in the in- and out-of-plane integrated diffraction curves shown in Figures 3.4b,c, respectively. For pure PSDTTT (black curve), we again see two populations of PSDTTT with different orientation. The in-plane data again shows an isotropic population with a larger π-stacking distance population (q ~ 1.35 $Å^{-1}$) whereas the out-of-plane data show the more ordered, face-on population with a smaller π-stacking distance (q ~ 1.65 $Å^{-1}$). Because of the sharpness of the diffraction arising from the more ordered, face-on population, we can see a clear trend of this (010) peak decreasing in intensity with increasing amounts of toluene (red → green → blue) in the out-of-plane scattering, despite the overlapping fullerene scattering. The same trend is observed when we again subtract of the isotropic diffraction collect at 45° in order to remove the fullerene scattering, as shown in Figure 3.4d. Using this analysis procedure, we confirm that the more tightly packed (010) peak is face-on oriented, whereas the more disordered, low q (010) peak is isotropic. Moreover, increased PC61BM incorporation with the uses of more toluene controllably disrupts both the polymer crystallinity and this domain orientation.

NR Characterization of the Polymer:Fullerene Active Layers. While GIWAXS provides structural information on the molecular level, it does not tell us about the distribution of fullerene within the film. For that, we can use neutron reflectometry (NR) to study the device level structure. With NR, the molecular distribution along the direction perpendicular to the plane of the film is probed. This is made possible due to the unique contrast in neutron scattering length densities (SLDs) between hydrogen-rich semiconducting polymers and hydrogen-deficient fullerene derivatives. In particular, P3HT and $PC_{61}BM$ have been extensively studied using NR in order to determine efficient methods for fullerene intercalation into the P3HT layer.[28,33,44,45] The reflectivity data is fit using a multilayer model with layers of varying SLDs to represent the vertical phase segregation profile. In the fitting, a guessed profile is iteratively refined until the model reflectivity matches with the experimental data. By limiting

values to known neutron scattering characteristics of the component material and using constraints to maintain a physically realistic system (film thicknesses and roughness profiles), a representative SLD profile of the active layer material can be obtained. Additional details regarding the NR fitting can be found in the SI.

We begin by determining the SLD for the pure components of our films. We find that PTB7 has an experimentally determined SLD = 0.6 x 10^{-6} $Å^{-2}$ (see SI, Figure S1) and that $PC_{61}BM$ has a SLD ~ 4.3 x 10^{-6} $Å^{-2}$, taken from the literature.[46] The resulting SLD profiles for PTB7:$PC_{61}BM$ using different solvent swelling blends can be seen in Figures 3.5a,b. For our BHJ films, we define three distinct regions: polymer-rich or low SLD (blue region), mixed or intermediate SLD (yellow region), and fullerene-rich or high SLD (green region). The 40:60 2CP:1-BuOH film (red curve) shows all three regions, as we would expect using SqP: a PTB7 rich region near the silicon substrate, a mixed PTB7:PC61BM region in the middle, and a fullerene-rich region at the top of the film. This SLD profile suggests that there is not enough swelling solvent to facilitate full

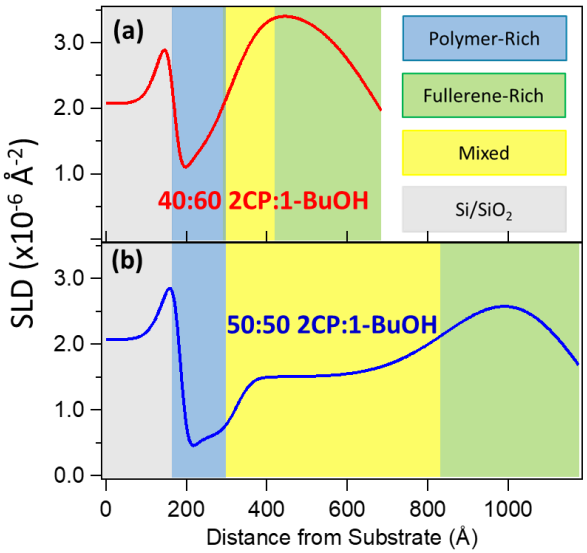

Figure 3.5. SLD vertical phase profiles for PTB7:$PC_{61}BM$ BHJ films using fullerene solvent blends of (a) 40:60 2CP:1-BuOH (red curve) and (b) 50:50 2CP:1-BuOH (blue curve). The data show the molecular distribution of polymer-rich regions (blue), mixed regions (yellow), and fullerene-rich regions (green) relative to the Si/SiO_2 substrate (gray). With more swelling (i.e. more 2CP), the fraction of mixed region increases.

fullerene intercalation into the film, so there is only a small mixed region and there is a large fullerene region atop of the film. This small mixed region can help explain the low fill factor and J_{sc} parameters seen in Figure 3.1. Upon increasing the amount of 2CP in our co-solvent blend to 50:50 (blue curve), there is a clear increase in both the size of the mixed region and the film thickness. The increase in amount of fullerene mixing due to solvent swelling is consistent with the improvement in device performance.

The SLD of PSDTTT was experimentally determined to be 0.4 x 10^{-6} $Å^{-2}$ (see Figure S2 for SLD profile and reflectivity fit), again providing adequate contrast to $PC_{61}BM$'s SLD of ~ 4.3 x 10^{-6} $Å^{-2}$. The resulting SLD profiles for the PSDTTT:$PC_{61}BM$ BHJ films are shown in Figures 6a-c. Similar to the PTB7:$PC_{61}BM$ films, there are three distinct regions of low SLD, polymer-rich region (blue section), intermediate SLD, mixed region (yellow section), and high SLD, fullerene-rich region (green region). For the 35:65 Tol:2CP BHJ film (red curve), which has the lowest amount of the good solvent, toluene, we again see a small mixed region which correlates with

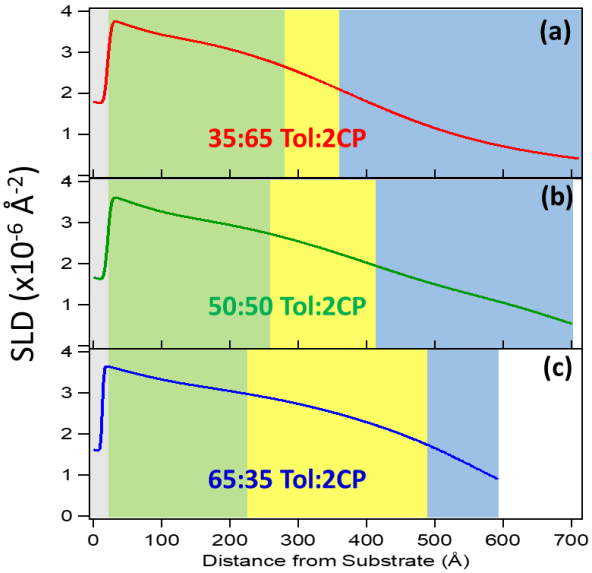

Figure 3.6. SLD vertical phase profiles for SqP processed PSDTTT:$PC_{61}BM$ films using fullerene deposition solvent blends of (a) 35:65 Tol:2CP (red curve), (b) 50:50 Tol:2CP (green curve), and (c) 65:35 Tol:2CP (blue curve). The data shows the molecular distribution of polymer-rich regions (blue), mixed regions (yellow), and fullerene-rich regions (green) relative to the Si/SiO_2 substrate (gray). With more toluene used, the fraction of mixed region increases.

its poor device efficiency. As we increase the amount of toluene to 50:50 Tol:2CP (green curve) we see this mixed area increase in size, while both the fullerene-rich and polymer-rich regions decrease. As we further increase the toluene amount to a 65:35 Tol:2CP ratio (blue curve), we see this mixed polymer:fullerene region grow even larger. This increase in mixed region in the SLD profiles for SqP processed PSDTTT:PC61BM films once again demonstrates our ability to tune the device performance by tuning the polymer:fullerene intercalation using solvent swelling.

Interestingly, we notice that despite adding in the fullerene on top of the PSDTTT layer, the SLD profiles show the fullerene-rich region (green area) is near the silicon substrate whereas the polymer-rich region is at the top of the film. This is counterintuitive to the SqP mechanics, wherein the fullerene is deposited onto an already established polymer matrix. We hypothesize that this is a thermodynamically favored state enabled by the amorphous nature of PSDTTT. Based on surface energies calculated from contact angle measurements (see SI for additional details), as seen in Table 3.2, we note that PSDTTT has a lower surface energy (22.4 mJ/m^2) than $PC_{61}BM$ (30.4 mJ/m^2) and the SiO_2/Si substrate (56.3 mJ/m^2). As materials with higher surface energy prefer to interact with other materials of similarly high surface energy,[47-49] we predict that $PC_{61}BM$ would preferentially reside at the high-energy SiO_2/Si substrate rather than PSDTTT. Importantly, this spatial arrangement indicates that the final distribution of fullerene in the PSDTTT device is thermodynamically, rather than kinetically controlled.

Organic Layer	Surface Energy (mJ/m^2)
PTB7	26.1
PCBM	30.4
PSDTTT	22.4
SiO_2/Si	22.4

Table 3.2. Calculated surface energies (mJ/m^2) from contact angle measurements for the active layer materials in our BHJ films.

3.3. Conclusions

Here we have investigated the effect of tuning the co-solvent blends used to deposit fullerenes in order to SqP process BHJ films for two different semiconducting polymer systems: semi-crystalline PTB7 and amorphous PSDTTT. Our results show that by tuning how effectively the solvent swells the polymer network, we are able to controllably improve the device performance and efficiencies from 4.1% to 6.0% and from 0.6% to 3.8% for PTB7 and PSDTTT, respectively. Using GIWAXS, we examine the molecular structure for these two polymer systems and see very similar trends despite having very different inherent crystallinities. We observe that with increasing amounts of solvent swelling, the amount of fullerene in the film, as measured by fullerene diffraction, increases without disrupting the polymer orientation. With NR, we are able to study the global morphology and obtain vertical phase SLD profiles of our BHJ films. We find that for both polymers, as the amount of solvent swelling is increased, a larger polymer:fullerene mixed region is created. The combined effect of intercalating more fullerene overall and larger polymer:fullerene mixing, corresponds well with the improved device efficiencies. Furthermore, for the PSDTTT:$PC_{61}BM$ system, we find that $PC_{61}BM$ intercalates closer to the SiO_2/Si substrate, as predicted by comparing the material surface energies. This result indicates that SqP fullerene intercalation can be viewed as a thermodynamically, rather than kinetically controlled process. Overall, this study demonstrates the ability to control polymer:fullerene mixing using solvent swelling and SqP. The use of solvent blends can be used to tune the driving force for fullerene intercalation, such that the thermodynamically favored morphology is obtained.

3.4. Experimental Methods

Film Fabrication. PTB7 was purchased commercially (Solarmer, Inc.) and PSDTTT was synthesized in-house41. All other materials used in this study were purchased commercially and

used as received. For polymer-based photovoltaic devices, sequentially processed active layers were prepared by spin-casting a 10 mg/mL polymer solution in chlorobenzene onto a PEDOT:PSS-covered ITO substrate, and then subsequently depositing the fullerene from a 10 mg/mL solution of $PC_{61}BM$ in 2-chlorophenol/co-solvent blend solutions. The exact co-solvent ratios are specific to each polymer and co-solvent being used, as stated in the main text. Electrodes were evaporated to produce the final device structure: ITO/PEDOT:PSS/Active Layer/Ca/Al. Films made for GIWAXS and NR studies using the same solutions made for active layer devices were cast onto silicon substrates (with a 1.8 nm SiO_2 native oxide layer). All film thicknesses were measured using a Dektak 150 stylus profilometer. Further fabrication details can be found in the Supporting Information (SI).

Structural Measurements. The two-dimensional GIWAXS measurements were performed at the Stanford Synchrotron Radiation Lightsource (SSRL) on beamline 11-3 using a wavelength of 0.09742 Å. Diffraction patterns were collected on a two-dimensional image plate with a sample to detector distance of 400 mm and a spot size of roughly 150 μm. A helium chamber was utilized to increase the signal-to-noise ratio. For the analysis of the GIWAXS data, the two-dimensional diffraction for each sample was integrated using WxDiff. The limits of the integration were changed on the basis of the orientation information desired. To obtain a full integration of a diffractogram, the integration limits over chi were from 0 to 180°. For in-plane, out-of-plane, and 45° integrations, the limits were 0-10°, 70-80°, and 40-50°, respectively. Each integration was background corrected for the substrate scattering. To ensure reproducibility in diffraction intensity and shape, all samples were made and measured in triplicate. NR experiments were performed at Oak Ridge National Laboratory using the Magnetism Reflectometer at the Spallation Neutron Source using a neutron wavelength of 4.41 Å and an effective q-range of 0.008-0.153 $Å^{-1}$ ($q = 4\pi/\lambda \sin\Theta$, where λ is the neutron wavelength

and Θ is the scattering angle). Motofit Software was used to determine the vertical distribution of the thin films by fitting the raw reflectivity data.

3.5. Supporting Information

Supporting Information is available in Appendix B.

3.6. References

(1) Yu, J.; Zheng, Y.; Huang, J. Towards High Performance Organic Photovoltaic Cells: A Review of Recent Development in Organic Photovoltaics. *Polymers (Basel)*. **2014**, 6 (9), 2473–2509.

(2) Hleli, E.; Alam, S.; Saaidia, A.; Kästner, C.; Hoeppener, S.; Ulbricht, C.; Romdhane, S.; Fredj, A. Ben; Egbe, D. A. M.; Schubert, U. S.; et al. Improvement of Polymer:Fullerene Bulk Heterojunction Morphology via Temperature and Anti-Solvent Effect. *Synth. Met.* **2018**, 243 (May), 8–16.

(3) Wang, T.; Chen, X. K.; Ashokan, A.; Zheng, Z.; Ravva, M. K.; Brédas, J. L. Bulk Heterojunction Solar Cells: Impact of Minor Structural Modifications to the Polymer Backbone on the Polymer–Fullerene Mixing and Packing and on the Fullerene–Fullerene Connecting Network. *Adv. Funct. Mater.* **2018**, 28 (14), 1–11.

(4) Gaspar, H.; Figueira, F.; Pereira, L.; Mendes, A.; Viana, J. C.; Bernardo, G. Recent Developments in the Optimization of the Bulk Heterojunction Morphology of Polymer: Fullerene Solar Cells. *Materials (Basel)*. **2018**, 11 (12).

(5) Osaka, I.; Saito, M.; Koganezawa, T.; Takimiya, K. Thiophene-Thiazolothiazole Copolymers: Significant Impact of Side Chain Composition on Backbone Orientation and Solar Cell Performances. *Adv. Mater.* **2014**, 26 (2), 331–338.

(6) Collins, B. A.; Tumbleston, J. R.; Ade, H. Miscibility, Crystallinity, and Phase Development in P3HT/PCBM Solar Cells: Toward an Enlightened Understanding of Device Morphology and Stability. *J. Phys. Chem. Lett.* **2011**, 2 (24), 3135–3145.

(7) Halls, J. J. M.; Walsh, C. A.; Greenham, N.; Marseglia, E. A.; Friend, R.; Moratti, S. C.; Holmes, A. Efficient Photodiodes from Interpenetrating Polymer Networks. *Nature* **1995**, 376 (6540), 498–500.

(8) Shaheen, S. E.; Brabec, C. J.; Sariciftci, N. S.; Padinger, F.; Fromherz, T.; Hummelen, J. C. 2.5% Efficient Organic Plastic Solar Cells. *Appl. Phys. Lett.* **2001**, 78 (6), 841–843.

(9) Shaw, P. E.; Ruseckas, A.; Samuel, I. D. W. Exciton Diffusion Measurements in Poly(3-Hexylthiophene). *Adv. Mater.* **2008**, 20 (18), 3516–3520.

(10) Peet, J.; Kim, J. Y.; Coates, N. E.; Ma, W. L.; Moses, D.; Heeger, A. J.; Bazan, G. C. Efficiency Enhancement in Low-Bandgap Polymer Solar Cells by Processing with Alkane Dithiols. *Nat Mater* **2007**, 6 (7), 497–500.

(11) Lee, J. K.; Ma, W. L.; Brabec, C. J.; Yuen, J.; Moon, J. S.; Kim, J. Y.; Lee, K.; Bazan, G. C.; Heeger, A. J. Processing Additives for Improved Efficiency from Bulk Heterojunction Solar Cells. *J. Am. Chem. Soc.* **2008**, 130 (11), 3619–3623.

(12) Zhao, Y.; Xie, Z.; Qu, Y.; Geng, Y.; Wang, L. Solvent-Vapor Treatment Induced Performance Enhancement of Poly(3-Hexylthiophene):Methanofullerene Bulk-Heterojunction Photovoltaic Cells. *Appl. Phys. Lett.* **2007**, 90 (4), 43503–43504.

(13) Kwon, S.; Kang, H.; Lee, J. H.; Lee, J.; Hong, S.; Kim, H.; Lee, K. Effect of Processing Additives on Organic Photovoltaics: Recent Progress and Future Prospects. *Adv. Energy Mater.* **2017**, 7 (10).

(14) Ma, W.; Yang, C.; Gong, X.; Lee, K.; Heeger, A. J. Thermally Stable, Efficient Polymer Solar Cells with Nanoscale Control of the Interpenetrating Network Morphology. *Adv. Funct. Mater.* **2005**, 15 (10), 1617–1622.

(15) Huttner, S.; Sommer, M.; Chiche, A.; Krausch, G.; Steiner, U.; Thelakkat, M. Controlled Solvent Vapour Annealing for Polymer Electronics. *Soft Matter* **2009**, 5 (21), 4206–4211.

(16) Verploegen, E.; Miller, C. E.; Schmidt, K.; Bao, Z.; Toney, M. F. Manipulating the Morphology of P3HT–PCBM Bulk Heterojunction Blends with Solvent Vapor Annealing. *Chem. Mater.* **2012**, 24 (20), 3923–3931.

(17) Ayzner, A. L.; Wanger, D. D.; Tassone, C. J.; Tolbert, S. H.; Schwartz, B. J. Room to Improve Conjugated Polymer-Based Solar Cells: Understanding How Thermal Annealing Affects the Fullerene Component of a Bulk Heterojunction Photovoltaic Device. *J. Phys. Chem. C* **2008**, 112 (48), 18711–18716.

(18) Heeger, A. J. 25th Anniversary Article: Bulk Heterojunction Solar Cells: Understanding the Mechanism of Operation. *Adv. Mater.* **2014**, 26 (1), 10–28.

(19) Aubry, T. J.; Ferreira, A. S.; Yee, P. Y.; Aguirre, J. C.; Hawks, S. A.; Fontana, M. T.; Schwartz, B. J.; Tolbert, S. H. Processing Methods for Obtaining a Face-On Crystalline Domain Orientation in Conjugated Polymer-Based Photovoltaics. *J. Phys. Chem. C* **2018**, 122, 15078–15089.

(20) Hawks, S. A.; Aguirre, J. C.; Schelhas, L. T.; Thompson, R. J.; Huber, R. C.; Ferreira, A. S.; Zhang, G.; Herzing, A. A.; Tolbert, S. H.; Schwartz, B. J. Comparing Matched Polymer:Fullerene Solar Cells Made by Solution-Sequential Processing and Traditional Blend Casting: Nanoscale Structure and Device Performance. *J. Phys. Chem. C* **2014**, 118 (31), 17413–17425.

(21) Fontana, M. T.; Kang, H.; Yee, P. Y.; Fan, Z.; Hawks, S. A.; Schelhas, L. T.; Subramaniyan, S.; Hwang, Y.; Jenekhe, S. A.; Tolbert, S. H.; et al. Low-Vapor-Pressure Solvent Additives Function as Polymer Swelling Agents in Bulk Heterojunction Organic Photovoltaics. *J. Phys. Chem. C* **2018**, 122, 16574–16588.

(22) Aguirre, J. C.; Hawks, S. A.; Ferreira, A. S.; Yee, P.; Subramaniyan, S.; Jenekhe, S. A.; Tolbert, S. H.; Schwartz, B. J. Sequential Processing for Organic Photovoltaics: Design Rules for Morphology Control by Tailored Semi-Orthogonal Solvent Blends. *Adv. Energy Mate*r. **2015**, 5 (11).

(23) Ayzner, A. L.; Tassone, C. J.; Tolbert, S. H.; Schwartz, B. J. Reappraising the Need for Bulk Heterojunctions in Polymer−Fullerene Photovoltaics: The Role of Carrier Transport in All-Solution-Processed P3HT/PCBM Bilayer Solar Cells. *J. Phys. Chem. C* **2009**, 113 (46), 20050–20060.

(24) Gevaerts, V. S.; Koster, L. J. A.; Wienk, M. M.; Janssen, R. A. J. Discriminating between Bilayer and Bulk Heterojunction Polymer:Fullerene Solar Cells Using the External Quantum Efficiency. *ACS Appl. Mater. Interfaces* **2011**, 3 (9), 3252–3255.

(25) Cheng, P.; Hou, J.; Li, Y.; Zhan, X. Layer-by-Layer Solution-Processed Low-Bandgap Polymer-PC61BM Solar Cells with High Efficiency. *Adv. Energy Mater.* **2014**, 4 (9), 1301349.

(26) Zhang, G.; Huber, R. C.; Ferreira, A. S.; Boyd, S. D.; Luscombe, C. K.; Tolbert, S. H.; Schwartz, B. J. Crystallinity Effects in Sequentially Processed and Blend-Cast Bulk-Heterojunction Polymer/Fullerene Photovoltaics. *J. Phys. Chem. C* **2014**, 118 (32), 18424–18435.

(27) Ferreira, A. S.; Aguirre, J. C.; Subramaniyan, S.; Jenekhe, S. A.; Tolbert, S. H.; Schwartz, B. J. Understanding How Polymer Properties Control OPV Device Performance: Regioregularity, Swelling, and Morphology Optimization Using Random Poly(3-Butylthiophene-Co-3-Octylthiophene) Polymers. *J. Phys. Chem. C* **2016**, 120 (39), 22115–22125.

(28) Keum, J. K.; Browning, J. F.; Xiao, K.; Shao, M.; Halbert, C. E.; Hong, K. Morphological Origin for the Stratification of P3HT:PCBM Blend Film Studied by Neutron Reflectometry. *Appl. Phys. Lett.* **2013**, 103 (22), 223301.

(29) Lee, K. H.; Zhang, Y.; Burn, P. L.; Gentle, I. R.; James, M.; Nelson, A.; Meredith, P. Correlation of Diffusion and Performance in Sequentially Processed P3HT/PCBM Heterojunction Films by Time-Resolved Neutron Reflectometry. *J. Mater. Chem. C* **2013**, 1 (14), 2593.

(30) Lee, K. H.; Schwenn, P. E.; Smith, A. R. G.; Cavaye, H.; Shaw, P. E.; James, M.; Krueger, K. B.; Gentle, I. R.; Meredith, P.; Burn, P. L. Morphology of All-Solution-Processed "Bilayer" Organic Solar Cells. *Adv. Mater.* **2011**, 23 (6), 766–770.

(31) Collins, B. a.; Gann, E.; Guignard, L.; He, X.; McNeill, C. R.; Ade, H. Molecular Miscibility of Polymer−Fullerene Blends. *J. Phys. Chem. Lett.* **2010**, 1 (21), 3160–3166.

(32) Tao, C.; Aljada, M.; Shaw, P. E.; Lee, K. H.; Cavaye, H.; Balfour, M. N.; Borthwick, R. J.; James, M.; Burn, P. L.; Gentle, I. R.; et al. Controlling Hierarchy in Solution-Processed Polymer Solar Cells Based on Crosslinked P3HT. *Adv. Energy Mater.* **2013**, 3 (1), 105–112.

(33) Herath, N.; Das, S.; Zhu, J.; Kumar, R.; Chen, J.; Xiao, K.; Gu, G.; Browning, J. F.; Sumpter, B. G.; Ivanov, I. N.; et al. Unraveling the Fundamental Mechanisms of Solvent-Additive-Induced Optimization of Power Conversion Efficiencies in Organic Photovoltaic Devices. *ACS Appl. Mater. Interfaces* **2016**, 8 (31), 20220–20229.

(34) Rochester, C. W.; Mauger, S. A.; Moulé, A. J. Investigating the Morphology of Polymer/Fullerene Layers Coated Using Orthogonal Solvents. *J. Phys. Chem. C* **2012**, 116 (13), 7287–7292.

(35) Van Franeker, J. J.; Kouijzer, S.; Lou, X.; Turbiez, M.; Wienk, M. M.; Janssen, R. A. J. Depositing Fullerenes in Swollen Polymer Layers via Sequential Processing of Organic Solar Cells. *Adv. Energy Mater.* **2015**, 5 (14), 1500464.

(36) Scholes, D. T.; Hawks, S. A.; Yee, P. Y.; Wu, H.; Lindemuth, J. R.; Tolbert, S. H.; Schwartz, B. J. Overcoming Film Quality Issues for Conjugated Polymers Doped with F4TCNQ by Solution Sequential Processing: Hall Effect, Structural, and Optical Measurements. *J. Phys. Chem. Lett.* **2015**, 6 (23), 4786–4793.

(37) Scholes, D. T.; Yee, P. Y.; Lindemuth, J. R.; Kang, H.; Onorato, J.; Ghosh, R.; Luscombe, C. K.; Spano, F. C.; Tolbert, S. H.; Schwartz, B. J. The Effects of Crystallinity on Charge Transport and the Structure of Sequentially Processed F4TCNQ-Doped Conjugated Polymer Films. *Adv. Funct. Mater.* **2017**, 1702654.

(38) Jacobs, I. E.; Aasen, E. W.; Oliveira, J. L.; Fonseca, T. N.; Roehling, J. D.; Li, J.; Zhang, G.; Augustine, M. P.; Mascal, M.; Moulé, A. J. Comparison of Solution-Mixed and Sequentially Processed P3HT:F4TCNQ Films: Effect of Doping-Induced Aggregation on Film Morphology. *J. Mater. Chem. C* **2016**, 4 (16), 3454–3466.

(39) Scholes, D. T.; Yee, P. Y.; McKeown, G. R.; Li, S.; Kang, H.; Lindemuth, J. R.; Xia, X.; King, S. C.; Seferos, D. S.; Tolbert, S. H.; et al. Designing Conjugated Polymers for Molecular Doping: The Roles of Crystallinity, Swelling, and Conductivity in Sequentially-Doped Selenophene-Based Copolymers. *Chem. Mater.* **2018**, 31, 73–82.

(40) Aubry, T. J.; Axtell, J. C.; Basile, V. M.; Winchell, K. J.; Lindemuth, J. R.; Porter, T. M.; Liu, J. Y.; Alexandrova, A. N.; Kubiak, C. P.; Tolbert, S. H.; et al. Dodecaborane-Based Dopants Designed to Shield Anion Electrostatics Lead to Increased Carrier Mobility in a Doped Conjugated Polymer. *Adv. Mater.* **2019**, 31 (11), 1–8.

(41) Liang, Y.; Xu, Z.; Xia, J.; Tsai, S. T.; Wu, Y.; Li, G.; Ray, C.; Yu, L. For the Bright Future-Bulk Heterojunction Polymer Solar Cells with Power Conversion Efficiency of 7.4%. *Adv. Mater.* **2010**, 22 (20).

(42) Subramaniyan, S.; Xin, H.; Kim, F. S.; Shoaee, S.; Durrant, J. R.; Jenekhe, S. A. Effects of Side Chains on Thiazolothiazole-Based Copolymer Semiconductors for High Performance Solar Cells. *Adv. Energy Mater.* **2011**, 1 (5), 854–860.

(43) Hwang, Y. J.; Courtright, B. A. E.; Ferreira, A. S.; Tolbert, S. H.; Jenekhe, S. A. 7.7% Efficient All-Polymer Solar Cells. *Adv. Mater.* **2015**, 27 (31), 4578–4584.

(44) Chen, H.; Peet, J.; Hsiao, Y. C.; Hu, B.; Dadmun, M. The Impact of Fullerene Structure on Its Miscibility with P3HT and Its Correlation of Performance in Organic Photovoltaics. *Chem. Mater.* **2014**, 26 (13), 3993–4003.

(45) Paternò, G. M.; Skoda, M. W. A.; Dalgliesh, R.; Cacialli, F.; Sakai, V. G. Tuning Fullerene Intercalation in a Poly (Thiophene) Derivative by Controlling the Polymer Degree of Self-Organisation. *Sci. Rep.* **2016**, 6 (October 2015), 34609.

(46) Clulow, A. J.; Armin, A.; Lee, K. H.; Pandey, A. K.; Tao, C.; Velusamy, M.; James, M.; Nelson, A.; Burn, P. L.; Gentle, I. R.; et al. Determination of Fullerene Scattering Length Density: A Critical Parameter for Understanding the Fullerene Distribution in Bulk Heterojunction Organic Photovoltaic Devices. *Langmuir* **2014**, 30 (5), 1410–1415.

(47) Huang, J. H.; Hsiao, Y. S.; Richard, E.; Chen, C. C.; Chen, P.; Li, G.; Chu, C. W.; Yang, Y. The Investigation of Donor-Acceptor Compatibility in Bulk-Heterojunction Polymer Systems. *Appl. Phys. Lett.* **2013**, 103 (4), 1–5.

(48) Germack, D. S.; Chan, C. K.; Hamadani, B. H.; Richter, L. J.; Fischer, D. A.; Gundlach, D. J.; Delongchamp, D. M. Substrate-Dependent Interface Composition and Charge Transport in Films for Organic Photovoltaics. *Appl. Phys. Lett.* **2009**, 94 (23), 92–95.

(49) Pan, D. H. K.; Prest, W. M. Surfaces of Polymer Blends: X-Ray Photoelectron Spectroscopy Studies of Polystyrene/Poly(Vinyl Methyl Ether) Blends. *J. Appl. Phys.* **1985**, 58 (8), 2861–2870.

Chapter 4. Overcoming Film Quality Issues for Conjugated Polymers Doped with F_4TCNQ by Solution Sequential Processing: Hall Effect, Structural, and Optical Measurements

Organic electronics utilize low-cost, solution-processable, and readily tunable semiconducting organic materials in a variety of applications such as LEDs,[1] photovoltaics,[2] thermoelectrics,[3] and transistors.[4] One common way to tune the important electronic properties of this class of materials is through molecular doping, that is, oxidizing or reducing the organic semiconductor to create an appreciable quantity of equilibrium charge carriers.[5–13] Recently, much interest has been focused on the dopant 2,3,5,6-tetrafluoro-7,7,8,8-tetracyanoquinodimethane (F_4TCNQ; see Figure 4.1a, below, for chemical structure), which has a LUMO level that is deep enough (approximately −5.2 eV relative to vacuum) to oxidize the HOMO of many organic semiconductors.[14] Although there is ample work concerning F_4TCNQ doping of small molecules,[15–20] much of the recent research has focused on the interaction of this dopant with semiconducting polymers.[21–34]

Traditionally, in order to dope conjugated polymers with F_4TCNQ, the two components are combined in solution in the desired dopant/polymer ratio. Due to the favorable energetic offset between the polymer HOMO and the F_4TCNQ LUMO, an electron is readily transferred from the polymer to F_4TCNQ when the two molecules come into contact, leading to charged species that remain closely bound in solution. The high polarity of these species causes them to easily precipitate out of the organic solvents that are used to process the individual materials.[28,35,36] As a result, large highly doped agglomerates form that are not fully solvated, making it difficult to fabricate thin films of sufficient quality to perform meaningful electrical and optical measurements. Raising the temperature of the blended solution can allow for small increases in the solubility of doped polymers in organic solvents;[21,25,28,29] however, high

temperatures also have a detrimental effect on doping both in solution[22] and in thin films (see Supporting Information (SI)). The degree of doping also can be raised slightly without hindering film quality by diluting the doped polymer solution in excess solvent, but this hinders the ability to make films of appreciable thickness by traditional spin-coating methods. Moreover, the neutral F_4TCNQ itself has a limited solubility in most of the organic solvents used to process polymer thin films. This limitation can be partially overcome by synthesizing new, related dopant molecules with increased solubility that can improve polymer/dopant interactions and lead to increased doping density, even with less favorable energetic offsets.[37,38]

Clearly, for molecular doping of semiconducting polymers to be practical, it is important to have a method that affords tunable (and large) doping concentrations as well as the ability to reproducibly fabricate high-quality films. Here, we show that solution-sequential processing (SqP)[39–43] readily yields films that meet both of these criteria. In SqP, the pure polymer is deposited first from any solvent that produces high-quality films. The molecular dopant is then deposited in a second step from a solvent in which the dopant is soluble and which also swells the polymer film without dissolving it. With the appropriate amount of swelling, molecular dopants can easily infiltrate throughout the polymer film without significantly changing the film's morphology, as our group and others have recently demonstrated for the construction of bulk heterojunction polymer photovoltaics.[43–45] It is important to note that what we call "SqP-based doping" has effectively been applied in the past to doping films of carbon nanotubes,[46–49] doping of polymer films with $NOPF_6$,[12,13] and for patterning conjugated polymer films by taking advantage of the large differential solubility of the doped and undoped regions of the polymer.[50]

In this Letter, we apply the SqP technique to the problem of creating high-quality, heavily doped, highly conductive (>1 S/ cm) films of poly(3-hexylthiophene) (P3HT; see Figure 4.4b, below, for chemical structure) with the molecular dopant F_4TCNQ. We show using optical

microscopy, profilometry, and 2-D grazing incidence wide-angle X-ray scattering (GIWAXS) that the SqP technique produces doped P3HT films with a morphology that is nearly identical to that of the original undoped film, save for the incorporation of F_4TCNQ. We perform a side-by-side comparison of doped films produced via the traditional blend-casting method and SqP and show that by changing the concentration of F_4TCNQ and the choice of solvent from which it is cast, we are able to tune the conductivity of P3HT films to virtually any desired level up to 5.5 S/cm. The excellent quality of these doped films allows for this relatively high conductivity to be measured over large distances (>1 cm) and also permits Hall effect measurements to determine the carrier concentration and mobility. Using ultrasensitive AC B-field Hall effect measurements, we find that, for example, a 1.57 S/cm F_4TCNQ SqP doped P3HT film is p-type and has a carrier concentration of $4.3 \pm 0.8 \times 10^{20}$ cm^{-3} with a mobility of 0.024 ± 0.006 cm^2 V^{-1} s^{-1}. With the free-carrier concentration determined, we are also afforded better insight into the UV−visible absorption spectrum of the doped films, and we see the nascent production of equilibrium bipolarons at high dopant concentrations.

We begin our report by first studying the film quality of F_4TCNQ-doped P3HT films produced by the traditional blend-casting method. For the purpose of this study, we maintained the concentration of P3HT in the solvent *o*-dichlorobenzene (ODCB) at 10 mg/mL and added varying amounts of F_4TCNQ to obtain the desired doping ratios, namely, 5, 10, 17, and 30 wt % F_4TCNQ relative to P3HT. We found that the spin-coating conditions that gave the best films were 800 rpm for 60 s, and more details of our sample preparation are given in the SI. The left portion of Figure 4.1 shows an optical micrograph of a doped blend-cast P3HT thin film. The film is highly non-uniform and made up of large regions of highly doped polymer agglomerates as well as some barren regions that are indicative of poor surface coverage of the blend-doped P3HT by spin-coating. The color difference between the pure, undoped film (right portion of

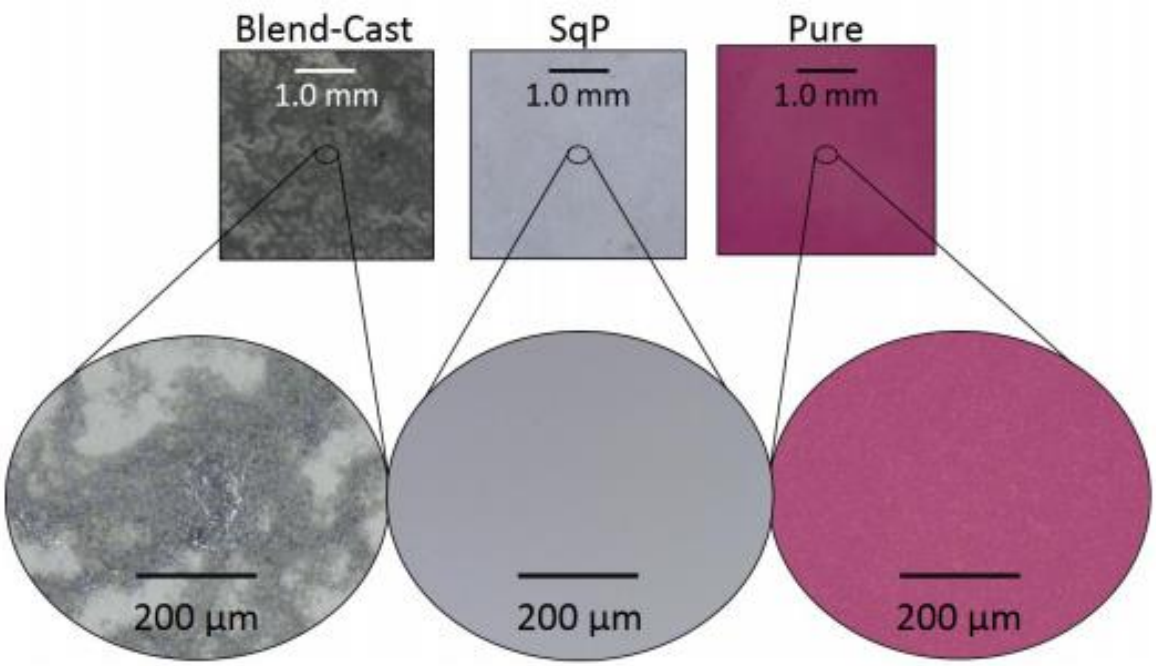

Figure 4.1. Color optical micrographs at two different length scales of thin films of left) doped P3HT prepared by the traditional blend-cast doping method with a 30 wt % F_4TCNQ to P3HT doping ration in ODCB; (center) doped P3HT prepared by the SqP method using 5 mg/mL F_4TCNQ in 75:25 THF/DCM as the casting solvent; and (right) pure, undoped P3HT spun from mg/mL solution in ODCB for reference.

Figure 4.1) and the doped films results from the doping, which significantly changes the absorption of P3HT, as discussed further below.

Figure 4.2a shows profilometry measurements of the surface roughness of blend-doped P3HT films as a function of the concentration of the F_4TCNQ dopant. The upper portion of Table 4.1 summarizes the average thickness (d) and root-mean-square (rms) surface roughness (R_{rms}) for these blend-cast films; the roughness continually increases from around 15 nm at 5 wt % F_4TCNQ to >400 nm at 30 wt %. Clearly, traditional blend-casting in the high-doping regime produces films of such poor uniformity that they are unsuitable for device applications or meaningful electrical measurements. The poor film quality of the blend-casting method can be seen by eye and has been noted by others.[35,36,51] As a result, some groups have chosen to study

the properties of doped P3HT nanofibers in part to avoid issues with the poor quality of doped blend-cast films.[33,34]

The SqP method, in contrast, allows us to easily overcome all of these issues. The right portion of Figure 4.1 shows an optical micrograph of a 110 nm thick pristine P3HT film cast

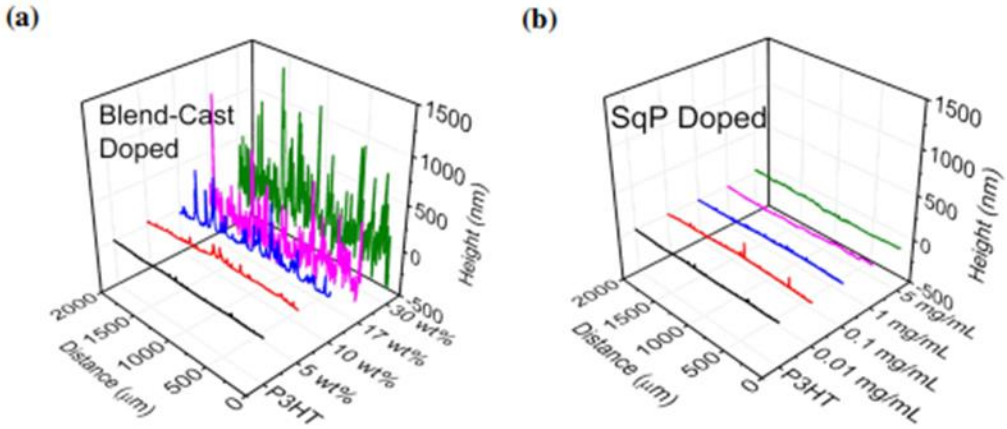

Figure 4.2. Surface height line scans of doped P3HT films measured by profilometry over a lateral distance of 2 mm prepared by (a) the traditional blend-casting method and (b) the SqP method. A range of dopant concentrations was prepared and measured for both methods. The average thickness and rms surface roughnesses from these scans are summarized in Table 4.1.

from a 20 mg/mL solution in ODCB at 1000 rpm for 60 s. As the corresponding line scans show in Figure 4.2, such undoped films are quite flat, with a rms surface roughness of only a few nm (Table 4.1) and no inhomogeneities on optically relevant length scales. When we then dope the film via SqP by spinning a 5 mg/mL solution of F_4TCNQ in a 75:25 tetrahydrofuran (THF)/dichloromethane (DCM) mixture on top of the pure P3HT film at 4000 rpm, the center part of Figure 4.1 shows that other than the change in film color due to doping, there is essentially no other alteration in the appearance of the film. Indeed, Figure 4.2b and Table 4.1 show that the surface roughness of the sequentially processed doped P3HT films stays close to that of the pure P3HT film prior to doping and that the roughness does not increase even as the concentration of the F_4TCNQ solution is increased to the solubility limit.

	R_{rms} (nm)	d (nm)	R_s ($\Omega/\square$)
pure P3HT	4 ± 1	105 ± 5	$>10^8$
	Blend Doped		
5 wt %	15 ± 2	56 ± 5	$>10^8$
10 wt %	77 ± 10	120 ± 30	6.5×10^7
17 wt %	220 ± 40	450 ± 100	3.7×10^4
30 wt %	418 ± 200	700 ± 300	2.1×10^4
	SqP Doped		
0.01 mg/mL	8 ± 2	110 ± 5	$>10^8$
0.1 mg/mL	8 ± 2	120 ± 12	6.5×10^4
1 mg/mL	11 ± 1	135 ± 5	2.0×10^4
5 mg/mL	8 ± 0.5	135 ± 5	1.5×10^4

Table 4.1. Comparison of the rms Surface Roughness (R_{rms}), Film Thickness (d), and Sheet Resistance (R_s) between Different Doping Methods.

In addition to the very different macroscopic film structure, we also have explored the molecular-level structural differences between F_4TCNQ-doped P3HT films created via traditional blend-casting and SqP using 2-D GIWAXS. By selectively integrating the 2-D diffraction patterns (as described in the SI), we are able to separate the out-of-plane scattering (corresponding to lattice planes oriented perpendicular to the substrate) and in-plane scattering (corresponding to lattice planes parallel to the substrate). These out-of-plane and in-plane scattering patterns are plotted in Figure 4.3a and b, respectively, for blend cast doped P3HT (1 and 17 wt %, orange and red curves, respectively), SqP doped P3HT (1 mg/mL from DCM, blue curves), and undoped P3HT (110 nm thick, green curves). We chose these two blend-cast concentrations because 1 wt % F_4TCNQ is the highest blend concentration that still produces a reasonable quality film and because 17 wt % F_4TCNQ gives approximately the same level of doping as the SqP film, as measured by UV−visible absorption. Because the film thickness and film quality vary drastically across these four samples (see Table 4.1), we did not

thickness-correct the diffraction intensity but instead normalized all of the diffraction patterns to the height of the (100) diffraction peak. The (100) diffraction peak, which corresponds to the lamellar stacking of the P3HT polymer chains, is centered at 0.39 $Å^{-1}$ in undoped P3HT, corresponding to a lamellar spacing of 16.11 Å. The (010) diffraction peak, which is associated with π−π stacking, appears at 1.67 $Å^{-1}$ (3.67 Å) in undoped P3HT films.

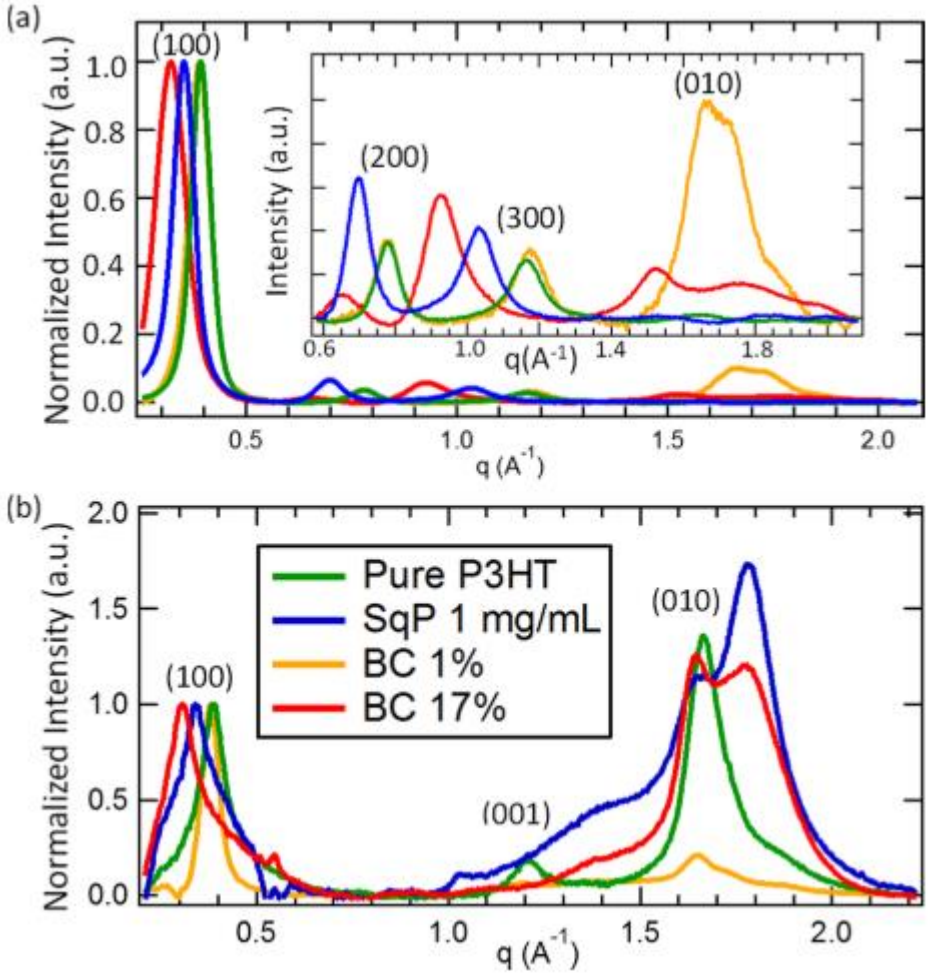

Figure 4.3. (a) Out-of-plane and (b) In-plane integrated portions of 2-D GIWAXS for films of blend-cast doped P3HT with 1% (orange) and 17% (red) F_4TCNQ by weight, sequentially processed doped P3HT (1 mg/mL, blue curves), and undoped P3HT (110 nm thick, green curves). For better comparison between films, which have large variations in thickness, the curves are normalized to the height of the (100) peaks. The inset in (a) shows the high-*q* region on an expanded vertical scale.

Although the lamellar diffraction peaks shift to higher *d*-spacing with increasing doping concentration and new peaks appear in the π−π stacking region, indicating that P3HT cation/F_4TCNQ anion co-crystals form for both SqP doped and blend-cast doped films (as discussed in more detail in the SI),[21,36,51,52] the most interesting comparison between films produced by the two processing techniques is in the crystalline polymer domain orientation. The domain orientation is determined in 2-D GIWAXS by examining the ratio of the out-of-plane to in-plane scattering intensity. For pure P3HT, the high out-of-plane to in-plane ratio seen for the (100) peak and a correspondingly low ratio measured for the (010) peak indicate that the polymer chains are preferentially oriented edge-on to the substrate, as is well-known for P3HT.[53] For the 1 mg/mL sequentially processed doped films, similar diffraction behavior is observed, with the (100) peak appearing most strongly out-of-plane and the (010) peaks appearing almost entirely in-plane. The new π−π stacking peaks that involve F_4TCNQ in this region at q ≈ 1.4 and 1.8 $Å^{-1}$ also show the same in-plane orientation. This indicates that despite doping with F_4TCNQ, the sequentially processed doped film maintains P3HT's edge-on molecular orientation with almost no disruption. By contrast, the 1 wt % blend-cast doped film shows significant (010) scattering and scattering from the q ≈ 1.8 $Å^{-1}$ F_4TCNQ-related peak in both the in-plane and out-of plane directions. This suggests that blend casting alters the P3HT domain orientation, changing it from predominantly edge-on to more isotropic. Presumably, this occurs because in blend-cast doping, solution-phase aggregation plays the dominant role in determining chain orientation in the resultant films.

We note that the scattering from the 17 wt % blend-cast doped film in the π−π region is more complicated than other samples as the positions of the F_4TCNQ-associated peaks are different in the in-plane and out-of-plane directions. This might arise from substrate orientation, perhaps involving excess F_4TCNQ,[51] or might reflect the fact that edge-on and face-on domains are differently ordered and thus have different π−π peak positions.[54] Regardless,

the presence of significant π−π scattering intensity in both the in-plane and out-of-plane directions in the 17 wt % doped blend-cast film also suggests that it is much more isotropic than pure P3HT.

It is also worth noting that our 1 mg/mL sequentially processed doped films show a ~15% increase in film thickness after incorporation of F_4TCNQ, as seen in Table 4.1. This is in reasonable agreement with the 11% increase seen in the lamellar spacing upon doping, suggesting that although there may be a small F_4TCNQ overlayer, the majority of the incorporated F_4TCNQ is intimately integrated into the P3HT lattice. Previous work exploring the use of SqP for polymer-based bulk heterojunction photovoltaics has shown that the swelling of the polymer film by the casting solvent from the second SqP step takes place primarily in the amorphous regions of the film.[44] This is why we believe that the majority of the F_4TCNQ dopant resides in the amorphous regions of our P3HT films. We also believe that the dopant interacts mostly with the surface of the pre-existing P3HT crystallites based on the fact that we see two different P3HT (010) peaks in the doped films. Thus, we expect that the molecular doping is homogeneous from optical length scales at least down to the crystallite size (~10 nm), but we remain unsure as to how much of the dopant actually penetrates into the crystallites and, if so, the dopant's distribution within the crystallites. Despite this uncertainty, all of our data support the idea that the swelling of the P3HT film during SqP allows for efficient intercalation of the F_4TCNQ dopant without significant changes to the P3HT domain orientation and thus the overall film morphology.[44]

Now that we have shown that the SqP method yields F_4TCNQ-doped P3HT films with excellent film quality and relatively unperturbed molecular morphology, we turn next to investigate the electrical properties of these layers. Fortunately, the SqP method allows the degree of doping to be easily tuned simply by altering the concentration of the dopant solution that is cast onto the polymer. We measured the electrical conductivity of a series of films that were doped to different levels via SqP with two different approaches over multiple length scales. The first method was a standard collinear four-point probe measurement with a distance between the probes of 2.5 mm. The second method was the Van der Pauw technique,[55] which used silver paste to make contacts on the corners of 1.5 × 1.5 cm doped films spun onto glass substrates. These measurements yielded values for the conductivity that were in agreement to within 1% of each other despite the large difference in measurement length scales. To further test the scalability of the SqP doping method, we also performed Van der Pauw measurements

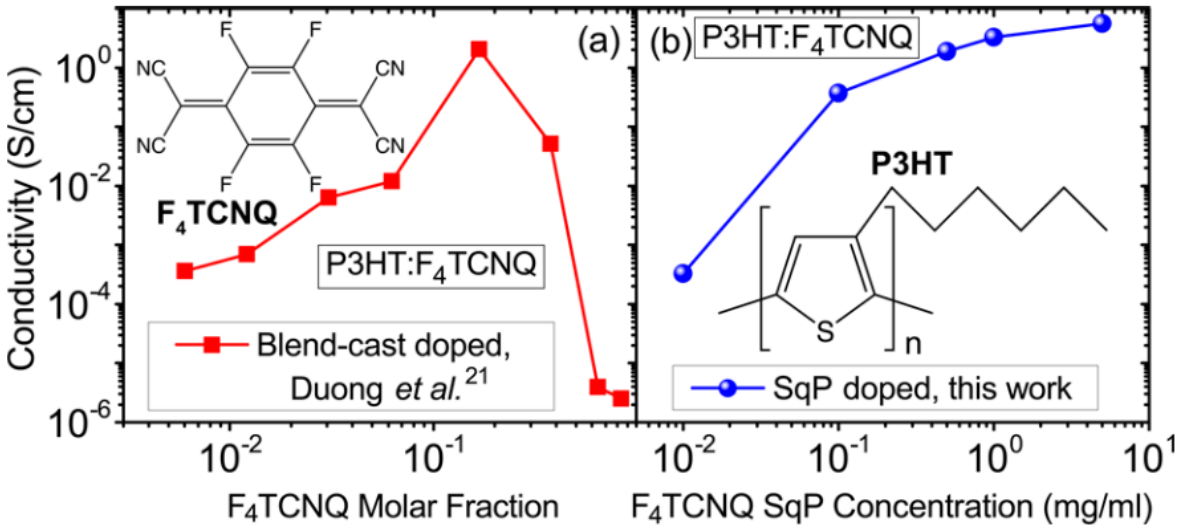

Figure 4.4. Comparison of the conductivity of P3HT thin films doped with F4TCNQ by (a) traditional blend-casting method (data taken from ref 21) and (b) our SqP method. The sequentially processed films were prepared by spinning various concentrations of F4TCNQ onto P3HT films at 4000 rpm. Thicknesses of the different sequentially processed films are given in Table 1. The horizontal axes for the two panels are different because of the differences in processing method; the doping level in (a) is given in units of the mole fraction of F4TCNQin the blended solution, while the horizontal axis for (b) is in units of mg/mL F4TCNQin the solution used for SqP.

at the corners of 1 in. square samples. This resulted in measured conductivities that were within 6% of those measured in the smaller samples, demonstrating exemplary scalability.

Figure 4.4 compares the conductivities of blend-cast doped P3HT films, taken from ref 21, (panel a) with those for the SqP doped films as a function of the concentration of F_4TCNQ in pure DCM (panel b). Although the horizontal axes for the two plots are different, meaning that direct comparison of conductivity at a particular doping level is not possible, the two plots do illustrate the overall trends in conductivity for the two different doping methods with increasing dopant concentration. Figure 4.4a shows that the amount of F_4TCNQ that can be used to dope P3HT via the blend-casting method is limited as the conductivity (measured over mm distances) peaks near 10 mol % doping and then declines rapidly due to film quality issues.[21] In contrast, Figure 4.4b shows that the conductivity of the sequentially processed doped films continues to increase monotonically with increasing dopant concentration to a maximum of 2.7 ± 0.6 S/cm when pure DCM is used as the casting solvent. The conductivity for SqP doped films appears to saturate at the highest dopant solution concentrations, and no decrease is ever observed. The average sheet resistance values that we measured for all of the doped P3HT films are reported in Table 4.1.

To further increase the amount of F_4TCNQ that intercalates into precast P3HT films, we used a solvent blend that was designed to simultaneously optimize swelling of the P3HT and F_4TCNQ solubility.[44] In this case, we used a 75:25 v/v THF/ DCM mixture. We chose THF as the co-solvent because it has much higher F_4TCNQ solubility than DCM, but we were limited to a maximum THF fraction of 75% v/v because any higher fraction of THF led to dissolution of the underlying P3HT films. With this particular solvent blend and a 5 mg/mL F_4TCNQ concentration, we were able to reproducibly fabricate doped P3HT films via SqP with a conductivity averaging 4.5 ± 0.6 S/cm and as high as 5.5 S/cm, which is the highest value reported that we are aware

of for a P3HT thin film doped by F_4TCNQ. We also performed experiments where we left the P3HT film to soak in various F_4TCNQ solutions for extended periods of time,[50] but this led to a slight degradation of film quality without achieving either higher doping levels or conductivities. We note that although P3HT has reached higher conductivities when doped with other species such as iodine[56] or FeCl3,[57] we hypothesize that our SqP method is already close to the site maximum for doping with F_4TCNQ as the interaction has been shown to saturate at approximately a 1:4 dopant-to-monomer ratio.[24]

The film quality with our SqP doping method is so exceptional that it is possible to detangle the carrier concentration and mobility underlying the conductivity via Hall effect measurements, despite the fact that the authors of ref 30 recently claimed that such measurements would likely never be possible on the F4TCNQ-doped P3HT system. Due to the low intrinsic carrier mobility of P3HT, we found that an AC magnetic field Hall effect measurement was required to obtain accurate and reliable results (see SI).[58,59] The results of these sensitive room-temperature measurements are presented in Table 4.2. Table 4.2 shows that all of our samples had the expected p-type conductivity with carrier concentrations ranging from 4.3×10^{16} to 4.3×10^{20} cm^{-3} and mobilities ranging from 3.3×10^{-3} to 2.4×10^{-2} $cm^2\ V^{-1}\ s^{-1}$

	0.01 mg/mL	0.1 mg/mL	1 mg/mL
V_H (μV)	2.02 ± 1.66	1.51 ± 0.3	15.28 ± 3.45
R_H (cm^3/C)	19.3 ± 15.7	$0.014 \pm .003$	0.015 ± 0.004
p (cm^{-3})	$(4.3 \pm 0.3) \times 10^{16}$	$(2.4 \pm 0.1) \times 10^{20}$	$(4.3 \pm 0.8) \times 10^{20}$
σ (S/cm)	$(1.70 \pm 0.02) \times 10^{-4}$	0.50 ± 0.01	1.57 ± 0.02
μ (cm^2/Vs)	$(3.3 \pm 2.7) \times 10^{-3}$	$(6.7 \pm 1.3) \times 10^{-3}$	$(2.4 \pm 0.6) \times 10^{-2}$

Table 4.2. Summary of Results of the Mean Values of the Hall Voltage (V_H), Hall Coefficient (R_H), Carrier Concentration (p), Resistivity (ρ), and Mobility (μ) from AC B-Field Hall Effect Measurements on SqP Doped P3HT Thin Films with Various Concentrations of F_4TCNQ Casting Solvent

for the doping levels examined. These mobility values are similar to previous findings for electrochemically gate-doped p-type P3HT,[60] which leads us to believe that conduction physics similar to those found in ref 60 also govern our samples. The highest charge carrier concentration of 4.3×10^{20} cm^{-3} that we observe corresponds to a doping density of roughly 1 carrier per 10 P3HT monomer units assuming a P3HT density of 1.1 g/cm^3. The fact that all of our samples registered as p-type suggests that there is no significant anomalous Hall effect due to certain types of hopping conduction or inhomogeneous distribution of doping.[5,61−63]

With these considerations in mind and the free-carrier concentration determined experimentally via the Hall effect, we now examine the UV−vis−NIR absorption in order to gain new understanding of the optical properties of F_4TCNQ/ P3HT films. We note that the absorption spectrum of blend-doped F_4TCNQ/P3HT films has been explored by several groups,[23,26,30] but a detailed assignment of the various bands and their cross sections has been obscured by the overlap of the anion and polaron spectra and the lack of an independent measurement of the carrier concentration. Using our experimentally determined carrier concentration, we attempted to decompose the absorption spectrum of one of our 1 mg/mL SqP doped films (Figure 4.5) using the F_4TCNQ solution cross section and previous assignments for the P3HT polaron peaks[30,64] (see the SI for detailed fitting and reference spectrum data). By assuming that the total carrier concentration must be at minimum the value of the free-carrier concentration measured by the Hall effect, then we also must assume this to be the minimum possible anion concentration (because there must be one anion per carrier, and the Hall effect measurement measures only free and not trapped carriers). When using our measured Hall carrier concentration to try to fit the absorption spectrum, however, it quickly became apparent that multiplying the carrier concentration by the solution cross section for the F_4TCNQ anion led to an absorbance more than twice as large as what we actually measured. Clearly, the actual cross section of the F_4TCNQ anion in the doped film must be quite a bit lower (and

have a different spectral shape) than that in solution, so that analyses of doped films using the solution spectrum and cross section are likely subject to significant error.

Since we are unable to completely detangle all of the various overlapping absorption bands in our measured spectrum because we do not know the spectrum and cross section for the anion in the film, we can instead analyze the P1 polaron transition, which peaks near 0.5 eV, as seen in Figure 4.5, because this spectral region is free from any overlap with the F_4TCNQ

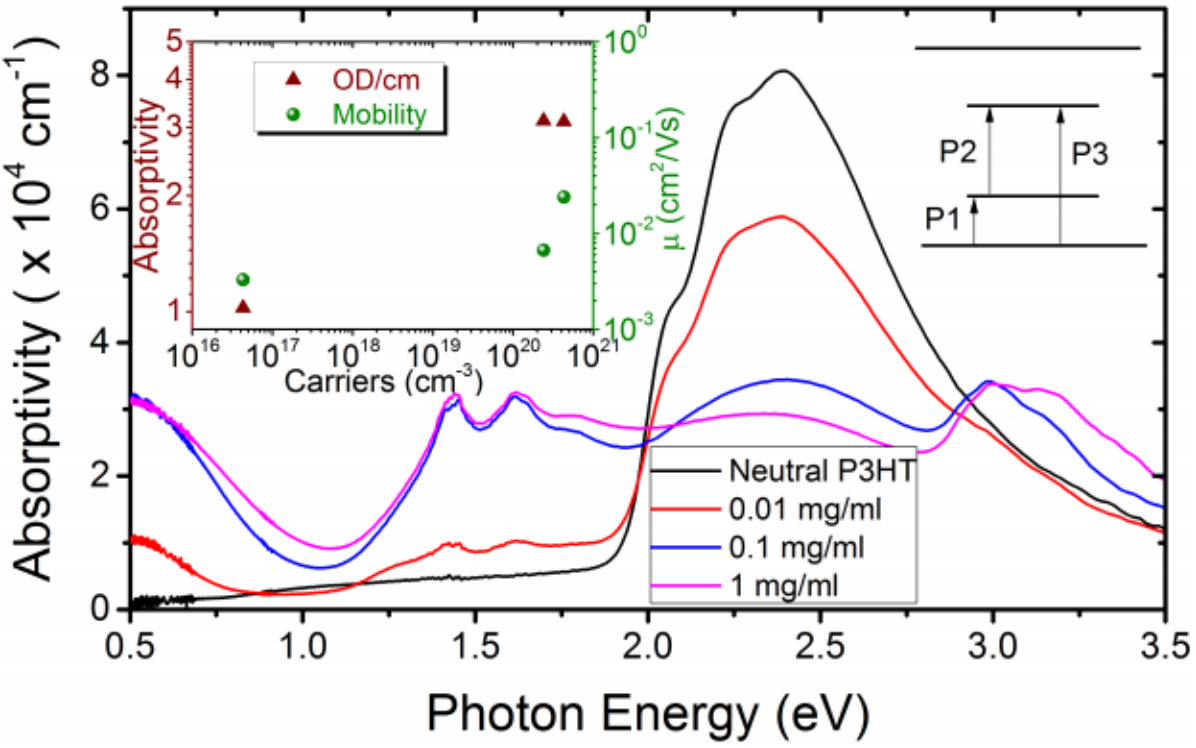

Figure 4.5. Thickness-normalized absorbance as a function of increasing F_4TCNQ casting concentration for P3HT films doped by the SqP method. The upper right inset shows an energy level diagram of the various polaron transitions, while the upper left inset shows a plot of how the peak absorbance of the P1 transition at 0.5 eV and mobility change with free-carrier concentration as measured by the AC B-field Hall Effect (Table 4.2).

anion (see SI). By tracking the response of this peak with respect to the free-carrier concentration determined by our Hall effect measurement, we are able to obtain a rough idea of the onset of bipolaron production at the highest doping concentrations. The inset of Figure 4.5 shows that the absorbance of the P1 polaron transition does not continue to increase as the

carrier concentration increases when going from the 0.1 mg/mL casting concentration to the 1 mg/mL casting concentration; this is strongly suggestive of bipolaron formation. Indeed, we observe that at around 0.75 eV, there is a noticeable broadening of the P1 band, which is most likely caused by the growth of the bipolaron transition that is located at a slightly higher energy than the P1 polaron transition, in agreement with other recent work.[57] The increased absorption that we see near 3.2 eV corresponds to neutral F_4TCNQ (see SI). We believe that this can be attributed to a slight overlayer of neutral F_4TCNQ, mentioned previously, that is present at high dopant concentrations as well as any F_4TCNQ incorporated into the film that did not undergo charge transfer, as has been seen previously for P3HT films doped with F_4TCNQ by blend-casting.[21,30]

The fact that our samples are sufficiently doped to show the beginnings of bipolaron formation also suggests that these samples have enough carriers to have filled all of the available traps. Decomposing the P1 absorption band into free and trapped carrier components is difficult. However, it has been shown previously through both theory and experiment that at low doping levels, a large portion of the generated polarons are trapped due to Coulomb interactions with the dopant anion, and at high doping levels, it becomes easier to generate free carriers due to screening and state-filling effects.[23,65,66] Because of the rapid increase in mobility that we observe between our 0.1 and 1 mg/mL SqP doped samples, we believe that we have exceeded the necessary amount of doping to lower the activation energy of the Coulomb traps, allowing for more efficient free-carrier generation and higher mobility.[66] The fact that the P1 absorptions of these two samples are hardly different while the Hall effect data show a large increase in the number of free carriers is also highly suggestive of liberating formerly trapped carriers in the more highly doped sample, so that at doping concentrations higher than 1 mg/mL, the vast majority of the carriers are free. We also note that the absorption of the neutral, undoped P3HT in the 2.0–2.8 eV range decreases between the 0.1

and 1 mg/mL SqP doped samples, indicating that the total amount of charge transfer is indeed somewhat higher with the higher concentration of dopant. Given that the P1 absorption does not change concomitantly, we can conclude from the data in Table 4.2 and Figure 4.5 that in our most highly doped samples, the majority of the carriers are free and there is a reasonably significant number of bipolarons, both of which we believe are directly attributable to the higher film quality of the SqP doping method.

In summary, we have shown that by utilizing the SqP method, we can overcome the issues of solubility and agglomeration at high dopant concentrations associated with blend-casting to easily prepare F_4TCNQ-doped films of P3HT with superior film quality, scalability, and electrical properties. Profilometry measurements show that our SqP doped films have a similar surface roughness to pristine films, and 2-D GIWAXS experiments show that sequentially processed F_4TCNQ incorporates neatly into the P3HT film structure, maintaining the crystalline domain orientation and much of the overall crystallinity. By varying the concentration of F_4TCNQ and choosing the appropriate casting solvent, the conductivity of doped films can be precisely tuned, achieving values for the P3HT/F_4TCNQ system as high as 5.5 S/cm. The film quality and doping levels are high enough to enable Hall effect measurements to detangle the carrier concentration and mobility, which can exceed 4×10^{20} cm^{-3} and 0.02 $cm^2\ V^{-1}\ s^{-1}$. In future work, we will take advantage of being able to fabricate highly doped films of sufficient electrical, optical, and morphological quality to decouple the effects of polymer crystallinity and the polymer/dopant energy level offset on the efficiency, stability, and electrical properties of doped semiconducting polymers. Overall, the application of SqP to the molecular doping of organic semiconductors provides another step toward the use of conjugated polymers for a wide variety of real-world device applications.

4.1. Experimental Methods

Materials & Sample Preparation. P3HT (Rieke Metals, Inc. Sepiolid P100) and F_4TCNQ (TCI Chemicals) were used as purchased. Glass substrates were cleaned by sequentially sonicating in water, acetone, and isopropanol. For SqP, P3HT films were spin coated at a rate of 1000 rpm for 60 s from a 20 mg/ml solution in ODCB, producing films that were ~110-nm thick. This was followed by a second spin-coating step where the P3HT film was infiltrated by a F_4TCNQ solution spin-coated on top of the dried P3HT film at 4000 rpm for 10 s. The solution for this second step was prepared by dissolving F_4TCNQ in DCM at 1 mg/ml and using the solution as-is or after serial dilution to produce the range of concentrations used. For higher-concentration 5 mg/ml F_4TCNQ solutions, we used a blend of 75:25 THF:DCM by volume as the solvent to increase the solubility of the dopant without dissolving the underlying P3HT film. For doped films prepared by the traditional blend-casting method, appropriate amounts of F_4TCNQ were added to the polymer solution to achieve the desired doping ratios while maintaining the P3HT concentration at 10 mg/ml in ODCB.

Film Characterization. Film thicknesses were measured using a Veeco Dektak 150 Profilometer. Surface roughness scans were measured using the profilometer over a lateral distance of 2 mm. Optical microscopy images were taken using a VHX-1000 microscope.

2-D grazing incidence wide-angle X-ray scattering (GIWAXS) experiments were performed at the Stanford Synchrotron Radiation Lightsource on beamline 11-3 using a wavelength of 0.9742 Å with an incidence angle of 0.12°.The full 2-D diffractograms were radially integrated to obtain the diffraction patterns (0-10° for in-plane, 70-80° for near out-of-plane, and 0-180° for full integrations) shown in the main text. The 2-D images were collected on a plate with the detector 250 mm away from the center of the measured sample. The beam spot had a width of ~150 μm and a helium chamber was used to reduce the noise. The software

package WxDiff was used to reduce the GIWAXS data and subsequent analysis was performed in IgorPro.

Conductivity Measurements. Collinear four-point probe measurements were performed using a custom-made apparatus in ambient atmosphere using a Keithley 2400 Sourcemeter sourcing a DC current of 1-100 μA with a probe spacing of 2.5 mm. Conductivity measurements in the Van der Pauw geometry were also performed using a custom made apparatus in ambient atmosphere using a Keithley 2400 Sourcemeter where the max current sourced was held to 1 mW total power. The current was swept from negative to positive, rotated 90°, and repeated. The slope of the I–V curves were then fit to the Van der Pauw equation. Samples in the Van der Pauw geometry were prepared as described in main text, with silver paste applied at the corners of the film to act as contacts. All reported data was averaged over 10 simultaneous measurements for multiple samples. An AC field Hall method was used to accurately measure carrier concentration and mobility for these low-mobility doped P3HT samples. The AC-field technique provides effectual measurements because the method can distinguish the Hall voltage signal from unwanted background signals, as standard DC-field Hall effect measurements proved ineffective. The samples were measured using the AC-field Hall method with a Lake Shore model 8407 system with an AC field amplitude of 1.2T RMS. The 0.01 mg/ml doped SqP sample used a current of 10 nanoamps, the 0.1 mg/ml sample used 10 μA, and both the 1 mg/ml and 5 mg/ml samples used 100 μA of current. Current reversal was used to remove the thermal electric and the inductive pickup voltages. The 0.01 mg/ml sample was measured 167 times over 24 hours, the 0.1 mg/ml samples were measured 287 times over 36 hours, and the 1 mg/ml and 5 mg/ml samples were measured 81 times each over 10 hours.

4.2. Supporting Information

Supporting Information is available in Appendix C.

4.3. References

(1) Burroughes, J. H.; Bradley, D. D. C.; Brown, A. R.; Marks, R. N.; Mackay, K.; Friend, R. H.; Burns, P. L.; Holmes, A. B. Light-emitting Diodes Based on Conjugated Polymers. *Nature* **1990**, 347, 539–541.

(2) Liang, Y.; Yu, L. Development of Semiconducting Polymers for Solar Energy Harvesting. *Polym. Rev.* **2010**, 50, 454–473.

(3) Chen, Y.; Zhao, Y.; Liang, Z. Solution Processed Organic Thermoelectrics: Towards Flexible Thermoelectric Modules. *Energy Environ. Sci.* **2015**, 8, 401–422.

(4) Lu, G.; Blakesley, J.; Himmelberger, S.; Pingel, P.; Frisch, J.; Lieberwirth, I.; Salzmann, I.; Oehzelt, M.; Di Pietro, R.; Salleo, A.; et al. Moderate Doping Leads to High Performance of Semiconductor/Insulator Polymer Blend Transistors. *Nat. Commun.* **2013**, 4, 1588.

(5) Seeger, K.; Gill, W.; Clarke, T.; Street, G. Conductivity and Hall Effect Measurements in Doped Polyacetylene. *Solid State Commun.* **1978**, 28, 873–878.

(6) Jarrett, C. P.; Friend, R. H.; Brown, A. R.; De Leeuw, D. M. Field Effect Measurements in Doped Conjugated Polymer Films: Assessment of Charge Carrier Mobilities. *J. Appl. Phys.* **1995**, 77, 6289–6294.

(7) Chiang, C. K.; Fincher, C. R.; Park, Y. W.; Heeger, A. J.; Shirakawa, H.; Louis, E. J.; Gau, S. C.; MacDiarmid, A. G. Electrical Conductivity in Doped Polyacetylene. *Phys. Rev. Lett.* **1977**, 39, 1098– 1101.

(8) Fincher, C. R.; Ozaki, J. M.; Tanaka, M.; Peebles, D.; Lauchlan, L.; Heeger, A. J.; MacDiarmid, A. G. Electronic Structure of Polyacetylene: Optical and Infrared Studies of Undoped Semiconducting $(CH)_x$ and Heavily Doped Metallic $(CH)_x$. Phys. Rev. B: Condens. Matter Mater. Phys. **1979**, 20, 1589–1602.

(9) Baughman, R. H.; Bredas, J.; Chance, R. R.; Elsenbaumer, R. L.; Shacklette, L. W. Structural Basis for Semiconducting and Metallic Polymer/Dopant Systems. *Chem. Rev.* **1982**, 82, 209–222.

(10) Bredas, J.; Street, G. Polarons, Bipolarons, and Solitons in Conducting Polymers. *Acc. Chem. Res.* **1985**, 18, 309–315.

(11) Kim, Y. H.; Spiegel, D.; Hotta, S.; Heeger, A. J. Photoexcitation and Doping Studies of Poly(3-hexylthienylene). *Phys. Rev. B: Condens. Matter Mater. Phys.* **1988**, 38, 5490–5495.

(12) Lögdlund, M.; Lazzaroni, R.; Stafström, S.; Salaneck, W. R. Direct Observation of Charge-Induced pi-Electronic Structural Changes in a Conjugated Polymer. *Phys. Rev. Lett.* **1989**, 63, 1841– 1844.

(13) Lazzaroni, R.; Lögdlund, M.; Stafström, S.; Salaneck, W. R.; Bredas, J. L. The Poly-3-hexylthiophene/$NOPF_6$ System: A Photoelectron Spectroscopy Study of Electronic Structural Changes Induced by the Charge Transfer in the Solid State. *J. Chem. Phys.* **1990**, 93, 4433–4439.

(14) Salzmann, I.; Heimel, G.; Duhm, S.; Oehzelt, M.; Pingel, P.; George, B. M.; Schnegg, A.; Lips, K.; Blum, R. P.; Vollmer, A.; et al. Intermolecular Hybridization Governs Molecular Electrical Doping. Phys. Rev. Lett. 2012, 108, 1–5.

(15) Maennig, B.; Pfeiffer, M.; Nollau, A.; Zhou, X.; Leo, K.; Simon, P. Controlled P-type Doping of Polycrystalline and Amorphous Organic Layers: Self-Consistent Description of Conductivity and Field-Effect Mobility by a Microscopic Percolation Model. *Phys. Rev. B: Condens. Matter Mater. Phys.* **2001**, 64, 1–9.

(16) Zhou, X.; Pfeiffer, M.; Blochwitz, J.; Werner, A.; Nollau, A.; Fritz, T.; Leo, K. Very-Low-Operating-Voltage Organic Light-Emitting Diodes Using a P-Doped Amorphous Hole Injection Layer. *Appl. Phys. Lett.* **2001**, 78, 410–412.

(17) Pfeiffer, M.; Beyer, A.; Fritz, T.; Leo, K.; Pfeiffer, M.; Beyer, A.; Fritz, T.; Leo, K. Controlled Doping of Phthalocyanine Layers by Cosublimation with Acceptor Molecules: A Systematic Seebeck and Conductivity Study. *Appl. Phys. Lett.* **1998**, 73, 3202–3204.

(18) Blochwitz, J.; Pfeiffer, M.; Fritz, T.; Leo, K.; Blochwitz, J.; Pfeiffer, M.; Fritz, T.; Leo, K. Low Voltage Organic Light Emitting Diodes Featuring Doped Phthalocyanine as Hole Transport Material. *Appl. Phys. Lett.* **1998**, 73, 729–731.

(19) Gao, W.; Kahn, A. Electrical Doping: the Impact on Interfaces of π-Conjugated Molecular Films. *J. Phys.: Condens. Matter* **2003**, 15, 52757–52770.

(20) Walzer, K.; Pfeiffer, M.; Leo, K.; Maennig, B. Highly Efficient Organic Devices Based on Electrically Doped Transport Layers. *Chem. Rev.* **2007**, 107, 1233–1271.

(21 Duong, D. T.; Wang, C.; Antono, E.; Toney, M. F.; Salleo, A. The Chemical and Structural Origin of Efficient P-Type Doping in P3HT. *Org. Electron.* **2013**, 14, 1330–1336.

(22) Duong, D. T.; Phan, H.; Hanifi, D.; Jo, P. S.; Nguyen, T.-Q.; Salleo, A. Direct Observation of Doping Sites in Temperature Controlled, P-Doped P3HT Thin Films by Conducting Atomic Force Microscopy. *Adv. Mater.* **2014**, 26, 6069–6073.

(23) Pingel, P.; Neher, D. Comprehensive Picture of P-Type Doping of P3HT with the Molecular Acceptor F_4TCNQ. *Phys. Rev. B: Condens. Matter Mater. Phys.* **2013**, 87, 115209.

(24) Pingel, P.; Zhu, L.; Park, K. S.; Vogel, J. O.; Janietz, S.; Kim, E. G.; Rabe, J. P.; Bredas, J. L.; Koch, N. Charge-Transfer Localization in Molecularly Doped Thiophene-Based Donor Polymers. *J. Phys. Chem. Lett.* **2010**, 1, 2037–2041.

(25) Ghani, F.; Opitz, A.; Pingel, P.; Heimel, G.; Salzmann, I.; Frisch, J.; Neher, D.; Tsami, A.; Scherf, U.; Koch, N. Charge Transfer in and Conductivity of Molecularly Doped Thiophene-Based Copolymers. *J. Polym. Sci., Part B: Polym. Phys.* **2015**, 53, 58–63.

(26) Gao, J.; Niles, E. T.; Grey, J. K. Aggregates Promote Efficient Charge Transfer Doping of Poly(3-hexylthiophene). *J. Phys. Chem. Lett.* **2013**, 4, 2953–2957.

(27) Glaudell, A. M.; Cochran, J. E.; Patel, S. N.; Chabinyc, M. L. Impact of the Doping Method on Conductivity and Thermopower in Semiconducting Polythiophenes. *Adv. Energy Mater.* **2015**, 5, 1–8.

(28) Cochran, J. E.; Junk, M. J. N.; Glaudell, A. M.; Miller, P. L.; Cowart, J. S.; Toney, M. F.; Hawker, C. J.; Chmelka, B. F.; Chabinyc, M. L. Molecular Interactions and Ordering in Electrically Doped Polymers: Blends of PBTTT and F_4TCNQ. *Macromolecules* **2014**, 47, 6836–6846.

(29) Aziz, E.; Vollmer, a.; Eisebitt, S.; Eberhardt, W.; Pingel, P.; Neher, D.; Koch, N. Localized Charge Transfer in a Molecularly Doped Conducting Polymer. *Adv. Mater.* **2007**, 19, 3257–3260.

(30) Wang, C.; Duong, D. T.; Vandewal, K.; Rivnay, J.; Salleo, A. Optical Measurement of Doping Efficiency in Poly(3-hexylthiophene) Solutions and Thin Films. *Phys. Rev. B: Condens. Matter Mater. Phys.* **2015**, 91, 1–7.

(31) Zhu, L.; Kim, E.-G.; Yi, Y.; Bredas, J.-L. Charge Transfer in Molecular Complexes with 2,3,5,6-Tetrafluoro-7,7,8,8-tetracyanoquinodimethane (F_4TCNQ): A Density Functional Theory Study. *Chem. Mater.* **2011**, 23, 5149–5159.

(32) Pingel, P.; Schwarzl, R.; Neher, D. Effect of Molecular P-Doping on Hole Density and Mobility in Poly(3-hexylthiophene). *Appl. Phys. Lett.* **2012**, 100, 143303/1–143303/3.

(33) Gao, J.; Stein, B. W.; Thomas, A. K.; Garcia, J. A.; Yang, J.; Kirk, M. L.; Grey, J. K. Enhanced Charge Transfer Doping Efficiency in J-Aggregate Poly(3-hexylthiophene) Nanofibers. *J. Phys. Chem. C* **2015**, 119, 16396–16402.

(34) Hu, J.; Clark, K. W.; Hayakawa, R.; Li, A. P.; Wakayama, Y. Enhanced Electrical Conductivity in Poly(3-hexylthiophene)/Fluorinated Tetracyanoquinodimethane Nanowires Grown with a Porous Alumina Template. *Langmuir* **2013**, 29, 7266–7270.

(35) Deschler, F.; Riedel, D.; Deak, A.; Ecker, B.; von Hauff, E.; Da Como, E. Imaging of Morphological Changes and Phase Segregation in Doped Polymeric Semiconductors. *Synth. Met.* **2015**, 199, 381–387.

(36) Gao, J.; Roehling, J. D.; Li, Y.; Guo, H.; Moule, A. J.; Grey, J. K. The Effect of 2,3,5,6-tetrafluoro-7,7,8,8-tetracyanoquinodimethane Charge Transfer Dopants on the Conformation and Aggregation of Poly(3-hexylthiophene). *J. Mater. Chem. C* **2013**, 1, 5638.

(37) Gao, Z. Q.; Mi, B. X.; Xu, G. Z.; Wan, Y. Q.; Gong, M. L.; Cheah, K. W.; Chen, C. H. An organic p-type dopant with high thermal stability for an organic semiconductor. *Chem. Commun.* **2008**, 117–119.

(38) Li, J.; Zhang, G.; Holm, D. E.; Jacobs, I. E.; Yin, B.; Stroeve, P.; Mascal, M.; Moule, A. J. Introducing Solubility Control for Improved Organic P-Type Dopants. *Chem. Mater.* **2015**, 27, 5765–5774.

(39) Ayzner, A. L.; Doan, S. C.; Tremolet De Villers, B.; Schwartz, B. J. Ultrafast Studies of Exciton Migration and Polaron Formation in Sequentially Solution-Processed Conjugated Polymer/Fullerene Quasi-Bilayer Photovoltaics. *J. Phys. Chem. Lett.* **2012**, 3, 2281–2287.

(40) Hawks, S. A.; Aguirre, J. C.; Schelhas, L. T.; Thompson, R. J.; Huber, R. C.; Ferreira, A. S.; Zhang, G.; Herzing, A. A.; Tolbert, S. H.; Schwartz, B. J. Comparing Matched Polymer:Fullerene Solar Cells Made by Solution-Sequential Processing and Traditional Blend Casting: Nanoscale Structure and Device Performance. *J. Phys. Chem. C* **2014**, 118, 17413–17425.

(41) Lee, K. H.; Schwenn, P. E.; Smith, A. R. G.; Cavaye, H.; Shaw, P. E.; James, M.; Krueger, K. B.; Gentle, I. R.; Meredith, P.; Burn, P. L. Morphology of All-Solution-Processed "Bilayer" Organic Solar Cells. *Adv. Mater.* **2011**, 23, 766–770.

(42) Wang, D. H.; Moon, J. S.; Seifter, J.; Jo, J.; Park, J. H.; Park, O. O.; Heeger, A. J. Sequential Processing: Control of Nanomorphology in Bulk Heterojunction Solar Cells. *Nano Lett.* **2011**, 11, 3163–3168.

(43) Zhang, G.; Huber, R. C.; Ferreira, A. S.; Boyd, S. D.; Luscombe, C. K.; Tolbert, S. H.; Schwartz, B. J. Crystallinity Effects in Sequentially Processed and Blend-Cast Bulk-Heterojunction Polymer/Fullerene Photovoltaics. *J. Phys. Chem. C* **2014**, 118, 18424–18435.

(44) Aguirre, J. C.; Hawks, S. A.; Ferreira, A. S.; Yee, P.; Subramaniyan, S.; Jenekhe, S. A.; Tolbert, S. H.; Schwartz, B. J. Sequential Processing for Organic Photovoltaics: Design Rules for Morphology Control by Tailored Semi-Orthogonal Solvent Blends. *Adv. Energy Mater.* **2015**, 5, 1–11.

(45) van Franeker, J. J.; Kouijzer, S.; Lou, X.; Turbiez, M.; Wienk, M. M.; Janssen, R. A. J. Depositing Fullerenes in Swollen Polymer Layers via Sequential Processing of Organic Solar Cells. *Adv. Energy Mater.* **2015**, 5, 1–10.

(46) Takenobu, T.; Kanbara, T.; Akima, N.; Takahashi, T.; Shiraishi, M.; Tsukagoshi, K.; Kataura, H.; Aoyagi, Y.; Iwasa, Y. Control of Carrier Density by a Solution Method in Carbon-Nanotube Devices. *Adv. Mater.* **2005**, 17, 2430–2434.

(47) Sasaki, Y.; Okimoto, H.; Yoshida, K.; Ono, Y.; Iwasa, Y.; Takenobu, T. Thermally and Environmentally Stable Carrier Doping Using a Solution Method in Carbon Nanotube Films. *Appl. Phys. Express* **2011**, 4, 085102.

(48) Matsuzaki, S.; Nobusa, Y.; Shimizu, R.; Yanagi, K.; Kataura, H.; Takenobu, T. Continuous Electron Doping of Single-Walled Carbon Nanotube Films Using Inkjet Technique. *Jpn. J. Appl. Phys.* **2012**, 51, 06FD18/1–06FD18/3.

(49) Hong, C. T.; Lee, W.; Kang, Y. H.; Yoo, Y.; Ryu, J.; Cho, S. Y.; Jang, K.-S. Effective Doping by Spin-Coating and Enhanced Thermoelectric Power Factors in SWCNT/P3HT Hybrid Films. *J. Mater. Chem. A* **2015**, 3, 12314–12319.

(50) Jacobs, I. E.; Li, J.; Burg, S. L.; Bilsky, D. J.; Rotondo, B. T.; Augustine, M. P.; Stroeve, P.; Moule, A. J. Reversible Optical Control of Conjugated Polymer Solubility with Sub-micrometer Resolution. *ACS Nano* **2015**, 9, 1905–1912.

(51) Cochran, J. E.; Junk, M. J. N.; Glaudell, A. M.; Miller, P. L.; Cowart, J. S.; Toney, M. F.; Hawker, C. J.; Chmelka, B. F.; Chabinyc, M. L. Molecular Interactions and Ordering in Electrically Doped Polymers: Blends of PBTTT and F_4TCNQ. *Macromolecules* **2014**, 47, 6836–6846.

(52) Mendez, H.; Heimel, G.; Opitz, A.; Sauer, K.; Barkowski, P.; Oehzelt, M.; Soeda, J.; Okamoto, T.; Takeya, J.; Arlin, J. B.; et al. Doping of Organic Semiconductors: Impact of Dopant Strength and Electronic Coupling. *Angew. Chem.* **2013**, 125, 7905–7909.

(53) Verploegen, E.; Mondal, R.; Bettinger, C. J.; Sok, S.; Toney, M. F.; Bao, Z. Effects of Thermal Annealing Upon the Morphology of Polymer-Fullerene Blends. *Adv. Funct. Mater.* **2010**, 20, 3519–3529.

(54) Li, H.; Hwang, Y.-J.; Earmme, T.; Huber, R. C.; Courtright, B. A. E.; O'Brien, C.; Tolbert, S. H.; Jenekhe, S. A. Polymer/Polymer Blend Solar Cells Using Tetraazabenzodifluoranthene Diimide Conjugated Polymers as Electron Acceptors. *Macromolecules* **2015**, 48, 1759–1766.

(55) *Resistivity and Hall Measurements*. http://www.nist.gov/pml/div683/hall_resistivity.cfm#resistivity (2015).

(56) Ukai, S.; Ito, H.; Marumoto, K.; Kuroda, S. I. Electrical Conduction of Regioregular and Regiorandom Poly(3-hexylthiophene) Doped with Iodine. *J. Phys. Soc. Jpn.* **2005**, 74, 3314–3319.

(57) Yamamoto, J.; Furukawa, Y. Electronic and Vibrational Spectra of Positive Polarons and Bipolarons in Regioregular Poly(3-hexylthiophene) Doped with Ferric Chloride. *J. Phys. Chem. B* **2015**, 119, 4788–4794.

(58) Lindemuth, J.; Mizuta, S.-I. Hall Measurements on Low Mobility Materials and High Resistivity Materials. *Proc. SPIE* **2011**, 8110, 81100I/1–81100I/7.

(59) Lindemuth, J. Variable Temperature Hall Measurements on Low-Mobility Materials. *Proc. SPIE* **2012**, 8470, 84700G/1–84700G/ 9.

(60) Wang, S.; Ha, M.; Manno, M.; Daniel Frisbie, C.; Leighton, C. Hopping Transport and the Hall Effect Near the Insulator-Metal Transition in Electrochemically Gated Poly(3-hexylthiophene) Transistors. *Nat. Commun.* **2012**, 3, 1210.

(61) Emin, D. The Sign of the Hall Effect in Hopping conduction. *Philos. Mag.* **1977**, 35, 1189–1198.

(62) Fukuhara, T.; Masubuchi, S.; Kazama, S. Hall effect in ClO4- doped polythiophene and poly(3-methylthiophene). *Synth. Met.* **1995**, 69, 359–360.

(63) Munn, R. W.; Siebrand, W. Sign of the Hall Effect for Hopping Transport in Molecular Crystals. *Phys. Rev. B* **1970**, 2, 3435–3437.

(64) Brown, P.; Sirringhaus, H.; Harrison, M.; Shkunov, M.; Friend, R. Optical Spectroscopy of Field-Induced Charge in Self-Organized High Mobility Poly(3-hexylthiophene). *Phys. Rev. B: Condens. Matter Mater. Phys.* **2001**, 63, 1–11.

(65) Arkhipov, V. I.; Heremans, P.; Emelianova, E. V.; Adriaenssens, G. J.; Bassler, H. Charge Carrier Mobility in Doped Semiconducting¨Polymers. *Appl. Phys. Lett.* **2003**, 82, 3245. (66) Arkhipov, V. I.; Emelianova, E. V.; Heremans, P.; Bassler, H.¨Analytic Model of Carrier Mobility in Doped Disordered Organic Semiconductors. *Phys. Rev. B: Condens. Matter Mater. Phys.* **2005**, 72, 235202.

Chapter 5. The Effects of Crystallinity on Charge Transport and the Structure of Sequentially Processed F_4TCNQ-Doped Conjugated Polymer Films

5.1. Introduction

One of the greatest advantages of organic electronics based on semiconducting polymers is the ease of device manufacturing through solution processing: techniques such as spin-coating, drop-casting, and blade-coating can be used to create reproducible active layers for organic electronic devices.[1-7] As with traditional inorganic semiconductors, the electronic properties of semiconducting polymers can be effectively tuned through doping,[8-13] by either removing (p-type doping) or adding (n-type doping) an electron to the polymer backbone. One of the most common ways to dope a semiconducting polymer is via the use of a molecular dopant, such as a small molecule, that can reduce or (much more commonly) oxidize the polymer backbone.[8,14-19] Indeed, the addition of small amounts of molecular dopants can improve the performance of polymer-based bulk heterojunction solar cells as the doped carriers fill intrinsic traps,[20-24] and more extensive molecular doping can vastly improve conductivity and carrier mobility for transistor[13,25] or thermoelectric[26,27] applications. Common p-type molecular dopants for semiconducting polymers include iodine (I_2),[28-30] iron chloride ($FeCl_3$),[17,31] and 2,3,5,6-tetrafluoro-7,7,8,8-tetracyanoquinodimethane (F_4TCNQ).[11,32,33]

Because of the large advantages offered by molecular doping, there has been a great deal of work done to characterize the structural, optical, and electronic properties of doped semiconducting polymers as a function of the degree of molecular doping.[8,11,17,29,34-44] There has been much less work, however, aimed at studying how systematically varying the structure or degree of crystallinity of a conjugated polymer affects the properties of the chemically doped

material.[40,45-48] One reason for this is that in many cases, molecular doping is performed in solution. The dopant and polymer are co-dissolved in what is typically a good solvent for the polymer, but as the dopant oxidizes the polymer, it becomes electrically charged and thus much less soluble in the nonpolar solvents typically used for semiconducting polymers. Thus, the structures of doped polymer films cast from such solutions are determined primarily by aggregation of the doped polymer and the choice of solvent, and the film quality is generally quite poor.[43,46,47,49-51] Post-doping processing methods to improve crystallinity, such as thermal annealing, also can be problematic, as exposure to increased temperatures can de-dope conjugated polymer films.[31,47,52,53]

To avoid issues with poor film quality at high doping levels, there has been a recent thrust in the literature to utilize methods where the dopant is applied to a precast film of the undoped semiconducting polymer. Techniques include relying on exposing a conjugated polymer film to a dopant in the vapor phase,[12,17,27,36] employing solid-state diffusion to infiltrate a molecular dopant into a conjugated polymer film,[54] soaking a conjugated polymer film in a dopant solution for extended time,[17,29,55] or using solution sequential processing (SqP), where a solution of the dopant is spin-cast directly onto an undoped conjugated polymer film.[47] Our group has performed a great deal of work characterizing the SqP method, which we originally developed for inserting fullerenes into precast conjugated polymer films to produce bulk heterojunction (BHJ) solar cells.[56-59] The SqP technique, however, is applicable to infiltration of any small molecule into a polymer film, including molecular dopants.[47] The key requirement is that the molecule to be infiltrated must be soluble at sufficient concentration in a solvent that optimally swells but does not dissolve the polymer film. Although this requirement may appear challenging, we have shown that solvent blends can be used to tune the Flory–Huggins x parameter to optimally swell any conjugated polymer film.[57] Moreover, because it relies on swelling, which minimally affects the more crystalline regions of conjugated polymer films, the

SqP method preserves the relative degree of crystallinity, crystalline domain orientation, and quality of an originally-cast polymer film even after infiltration of a molecule or a molecular dopant.[58-61s]

In this work, we take advantage of the fact that SqP preserves the crystallinity and crystalline domain orientation in conjugated polymer films to study the electrical properties of a single semiconducting polymer doped with F_4TCNQ as the crystallinity and chain morphology are systematically varied. We have chosen to focus our studies on the workhorse material poly(3-hexylthiophene-2,5-diyl) (P3HT), both because it allows us to compare directly to a large amount of previous work in the literature[11,12,17,19,25,26,29,33,36-38,40,42-47,49,50,62,63] and because the nature of this polymer allows the film crystallinity to be tuned relatively easily. We tune the crystallinity of P3HT in two different ways. First, we simply cast the original P3HT film from either a slowly or a rapidly evaporating solvent,[57,64] allowing direct control over the crystallinity of the originally cast film and thus also over the doped film after SqP. Second, we take advantage of P3HT produced by a synthetic method that yields essentially 100% regioregular material,[65] providing additional enhancement of the crystallinity of both the original and doped films created by SqP.[58,66] We characterize the film morphology in each case by 2D grazing-incidence wide-angle X-ray scattering (GIWAXS), and in conjunction with theoretical modeling of the observed polaron spectrum, argue that the dopant does not π-stack within the polymer crystallites, but instead resides mainly in the films' amorphous regions and in the lamellae of the P3HT crystallites. Moreover, all of our SqP-produced films are of high enough quality that we can make conductivity and AC Hall effect measurements using electrodes spaced more than 1 cm apart. We find that the conductivity of the doped films is directly correlated to the crystallinity and crystallite domain orientation in the doped films. Despite having similar doping levels, the films with the most anisotropic edge-on orientation and overall highest degree of crystallinity show large improvements in mobility over more isotropic, amorphous films. The

increased mobility comes directly from the doped carriers being able to delocalize more along the polymer chain in the more ordered systems, as reflected in AC Hall effect, temperature-dependent conductivity and optical absorption measurements, as well as theoretical modeling.

5.2. Results and Discussion

5.2.1. Controlling the Crystallinity of Molecularly Doped Conjugated Polymer Films

5.2.1.1. Tuning the Morphology of Initially-Cast and SqP-Doped P3HT Films

As mentioned above, the goal of this study is to systematically control the crystallinity of a single conjugated polymer, in this case P3HT, to understand the relationship between morphology, conductivity, and carrier mobility when the films are molecularly doped with F_4TCNQ. To modify the crystallinity of our doped P3HT films, we start by simply spin-casting films of commercially purchased P3HT (Rieke metals, M_n = 55 kg mol^{-1}, polydispersity $Đ$= 2.4, regioregularity (RR) 93%) from two different solvents. It is well known that changing the solvent evaporation kinetics provides an effective way to manipulate the kinetics of conjugated polymer thin film formation, resulting in some control over the final morphology of the films.[64,67,68] Thus, to produce highly amorphous P3HT films with relatively little degree of crystallinity, we spin-coated the films at 1000 rpm for 60 s from a 1% w/v solution in chloroform (CF), which is a relatively fast-drying solvent. To generate films with higher degrees of crystalline content, we spin-coated P3HT at 1160 rpm for 20 s from a 2% solution in the relatively slow-drying solvent, *o*-dichlorobenzene (ODCB), allowing us to place the still-wet films in a closed Petri dish until dry, which effectively "solvent anneals" them.[68] Because we use the same batch of polymer for both film casting conditions, any chemical defects (e.g., fraction of oxidized segments along the polymer backbone, unexpected chemical species associated with the chain ends or catalyst/other materials leftover from the polymer synthesis,

differences in molecular weight, or regioregularity) that might affect the physics of the doped carriers are the same for both sets of films. Thus, because the SqP process allows us to dope these films and preserve their relative degree of crystallinity, any differences we observe in the doped films' conduction behavior must arise from differences in morphology and not from differences in chemistry.

Because commercial P3HT has only a relatively modest regioregularity, we are limited in the degree of crystallinity we can produce in spin-cast films of the commercial material.[60] Thus, to explore what happens when P3HT is made highly crystalline, we also worked with an in-house synthesized batch of P3HT that is essentially perfectly regioregular (100% RR P3HT; M_n = 17.5 kg mol^{-1}, $Đ$ = 1.09).[65] The increased regioregularity produces significantly less disorder in spin-cast films, increasing the overall degree of crystallinity,[66] even after the films have been infiltrated by small molecules using SqP.[58] Because the polymer was produced via a different synthesis route, it is possible that compared to the commercial P3HT, the 100% RR material has different types and/or amounts of intrinsic chemical defects. At high doping levels, however, the properties of the doped material are dominated by the explicitly introduced doped polarons, so we believe that it is still legitimate to use this material as a means to understand the relationship between film morphology and the electrical behavior of the charge carriers. We used the same procedure to cast 100% RR P3HT films as we did for films of the commercial material cast from ODCB, with the exception of heating the 100% RR P3HT solution to 60 °C and casting it while hot in order to fully dissolve the material. The difference in film structure between the commercial material and the 100% RR material is apparent on the macroscale, where optical microscopy shows clear aggregates of crystallites with aggregate sizes on the order of tens of micrometers for the 100% RR P3HT films (see the Supporting Information for optical micrographs and additional details).

Once the initial P3HT films were prepared, we then doped the films using the SqP method by spin-coating solutions of 1 mg mL^{-1} F_4TCNQ in dichloromethane (DCM) on top of the P3HT films at 4000 rpm for 10 s. For all of our pristine and F_4TCNQ-doped P3HT samples, as discussed further below, we characterized the nanoscale structure of the films by GIWAXS, UV-vis absorption and Fourier-transform infrared (FTIR) spectroscopy, and ellipsometric porosimetry to directly measure swelling of the polymer films by the solvent.

5.2.1.2. Characterizing Crystallinity and Crystalline Orientation Pristine and SqP-Doped P3HT Films

In order to determine the relative crystallinity, average crystallite size, and domain orientation in our pristine and doped P3HT films, we performed a series of 2D GIWAXS measurements. P3HT crystallites are well known to prefer an edge-on orientation of the chains. In this geometry, the π–π stacking or (010) diffraction peak is observed predominantly in the in-plane direction and the lamellar or (100) diffraction peak, which corresponds to interchain stacking along the direction of the side chains, is observed predominantly in the out-of-plane direction.[69,70] Charge carriers in conjugated polymer films move most freely along the conjugated polymer backbone, but for 2D and 3D transport, the carriers eventually need to hop between chains. The barrier for hopping between chains in the π-stacking direction is much lower than between chain backbones along the lamellar direction, which involves carrier motion through the side chains, so that charge transport in-plane is more facile than out-of-plane in the case of P3HT. In addition, crystalline regions of the film are expected to be more conductive than amorphous regions because of increased π-stacking in the crystalline regions. This is why it is important to understand and control the degree of crystallinity and the crystalline orientation within a doped polymer film. Since SqP largely preserves both the degree of

crystallinity and the domain orientation,[58-60] it provides an excellent route to preparing molecularly doped P3HT films with controlled crystallinity.[47]

The 2D GIWAXS diffraction data in Figure 5.1 provide information on the trends in relative crystallinity, polymer orientation, and typical crystallite size (or more formally,

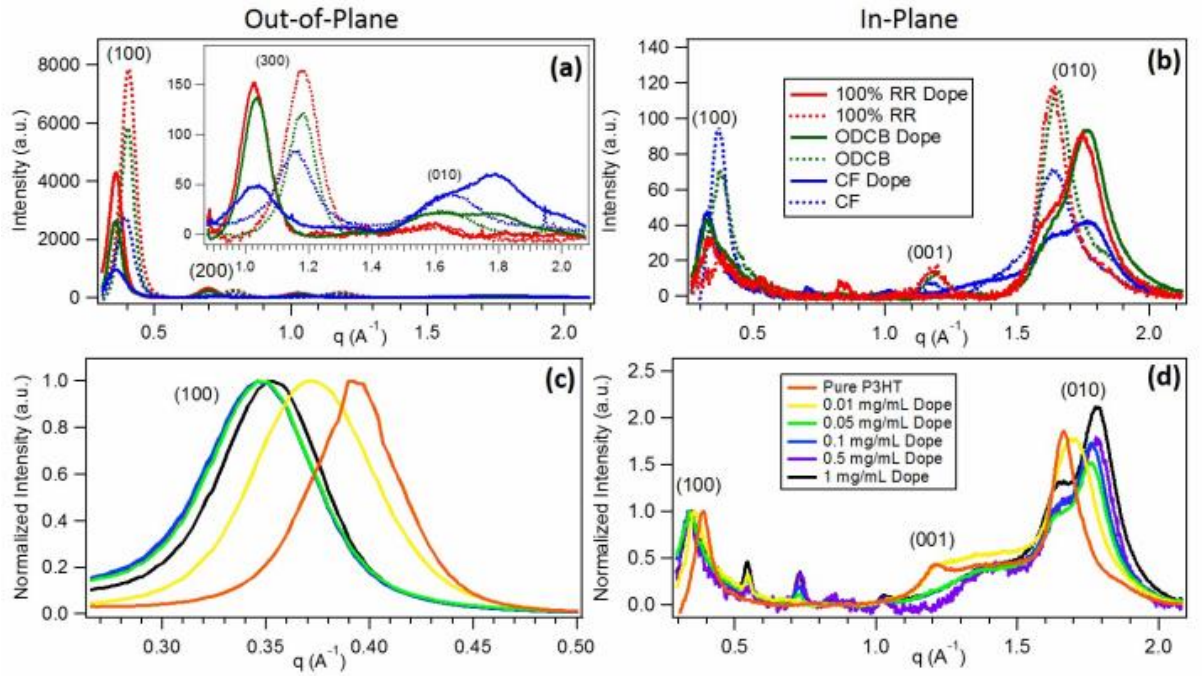

Figure 5.1. Integrated (a) out-of-plane and (b) in-plane x-ray diffraction patterns for chloroform (CF)-cast (blue dashed curves), *o*-dichlorobenzene (ODCB)-cast (green dashed curves), and 100% RR P3HT ODCB-cast polymer films (red dashed curves), as well as the same films after doping by SqP with 1 mg/mL of F_4TCNQ in dichloromethane (DCM; solid curves of the same colors, respectively). The inset in (a) shows the region around the P3HT out-of-plane (010) peak on an expanded scale. The combination of in-plane and out-of-plane data for both the (100) and (010) diffraction can be used to conclude that for the pristine films, both the relative crystallinity and degree of edge-on crystallite orientation increases in the order CF-cast, ODCB-cast, 100% RR. Moreover, the data make clear that this order is maintained following doping with F_4TCNQ by SqP. We also used GIWAXS to follow the doping process by examining films with progressively higher doping levels, as seen in integrated and normalized (c) out-of-plane and (d) in-plane x-ray diffraction peaks for P3HT films cast from ODCB at 1000 rpm for 60 s (red curves), followed by doping via SqP with different concentrations of F_4TCNQ in DCM (various colored curves). Increasing doping levels causes a shift of the (100) diffraction peak to lower q, the appearance of a new (010) diffraction peak at higher q, and a complete loss of the (001) diffraction peak, indicative of the dopant residing in the lamellar regions of the sample but not the P3HT crystalline π-stacks, as suggested in Fig. 5.2.

scattering coherence length) in the various pristine and doped P3HT films, as summarized in Table 5.1. For the pristine P3HT films, based on the integrated (100) peak area, there is a clear trend in relative crystallinity with the CF-cast film being the least crystalline, the ODCB-cast film being more crystalline, and the 100% RR P3HT film having the highest degree of crystallinity. Figure 5.1a also shows that there is relatively little out-of-plane scattering for the (010) peak near 1.6 $Å^{-1}$ in all three films, consistent with a predominantly edge-on orientation of the P3HT crystallites. The inset shows that the 100% RR material, which has the highest degree of crystallinity, also has the lowest out-of-plane (010) scattering, indicative of an even greater preference for edge-on orientation for the crystallites in this film. The general trend is clearly that the more crystalline the film, the more edge-on oriented are the crystallites. These trends are consistent with those seen in previous work using these same materials in BHJ solar cells.[58]

After doping via SqP using a 1 mg mL^{-1} solution of F_4TCNQ in DCM, the GIWAXS data (solid curves) in Figure 5.1 show that the (100) peaks shift to lower *q* (larger *d*-spacing) and that the trend in both overall crystallinity and domain orientation seen in the pristine P3HT films is maintained through the SqP doping process, as expected.[47,48] Indeed, the doped 100% RR P3HT shows little in-plane (100) and out-of-plane (010) scattering, indicating that the high anisotropy of the edge-on oriented crystallites is maintained throughout the SqP doping process. Crystalline domain size, or more properly crystallite coherence length, calculated using the standard Scherrer equation, is also well-preserved in both the (100) and (010) directions upon doping (Table 5.1). Indeed, coherence length actually appears to increase slightly in the (100) direction upon doping, indicating that inclusion of F_4TCNQ into the lattice does not disrupt the ability of the polymer chains to pack in a regular manner.

Perhaps the most striking change observed upon doping in all three processing conditions, however, is a splitting of the (010) peak; like the (100) peak, the original (010) shifts slightly to lower *q*, but a second π–π stacking peak appears at higher *q*, around 1.8 $Å^{-1}$. This new peak has also been seen in previous studies of P3HT doped with F_4TCNQ,[38,46,71] and has been attributed in the literature as evidence of π-stacking of P3HT:F_4TCNQ co-crystallites and used to argue that F_4TCNQ anions intercalate within the P3HT crystallite π-stacks.[38,50,71,72]

The argument that the new (010) peak at higher *q* in the doped films could be representative of the distance between the P3HT cation and F_4TCNQ anion is based on the idea that the Coulomb attraction between the opposite charges pulls the two π-systems close together, decreasing their *d*-spacing; this reasoning is loosely based on the idea that the anion stacks with the polymer π-system in much the same way as in charge transfer crystals, such as tetrathiafulvalene:TCNQ. This type of close contact, however, would lead to significant localization of the polarons on the P3HT chains which is not reflected in either our optical or electrical measurements, as discussed further below. Moreover, if π-stacked $P3HT^+$:F_4TCNQ^-co-crystals did form in the doped films, this would lead to a doubling of the unit cell size in the (010) direction. Figure 5.1b, however, clearly shows that there is no new peak near in the 0.8–0.9 $Å^{-1}$ range that would be reflective of a doubled unit cell.

Given these observations, combined with the fact that P3HT crystallites are known not to swell during SqP,[57] and the fact that there is little change in the integrated in-plane (010) scattering intensity upon doping, we find no reasonable mechanism for or evidence of F_4TCNQ insertion into the P3HT π-stacks.[57] Indeed, the idea of π-stacked $P3HT^+$:F_4TCNQ^-co-crystals being the dominant structure is not supported by the data presented here. Since the X-ray data presented here for P3HT doped with F_4TCNQ by SqP are quite similar to that associated with doping by the traditional blend-casting method,[38,47] we believe that F_4TCNQ anions do not

intercalate into the P3HT crystalline π-stacks when doped by any method. Further support for this idea was recently offered by Hamidi-Sakr *et al.*, who prepared films of sequentially processed F_4TCNQ-doped P3HT where the polymer chains were aligned by rubbing, and found that the anion's absorption transition dipole was not parallel to that of the polaron, again suggesting that the anion does not π-stack in the P3HT crystallites.[48] Instead, when the P3HT crystallites are doped, the delocalization of the polaron among multiple adjacent chains slightly pulls the chains together, leading to the presence of the new peak at higher *q*. The fact that we see two peaks suggests that not every crystallite in the film is doped or fully doped, so that there are both neutral and charged crystalline regions in the doped films with different π-stacking distances.

In addition, the data in Figure 5.1a and Table 5.1 show that there is a fairly significant loss in the out-of-plane (100) peak scattering intensity upon doping. When the polymer films swell during SqP, it is primarily the amorphous regions of the film that swell,[57] but apparently the films can also swell slightly in the lamellar direction. This swelling provides a route for F_4TCNQ to infiltrate between the P3HT side chains in the crystallites, increasing the lamellar spacing and causing both the observed shift of the (100) peak to lower *q* and the decrease in scattering intensity due to intercalation-induced disorder.

To better understand the process of F_4TCNQ intercalation into P3HT films, we measured 2D GIWAXS on P3HT films SqP doped using a wide range of F_4TCNQ concentrations in DCM. Figure 5.1c shows the region of the out-of-plane (100) peak on an enlarged scale. This panel reveals that the (100) peak shifts to lower *q* even at our lowest measured dopant concentration of 0.01 mg mL^{-1} F_4TCNQ, and further shifts to even lower *q* when the dopant concentration was increased to 0.05 mg mL^{-1}.[48] Higher dopant concentrations than this do not further shift the (100) peak position, even though they continue to change the optical and electrical properties

	CF-cast	ODCB-cast	100% RR P3HT	Doped CF-cast	Doped ODCB-cast	Doped 100% RR P3HT
Rel. OOP (100) peak area	1.0	2.0	2.5	0.5	2.0	3.0
Ratio of OOP (100)/(010)	37	230	506	36	253	481
(100) Coherence Length (Å)	74.9	95.6	85.5	92.4	105.1	103.4
(010) Coherence Length (Å)	38.4	49.7	52.3	28.8, 35.7	41.9, 47.5	45.1, 45.6
(100) *d*-spacing (Å)	16.0	15.6	15.5	17.8	17.5	17.5
(010) *d*-spacing (Å)	3.8	3.8	3.9	3.5, 3.9	3.6, 3.9	3.6, 3.9
% DCM in swollen film	11	9	7	-	-	-
Exciton Bandwidth (eV)	0.135	0.11	0.044	-	-	-
%-Aggregates	39	43	47	-	-	-

Table 5.1. Comparison of crystallinity (as determined by integrated out-of-plane peak area), orientation (out-of-plane (100)/(010) area ratio), crystallite coherence length (Å), volume fraction of pristine film swollen by saturated DCM vapor (%), exciton bandwidth (eV), and fraction aggregates (%) for pristine and doped CF-cast, ODCB-cast, and 100% RR P3HT films.

of the films. Similarly, the π-stacking (010) peak shows concentration-dependent changes at the same low dopant concentrations but remains relatively fixed past 0.05 mg mL^{-1} doping concentration. Figure 5.1d shows that relative to pure P3HT, the 0.01 mg mL^{-1} doped in-plane (010) peak appears broadened and shifted to higher *q*. By 0.05 mg mL^{-1}, the (010) peak becomes clearly distinguishable as two different peaks, one at roughly the same *q* as the undoped P3HT (010) and one at higher *q*. The fact that the peak shifts happen only at low doping concentrations suggests that only a modest amount of F_4TCNQ can penetrate into the crystalline lamellae. Once the crystalline lamellar regions are as "filled" as possible, the rest of the dopant presumably resides in the amorphous regions of the sample. Since the amorphous regions are not visible by X-ray scattering, we see no further changes in the films' crystalline structure via GIWAXS.

In addition to the changes in the (100) and (010) peaks, the data in Figure 5.1b,d also show that the (001) peak near 1.2 $Å^{-1}$, which is reflective of monomer-to-monomer registry along the P3HT backbone, exists in the pristine films but completely disappears upon molecular doping at concentrations $\gtrsim$0.05 mg mL^{-1} F_4TCNQ. This indicates that doping by F_4TCNQ causes a lateral shift of the polymer chains relative to each other in the P3HT crystallites, leading to

a loss of registry in the along-the-chain direction. One possible cause for this shift could be reorganization of the optimal polymer backbone conformation upon doping.

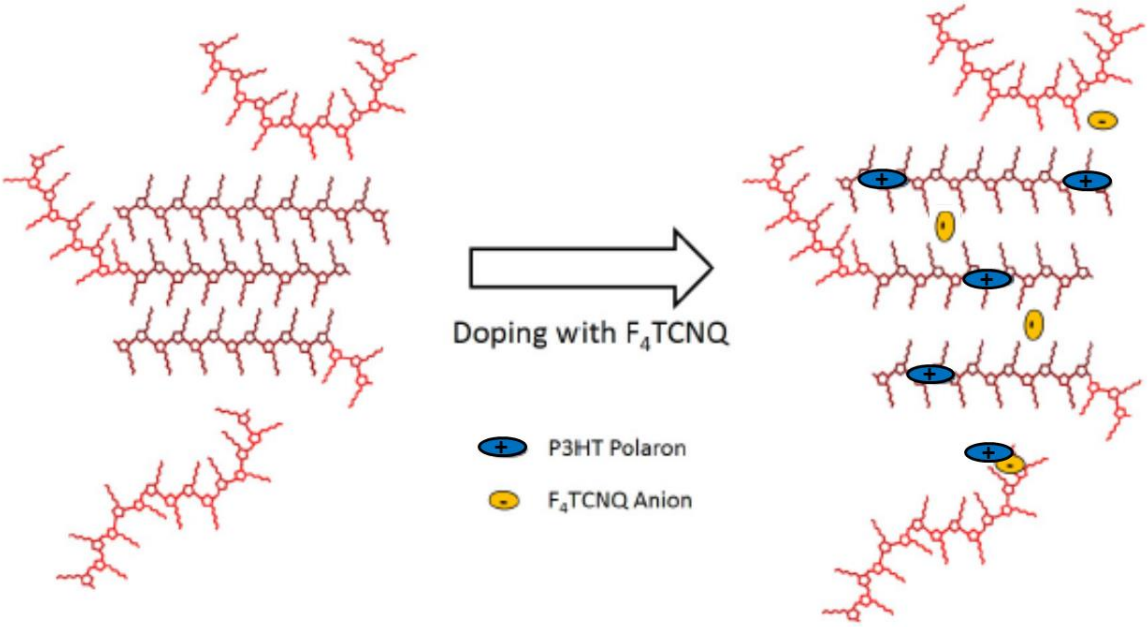

Figure 5.2. Cartoon consistent with the GIWAXS data illustrating how F_4TCNQ anions could incorporate into the lamellar regions of the crystallites as well as the amorphous regions of the film. The presence of the anion causes the side chains to shift in order to incorporate the new F_4TCNQ volume, which in turn causes the increase in spacing in the lamellar direction and the loss of along-the-chain registry. Polarons can also delocalize between chains in the π-stacking direction, leading to a decrease in the π–π stacking distance (not shown).

When we combine this observation with the fact that the (100) peak shifts to lower *q* upon doping, we can construct a picture of how F_4TCNQ infiltrates the different P3HT films, which is consistent with the data. Swelling during SqP allows some dopant molecules to enter the lamellar regions of the P3HT crystallites at low doping concentrations.[48] This increases the lamellar *d*-spacing and potentially also changes the angle of the side chains relative to the polymer backbone. Changing the side-chain angle would cause a concomitant registry shift along the backbone, as illustrated in Figure 5.2, which could also explain the observed loss of the (001) peak. The polarons created by doping prefer to delocalize in the aromatic regions of the polymer, leading to an attraction between the polymer chains in the π-stacking direction and thus the observed new (010) peak. There is no structural evidence that F_4TCNQ anions can

π-stack with the crystalline polymer, so any anions that cannot fit into the side-chain regions of the polymer crystallites must sit in the amorphous regions of the films. In Section 5.2.2.1, we also will argue on the basis of theoretical modeling of the observed optical spectra that on average, the anions must sit at a distance of at least 0.6–0.8 nm from the polarons, which is also consistent with anions sitting in the lamellae or in the amorphous regions outside of the crystallites where the polarons reside.

5.1.2.3. The Swellability of Pristine P3HT Films with Different Degrees of Crystallinity

The SqP method relies heavily on the ability of the solvent in the second casting step to swell (but not dissolve) the underlying polymer. Perhaps not surprisingly, the differences in crystallinity between the different P3HT films that we observed via GIWAXS also affect the films' swellability; since amorphous polymer domains are the easiest to swell, the more crystalline a film is, the less ability it has to absorb solvent and increase its volume.[57] In order to measure swellability, we used spectroscopic ellipsometry to measure the optical properties (*n* and *k*) of the different crystallinity polymer films both as-cast and after being exposed to the saturated vapor of the secondary casting solvent, DCM. Using the ellipsometric data in conjunction with the effective medium approximation, we were able to quantify the volume fraction of polymer and solvent in the swollen film;[57] a more detailed explanation of this procedure is included in the Supporting Information, and the experimental results are summarized in Table 5.1. Not surprisingly, the CF-cast film shows the greatest ability to swell, taking up 11% by volume DCM, followed by 9% DCM for the ODCB-cast film, and only 7% DCM for the 100% RR P3HT. This follows the expected trend of less swelling with higher-crystalline films, in good agreement with the GIWAXS data, discussed above.

Although the swelling trend is as expected, the swelling data are important in their own right because the ability to dope the films depends directly on their swellability; infiltration of

F_4TCNQ via SqP depends directly on the degree of swelling. We note that it has been argued in the literature that it easier to dope more crystalline P3HT because the more crystalline the polymer is, the more delocalized and thus the more stable the polarons become.[45,73] Thus, when doping P3HT by SqP, we anticipate a trade-off with polymer crystallinity; it becomes harder to infiltrate molecules by SqP into more crystalline polymer films,[58] but the molecules that do infiltrate should be able to dope the polymer more effectively, as discussed further below.

5.2.2. The Optical and Electrical properties of Sequentially Processed Controlled-Crystallinity F_4TCNQ-Doped P3HT Films

5.2.2.1. The Spectroscopy of Controlled-Crystallinity SqP-Doped P3HT Films

We now shift our focus to the optical properties of our sequentially processed F_4TCNQ-doped P3HT films. Figure 5.3a shows the absorption spectra of the three different pristine P3HT films prior to doping via SqP. The redshift of the main exciton absorption band and increase in vibronic structure seen in the 100% RR film relative to the ODCB- and CF-cast films are a direct reflection of increased crystalline order. The absorption of the films with different degrees of crystallinity can be quantitatively analyzed using a theoretical model that has been described previously,[74,75] and the results are summarized in Table 5.1. The general trend shows decreasing exciton bandwidth and an increasing percentage of crystalline aggregates, in the order CF-cast < ODCB-cast < 100%-RR. These results directly support the conclusions we reached via GIWAXS, which show that the CF-cast film is the most amorphous, followed by the ODCB-cast film, with the 100% RR P3HT having the largest amount of crystalline order.

In addition to changes in the spectrum of P3HT excitons with polymer structure, it is also known that polarons become increasingly delocalized as the effective conjugation length is increased.[76] Our ability to tune the degree of order/crystallinity of our SqP-doped films

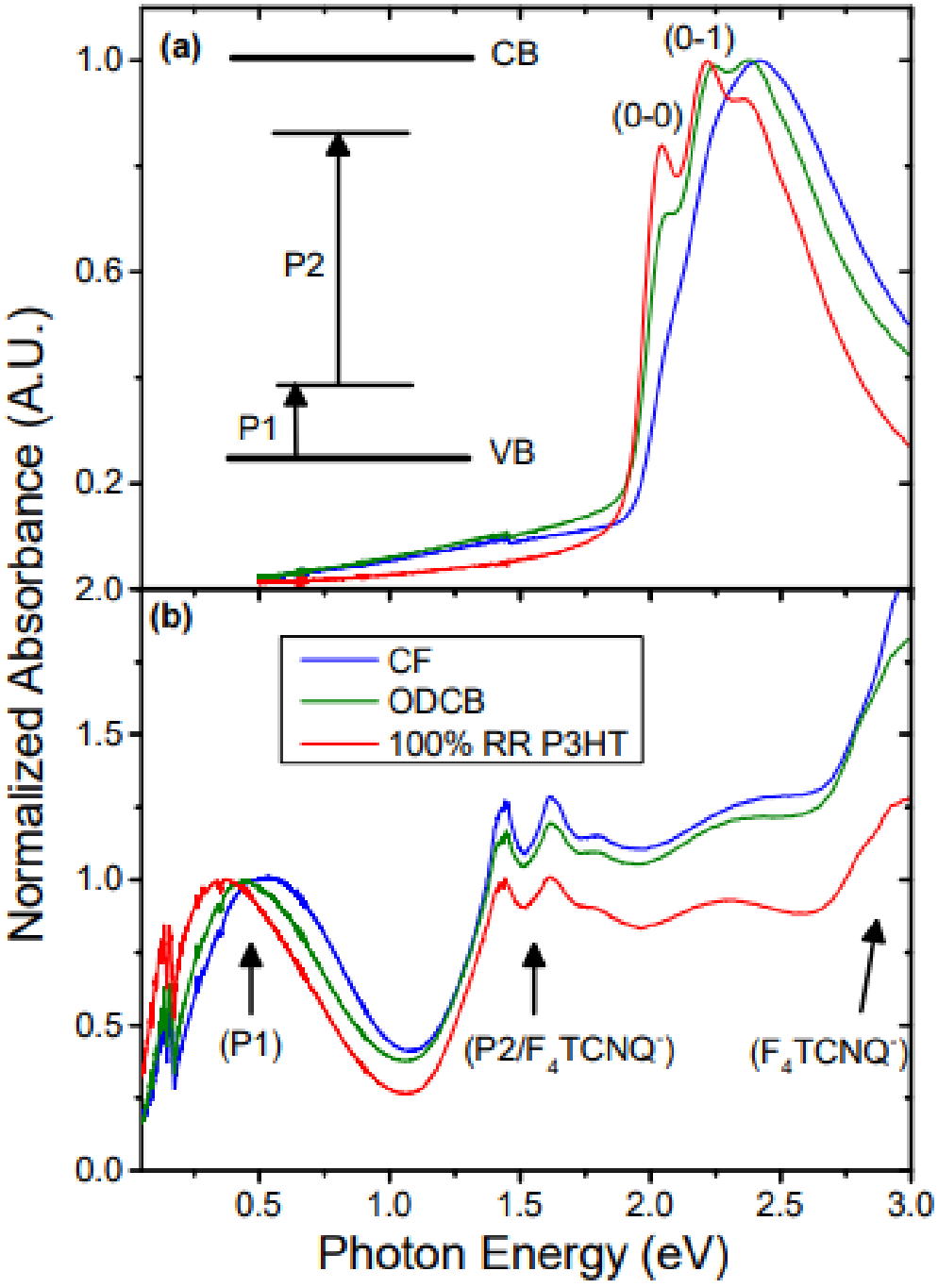

Figure 5.3. (a) UV-vis absorption data for pristine CF-cast P3HT (blue curve), ODCB-cast P3HT (green curve), and 100% RR P3HT (red curve) films. (b) Combined FTIR (0.05 to 0.5 eV) and UV-Vis (0.5-3.0 eV) absorption spectra for the same P3HT films after doping via SqP with 1 mg/mL F_4TCNQ in DCM. The data are normalized to the peak intensity of the P1 absorption band in the 0.3-0.5 eV region. Clearly the polaron P1 band redshifts, the relative absorption intensity below 0.18 eV increases, and the overall P1 absorption cross-section increases with increasing polymer crystallinity. The inset in panel (a) shows a representative energy level diagram for the P1 and P2 transitions of the polaron.

spectra of the same P3HT films in panel (a) after doping by SqP with 1 mg mL^{-1} F_4TCNQ in DCM; the doped spectra are normalized to the intensity of the mid-IR peak near 0.5 eV for ease of comparison. The data show clearly that upon doping, the neutral P3HT exciton absorption between 2.0 and 2.75 eV is decreased in all three films, and that a new feature appears near 3.0 eV, corresponding to absorption by both the neutral and anionic forms of F_4TCNQ. There is also new absorption in the 1.3–1.8 eV region, corresponding to the P2 absorption band of the P3HT polaron,[17,37,42,77] which unfortunately also overlaps an additional absorption band of the F_4TCNQ anion (which is responsible for the observed vibronic peaks in this region).[37,47,78]

Since the data in Figure 5.3b are normalized to the peaks of the P1 bands, it is clear that for the same intensity of P1 polaron absorption, the intensities of the P2/F_4TCNQ^- and depleted neutral P3HT absorptions are not the same for the three films with different crystallinities, even though the three films were doped by SqP with the same 1 mg mL^{-1} F_4TCNQ solution. Instead, relative to the P1 band absorption intensity, the more crystalline films have a greater depletion of the neutral P3HT exciton absorption, as well as a lower P2/F_4TCNQ^- absorption. The fact that the P1, P2, and depleted exciton peaks do not have the same ratio strongly suggests that either the cross section of the P1 absorption is sensitive to the film crystallinity, or that the films have different numbers of trapped and free polarons, which may have similar absorption spectra but different absorption cross sections. It is also possible that the absorption cross section of the F_4TCNQ anion may be different in different crystalline environments. Indeed, despite great effort, it has proven difficult to pin down the cross section of the anion in a solid film environment, where it is at least an order of magnitude different from that in solution.[47] Unfortunately, the uncertainties of the cross sections of the anion, trapped P3HT polarons, and free P3HT polarons with different degrees of delocalization mean that it is not possible to rely solely on optical means to quantify carrier densities in P3HT that

is highly doped with F_4TCNQ. This is why we rely on AC Hall effect measurements to determine the free carrier concentration, as discussed further below.

Figure 5.4a shows the P1 polaron absorption band for all three films on an expanded scale. Clearly, the P1 peak redshifts with increasing crystallinity of the doped P3HT film, from 0.55 eV for the CF-cast to 0.35 eV for the 100% RR P3HT, indicating greater delocalization of the polaron in the more crystalline material.[76] The structure seen in the region below 0.18 eV is due to P3HT vibrations (so-called infrared IR-active vibrations, or IRAVs); overtones of the IRAVs as well as absorption from atmospheric water and CO_2 are responsible for the small peaks superimposed on the main band at higher energies. This figure also makes clear that the IRAV portion of the absorption spectrum below 0.18 eV increases in intensity relative to the main band as the crystallinity of the polymer increases. The absorption spectrum of doped P3HT has been simulated in recent theoretical work,[79,80] with the lower energy IRAV-structured band arising mainly from interchain transitions in more ordered polymers but becoming dominated by intrachain transitions in more disordered material. The simulations accurately predicted the spectrum of P3HT doped by charge modulation,[79] when no anions were present (cf., red dashed curve in Figure 5.4b).

By comparison to the previous simulations of doping by charge modulation,[79] the P1 absorptions of our F_4TCNQ-doped P3HT samples show considerable Gaussian broadening, which must be due to the presence of the anions. Figure 5.4b shows simulated IR spectra for P3HT using the same theoretical model from Ghosh et al.,[79] but with the addition of a negative point charge to account for the presence of the anion. The point charge was located in several different regions inside and at the edge of the simulated P3HT crystallites, but the results depended more on the distance of the point charge from the polaron than the direction; see the Supporting Information for details. As discussed in the Supporting Information, the choice

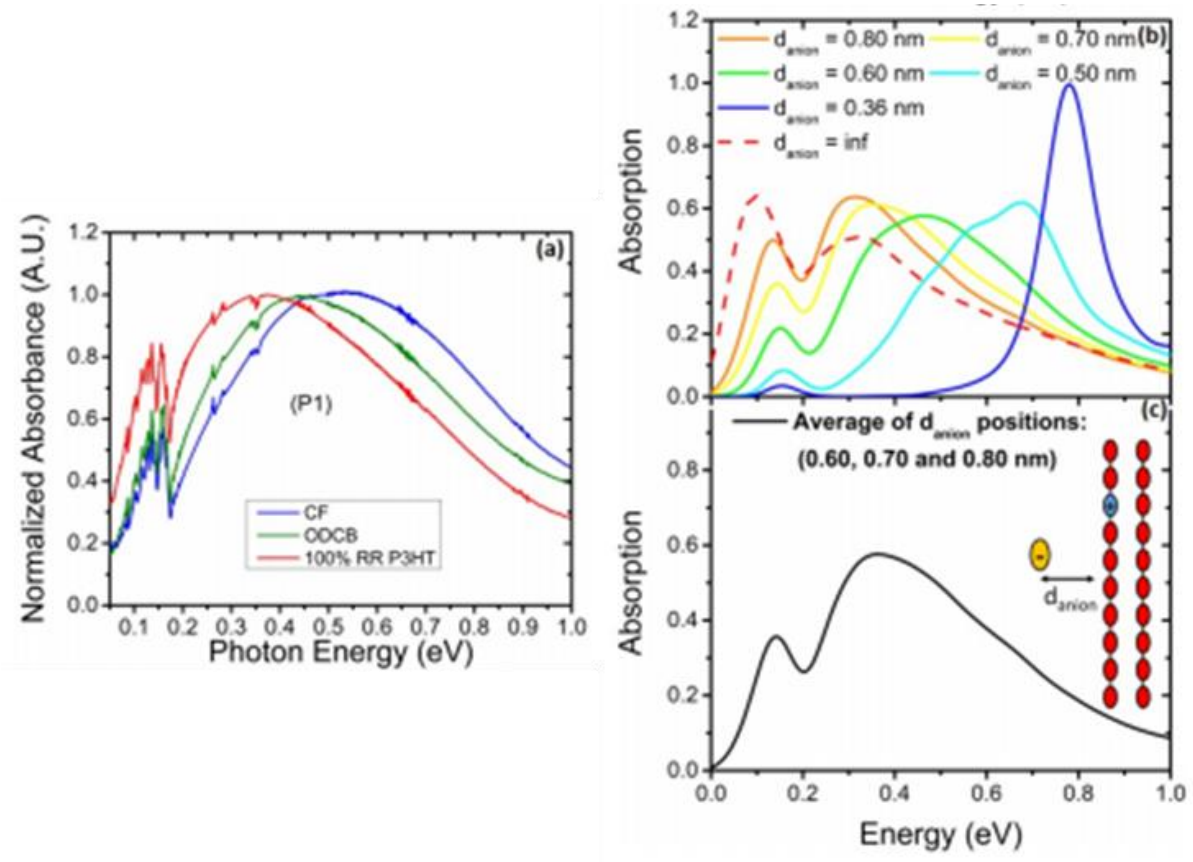

Figure 5.4. (a) Experimental absorption spectra of the P1 polaron transition for CF-cast (blue curve), ODCB-cast (green curve), and 100% RR (red curve) P3HT doped via SqP with 1 mg/mL F_4TCNQ in DCM. (b) Simulated P1 absorption band with a negative point charge representing the anion placed 0.36 nm (blue curve), 0.5 nm (light blue curve), 0.6 nm (green curve), 0.7 nm (yellow curve), 0.8 nm (orange curve), and infinitely far away (red dashed curve) from a 10×2 P3HT chain array. Spectra were obtained by averaging over 1000 configurations of random site disorder; see the Supporting Information. (c) Simulated P1 absorption band obtained by further averaging over different anion distances ranging from 0.6-0.8 nm, giving good general agreement with the spectral shape and peak position seen experimentally in (a). The inset in panel (c) is a cartoon representation of the simulation. The fact that the experimental spectra are not strongly blue-shifted or narrowed suggests that anions do not lie within 5 Å of the polymer, reinforcing the conclusion that the F_4TCNQ anion does not π-stack with crystalline P3HT.

of dielectric constant used in the calculation to account for screening of the polaron–anion Coulomb interaction is important to simulating our experimental P1 absorption spectra. We chose a distance-dependent dielectric constant[81] that we believe makes the most physical sense for our system, details of which are in the Supporting Information. The results of the calculations are shown in Figure 5.4b, which indicate that proximity of the anion dramatically

changes the location, shape, and cross section of the P1 absorption peak. Close proximity (≲4 Å) severely localizes the polaron to the region of the anion, leading to a large blueshift and narrowing of the main P1 peak and lowering of the IRAV portion of the peak at low energy (blue curve) relative to the simulated band with the anion at infinite distance (red dashed curve). As the anion is moved farther from the polaron, the polaron delocalizes, leading to a redshift and broadening of the intrachain peak, and a relative increase in the intensity of the low-energy intramolecular IRAV peak (light blue, green, yellow, and orange curves). These calculations also show that as the polaron localizes, the total absorption cross section of the P1 band decreases, further emphasizing the difficulty in using absorption spectra to extract accurate carrier concentrations.

The broadened and redshifted experimental intrachain absorption that we see for the polarons in Figure 5.4a, along with the fact that the intensity of the IRAV portion of the band is at least half that of the intrachain band, strongly suggests that the polarons in our samples are not localized immediately next to anions. This is consistent with our conclusions from the GIWAXS data that suggested that the F_4TCNQ anions lie in either the P3HT lamellae or in the amorphous regions near the P3HT crystallites, and do not form π-stacked co-crystals with the polymer (distance ≈ 3.5 Å).[48] We conclude that while there may be some small contributions to the spectrum from anions at the π-stacking distance from the polaron in the amorphous regions, which serve to increase the broadening of the P1 absorption spectral envelope, π-stacking does not appear to be the dominant structural motif to accommodate the F_4TCNQ in our SqP-doped samples.

Figure 5.4c shows a simulated polaron spectrum constructed by averaging over 1000 different configurations of random site disorder (see the Supporting Information) and anion distances in the range 0.6–0.8 nm from the polymer backbone, which gives good general

agreement with both the spectral shape and the peak position of our measured spectra in Figure 5.4a. Interestingly, in order to reproduce the peak position in the measured IR absorption spectrum near 0.35 eV for 100% RR P3HT, the anion must be at least 0.5 nm from the stack, with the exact value depending on the dielectric constant chosen for the simulations (see the Supporting Information). This again points to the idea that in such well-ordered crystals with minimal amorphous regions, π-stacking of the anion with the polymer is not permitted. In less-ordered samples, some π-stacking may occur in the amorphous regions. The more disordered π-stacks in the amorphous regions may contribute to the width of the polaron absorption band, but they are not visible by GIWAXS. The idea that the polarons in our samples are delocalized is also consistent with the mobilities we extract from our electrical measurements, described below, which are comparable to those seen in doped samples without anions present.[82-87]

Given the results of the modeling in Figure 5.4b,c, the redshift we see of the intrachain polaron band with increasing P3HT crystallinity has two possible origins: the band could redshift because the polarons are more intrinsically delocalized in more crystalline films[76] or the band could redshift because the polarons are farther, on average, from the anions, so there is less anion-induced localization in more crystalline films. Table 5.1 shows that although the average size of the P3HT crystallites increases from the CF-cast to 100% RR P3HT films, our simulations suggest that the size change alone is not enough to account for the shift of the intrachain P1 peaks: the average crystallite size simply does not change enough to cause a significant change in d_{anion} (presuming that the anions are located outside the crystallites). Films with an increased fraction of amorphous regions, however, could possibly have F_4TCNQ anions located in disordered π-stacks, placing them closer to the location of the polaron than in the crystallites. Thus, we believe that it is a combination of both increased intrinsic delocalization and decreased localization from the anion that leads to the more redshifted polaron absorption in the more crystalline films.

5.2.2.2. AC Hall Effect Measurements on Controlled-Crystallinity SqP-Doped P3HT Films

With the optical and structural properties of the doped films characterized, we turn in this section to correlating the controlled crystallinity of the SqP-doped films with their electrical properties. We examined the conductivities of all three of our P3HT films SqP doped with 1 mg mL^{-1} F_4TCNQ in DCM using both collinear four-point probe (2.5 mm spacing between electrodes) and van der Pauw measurements (electrodes at the corners of a 1.5 × 1.5 cm square),[88] and found that as in our previous work,[47] the two methods always gave conductivities that agreed to within a few percent. At room temperature, we find that the conductivity of the doped CF-cast P3HT film is only 2.1 S cm^{-1}, but that increasing the crystallinity by casting the film from ODCB yields a conductivity of 5.7 S cm^{-1}, with a further increase to $\geqslant$10 S cm^{-1} for the 100% RR P3HT (see the Supporting Information); our highest measured conductivity for the 100% RR material reached 12 S cm^{-1}, effectively an order of magnitude higher than what is typically reported for P3HT films doped with F_4TCNQ by traditional blend-casting methods.[11,37,38]

The improvement in conductivity that we observe with the SqP method leads to an important question: since the conductivity σ varies as the product of carrier concentration *n* and mobility μ according to $\sigma = nq\mu$, where *q* is the fundamental unit of charge, does the improved conductivity result from an increased number of carriers, increased polaron mobility, or some combination of the two? To answer this question, we employed AC magnetic field Hall effect measurements. This relatively new technique has been shown previously to give reliable results for low-mobility materials, which typically have Hall voltages too small to accurately distinguish from the noise present in DC Hall measurement techniques.[89-91]

It is important to note that although the AC Field Hall technique is reliable, the interpretation of the data for low-mobility materials with hopping-dominated carrier transport is not entirely straightforward. In traditional measurements, the Hall voltage, V_H, provides a measure of the potential created by the Lorentz force acting to bend charges with band-like transport around a magnetic field: $V_H = IB/nq$, where I is the magnitude of the sourced current and B is the value of the applied magnetic field.[89] Carriers that move by hopping, however, are not influenced by the magnetic field in the same way as band-like carriers, effectively screening the applied magnetic field. This can lead to smaller measured V_H values, which in turn can affect estimates of the carrier concentration (and via the measured conductivity, also affect estimates of the carrier mobility), as has been discussed in detail in recent work by Podzorov and co-workers.[92] Even if the largest AC Hall mobilities we measure for the doped 100% RR P3HT underestimate the actual mobility, it is worth noting that all of our values are in the general range of those determined previously by field-effect transistor (FET) and DC Hall effect measurements for doped P3HT.[93]

Given these issues with the interpretation of Hall data in low-mobility molecularly doped conjugated polymers, for this study we focus on qualitative trends presented by the data, rather than the exact quantitative values, to gain insights into the effects of controlling crystallinity on the charge transport properties of our doped samples. Table 5.2 summarizes the results of AC magnetic field Hall effect measurements on our various SqP-doped P3HT films; in the values

	n (cm^{-3})	μ ($cm^2/V{\cdot}s$)	σ (S/cm)
CF-cast	5.9×10^{20}	0.02	1.4
ODCB-cast	7.1×10^{20}	0.05	5.7
100% RR P3HT	4.9×10^{20}	0.12	9.1

Table 5.2. Comparison of carrier density (n), mobility (μ), and conductivity (σ) measured by the AC magnetic field Hall effect technique for F_4TCNQ-doped P3HT samples by SqP.

we report, we calculate the carrier concentration using the traditional Hall coefficient equations, which assume band-like transport. We note that the trends we report are valid as long as the three samples have roughly equivalent amounts of screening of the applied *B* field, and we expect that this screening leads to a slight overestimate of the reported carrier densities. The data show a clear trend of increasing Hall-based carrier mobility, μ, with increasing crystallinity. In contrast, the carrier concentration *n* remains roughly constant as the crystallinity increases, so we can assign the large increase in conductivity as resulting from increasing carrier mobility with increasing film crystallinity. The slight decrease in carrier concentration for the 100% RR film could be the result of poorer intercalation of F_4TCNQ due to decreased swelling, as discussed above. Moreover, the lower concentration in the 100% RR sample, along with the higher absorption intensity, emphasizes the idea that the polarons in more crystalline samples have a higher absorption cross section than those in less crystalline samples.

The measured increase in carrier mobility with increasing P3HT crystallinity likely results from a combination of the improvement in "intrinsic" mobility of the undoped polymer, which persists upon SqP doping, with less anion-induced localization of the polarons as the anions are, on average, slightly farther away in the more crystalline material. This idea that much of the mobility improvement comes from intrinsic polaron delocalization is in accord with measurements on gate-doped P3HT films in field-effect transistors that also observed that in-plane mobility increases with increased polymer crystallinity.[2,94] We note that increasing M_w of the polymer is also known to increase carrier mobility by allowing for better formation of tie chains between crystalline domains,[86,95] but this effect clearly plays no role in our data. This is because our highest observed mobility is in the 100% RR P3HT sample, which has a much lower degree of polymerization than the commercially available P3HT used for the CF- and ODCB-cast

films. Clearly, the increase in the quantity and size of the crystalline regions reported in Table 5.1 is what is responsible for the observed mobility increase.

5.2.2.3. Temperature-Dependent Conductivity of Controlled-Crystallinity SqP-Doped P3HT Films

To better understand the nature of the carrier transport in our SqP-doped P3HT films with three different degrees of crystallinity, we measured the temperature dependence of the conductivity from 50 to 300 K (see the Supporting Information for details). The data demonstrate that all of our doped films exhibit classic disordered organic semiconductor behavior with a conductivity that increases with increasing temperature.[84] We investigated the specific charge transport mechanism for each film condition by fitting the data to several different theoretical models, which are discussed in more detail in the Supporting Information.

In order to best fit the experimental data to known models over the full temperature range measured, we followed the method in refs. 28 and 93 by performing logarithmic differentiation to linearize the temperature-dependent conductivity, $\sigma \propto \exp[(-1/T)^x]$, the results of which are shown in Figure 5.5. In general, the observed temperature dependence of our samples is in good agreement with other works that observed that the Mott variable-range-hopping (VRH) model described the temperature-dependent conductivity of doped conjugated polymers.[28,29,93,96] More specifically, the ODCB-cast and 100% RR P3HT films show a T-dependent conductivity that is well described by the Efros–Shklovskii (ES) VRH model[97] at low temperatures and by the more traditional Mott VRH model[98] at higher temperatures. ES VRH accounts for the Coulomb interaction, predicting conductivity with a characteristic temperature dependence of $T^{-1/2}$.[97] The Coulomb interaction can be neglected above a critical T, leading to the more traditional Mott VRH model, which predicts a temperature dependence of the conductivity that goes as $T^{-1/4}$. In contrast to those of the more crystalline films, the T-dependent conductivity

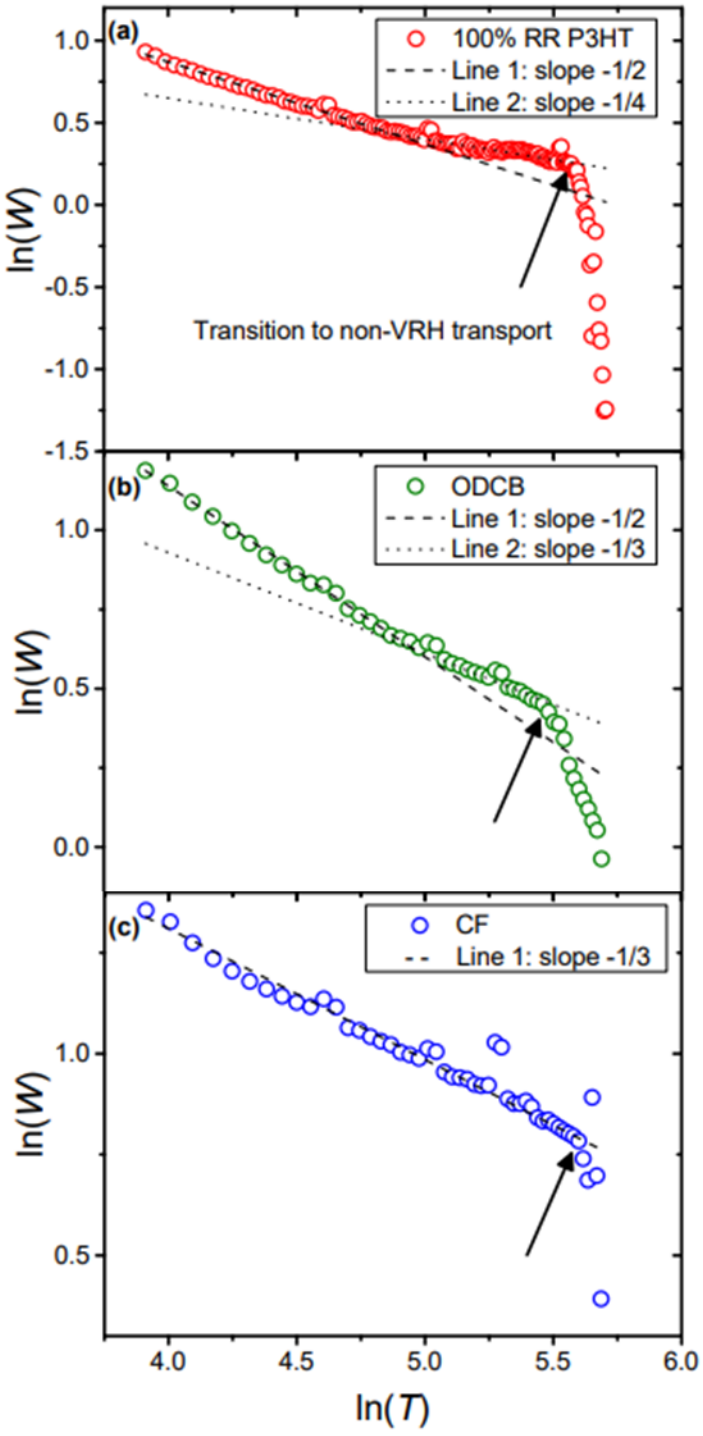

Figure 5.5. Logarithmic derivative plot of the conductivity of different P3HT films doped via SqP with 1 mg/mL F_4TCNQ in DCM versus temperature: (a) 100% RR P3HT (red circles), (b) ODCB cast (green circles), and (c) CF-cast (blue circles). The dashed and dotted lines are linear fits with the corresponding slopes listed in the legend. The arrows mark the temperature at which the behavior deviates from traditional variable-range-hopping transport.

indicating that the increased disorder in the CF-cast samples results in a different (hopping) conduction mechanism. For all of our samples, as we approach room temperature there is a drastic decrease in the *T*-dependence of the conductivity (marked by the arrows in Figure 5.5), indicating a regime that deviates from hopping-dominated transport and is approaching a more diffusive transport mechanism. These observations for our SqP-doped samples are consistent with previous results for electrochemically doped P3HT films with high carrier densities.[93]

Since all three of our doped samples with different crystallinities are roughly in this same transport regime at room temperature, it means that whatever the balance of band-like and hopping-based transport, all of our samples have approximately the same degree of screening of the applied magnetic field. This means that even if the absolute values of the mobilities we extract from the AC Hall measurements are underestimated, the degree of underestimation is likely similar for all three of our samples, allowing us to make meaningful relative mobility comparisons between the samples. Since the transition from hopping to diffusive transport starts at slightly lower temperatures with increasing polymer crystallinity, it is possible that further improvements in the crystallinity might actually bring about a complete transition to band-like transport at similar carrier concentrations at room temperature.

5.3. Conclusions

We have shown that modifying the crystallinity of a conjugated polymer film prior to doping can lead to improved electrical properties after molecular doping, and we demonstrated this for the P3HT:F_4TCNQ system by preserving the crystalline properties of pristine films by introducing the dopant via SqP. By changing the solvent used to cast P3HT films and by synthetically improving the polymer regioregularity, we were able to prepare pristine P3HT films with three distinct degrees of crystallinity, as confirmed by GIWAXS, swelling

measurements, and UV–vis spectroscopy. In addition to overall crystallinity, we also saw that the edge-on preferred crystalline domain orientation was enhanced in the more crystalline P3HT samples, and that both the degree of crystallinity and orientation could be maintained after doping with F_4TCNQ via SqP. Our GIWAXS measurements showed that no matter what the overall degree of crystallinity is, doping led to an increase of the lamellar crystalline spacing, a decrease in the π-stack spacing, and a loss of registry in the along-the-chain direction. Together, these observations suggest that the F_4TCNQ anions go first into the crystalline lamellar regions and then begin to incorporate into the polymer amorphous regions, but they do not π-stack in the polymer crystallites.

When we performed optical measurements of the doped P3HT films, we found redshifted absorption bands with higher cross sections that indicated greater delocalization of the polarons in the more crystalline films. Simulations of the polaron absorption spectra suggest that close contact between the anion and polaron (such as that would occur if the anions π-stacked in the polymer crystallites) would lead to localized polarons characterized by blueshifted and narrowed absorption bands with a lower cross section, which is not what we observed. Instead, the simulations are consistent with F_4TCNQ anions residing, on average, between 6 and 8 Å from the polaron location, consistent with the GIWAXS assignment of the anions residing in the lamellar regions of the crystallites as well as the amorphous regions of the film.

The increased polaron delocalization upon increased P3HT crystallinity also leads to improved in-plane conductivity, reaching over 10 S cm^{-1}, as verified by four-point probe measurements. AC field Hall effect measurements strongly suggest that the improved conductivity results directly from improved carrier mobility; the mobility increased by a factor of 5 from the most amorphous to the most crystalline sample. The improvement in mobility comes mostly in the form of increased charge carrier delocalization in the crystalline regions of the film, as well as

decreased polaron localization caused by the proximity of F_4TCNQ anions. Temperature-dependent conductivity measurements confirmed that the carrier transport at low temperatures takes place by variable-range hopping, with the beginning of a transition to a more diffusive transport mechanism taking place around room temperature. This transition was most apparent for the 100% RR P3HT film, alluding to the possibility that further structural engineering or material design could potentially allow reaching pure band-like conduction in molecularly doped semiconducting polymers at room temperature. Overall, the ability to independently modify the structure of a polymer film and then preserve that structure upon doping by SqP offers significant advantages for fabricating high-quality semiconducting polymer thin films for organic electronic devices.

5.4. Experimental Methods

Material & Film Preparation. The poly(3-hexylthiophene-2,5-diyl) (P3HT) material used in preparation of the thin films denoted "CF-cast" and "ODCB-cast" was purchased from Rieke Metals, and was used without further alterations. The P3HT material denoted "100% RR P3HT" in the main text was synthesized under inert atmosphere per a literature procedure. All substrates were cleaned by sequentially sonicating in soapy water, DI water, acetone, and isopropanol for 5-10 minutes each, then placed under rough vacuum to remove all traces of residual solvent, and finally transferred into a nitrogen glove box for use. The films cast from chloroform were dissolved in chloroform at a concentration of 10 mg/mL and spin cast at 1000 rpm for 60 seconds. These films were dry upon removal from the spin coater. The films cast from ODCB (both the Rieke and the in-house synthesized 100% RR) were dissolved in ODCB at a concentration of 20 mg/mL and spin cast at 1160 rpm for 20 seconds, then 3000 rpm for 1 second. This allowed for even distribution of the polymer on the substrate and removal of excess solution while leaving the film still wet. These films were then removed

and placed immediately in a small glass petri dish with a lid placed over the top. This allowed for a solvent saturated environment and slower drying time of the P3HT films.

Materials Characterization. 2-D grazing incidence wide angle X-ray scattering (GIWAXS) experiments were performed at the Stanford Synchrotron Radiation Lightsource on beamline 11-3 using a wavelength of 0.9742 Å with an incidence angle of 0.12°.The full 2-D diffractograms were radially integrated to obtain the diffraction patterns (0-10° for in-plane, 70-80° for out-of-plane, and 0-180° for full) shown in the main text. The 2-D images were collected on a plate with the detector 250 mm away from the center of the measured sample. The beam spot had a width of ~150 μm and a helium chamber was used to reduce the noise. The software package WxDiff was used to reduce the GIWAXS data and subsequent analysis was performed in IgorPro.

To study polymer swelling, spectroscopic ellipsometry was performed on a PS-1000 instrument from Semilab at room temperature. A UV-visible CCD detector adapted to a grating spectrograph analyzes the signal reflected by the sample. The light source is a 75 W Hamamatsu Xenon lamp. For these measurements only, the various P3HT films were spun onto Si substrates with a thin (~2 nm) native oxide layer, and the samples were then placed in a glass container custom-designed to contain the vapor of a solvent (i.e., dichloromethane, DCM) around the sample while still allowing unencumbered access and egress of the optical beams. The film thickness is monitored until it reaches steady state while being exposed to DCM vapor in the container. With a series of calibration measurements, we found that the partial pressure of DCM solvent in the container reached 90% of the known room-temperature vapor pressure of DCM. Data analysis was performed using the associated SEA software. The thickness was obtained by fitting only the 600-1000 nm spectral region (to avoid the excitonic P3HT absorption of the films) using the Cauchy model. For quantitative analysis, the

Bruggemann effective medium approximation (EMA) was applied to experimentally determine the refractive index of the binary polymer/solvent mixture using the known refractive indices of the pure film and solvent. We measured the refractive index as a function of wavelength for each P3HT film of different crystallinity prior to DCM exposure. When used for the EMA along with the refractive index of DCM, the volume fraction of P3HT and DCM become quantifiable in the swelled P3HT film.

The UV-vis absorption data were acquired from 3.5-0.5 eV using a Shimadzu UV3101PC UV-VIS-NIR Scanning Spectrophotometer for films prepared independently on both glass substrates and a KBr plate. FTIR data was acquired for films prepared on KBr plates using a Jasco FT/IR-420 spectrometer from 220-7000 cm−1 in transmittance mode, which was subsequently converted to absorbance.

Conductivity Measurements. In-plane conductivity was measured for all doped samples using both collinear 4-point probe and the Van der Pauw method. The room-temperature values in in-house at UCLA by the Van der Pauw method, and were also measured independently in the Van der Pauw geometry at Lake Shore Cryotronics. The temperature-dependent conductivity was measured using a Lake Shore model 8404 series AC/DC Hall Measurement System at Lake Shore. AC magnetic field Hall measurements were taken with a Lake Shore model 8400 series AC Hall probe system. In this technique, the magnetic field is oscillated at a particular frequency to make the voltage that is a result of the Lorentz force become time dependent, allowing it to be distinguished from the static misalignment offset voltage.

5.5. Supporting Information

Supporting Information is available in Appendix D.

5.5. References

(1) Burroughes, J. H.; Bradley, D. D. C.; Brown, A. R.; Marks, R. N.; Mackay, K.; Friend, R. H.; Burns, P. L.; Holmes, A. B. Light-emitting Diodes Based on Conjugated Polymers. *Nature* **1990**, 347, 6283.

(2) Sirringhaus, H.; Tessler, N.; Friend, R. H. Integrated Optoelectronic Devices Based on Conjugated Polymers. *Science* **1998**, *280* (5370), 1741 LP – 1744.

(3) Fukada, E. History and Recent Progress in Piezoelectric Polymer Research. *1998 IEEE Ultrason. Symp. Proc. (Cat. No. 98CH36102)* **1998**, *1* (6), 597–605.

(4) Yu, G.; Gao, J.; Hummelen, J. C.; Wudl, F.; Heeger, A. J. Polymer Photovoltaic Cells: Enhanced Efficiencies via a Network of Internal Donor-Acceptor Heterojunctions. *Science* **1995**, *270* (5243), 1789–1791.

(5) Gunes, S.; Neugebauer, H.; Sariciftci, N. S. Conjugated Polymer-Based Organic Solar Cells. *Chem. Rev.* **2007**, *107* (4), 1324–1338.

(6) Liang, Y.; Yu, L. Development of Semiconducting Polymers for Solar Energy Harvesting. *Polym. Rev.* **2010**, *50* (4), 454–473.

(7) Bubnova, O.; Crispin, X. Towards Polymer-Based Organic Thermoelectric Generators. *Energy Environ. Sci.* **2012**, *5* (11), 9345–9362.

(8) Kim, Y. H.; Hotta, S.; Heeger, A. J. Infrared Photoexcitation and Doping Studies of Poly(3-Methylthienylene). *Phys. Rev. B* **1987**, *36* (14), 7486–7490.

(9) Lögdlund, M.; Lazzaroni, R.; Stafström, S.; Salaneck, W.; Brédas, J.-L. Direct Observation of Charge-Induced π-Electronic Structural Changes in a Conjugated Polymer. *Phys. Rev. Lett.* **1989**, *63* (17), 1841–1844.

(10) Aziz, E. F.; Vollmer, A.; Eisebitt, S.; Eberhardt, W.; Pingel, P.; Neher, D.; Koch, N. Localized Charge Transfer in a Molecularly Doped Conducting Polymer. *Adv. Mater.* **2007**, *19* (20), 3257–3260.

(11) Yim, K.-H.; Whiting, G. L.; Murphy, C. E.; Halls, J. J. M.; Burroughes, J. H.; Friend, R. H.; Kim, J.-S. Controlling Electrical Properties of Conjugated Polymers via a Solution-Based p-Type Doping. *Adv. Mater.* **2008**, *20* (17), 3319–3324.

(12) Kao, C. Y.; Lee, B.; Wielunski, L. S.; Heeney, M.; McCulloch, I.; Garfunkel, E.; Feldman, L. C.; Podzorov, V. Doping of Conjugated Polythiophenes with Alkyl Silanes. *Adv. Funct. Mater.* **2009**, *19* (12), 1906–1911.

(13) Lüssem, B.; Keum, C.-M.; Kasemann, D.; Naab, B.; Bao, Z.; Leo, K. Doped Organic Transistors. *Chem. Rev.* **2016**, *116* (22), 13714–13751.

(14) Gao, Z. Q.; Mi, B. X.; Xu, G. Z.; Wan, Y. Q.; Gong, M. L.; Cheah, K. W.; Chen, C. H. An Organic P-Type Dopant with High Thermal Stability for an Organic Semiconductor. *Chem. Commun.* **2008**, No. 1, 117–119.

(15) Alveroglu, E. Doping Effect of Dodecyl Benzene Sulphonic Acid in Poly(3-Hexylthiophene)-P3HT-Films. *J. Mol. Struct.* **2015**, *1086*, 86–92.

(16) Li, J.; Zhang, G.; Holm, D. M.; Jacobs, I. E.; Yin, B.; Stroeve, P.; Mascal, M.; Moulé, A. J. Introducing Solubility Control for Improved Organic P-Type Dopants. *Chem. Mater.* **2015**, *27* (16), 5765–5774.

(17) Yamamoto, J.; Furukawa, Y. Electronic and Vibrational Spectra of Positive Polarons and Bipolarons in Regioregular Poly(3-Hexylthiophene) Doped with Ferric Chloride. *J. Phys. Chem. B* **2015**, *119* (13), 4788–4794.

(18) Qu, S.; Yao, Q.; Shi, W.; Wang, L.; Chen, L. The Influence of Molecular Configuration on the Thermoelectrical Properties of Poly(3-Hexylthiophene). *J. Electron. Mater.* **2016**, *45* (3), 1389–1396.

(19) Kolesov, V. A.; Fuentes-Hernandez, C.; Chou, W.-F.; Aizawa, N.; Larrain, F. A.; Wang, M.; Perrotta, A.; Choi, S.; Graham, S.; Bazan, G. C.; et al. Solution-Based Electrical Doping of Semiconducting Polymer Films over a Limited Depth. *Nat. Mater.* **2016**, *16*, 474.

(20) Loiudice, A.; Rizzo, A.; Biasiucci, M.; Gigli, G. Bulk Heterojunction versus Diffused Bilayer: The Role of Device Geometry in Solution p-Doped Polymer-Based Solar Cells. *J. Phys. Chem. Lett.* **2012**, *3* (14), 1908–1915.

(21) Han, X.; Wu, Z.; Sun, B. Enhanced Performance of Inverted Organic Solar Cell by a Solution-Based Fluorinated Acceptor Doped P3HT:PCBM Layer. *Org. Electron. Physics, Mater. Appl.* **2013**, *14* (4), 1116–1121.

(22) Zhang, Y.; Zhou, H.; Seifter, J.; Ying, L.; Mikhailovsky, A.; Heeger, A. J.; Bazan, G. C.; Nguyen, T. Q. Molecular Doping Enhances Photoconductivity in Polymer Bulk Heterojunction Solar Cells. *Adv. Mater.* **2013**, *25* (48), 7038–7044.

(23) Yan, H.; Manion, J. G.; Yuan, M.; García de Arquer, F. P.; McKeown, G. R.; Beaupré, S.; Leclerc, M.; Sargent, E. H.; Seferos, D. S. Increasing Polymer Solar Cell Fill Factor by Trap-Filling with F4-TCNQ at Parts Per Thousand Concentration. *Adv. Mater.* **2016**, *28* (30), 6491–6496.

(24) Yu, S.; Frisch, J.; Opitz, A.; Cohen, E.; Bendikov, M.; Koch, N.; Salzmann, I. Effect of Molecular Electrical Doping on Polyfuran Based Photovoltaic Cells. *Appl. Phys. Lett.* **2015**, *106* (20).

(25) Lu, G.; Blakesley, J.; Himmelberger, S.; Pingel, P.; Frisch, J.; Lieberwirth, I.; Salzmann, I.; Oehzelt, M.; Di Pietro, R.; Salleo, A.; et al. Moderate Doping Leads to High Performance of Semiconductor/Insulator Polymer Blend Transistors. *Nat. Commun.* **2013**, *4*, 1588.

(26) Glaudell, A. M.; Cochran, J. E.; Patel, S. N.; Chabinyc, M. L. Impact of the Doping Method on Conductivity and Thermopower in Semiconducting Polythiophenes. *Adv. Energy Mater.* **2015**, *5* (4).

(27) Patel, S. N.; Glaudell, A. M.; Kiefer, D.; Chabinyc, M. L. Increasing the Thermoelectric Power Factor of a Semiconducting Polymer by Doping from the Vapor Phase. *ACS Macro Lett.* **2016**, *5* (3), 268–272.

(28) Yoon, C. O.; Reghu, M.; Moses, D.; Heeger, A. J.; Cao, Y.; Chen, T.-A.; Wu, X.; Rieke, R. D. Hopping Transport in Doped Conducting Polymers in the Insulating Regime near the Metal-Insulator Boundary: Polypyrrole, Polyaniline and Polyalkylthiophenes. *Synth. Met.* **1995**, *75* (3), 229–239.

(29) Sota, U.; Hiroshi, I.; Kazuhiro, M.; Shin-ichi, K. Electrical Conduction of Regioregular and Regiorandom Poly(3-Hexylthiophene) Doped with Iodine. *J. Phys. Soc. Japan* **2005**, *74* (12), 3314–3319.

(30) Koizumi, H.; Dougauchi, H.; Ichikawa, T. Mechanism of Dedoping Processes of Conducting Poly(3-Alkylthiophenes). *J. Phys. Chem. B* **2005**, *109* (32), 15288–15290.

(31) Wang, Y.; Rubner, M. F. Stability Studies of the Electrical Conductivity of Various Poly(3-Alkylthiophenes). *Synth. Met.* **1990**, *39* (2), 153–175.

(32) Bryce, M. R.; Murphy, L. C. Organic Metals. *Nature* **1984**, *309* (5964), 119–126.

(33) Salzmann, I.; Heimel, G. Toward a Comprehensive Understanding of Molecular Doping Organic Semiconductors (Review). *J. Electron Spectros. Relat. Phenomena* **2015**, *204*, 208–222.

(34) Lazzaroni, R.; Lögdlund, M.; Stafström, S.; Salaneck, W. R.; Brédas, J. L. The Poly-3-Hexylthiophene/NOPF6 System: A Photoelectron Spectroscopy Study of Electronic Structural Changes Induced by the Charge Transfer in the Solid State. *J. Chem. Phys.* **1990**, *93* (6), 4433–4439.

(35) Arkhipov, V. I.; Emelianova, E. V; Heremans, P.; Bässler, H. Analytic Model of Carrier Mobility in Doped Disordered Organic Semiconductors. *Phys. Rev. B* **2005**, *72* (23), 235202.

(36) Khatib, O.; Lee, B.; Yuen, J.; Li, Z. Q.; Di Ventra, M.; Heeger, A. J.; Podzorov, V.; Basov, D. N. Infrared Signatures of High Carrier Densities Induced in Semiconducting Poly(3-Hexylthiophene) by Fluorinated Organosilane Molecules. *J. Appl. Phys.* **2010**, *107* (12).

(37) Pingel, P.; Neher, D. Comprehensive Picture of P-Type Doping of P3HT with the Molecular Acceptor F4TCNQ. *Phys. Rev. B - Condens. Matter Mater. Phys.* **2013**, *87* (11), 1–9.

(38) Duong, D. T.; Wang, C.; Antono, E.; Toney, M. F.; Salleo, A. The Chemical and Structural Origin of Efficient P-Type Doping in P3HT. *Org. Electron.* **2013**, *14* (5), 1330–1336.

(39) Cochran, J. E.; Junk, M. J. N.; Glaudell, A. M.; Miller, P. L.; Cowart, J. S.; Toney, M. F.; Hawker, C. J.; Chmelka, B. F.; Chabinyc, M. L. Molecular Interactions and Ordering in Electrically Doped Polymers: Blends of PBTTT and F4TCNQ. *Macromolecules* **2014**, *47* (19), 6836–6846.

(40) Duong, D. T.; Phan, H.; Hanifi, D.; Jo, P. S.; Nguyen, T. Q.; Salleo, A. Direct Observation of Doping Sites in Temperature-Controlled, p-Doped P3ht Thin Films by Conducting Atomic Force Microscopy. *Adv. Mater.* **2014**, *26* (35), 6069–6073.

(41) Di Nuzzo, D.; Fontanesi, C.; Jones, R.; Allard, S.; Dumsch, I.; Scherf, U.; Von Hauff, E.; Schumacher, S.; Da Como, E. How Intermolecular Geometrical Disorder Affects the Molecular Doping of Donor-Acceptor Copolymers. *Nat. Commun.* **2015**, *6*, 1–8.

(42) Wang, C.; Duong, D. T.; Vandewal, K.; Rivnay, J.; Salleo, A. Optical Measurement of Doping Efficiency in Poly(3-Hexylthiophene) Solutions and Thin Films. *Phys. Rev. B* **2015**, *91* (8), 085205.

(43) Deschler, F.; Riedel, D.; Deák, A.; Ecker, B.; Von Hauff, E.; Da Como, E. Imaging of Morphological Changes and Phase Segregation in Doped Polymeric Semiconductors. *Synth. Met.* **2015**, *199*, 381–387.

(44) Salzmann, I.; Heimel, G.; Oehzelt, M.; Winkler, S.; Koch, N. Molecular Electrical Doping of Organic Semiconductors: Fundamental Mechanisms and Emerging Dopant Design Rules. *Acc. Chem. Res.* **2016**, *49* (3), 370–378.

(45) Gao, J.; Stein, B. W.; Thomas, A. K.; Garcia, J. A.; Yang, J.; Kirk, M. L.; Grey, J. K. Enhanced Charge Transfer Doping Efficiency in J-Aggregate Poly(3-Hexylthiophene) Nanofibers. *J. Phys. Chem. C* **2015**, *119* (28), 16396–16402.

(46) Müller, L.; Nanova, D.; Glaser, T.; Beck, S.; Pucci, A.; Kast, A. K.; Schröder, R. R.; Mankel, E.; Pingel, P.; Neher, D.; et al. Charge-Transfer–Solvent Interaction Predefines Doping Efficiency in p-Doped P3HT Films. *Chem. Mater.* **2016**, *28* (12), 4432–4439.

(47) Scholes, D. T.; Hawks, S. A.; Yee, P. Y.; Wu, H.; Lindemuth, J. R.; Tolbert, S. H.; Schwartz, B. J. Overcoming Film Quality Issues for Conjugated Polymers Doped with F4TCNQ by Solution Sequential Processing: Hall Effect, Structural, and Optical Measurements. *J. Phys. Chem. Lett.* **2015**, *6* (23), 4786–4793.

(48) Hamidi-Sakr, A.; Biniek, L.; Bantignies, J. L.; Maurin, D.; Herrmann, L.; Leclerc, N.; Lévêque, P.; Vijayakumar, V.; Zimmermann, N.; Brinkmann, M. A Versatile Method to Fabricate Highly In-Plane Aligned Conducting Polymer Films with Anisotropic Charge Transport and Thermoelectric Properties: The Key Role of Alkyl Side Chain Layers on the Doping Mechanism. *Adv. Funct. Mater.* **2017**, *27* (25), 1–13.

(49) Gao, J.; Niles, E. T.; Grey, J. K. Aggregates Promote Efficient Charge Transfer Doping of Poly(3-Hexylthiophene). *J. Phys. Chem. Lett.* **2013**, *4* (17), 2953–2957.

(50) Gao, J.; Roehling, J. D.; Li, Y.; Guo, H.; Moulé, A. J.; Grey, J. K. The Effect of 2,3,5,6-Tetrafluoro-7,7,8,8-Tetracyanoquinodimethane Charge Transfer Dopants on the

Conformation and Aggregation of Poly(3-Hexylthiophene). *J. Mater. Chem. C* **2013**, *1* (36), 5638.

(51) Jacobs, I. E.; Aasen, E. W.; Oliveira, J. L.; Fonseca, T. N.; Roehling, J. D.; Li, J.; Zhang, G.; Augustine, M. P.; Mascal, M.; Moulé, A. J. Comparison of Solution-Mixed and Sequentially Processed P3HT:F4TCNQ Films: Effect of Doping-Induced Aggregation on Film Morphology. *J. Mater. Chem. C* **2016**, *4* (16), 3454–3466.

(52) Li, J.; Rochester, C. W.; Jacobs, I. E.; Aasen, E. W.; Friedrich, S.; Stroeve, P.; Moulé, A. J. The Effect of Thermal Annealing on Dopant Site Choice in Conjugated Polymers. *Org. Electron.* **2016**, *33*, 23–31.

(53) Li, J.; Rochester, C. W.; Jacobs, I. E.; Friedrich, S.; Stroeve, P.; Riede, M.; Moulé, A. J. Measurement of Small Molecular Dopant F4TCNQ and C60F36 Diffusion in Organic Bilayer Architectures. *ACS Appl. Mater. Interfaces* **2015**, *7* (51), 28420–28428.

(54) Kang, K.; Watanabe, S.; Broch, K.; Sepe, A.; Brown, A.; Nasrallah, I.; Nikolka, M.; Fei, Z.; Heeney, M.; Matsumoto, D.; et al. 2D Coherent Charge Transport in Highly Ordered Conducting Polymers Doped by Solid State Diffusion. *Nat. Mater.* **2016**, *15* (8), 896–902.

(55) Xuan, Y.; Liu, X.; Desbief, S.; Leclère, P.; Fahlman, M.; Lazzaroni, R.; Berggren, M.; Cornil, J.; Emin, D.; Crispin, X. Thermoelectric Properties of Conducting Polymers: The Case of Poly(3-Hexylthiophene). *Phys. Rev. B* **2010**, *82* (11), 115454.

(56) Ayzner, A. L.; Tassone, C. J.; Tolbert, S. H.; Schwartz, B. J. Reappraising the Need for Bulk Heterojunctions in Polymer−Fullerene Photovoltaics: The Role of Carrier Transport in All-Solution-Processed P3HT/PCBM Bilayer Solar Cells. *J. Phys. Chem. C* **2009**, *113* (46), 20050–20060.

(57) Aguirre, J. C.; Hawks, S. A.; Ferreira, A. S.; Yee, P.; Subramaniyan, S.; Jenekhe, S. A.; Tolbert, S. H.; Schwartz, B. J. Sequential Processing for Organic Photovoltaics: Design Rules for Morphology Control by Tailored Semi-Orthogonal Solvent Blends. *Adv. Energy Mater.* **2015**, *5* (11).

(58) Zhang, G.; Huber, R. C.; Ferreira, A. S.; Boyd, S. D.; Luscombe, C. K.; Tolbert, S. H.; Schwartz, B. J. Crystallinity Effects in Sequentially Processed and Blend-Cast Bulk-Heterojunction Polymer/Fullerene Photovoltaics. *J. Phys. Chem. C* **2014**, *118* (32), 18424–18435.

(59) Hawks, S. A.; Aguirre, J. C.; Schelhas, L. T.; Thompson, R. J.; Huber, R. C.; Ferreira, A. S.; Zhang, G.; Herzing, A. A.; Tolbert, S. H.; Schwartz, B. J. Comparing Matched Polymer:Fullerene Solar Cells Made by Solution-Sequential Processing and Traditional Blend Casting: Nanoscale Structure and Device Performance. *J. Phys. Chem. C* **2014**, *118* (31), 17413–17425.

(60) Ferreira, A. S.; Aguirre, J. C.; Subramaniyan, S.; Jenekhe, S. A.; Tolbert, S. H.; Schwartz, B. J. Understanding How Polymer Properties Control OPV Device Performance: Regioregularity, Swelling, and Morphology Optimization Using Random

Poly(3-Butylthiophene-Co-3-Octylthiophene) Polymers. *J. Phys. Chem. C* **2016**, *120* (39), 22115–22125.

(61) Van Franeker, J. J.; Kouijzer, S.; Lou, X.; Turbiez, M.; Wienk, M. M.; Janssen, R. A. J. Depositing Fullerenes in Swollen Polymer Layers via Sequential Processing of Organic Solar Cells. *Adv. Energy Mater.* **2015**, *5* (14), 1500464.

(62) Kislyuk, V. V.; Dimitriev, O. P.; Pud, A. A.; Lautru, J.; Ledoux-Rak, I. In-Situ Conductivity and UV-VIS Absorption Monitoring of Iodine Doping-Dedoping Processes in Poly(3-Hexylthiophene) (P3HT). *J. Phys. Conf. Ser.* **2011**, *286* (1).

(63) Zhu, L.; Kim, E.; Yi, Y.; Brédas, J.-L. Charge Transfer in Molecular Complexes with 2,3,5,6-Tetrafluoro-7,7,8,8-Tetracyanoquinodimethane (F4-TCNQ): A Density Functional Theory Study. *Chem. Mater.* **2011**, *23* (23), 5149–5159.

(64) Chang, J. F.; Sun, B.; Breiby, D. W.; Nielsen, M. M.; Sölling, T. I.; Giles, M.; McCulloch, I.; Sirringhaus, H. Enhanced Mobility of Poly(3-Hexylthiophene) Transistors by Spin-Coating from High-Boiling-Point Solvents. *Chem. Mater.* **2004**, *16* (23), 4772–4776.

(65) Bronstein, H. A.; Luscombe, C. K. Externally Initiated Regioregular P3HT with Controlled Molecular Weight and Narrow Polydispersity. *J. Am. Chem. Soc.* **2009**, *131* (36), 12894–12895.

(66) Mazzio, K. A.; Rice, A. H.; Durban, M. M.; Luscombe, C. K. Effect of Regioregularity on Charge Transport and Structural and Excitonic Coherence in Poly(3-Hexylthiophene) Nanowires. *J. Phys. Chem. C* **2015**, *119* (27), 14911–14918.

(67) Yang, H.; Shin, T. J.; Yang, L.; Cho, K.; Ryu, C. Y.; Bao, Z. Effect of Mesoscale Crystalline Structure on the Field-Effect Mobility of Regioregular Poly(3-Hexyl Thiophene) in Thin-Film Transistors. *Adv. Funct. Mater.* **2005**, *15* (4), 671–676.

(68) Li, G.; Shrotriya, V.; Huang, J.; Yao, Y.; Moriarty, T.; Emery, K.; Yang, Y. High-Efficiency Solution Processable Polymer Photovoltaic Cells by Self-Organization of Polymer Blends. *Nat. Mater.* **2005**, *4* (11), 864–868.

(69) Verploegen, E.; Mondal, R.; Bettinger, C. J.; Sok, S.; Toney, M. F.; Bao, Z. Effects of Thermal Annealing upon the Morphology of Polymer-Fullerene Blends. *Adv. Funct. Mater.* **2010**, *20* (20), 3519–3529.

(70) Brinkmann, M.; Wittmann, J. C. Orientation of Regioregular Poly(3-Hexylthiophene) by Directional Solidification: A Simple Method to Reveal the Semicrystalline Structure of a Conjugated Polymer. *Adv. Mater.* **2006**, *18* (7), 860–863.

(71) Méndez, H.; Heimel, G.; Winkler, S.; Frisch, J.; Opitz, A.; Sauer, K.; Wegner, B.; Oehzelt, M.; Röthel, C.; Duhm, S.; et al. Charge-Transfer Crystallites as Molecular Electrical Dopants. *Nat. Commun.* **2015**, *6*, 8560.

(72) Harrelson, T. F.; Cheng, Y. Q.; Li, J.; Jacobs, I. E.; Ramirez-Cuesta, A. J.; Faller, R.; Moulé, A. J. Identifying Atomic Scale Structure in Undoped/Doped Semicrystalline P3HT Using Inelastic Neutron Scattering. *Macromolecules* **2017**, *50* (6), 2424–2435.

(73) Gao, J.; Niles, E. T.; Grey, J. K. Aggregates Promote Efficient Charge Transfer Doping of Poly(3- Hexylthiophene). *J. Phys. Chem. Lett.* **2013**, *4* (17), 2953–2957.

(74) Spano, F. C. Modeling Disorder in Polymer Aggregates: The Optical Spectroscopy of Regioregular Poly(3-Hexylthiophene) Thin Films. *J. Chem. Phys.* **2005**, *122* (23), 234701–234715.

(75) Clark, J.; Chang, J. F.; Spano, F. C.; Friend, R. H.; Silva, C. Determining Exciton Bandwidth and Film Microstructure in Polythiophene Films Using Linear Absorption Spectroscopy. *Appl. Phys. Lett.* **2009**, *94* (16), 2007–2010.

(76) Wohlgenannt, M.; Jiang, X. M.; Vardeny, Z. V. Confined and Delocalized Polarons in π-Conjugated Oligomers and Polymers: A Study of the Effective Conjugation Length. *Phys. Rev. B - Condens. Matter Mater. Phys.* **2004**, *69* (24), 1–4.

(77) Brown, P. G.; Sirringhaus, H.; Harrison, M.; Shkunov, M.; Friend, R. H. Optical Spectroscopy of Field-Induced Charge in Self-Organized High Mobility Poly(3-Hexylthiophene). *Phys. Rev. B - Condens. Matter Mater. Phys.* **2001**, *63* (12), 1–11.

(78) Le, T. H.; Nafady, A.; Qu, X.; Martin, L. L.; Bond, A. M. Detailed Electrochemical Analysis of the Redox Chemistry of Tetrafluorotetracyanoquinodimethane TCNQF4, the Radical Anion [TCNQF4]-, And the Dianion [TCNQF 4]2- in the Presence of Trifluoroacetic Acid. *Anal. Chem.* **2011**, *83* (17), 6731–6737.

(79) Ghosh, R.; Pochas, C. M.; Spano, F. C. Polaron Delocalization in Conjugated Polymer Films. *J. Phys. Chem. C* **2016**, *120* (21), 11394–11406.

(80) Pochas, C. M.; Spano, F. C. New Insights on the Nature of Two-Dimensional Polarons in Semiconducting Polymers: Infrared Absorption in Poly(3-Hexylthiophene). *J. Chem. Phys.* **2014**, *140* (24), 244902.

(81) Nagata, Y.; Lennartz, C. Atomistic Simulation on Charge Mobility of Amorphous Tris(8-Hydroxyquinoline) Aluminum (Alq3): Origin of Poole-Frenkel-Type Behavior. *J. Chem. Phys.* **2008**, *129* (3).

(82) Sirringhaus, H.; Brown, P. J.; Friend, R. H.; Nielsen, M. M.; Bechgaard, K.; Langeveld-Voss, B. M. W.; Spiering, a. J. H.; Janssen, R. a. J.; Meijer, E. W.; Herwig, P.; et al. Two-Dimensional Charge Transport in Self-Organized, High-Mobility Conjugated Polymers. *Nature* **1999**, *401* (6754), 685–688.

(83) Sirringhaus, H. Device Physics of Solution-Processed Organic Field-Effect Transistors. *Adv. Mater.* **2005**, *17* (20), 2411–2425.

(84) Coropceanu, V.; Cornil, J.; da Silva Filho, D. A.; Olivier, Y.; Silbey, R.; Brédas, J.-L. Charge Transport in Organic Semiconductors. *Chem. Rev.* **2007**, *107* (4), 926–952.

(85) Salleo, A.; Kline, R. J.; DeLongchamp, D. M.; Chabinyc, M. L. Microstructural Characterization and Charge Transport in Thin Films of Conjugated Polymers. *Adv. Mater.* **2010**, *22* (34), 3812–3838.

(86) Noriega, R.; Rivnay, J.; Vandewal, K.; Koch, F. P. V; Stingelin, N.; Smith, P.; Toney, M. F.; Salleo, A. A General Relationship between Disorder, Aggregation and Charge Transport in Conjugated Polymers. *Nat. Mater.* **2013**, *12* (8), 1–7.

(87) Sirringhaus, H. 25th Anniversary Article: Organic Field-Effect Transistors: The Path beyond Amorphous Silicon. *Adv. Mater.* **2014**, *26* (9), 1319–1335.

(88) van der Pauw, L. J. Summary for Policymakers. In *Climate Change 2013 - The Physical Science Basis*; 1958; Vol. 13, pp 1–30.

(89) Lindemuth, J.; Mizuta, S.-I. Hall Measurements on Low-Mobility Materials and High Resistivity Materials. In *Thin Film Solar Technology III*; Eldada, L. A., Ed.; 2011; Vol. 8110, p 81100I.

(90) Lindemuth, J. Variable Temperature Hall Measurements on Low-Mobility Materials. In *Thin Film Solar Technology IV*; Eldada, L. A., Ed.; 2012; Vol. 8470, p 84700G.

(91) Chen, Y.; Yi, H. T.; Podzorov, V. High-Resolution Ac Measurements of the Hall Effect in Organic Field-Effect Transistors. *Phys. Rev. Appl.* **2016**, *5* (3), 034008.

(92) Yi, H. T.; Gartstein, Y. N.; Podzorov, V. Charge Carrier Coherence and Hall Effect in Organic Semiconductors. *Sci. Rep.* **2016**, *6* (January), 1–11.

(93) Wang, S.; Ha, M.; Manno, M.; Daniel Frisbie, C.; Leighton, C. Hopping Transport and the Hall Effect near the Insulator-Metal Transition in Electrochemically Gated Poly(3-Hexylthiophene) Transistors. *Nat. Commun.* **2012**, *3*, 1210.

(94) Bao, Z.; Dodabalapur, A.; Lovinger, A. J. Soluble and Processable Regioregular Poly(3-Hexylthiophene) for Thin Film Field-Effect Transistor Applications with High Mobility. *Appl. Phys. Lett.* **1996**, *69* (26), 4108.

(95) Brinkmann, M.; Rannou, P. Effect of Molecular Weight on the Structure and Morphology of Oriented Thin Films of Regioregular Poly(3-Hexylthiophene) Grown by Directional Epitaxial Solidification. *Adv. Funct. Mater.* **2007**, *17* (1), 101–108.

(96) Singh, R. K.; Kumar, J.; Singh, R.; Kant, R.; Chand, S.; Kumar, V. Micromorphology, Photophysical and Electrical Properties of Pristine and Ferric Chloride Doped Poly(3-Hexylthiophene) Films. *Mater. Chem. Phys.* **2007**, *104* (2), 390–396.

(97) Efros, A. L.; Shklovskii, B. I. Coulomb Gap and Low Temperature Conductivity of Disordered Systems. *J. Phys. C Solid State Phys.* **1975**, *8* (4).

(98) Mott, N. F. Conduction in Glasses Containing Transition Metal Ions. *J. Non. Cryst. Solids* **1968**, *1* (1), 1–17.

Chapter 6. Designing Conjugated Polymers for Molecular Doping: The Roles of Crystallinity, Swelling, and Conductivity in Sequentially-Doped Selenophene-Based Copolymers

6.1. Introduction

Molecular doping has been shown to be a promising way to tune the electrical properties of semiconducting polymers for a variety of applications; for example, doped conjugated polymers show promise as the active material in organic thermoelectrics.[1] This is because when conjugated polymers are chemically doped with strong oxidizing agents such as 2,3,5,6-tetrafluoro-7,7,8,8-tetracyanoquinodimethane (F_4TCNQ; see Figure 6.1(f) for chemical structure)[2–4] or FeCl3,[5] their intrinsically low electrical conductivities can be improved by orders of magnitude.[3] To achieve the highest possible conductivities, extremely high doping concentrations are usually required. Depending on the processing conditions, however, high doping levels can be difficult to achieve without disrupting the polymer film morphology.[6,7] This is because most conjugated polymers are soluble in weakly polar aromatic solvents, but when such polymers are heavily doped in solution and thus become electrically charged, they are generally no longer soluble, making it difficult to form good films by solution processing.

There have been several recent approaches in the literature to overcome the difficulties with producing high-quality films of heavily doped conjugated polymers. One method has been to synthetically improve the solubility of the materials,[8,9] allowing for higher doping concentrations to be used without ultimately disturbing the doped film morphology.[7,10–12] Another method is based on doping by sequential processing (SqP), which has recently been shown to produce highly doped semiconducting polymer films without compromising film

quality.[7,11] Doping by SqP works by first pre-casting a neutral polymer film and then infiltrating the dopant in a second casting step using a solvent that swells but does not dissolve the underlying film.

Although it requires two processing steps, doping by SqP provides the advantage that the original neutral film morphology is largely preserved through the doping process. Thus, doping by SqP not only allows the fabrication of heavily doped films with outstanding morphology but also allows the crystallinity of the doped film to be controlled by choosing the conditions under which the original neutral film is cast.[13] For example, in previous work, we were able to use SqP to study how the optical and electrical properties of F_4TCNQ-doped films of poly(3-hexylthiophene2,5-diyl) (P3HT) changed as the crystallinity of the P3HT was controllably varied.[13] Although P3HT has been the workhorse conjugated polymer when it comes to studies of molecular doping, it is generally straightforward to rationally modify the chemical structure of conjugated polymers via synthesis to yield desired electrical or structural properties. One way to do this is to start with the traditional P3HT backbone, but to statistically replace some of the 3-hexylthiophene units with 3-heptylselenophene (37S), resulting in P37S-*stat*-P3HT copolymers with the structure indicated in Figure 6.1(a).[14,15] (We choose the heptyl side chain for the selenophene units instead of hexyl because the heptyl side chains both improve solubility and give a film morphology closer to that of P3HT.[15] see the Supporting Information for synthetic details.) The incorporation of the larger Se atom is known to increase the polymer crystallinity,[14,16,17] which is expected to be related to carrier mobility.[13] The addition of precise amounts of selenophene to the P3HT backbone also controllably shrinks the bandgap (Figures 6.1(b−d)) due to both lowering the conduction band and slightly raising the valence band relative to unmodified P3HT[16] (Figure 6.1(c)), both of which have significant implications for doping.

The purpose of this paper is to use a series of doped P37S-*stat*-P3HT copolymers to study the interplay of energy level offset and polymer crystallinity in determining the ease of doping and the resultant carrier mobility as both the energy level offset and crystallinity are incrementally tuned with polymer composition. We characterize the structure and crystallinity of the neutral and doped copolymer films using 2-D grazing incidence wide-angle X-ray scattering (GIWAXS) and differential scanning calorimetry (DSC) measurements. We then examine the swellability of the different statistical copolymer films using spectroscopic ellipsometry/porosimetry and find that both the density of mobile carriers produced by doping

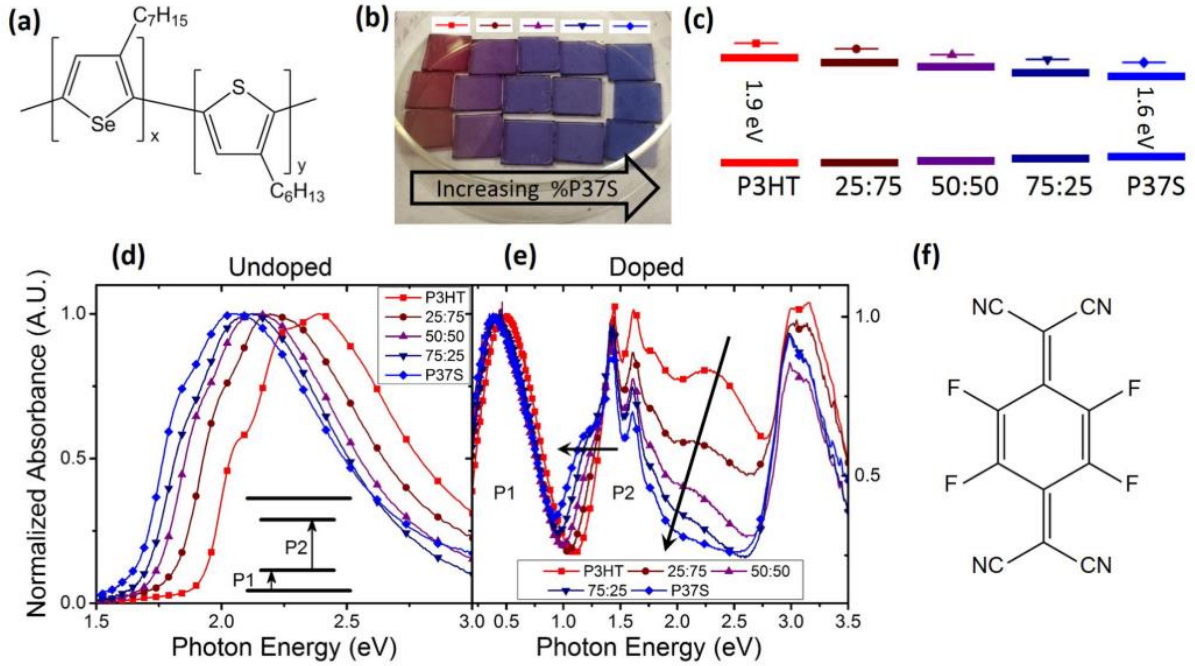

Figure 6.1. (a) Chemical structure of P37S-*stat*-P3HT copolymers; (b) optical image of P37S-*stat*-P3HT films ranging in composition from 0 to 100% P37S in 25% increments, showing three films of each composition; (c) cartoon schematic of the estimated change in valence and conduction band levels (consistent with the measured optical bandgap) of the copolymers as a function of P37S composition; (d) UV-Visible absorbance of P37S-*stat*-P3HT copolymer films, normalized to the absorption maximum. The inset shows an energy level diagram indicating the allowed polaron transitions upon chemical doping; (e) UV-Visible-NIR absorbance of P37S-*stat*-P3HT copolymer films that were doped by SqP with 1 mg/mL F_4TCNQ in DCM, normalized to the intensity of the P1 polaron absorption near 0.5 eV; (f) chemical structure of F_4TCNQ. The arrows in panel (e) show the trends in doped-film absorption with increasing selenophene content.

and the crystallinity of the polymer film after doping are directly influenced by the ability of the pre-doped film to swell during SqP.

We find that the doped film crystallinity has a pronounced effect on the conductivity and other optoelectrical properties. We use optical/NIR spectroscopy to show that the degree of polaron delocalization depends more on the film crystallinity than the band gap. We also use AC magnetic field Hall effect measurements to show that the carrier mobility, and thus the conductivity, is more influenced by the local structural environment than the energy level offset. Overall, the use of a tunable series of copolymers allows us to optimize carrier conductivity by balancing the trade-off between doped carrier concentration and carrier mobility.

6.2 Characterizing neutral and doped-P37S-*stat*-P3HT Copolymers

As described in more detail in the Supporting Information, we synthesized a series P37S-*stat*-P3HT copolymers with selenophene content ranging from 0 to 100% in 25% increments. Films of each of the copolymers, photos of which are shown in Figure 6.1(b), were prepared by dissolving the polymer powders in *o*-dichlorobenzene (ODCB) at a concentration of 1.5 mg/mL, while films of the P3HT and P37S homopolymers were prepared from solutions at a concentration of 2 mg/mL. Because heating was required to achieve full dissolution of the higher-Se-ratio copolymers, for consistency, we heated all of the polymer solutions to 100 °C prior to spin-coating at a rate of 1000 rpm for 60 s. Doped copolymer films were prepared via SqP by dissolving F_4TCNQ at a concentration of 1 mg/mL in dichloromethane (DCM) and spin-coating this solution on top of the pre-cast polymer films at 4000 rpm for 10 s. Successful employment of the SqP doping method requires a detailed understanding of both how the solvent and the dopant interact with each copolymer, which we describe in detail below.

6.2.1. The optical absorption of SqP-doped P37S-*stat*-P3HT copolymers

After incorporation of the dopant into the polymer film has occurred, the molecular interaction of the dopant and the polymer is largely dependent on the energy level offset between the HOMO/valence band of the polymer and the LUMO of F_4TCNQ. As the selenophene ratio increases across the copolymer series, the optical bandgap changes from 1.9 eV for pure P3HT to 1.6 eV for pure P37S (see Figure 6.1(c)),[16] with the gap reduction mostly coming from a decrease of the copolymer LUMO/conduction band level. This shrinking of the bandgap is manifest as a redshift in the UV−visible absorption of the films, as seen in Figure 6.1(d), resulting in a noticeable color change across the copolymer series (as also shown in the photo of three films of each composition in Figure 6.1(b)).

We note that others have observed that the open circuit voltage (V_{OC}) of polymer-based photovoltaics containing a selenophene homopolymer is ~0.1 eV lower than similar devices based on the thiophene analogues.[16] Because the V_{OC} of a bulk heterojunction photovoltaic can be used as a rough approximation of the energy level offset between the polymer donor HOMO level and the acceptor molecule LUMO level, and because the acceptor molecule used for both selenophene and thiophene analogues was the same, it is reasonable to assume that the difference in V_{OC} was purely due to a change in the polymer HOMO level. This indicates that the narrowing of the bandgap for the copolymer series from 100% P3HT to 100% P37S is a result of both the HOMO slightly raising[18] by ~0.1 eV and the LUMO lowering[15,16,19] by ~0.2 eV to account for the rest of the difference in bandgap. This implies that the HOMO levels of the copolymers are compositionally dependent, with more Se-heavy copolymer compositions having shallower HOMO levels. To verify this, we performed cyclic voltammetry (CV) measurements on the copolymer series; the details of which can be found in the Supporting Information. Within error, the CV measurements confirm that the HOMO levels of the copolymers slightly increase

in energy with increasing selenophene content. This composition dependence of the HOMO level could affect the driving force for charge transfer from the polymer to the dopant.[3]

Figure 6.1(e) shows what happens to the optical properties when we take these same copolymer films and dope them by SqP with 1 mg/mL F_4TCNQ in DCM. The figure shows that the magnitude of the neutral exciton absorption peak decreases the most for the 100% P37S film relative to the rest of the series, which is summarized by the downward-pointing black arrow in Figure 6.1(e) and more quantitatively by the black crosses in Figure6. 2(b). This suggests that there is a higher level of integer charge transfer with increasing selenophene content, consistent with the idea that increased selenophene content results in a larger energy level offset between the valence band of the copolymer and F_4TCNQ.

Quantifying the extent of doping from the loss of the neutral exciton peak is not straightforward, however, because the F4TCNQ anion absorbs strongly with peaks at ~1.45 and ~1.65 eV, overlapping with the neutral absorption of the higher-selenophene content copolymers. Subtracting the anion absorption to uncover the loss of neutral copolymer absorption is also not readily achievable because the so-called P2 polaron peak, centered between ~1.2 and ~1.5 eV, also absorbs in this region. Moreover, the P2 absorption shifts with copolymer composition, as indicated by the horizontal arrow in Figure 6.1(e). In addition, we recently showed that for pure P3HT, the absorption cross-section of the polaron varies with the local polymer structural environment, and more importantly, that the number of mobile (as opposed to trapped) carriers created by doping is not a constant fraction of the total number of charged carriers created.[13] Thus, it is not possible with the information at hand to utilize absorption spectroscopy to quantify the number of mobile carriers produced upon doping of our copolymer series. A more detailed discussion on why absorption spectroscopy is not a reliable

method for estimating the electrical properties of doped films is included in the Supporting Information.

Even though the absorption amplitudes are not useful for extracting quantitative information about mobile carriers, the position and shape of the spectra can tell us a lot about the local polaron environment.[13,20,21] Figure 6.2(a) shows a zoomed-in region of the "P1" polaron absorption constructed by stitching together UV–visible–NIR and FTIR spectra. The P1 polaron peak is split between an intrachain component in the 0.2–1.0 eV region and an interchain component in the region below 0.17 eV;[20,21] the spectra shown have been smoothed to allow for better comparison of the relative amplitudes of the two components. It is known that as the polaron becomes more delocalized and thus more mobile, the main intrachain peak redshifts and the relative amplitude of the lower-energy interchain absorption component increases.[13,20] Thus, the ratios of the intrachain and interchain components, which are

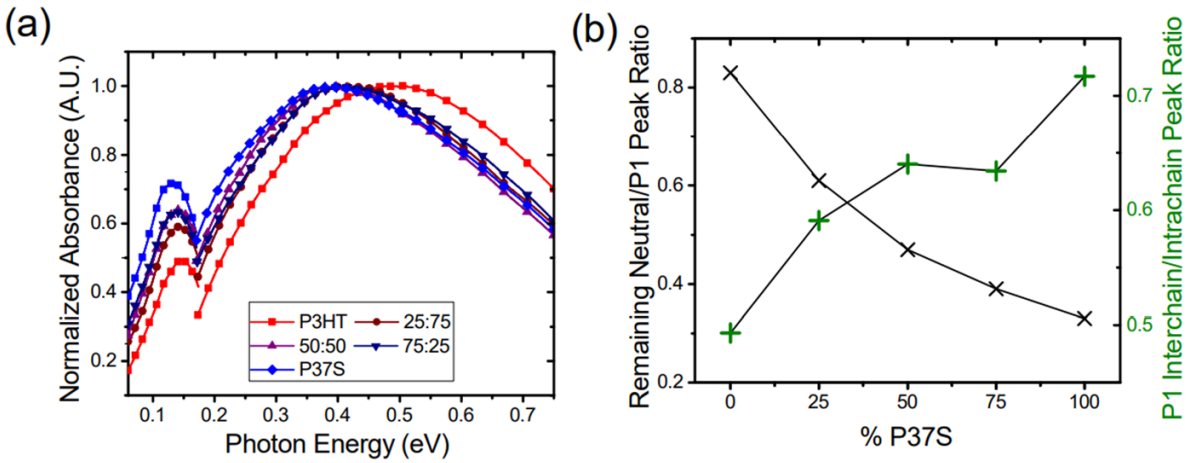

Figure 6.2. Absorbance of the P1 polaron peak in P37S-stat-P3HT copolymer films doped by SqP with 1 mg/mL F4TCNQ in DCM; the spectra are normalized by the height of the peak near ~0.45 eV for ease of comparison. All the spectra, including the IR active vibration peaks, have been smoothed to allow for better visualization of relative peak locations and heights; the raw unsmoothed data are available in the Supporting Information. (b) Plots quantifying the depletion of the neutral absorbance intensity (black crosses) and the interchain to intrachain polaron peak ratio (green plus signs, from the data in panel (a)).

presented as the green plus signs in Figure 6.2(b), are a reasonable measure of polaron delocalization and mobility.

The data in Figure 6.2(a) show that instead of the main polaron peak redshifting with increasing selenophene content, as expected based on the redshift of the bandgap,[22] the position of the main peak is non-monotonic with composition, with a particularly large blue-shifted deviation for the 75:25 selenophene:thiophene material. This blue-shifted peak for the 75:25 composition is also accompanied by a lower inter/intrachain peak ratio (panel b)), suggesting that the polarons in this particular copolymer are less delocalized than would otherwise be expected given this material's position in the series. Moreover, the fact that the P2 transition (Figure 6.1(e)) shifts monotonically with the copolymer bandgap but the P1 transition does not reinforces the idea that the shape of the P1 polaron transition is extremely sensitive to its local structural environment. All of this indicates that when designing new materials for chemical doping, the energy levels are not the only important parameters to consider as other structural factors, considered in the next sections, can more drastically affect the functional properties of the doped material.

6.2.2. The crystallinity of undoped P37S-*stat*-P3HT copolymer films

The advantage of studying a tunable series of thiophene-selenophene copolymers is that we can begin to decouple the effects of energy levels and crystallinity on the electrical properties of doped conjugated polymer films. We began our structural characterization by performing 2-D GIWAXS measurements on the undoped copolymers to quantify the relative crystallinity across the series. Figure 6.3(a) shows the radially integrated results for the undoped copolymers, with Table 1 reporting the integrated area and the *d*-spacing of the lamellar (100) peak, which represents the distance between polymer backbones in the direction

along the polymer side chains. In- and out-of-plane integrations, which provide information on the crystalline domain orientation in each material, are given in the Supporting Information.

The GIWAXS data in Figure 6.3(a) show a clear trend of the (100) peak position shifting to smaller *q* (larger *d*-spacing), and the peak intensity increasing as the selenophene content is increased. The general trend of increasing *d*-spacing with increasing selenophene content makes sense given the fact that the selenophene units have heptyl side chains, while the thiophene monomers have slightly shorter hexyl side chains. We also examined the π-stacking (010) peak across the copolymer series and found similar trends as seen for the (100) peak. Details are given in the Supporting Information.

The exception to this trend is the (100) peak of the 100% P37S film, which shows a smaller lamellar spacing as well as significantly decreased intensity and broadening compared to the rest of the series. The fact that the 100% P37S film does not follow the trend is because pure P37S does not have the same crystal structure as the rest of the samples in the series. Instead of the more common Type-I polymorph, the pure P37S material exists as a Type-II polymorph, where the heptyl side chains are more interdigitated, explaining the smaller lamellar *d*-spacing in this sample.[17,23]

The increased *d*-spacing along the lamellar direction with greater selenophene content has important implications for the properties of the copolymer materials after doping. This is because when dopants such as F_4TCNQ reside in the crystalline regions of the film, they do so in the lamellar regions between the side chains.[12,13,24] The fact that the higher-selenophene content materials have more space along the side-chain direction potentially allows for the dopant anions to reside farther from the polymer backbones where the polarons are located, which would reduce the Coulomb interaction between them. Thus, the increased lamellar spacing could potentially help allow for reduced polaron localization.[13]

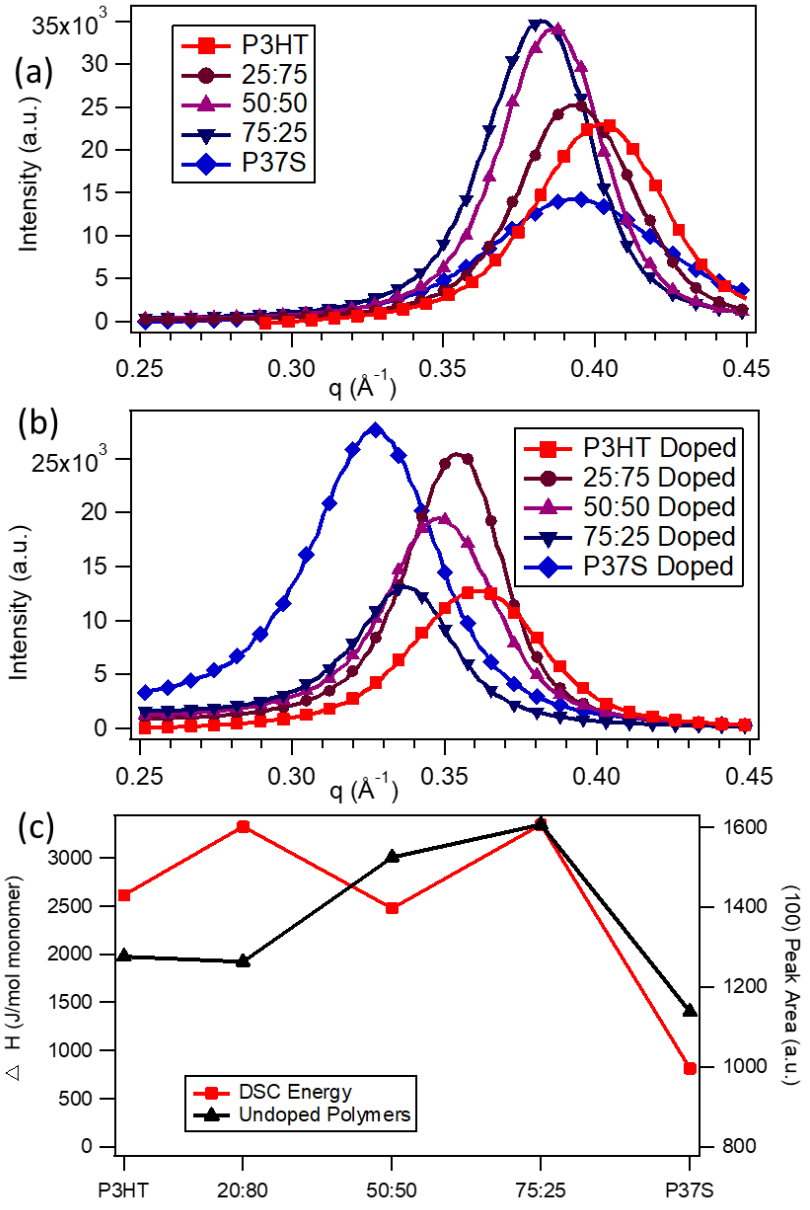

Figure 6.3. Radially integrated GIWAXS data for (a) the undoped copolymers and (b) the same polymer films after SqP doping with 1 mg/mL F_4TCNQ in DCM. The (100) peak of the undoped films shifts monotonically to larger d-spacing as the selenophene content is increased, as expected for the larger Se atom and longer side chains of the P37S monomer compared to P3HT, except for 100% P37S, as discussed in the text. The (100) peak of the doped films shifts to even larger *d*-spacing after F_4TCNQ has been incorporated. The peak positions and areas are summarized in Table 1; see the text for details. (c) DSC melting enthalpy (normalized per monomer unit) and integrated (100) peak area from GIWAXS and DSC as a function of increasing selenophene content. The good correlation indicates that GIWAXS does provide a good measure of relative crystallinity in each sample.

The trend in the radially integrated (100) peak intensities seen in Figure 6.3(a) reflect, in part, the relative crystallinities of the different copolymers. Unfortunately, conclusions about relative crystallinity are complicated by the fact that the different copolymers have different fractions of heavy selenophene atoms, which can affect both the structure factor and overall X-ray scattering power of each sample in the series. Taken at face value, the peak intensity increase with increasing selenophene content indicates increasing crystallinity, but some or all of this increased peak intensity could be due to increasing scattering contrast or a change in structure factor.

To better understand how the integrated (100) peak areas are related to relative copolymer crystallinity, we performed a series of DSC measurements on the as-synthesized copolymer powders to measure the enthalpies of melting (details in the Supporting Information); we could not perform the measurements directly on our spin-cast films due to the small amount of material present. Although the crystallinity of the powders may be different than that of spin-cast films, we do expect the enthalpy of melting for crystalline materials to be relatively constant across this series of copolymers, so any change in melting enthalpy can be associated with changes in the relative crystalline fraction of the materials.

The DSC-determined melting enthalpies, normalized per mole of monomer unit, are plotted as a function of selenophene content alongside the integrated (100) peak areas of the undoped samples in Figure 6.3(c). We chose the first melt enthalpy for this plot as we felt that this provided the best comparison to the properties of our solution-cast films, but we observed almost identical trends across the copolymer series for the melting and freezing enthalpies in both the first and second cycles. The general agreement between the DSC- and GIWAXS-derived data seen in Figure 6.3(c) suggests that although variations in structure factors and scattering power may influence the absolute X-ray scattering between different samples, the general

trend of increasing crystallinity with increasing selenophene content observed by GIWAXS is correct.

Table 6.1 summarizes the results of Figure 6.3(a), of which the most important message is that the relative copolymer crystallinity does not scale monotonically with selenophene content. Instead, the undoped 75:25 selenophene:thiophene material is the most crystalline of

	100% P3HT	25:75	50:50	75:25	100% P37S
undoped (100) *d*-spacing (Å)	15.65	15.96	16.30	16.48	N/A
doped (100) *d*-spacing (Å)	17.43	17.80	18.06	18.74	19.30
shift in *d*-spacing (Å)	1.78	1.84	1.76	2.26	N/A
undoped (100) peak area	1276	1263	1525	1607	N/A
doped (100) peak area	716	1067	953	613	1592
ratio of doped/undoped	0.56	0.84	0.62	0.38	N/A

Table 6.1. Relative Crystallinities, Based on the Radially- Integrated (100) Peak Area, and *d*-Spacings in Å, for both Pure and Doped Selenophene:Thiophene Copolymer Films, Along with the Shift in *d*-Spacing after Doping. The values for undoped 100% P37S are not included because the material has a different crystal structure (Type-II polymorph).

the series, a fact that will become important when we consider how the SqP doping process alters the film crystallinity, as discussed in the next section.

6.2.3. The crystallinity of P37S-*stat*-P3HT copolymer films after doping with F_4TCNQ by SqP

With the relative crystallinities of the undoped copolymer series characterized, we turn next to understanding the film structure after doping via SqP with 1 mg/mL F_4TCNQ in DCM. Figure 6.3(b) and Table 6.1 summarize the radially integrated GIWAXS data for the doped copolymers. The data show that the *d*-spacing of the (100) peak shifts to larger distances after

F_4TCNQ has been introduced, as has been seen previously for other conjugated polymers.[2,7,13] Of particular note is that the (100) peak for doped 100% P37S shows the largest *d*-spacing, whereas this material had one of the smaller *d*-spacings of the undoped materials. We saw above that the undoped 100% P37S has a crystal structure (Type-II polymorph) different than that of the other copolymers, one with an inherently smaller lamellar *d*-spacing due to chain interdigitation. We also know that F_4TCNQ prefers to reside in the lamellar regions of P3HT crystallites,[12,13] leading us to believe that the incorporation of F_4TCNQ into the lamellar regions of the P37S crystallites is incompatible with this side-chain interdigitation. Thus, the doping process effectively converts the Type-II polymorph of 100% P37S to the more commonly observed Type-I polymorph, bringing the doped P37S material in line with the rest of the copolymers in the series.

Figure 6.3(b) also shows that the relative scattering intensities of the doped copolymers behave rather differently than those of the undoped films. Because of the scattering differences for polymers with different Se content, it is not straightforward to map these intensity differences onto changes in crystallinity. Thus, to best quantify changes in crystallinity after doping with F_4TCNQ, we calculated the ratios of the radially integrated (100) peak area before and after SqP doping (Figure 6.5 and Table 6.1). Because the Se/S ratio does not change before and after SqP doping, the before-to-after doping (100) peak area ratio should provide a good measure of the changes in crystallinity caused by doping. For P3HT, we note that recent work has argued that doping with F_4TCNQ causes changes in film morphology, including an increase in the average conjugation length of the amorphous chains outside the polymer crystallites.[25]

For our copolymers, we see that the change in overall crystallinity of the films as a result of the solution sequential doping process varies depending on the composition. The total crystallinity decreases significantly for the doped 100% P3HT film relative to the undoped film.

This decrease in overall crystallinity is partly reversed for the 25:75 Se:S sample but then decreases slightly in the 50:50 material and significantly for the 75:25 Se:S sample. Note that the change in the 100% P37S upon doping cannot properly be compared to the other polymers in the series due to the fact that it undergoes a change in crystal structure upon doping, as mentioned above. The GIWAXS data for the π−π stacking peak for the doped copolymer films show similar trends as for the lamellar stacking peak (see Supporting Information).

The changes in crystallinity we see upon doping can be explained by the idea that the dopant either disrupts or enhances some of the coherence in polymer chain packing as it sits in the lamellar regions of the crystallites. The solvent used during the sequential doping step swells the film, allowing some reorganization of the film morphology. Normally, as the solvent dries, the film would return to its pre-swollen state. However, by introduction of dopant molecules into the swollen polymer matrix, a new morphology can be created after the solvent evaporates. This is what allows the dopant to either disrupt some of the crystallinity within the crystalline domains or induce ordering in previously amorphous or poorly crystalline regions, depending on the interaction between the dopant and the polymer.

We note that the ability of the dopant to interact with and rearrange the film morphology is also dependent on the ability of the solvent to swell the polymer film, and that swelling ability generally decreases with increasing polymer crystallinity. This emphasizes the importance of the role the solvent plays for doping via SqP, as discussed in the next Section 6.2.4.

6.2.4. Quantifying the solvent:polymer interaction for P37S-*stat*-P3HT copolymers

Because the interaction between the solvent and the polymer is critical to being able to manipulate the morphology through the addition of dopant molecules, in this section we

quantify the copolymer:solvent interaction to better understand the structural changes that take place as a result of the SqP doping process. In general, the swellability of a polymer film depends inversely on its crystallinity,[13,26] which varies across our copolymer series. We thus performed a series of swelling measurements by exposing the copolymer films to saturated DCM vapor, which mimics the exposure of the films to the DCM solvent we use in the SqP doping process. We then quantify the extent to which the films swell as they interact with the DCM vapor using spectroscopy ellipsometry (see the Supporting Information for experimental details and fits).

Figure 6.4 shows the swellability of the undoped copolymer films (bars). The data show that the swellability does not depend linearly or even monotonically on the copolymer composition. The undoped 75:25 selenophene:thiophene copolymer shows the least

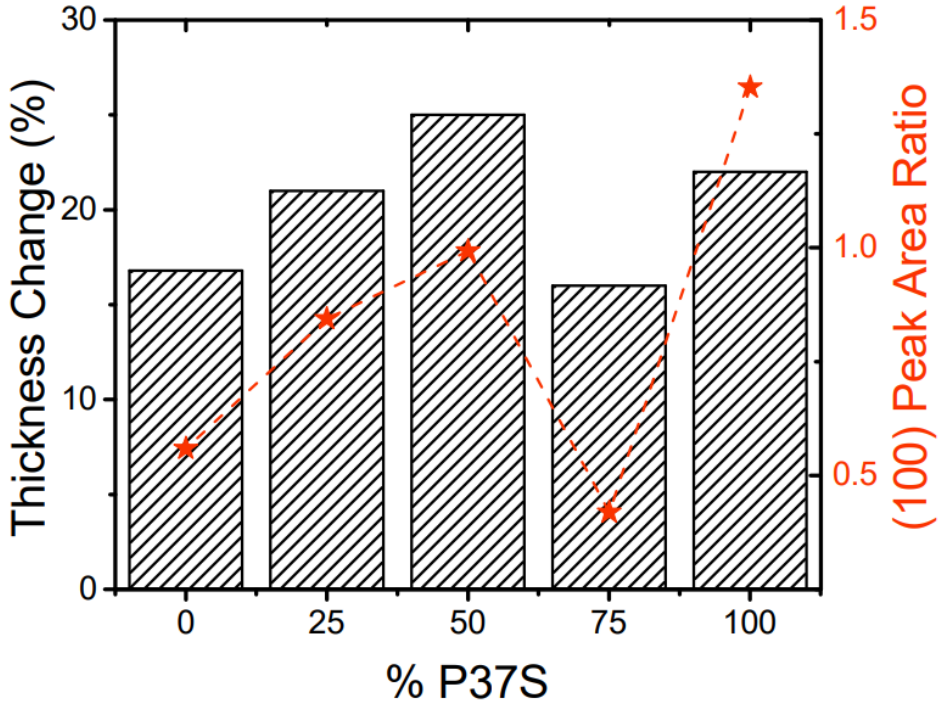

Figure 6.4. % change in film thickness due to swelling caused by exposure to DCM vapors as measured by ellipsometry (black bars) for the P37S-stat-P3HT copolymer series. Also plotted is the change in relative crystallinity as quantified by the ratio of the SqP doped film (100) peak area over the undoped film (100) peak area for the P37S-*stat*-P3HT copolymer series (orange stars).

swellability, which is perhaps not surprising as this material is the most crystalline of the series.[13,26] The higher swellability of the other copolymers relative to 100% P3HT can be explained by the fact that the larger, more polarizable Se atoms provide for increased interactions with DCM relative to the smaller, less polarizable S atoms.

Figure 6.4 also compares the copolymer swellability with the change in crystallinity of the films upon doping, as quantified by the ratio of the doped-to-undoped integrated (100) peak areas (orange stars); the trends of these two measures are in good general agreement. This correlation between swellability and change in crystallinity suggests that SqP for fullerene infiltration and SqP for doping can affect film structure in different ways. When SqP is used for fullerene infiltration, fullerene is deposited only into the amorphous regions of the film and the crystalline structure of the pre-cast polymer film is preserved. The SqP doping process, in contrast, requires dopant infiltration into crystalline domains, so materials where the crystalline domains are not effectively swollen are also not effectively doped. This direct correlation between swelling and crystallinity after doping has not been previously observed or investigated, although dopant-induced increases in crystallinity have been reported.[24,25]

Clearly, optimization of the solvent:polymer interaction is not only possible but critical to the success of SqP doping, as different solvents produce different degrees of swelling, which in turn alters the ability of dopants to induce changes in the film morphology. We will investigate such optimization in future work.

6.2.5. Electrical characterization of SqP-doped P37S-*stat*-P3HT

Given the non-monotonic trend of swellability and crystallinity change upon doping across the copolymer series, the next logical question to address is how these structural trends correlate with the functional electrical properties of the doped copolymers. We performed

electrical conductivity measurements using four-point-probe measurements in both collinear and Van der Pauw geometries; details are given in the Supporting Information. The results, summarized in Figure 6.5(a), show that the conductivity increases for the 25:75 and 50:50 selenophene:thiophene copolymers but then drops significantly for the 75:25 selenophene:thiophene copolymer. Notably, the conductivity follows a similar trend to the change in crystallinity upon doping, as quantified by doped:undoped (100) peak area ratio (Figure 6.5(b)). Moreover, for 100% P37S, the conductivity can exceed 20 S/cm, providing an order of magnitude increase over the conductivity of 100% P3HT simply by substituting selenophene for thiophene.

To determine whether the improvement in conductivity results from the higher valence band of P37S, the larger swellability of the selenophene polymer in DCM, the increased relative crystallinity of the selenophene polymer after doping, or some combination of all of these, we employed AC magnetic field Hall effect measurements[7,13,27–30] to determine how the conductivity of each copolymer results from the product of carrier mobility and carrier concentration. AC Hall measurements are different from traditional DC Hall effect measurements in that the magnetic field is alternated in a time dependent manner such that the Hall voltage becomes similarly time dependent. This allows one to lock in on the Hall voltage and disregard the intrinsic offset voltage which is not time dependent and is often large enough to obscure the Hall voltage in low mobility materials such as semiconducting polymers.

The results of the AC Hall measurements yield Hall charge carrier densities (n_H, shown for the copolymer series in Figure 6.5(c)), which are connected to the carrier mobility (μ_H, Figure 6.5(d)) and conductivity (σ, Figure 6.5(a)) by $\sigma = n_H q \mu_H$, where q is the fundamental charge. We note that in low-mobility materials such as doped conjugated polymers, the carrier density extracted from AC Hall effect measurements can be subject to error because carriers

that move by hopping can screen the magnetic field of neighboring carriers.[30,31] Based on our previous work studying P3HT[13] and the results discussed below, however, we believe that the copolymers studied here all share a similar hopping-dominated transport mechanism, and thus even if the absolute carrier densities are subject to some error, the relative comparison across the copolymer series should be fairly accurate.

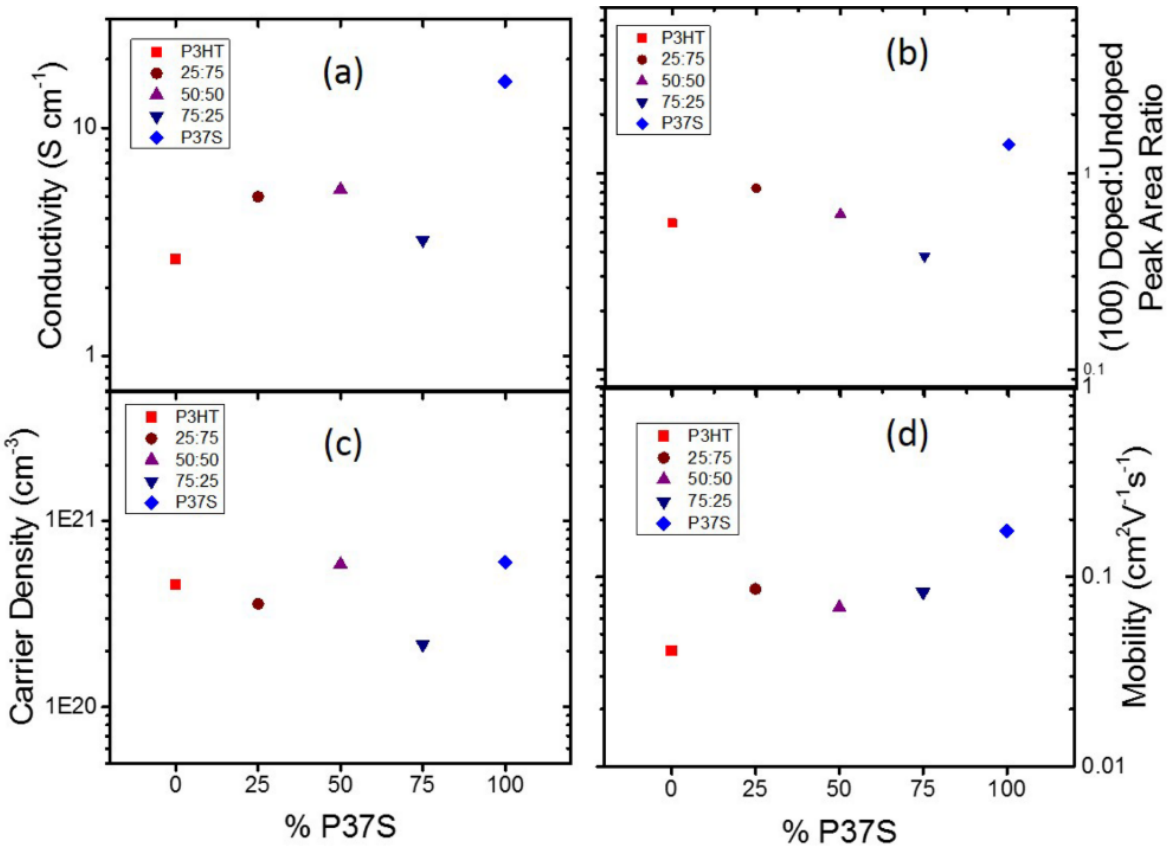

Figure 6.5. Semilogarithmic plots of (a) electrical conductivity, (b) doped:undoped (100) peak area ratio, (c) carrier density, extracted from AC Hall effect measurements, and (d) carrier mobility, calculated from the ratio of the conductivity and carrier density, all as a function of selenophene content across the copolymer series. All of the electrical measurements were for films doped by SqP with 1 mg/mL F_4TCNQ in DCM.

Figure 6.5(c) shows the mobile carrier density extracted from the AC Hall effect measurements made on the SqP-doped P37S-*stat*-P3HT series; details of how measurements were made are given in the Supporting Information. The data make clear that the mobile carrier density remains nearly constant (or perhaps slightly increases) with increasing selenophene

content, with the exception of the 75:25 selenophene:thiophene copolymer, which has a significantly lower mobile carrier density (note that Figure 6.5(c) has the carrier density plotted on a logarithmic scale). The slight increase across the series would fit well with the idea that there is increased driving force for doping as the energy level offset increases with increasing selenophene content (and also fits with the increase in quenching of the neutral polymer absorbance seen in Figure 6.2(b)), although this is a relatively minor effect.

The drop in mobile carrier density for the 75:25 selenophene:thiophene copolymer correlates with the significant decrease in crystallinity upon doping in this material, as seen in Figure 6.5(b). The high crystallinity likely prevents the F_4TCNQ dopant from effectively incorporating into crystalline parts of this copolymer during the SqP doping process. Instead, reaction with F_4TCNQ drives a transition to an amorphous geometry where the F_4TCNQ anion can find space in the polymer network. The mobility data can then be explained by the hypothesis that the majority of mobile carriers are formed by doping the crystalline regions of the film, where the dopant anions are forced to lie farther away from the polarons on the polymer backbone, thus reducing Coulomb trapping and increasing polaron mobility. Dopant anions in the amorphous regions of the film, in contrast, can sit in closer Coulomb contact to their corresponding polarons. These Coulombically bound carriers would appear optically but would not contribute to the Hall voltage because they are effectively trapped. This idea is consistent with the fact that the 72:25 selenophene:thiophene sample shows a P1 absorption that is blue-shifted and has a low interchain to intrachain absorption ratio, both of which are signatures of a higher fraction of less mobile or trapped carriers.

We also might expect the depletion of the neutral absorption peak across the series after doping to track with the carrier concentration, but a comparison of Figure 6.5(c) to Figure 6.2(b) shows that this is not the case, verifying our argument above that UV−visible absorption

is not a good method for determining the mobile carrier concentration in doped conjugated polymer films: the facts that both trapped and mobile carriers contribute to the absorption and that the degree of mobility/trapping changes the absorption position, shape and cross-section make it effectively impossible to correlate optical properties with electrical properties that depend only on mobile carriers.

Figure 6.5(d) shows the carrier mobility extracted from the Hall effect measurements. The mobility shows a very different trend from the carrier concentration, with no dramatic dip for the 75:25 composition and instead a gradual increase in mobility with increasing selenophene content. This general increase in carrier mobility with selenophene content is largely responsible for the increased conductivity across the series, as the carrier density remains relatively constant from 100% P3HT to 100% P37S, with the exception of the highly crystalline 75:25 material.

Overall, by far the strongest correlation of the conductivity to film structure is the fractional change in crystallinity of the doped material. This suggests that if the dopant cannot fit well into the polymer lattice in an ordered manner, there will be an energetic penalty for incorporation. In this situation, less dopant will incorporate in positions that produce mobile carriers. Although trapped carriers can be produced (and observed by optical absorption), these trapped carriers do not contribute to the overall conductivity, as discussed above.

We reached a similar conclusion concerning polymer structure and carrier mobility in our previous work studying doped P3HT films with different controlled amounts of crystallinity.[13] This work, however, highlights the fact that the crystallinity of the undoped film is not the key parameter in determining carrier mobility, but rather the crystallinity of the film after doping. The crystallinity of films doped by SqP, in turn, depends on both their original crystallinity, their swellability, and the ability of the polymer lattice to accommodate dopant

molecules within the crystal structure. Thus, when designing new conjugated polymers for applications with chemical doping, it is important to consider not only the crystallinity of the neutral polymer but the ability of the polymer to swell during SqP and then crystallize when doped. The 100% P37S polymer does both of these well, allowing us to readily achieve electrical conductivities exceeding 20 S/cm by SqP doping with only 1 mg/mL F_4TCNQ.

6.3. Summary and Conclusions

We showed that the bandgap, valence band position, crystallinity, and swellability of undoped P3HT, as well as the change in crystallinity after doping by SqP with F_4TCNQ, can be controllably tuned by synthetic statistical substitution with selenophene units, although not all the changes are monotonic with fractional selenophene composition. The bandgap decreases monotonically, and the valence band slightly increases monotonically as the copolymer composition is tuned from 100% P3HT to 100% P37S. The change in valence band position provides for an increase in carrier concentration upon doping as the fraction of selenophene increases, but not all the carriers created are mobile. Instead, it is the way increasing selenophene content changes polymer structure and crystallinity that provides the best correlation with the optical and electrical properties of the materials after doping. The key relation is that electrical conductivity depends on the ability of the dopant to restructure the polymer, which in turn depends on the polymer's ability to swell and its ability to accommodate the dopant within its lattice.

The 75:25 selenophene:thiophene copolymer is the most crystalline in its undoped form, making it the least swellable material in our copolymer series. This lack of swellability also gives this material the lowest mobile carrier concentration when doped, despite having a relatively high valence band and good energy level offset from F_4TCNQ and a strong depletion of the neutral exciton absorption. Correlated with the fact that this copolymer has a lower

mobile carrier concentration is that it shows the largest decrease in crystallinity upon doping, suggesting that this material simply cannot effectively accommodate F_4TCNQ molecules within its lattice. The free carrier concentration measured by the AC Hall effect does not match with the depletion of the neutral absorption peak, indicating that there are either large changes in absorption cross-section and/or significant fractions of trapped carriers. The hypothesis that many carriers are trapped is supported by the relatively blue-shifted polaron absorption of this member of the series.

Across the copolymer series, we see that it is the crystallinity of the doped state that ultimately determines the mobile carrier concentration. This suggests that the majority of dopants in amorphous regions of the polymer produced trapped carriers, and that mobile carriers are only produced when they are spatially separated from their counterions because of the limited number of places that the F_4TCNQ anions can reside within the crystalline lattice. This idea is corroborated by optical spectroscopy, which shows excellent correlation between the position and shape of the polaron P1 transition, the crystallinity of the doped film, and the mobile carrier mobility. The polaron P2 transition, however, does not appear to be strongly affected by the local environment and instead scales simply with the bandgap of the polymer. The P1 and P2 absorption amplitudes do not correlate with the number of mobile carriers in the films, preventing optical spectroscopy from being used to quantify the mobile carrier concentration.

In the end, achieving the highest mobilities requires not only a good degree of intrinsic crystallinity but also swellability, which determines how well the dopant can infiltrate the material, and the general ability of the polymer lattice to accommodate dopants within their crystalline domains. For our copolymer series, these requirements were best met by the 100% P37S material, giving it the highest carrier concentration and highest carrier mobility, leading

to electrical conductivities that exceed 20 S/cm at higher doping levels. Overall, the electrical, structural, and optical measurements across the P3HT-*stat*-P37S copolymer series all corroborate the crystallinity of the doped state being the dominant factor that influences the properties of highly doped semiconducting polymer films.

6.4. Experimental Methods

Materials Characterization. The UV-vis-NIR region from 3.5−0.5 eV was measured using a Shimadzu UV-3101PC UV-VIS-NIR Scanning Spectrophotometer for films prepared on KBr plates. The IR region from 220-7000 cm−1 was measured using a Jasco FT/IR-420 Spectrometer in transmittance mode on the same films prepared on KBr plates. The FTIR data was converted to absorbance and then combined with the UV-VIS-NIR data.

2-D grazing incidence wide angle X-ray scattering (GIWAXS) experiments were performed at the Stanford Synchrotron Radiation Lightsource on beamline 11-3 using a wavelength of 0.9742Å with an incident angle of 0.12°. The full 2-D diffractograms of our different polymer systems were radially integrated to obtain the diffraction patterns (0-10° for in-plane, 70−80° for out-of-plane, and 0-180° for full). The 2-D images were collected with a Rayonix model MX225 X-ray CCD 250 mm away from the center of the measured sample. The beam spot had a width of ∼150 μm and a helium chamber was used to reduce the noise. The software package WxDiff was used to reduce the GIWAXS data and subsequent analysis was performed in IgorPro.

Differential scanning calorimetry (DSC) was performed on as-synthesized copolymer powders. The DSC change in enthalpy of melting and crystallization were obtained using a Perkin Elmer R DSC 8000, a dual furnace instrument equipped with an IntraCooler. The samples were measured in vented Al pans in an inert N2 atmosphere. The heat flow from 30 °C to 300 °C at

a rate of 10 °C/min was recorded then the area under the peaks was used to determine the change in enthalpy

Electrochemical measurements were recorded on films drop-cast on a Pt working electrode in MeCN/NBu4PF6 (0.1 M) versus Ag/AgCl (scan rate 100 mV·s −1) with Fc/Fc+ as an internal standard, using a BASi Epsilon potentiostat. The HOMO levels have been calculated from the oxidation onset values.

To study polymer swelling, spectroscopic ellipsometry was performed on a PS-1000 instrument from Semilab at room temperature. A UV-visible CCD detector adapted to a grating spectrograph analyzed the signal reflected by the sample. The light source was a 75-W Hamamatsu Xenon lamp. For these measurements, the various polymer films were spun onto Si substrates with a thin (~2 nm) native oxide layer, and the samples were placed in a glass container custom-designed to contain the vapor of a solvent (i.e., dichloromethane, DCM) around the sample while still allowing unencumbered access and egress of the optical beams. The film thickness was monitored until it reached steady state while being exposed to DCM vapor in the container. With a series of calibration measurements, we found that the partial pressure of DCM solvent in the container reached 90% of the known room-temperature vapor pressure of DCM. Data analysis was performed using the associated SEA software. The thickness was obtained by fitting only the 860−1000 nm spectral region (to avoid the excitonic absorption of the various copolymer films) using the Cauchy model. By fitting the thickness prior to swelling and during swelling we can extract the percent change in film thickness caused by swelling.

Electrical Measurements. In-house conductivity measurements were performed on samples prepared as described in the main text on glass substrates with dimensions of 1.5×1.5 cm. We

performed both collinear 4-point probe measurements with a probes spacing of 1.5 mm and Van der Pauw measurements with silver paste electrodes on the corners of the substrates.

AC magnetic field Hall measurements were performed with a LakeShore model 8400 series AC/DC Hall Measurement System. The samples were measured with N_2 gas flowing through the sample chamber to reduce degradation. This limited the change in conductivity over time to < 5% of the total during the 15-hour time span of data collection. The slightly lower conductivity values for our AC-Hall samples compared to what we measured in-house was due to the several-day time delay between fabrication and completion of the AC Hall measurements (whereas the in-house measurements were also performed on the same day the samples were fabricated).

6.5. Supporting Information

Supporting Information is available in Appendix E.

6.6. References

(1) Russ, B.; Glaudell, A.; Urban, J. J.; Chabinyc, M. L.; Segalman, R. A. Organic thermoelectric materials for energy harvesting and temperature control. *Nat. Rev. Mater.* **2016**, 1, 16050.

(2) Duong, D. T.; Wang, C.; Antono, E.; Toney, M. F.; Salleo, A. The chemical and structural origin of efficient p-type doping in P3HT. *Org. Electron.* **2013**, 14, 1330–1336.

(3) Yim, K.-H.; Whiting, G. L.; Murphy, C. E.; Halls, J. J. M.; Burroughes, J. H.; Friend, R. H.; Kim, J.-S. Controlling Electrical Properties of Conjugated Polymers via a Solution-Based p-Type Doping. *Adv. Mater.* **2008**, 20, 3319–3324

(4) Pingel, P.; Neher, D. Comprehensive picture of p-type doping of P3HT with the molecular acceptor F4TCNQ. *Phys. Rev. B: Condens. Matter Mater. Phys.* **2013**, 87, 115209.

(5) Yamamoto, J.; Furukawa, Y. Electronic and Vibrational Spectra of Positive Polarons and Bipolarons in Regioregular Poly(3- hexylthiophene) Doped with Ferric Chloride. *J. Phys. Chem. B* **2015**, 119, 4788–4794.

(6) Deschler, F.; Riedel, D.; Deak, A.; Ecker, B.; von Hauff, E.; Da Como, E. Imaging of morphological changes and phase segregation in doped polymeric semiconductors. *Synth. Met.* **2015**, 199, 381–387.

(7) Scholes, D. T.; Hawks, S. A.; Yee, P. Y.; Wu, H.; Lindemuth, J. R.; Tolbert, S. H.; Schwartz, B. J. Overcoming Film Quality Issues for Conjugated Polymers Doped with F4 TCNQ by Solution Sequential Processing: Hall Effect, Structural, and Optical Measurements. *J. Phys. Chem. Lett.* **2015**, 6, 4786–4793.

(8) Li, J.; Zhang, G.; Holm, D. M.; Jacobs, I. E.; Yin, B.; Stroeve, P.; Mascal, M.; Moule, A. J. Introducing Solubility Control for Improved Organic P-Type Dopants. *Chem. Mater.* **2015**, 27, 5765–5774.

(9) Kroon, R.; Kiefer, D.; Stegerer, D.; Yu, L.; Sommer, M.; Müller, C. Polar Side Chains Enhance Processability, Electrical Conductivity, and Thermal Stability of a Molecularly p-Doped Polythiophene. *Adv. Mater.* **2017**, 29, 1700930.

(10) Müller, L.; Nanova, D.; Glaser, T.; Beck, S.; Pucci, A.; Kast, A. K.; Schröder, R. R.; Mankel, E.; Pingel, P.; Neher, D.; Kowalsky, W.; Lovrincic, R. Charge-Transfer-Solvent Interaction Predefines Doping Efficiency in p-Doped P3HT Films. *Chem. Mater.* **2016**, 28, 4432– 4439.

(11) Jacobs, I. E.; Aasen, E. W.; Oliveira, J. L.; Fonseca, T. N.; Roehling, J. D.; Li, J.; Zhang, G.; Augustine, M. P.; Mascal, M.; Moule, A. J. Comparison of solution-mixed and sequentially processed P3HT:F4TCNQ films: effect of doping-induced aggregation on film morphology. *J. Mater. Chem. C* **2016**, 4, 3454–3466.

(12) Hamidi-Sakr, A.; Biniek, L.; Bantignies, J.-L.; Maurin, D.; Herrmann, L.; Leclerc, N.; Lévêque, P.; Vijayakumar, V.; Zimmermann, N.; Brinkmann, M. A Versatile Method to Fabricate Highly In-Plane Aligned Conducting Polymer Films with Anisotropic Charge Transport and Thermoelectric Properties: The Key Role of Alkyl Side Chain Layers on the Doping Mechanism. *Adv. Funct. Mater.* **2017**, 27, 1700173.

(13) Scholes, D. T.; Yee, P. Y.; Lindemuth, J. R.; Kang, H.; Onorato, J.; Ghosh, R.; Luscombe, C. K.; Spano, F. C.; Tolbert, S. H.; Schwartz, B. J. The Effects of Crystallinity on Charge Transport and the Structure of Sequentially Processed F 4 TCNQ-Doped Conjugated Polymer Films. *Adv. Funct. Mater.* **2017**, 27, 1702654.

(14) Hollinger, J.; Jahnke, A. A.; Coombs, N.; Seferos, D. S. Controlling Phase Separation and Optical Properties in Conjugated Polymers through Selenophene-Thiophene Copolymerization. *J. Am. Chem. Soc.* **2010**, 132, 8546−8547.

(15) Hollinger, J.; Sun, J.; Gao, D.; Karl, D.; Seferos, D. S. Statistical Conjugated Polymers Comprising Optoelectronically Distinct Units. *Macromol. Rapid Commun.* **2013**, 34, 437−441.

(16) Heeney, M.; Zhang, W.; Crouch, D. J.; Chabinyc, M. L.; Gordeyev, S.; Hamilton, R.; Higgins, S. J.; McCulloch, I.; Skabara, P. J.; Sparrowe, D.; Tierney, S. Regioregular poly(3-hexyl)selenophene: a low band gap organic hole transporting polymer. *Chem. Commun.* **2007**, 5061.

(17) Li, L.; Hollinger, J.; Jahnke, A. a.; Petrov, S.; Seferos, D. S. Polyselenophenes with distinct crystallization properties. *Chem. Sci.* **2011**, 2, 2306.

(18) Manion, J. G.; Ye, S.; Proppe, A. H.; Laramee, A. W.; McKeown, G. R.; Kynaston, E. L.; Kelley, S. O.; Sargent, E. H.; Seferos, D. S. Examining Structure−Property−Function Relationships in Thiophene, Selenophene, and Tellurophene Homopolymers. *ACS Applied Energy Materials* **2018**, 1, 5033

(19) Yan, H.; Hollinger, J.; Bridges, C. R.; McKeown, G. R.; AlFaouri, T.; Seferos, D. S. Doping Poly(3-hexylthiophene) Nanowires with Selenophene Increases the Performance of Polymer-Nanowire Solar Cells. *Chem. Mater.* **2014**, 26, 4605−4611.

(20) Ghosh, R.; Pochas, C. M.; Spano, F. C. Polaron Delocalization in Conjugated Polymer Films. *J. Phys. Chem. C* **2016**, 120, 11394− 11406.

(21) Pochas, C. M.; Spano, F. C. New insights on the nature of two-dimensional polarons in semiconducting polymers: Infrared absorption in poly(3-hexylthiophene). *J. Chem. Phys.* **2014**, 140, 244902.

(22) Wohlgenannt, M.; Jiang, X. M.; Vardeny, Z. V. Confined and delocalized polarons in π-conjugated oligomers and polymers: A study of the effective conjugation length. Phys. Rev. B: *Condens. Matter Mater. Phys.* **2004**, 69, 241204.

(23) Prosa, T. J.; Winokur, M. J.; McCullough, R. D. Evidence of a novel side chain structure in regioregular poly(3-alkylthiophenes). *Macromolecules* **1996**, 29, 3654−3656.

(24) Kang, K.; Watanabe, S.; Broch, K.; Sepe, A.; Brown, A.; Nasrallah, I.; Nikolka, M.; Fei, Z.; Heeney, M.; Matsumoto, D.; Marumoto, K.; Tanaka, H.; Kuroda, S.-i.; Sirringhaus, H. 2D coherent charge transport in highly ordered conducting polymers doped by solid state diffusion. *Nat. Mater.* **2016**, 15, 896–902.

(25) Chew, A. R.; Ghosh, R.; Shang, Z.; Spano, F. C.; Salleo, A. Sequential Doping Reveals the Importance of Amorphous Chain Rigidity in Charge Transport of Semi-Crystalline Polymers. *J. Phys. Chem. Lett.* **2017**, 8, 4974–4980.

(26) Aguirre, J. C.; Hawks, S. A.; Ferreira, A. S.; Yee, P.; Subramaniyan, S.; Jenekhe, S. A.; Tolbert, S. H.; Schwartz, B. J. Sequential Processing for Organic Photovoltaics: Design Rules for Morphology Control by Tailored Semi-Orthogonal Solvent Blends. *Adv. Energy Mater.* **2015**, 5, 1402020.

(27) Lindemuth, J.; Mizuta, S.-I. Hall measurements on low-mobility materials and high resistivity materials. *Proc. SPIE* **2011**, 8110, 81100I.

(28) Lindemuth, J. Variable temperature Hall measurements on low mobility materials. *Proc. SPIE* **2012**, 8470, 84700G.

(29) Chen, Y.; Yi, H. T.; Podzorov, V. High-Resolution ac Measurements of the Hall Effect in Organic Field-Effect Transistors. *Phys. Rev. Appl.* **2016**, 5, 034008.

(30) Fujimoto, R.; Watanabe, S.; Yamashita, Y.; Tsurumi, J.; Matsui, H.; Kushida, T.; Mitsui, C.; Yi, H. T.; Podzorov, V.; Takeya, J. Control of molecular doping in conjugated polymers by thermal annealing. *Org. Electron.* **2017**, 47, 139–146.

(31) Yi, H. T.; Gartstein, Y. N.; Podzorov, V. Charge carrier coherence and Hall effect in organic semiconductors. *Sci. Rep.* **2016**, 6, 23650.

Chapter 7. Dopant-Induced Ordering of Amorphous Regions in Regiorandom P3HT

Semiconducting polymers have the potential for use in a variety of optoelectronic applications due to their affordability, ease of device manufacturing, and tunable characteristics.[1-3] The electronic properties of semiconducting polymers can be tuned via chemical doping with small molecule dopants like iron (III) chloride ($FeCl_3$)[4,5] and 2,3,5,6-tetrafluoro-7,7,8,8-tetracyanoquinodimethane (F_4TCNQ),[6-12] which add mobile carriers to the system. Adding small amounts of dopant has been shown to improve the performance of polymer-based organic photovoltaics by filling traps,[13] and more extensive doping can increase the conductivity for transistor[14,15] or thermoelectric[16,17] applications. Although a lot of work has been done, the ways that dopants affect the optical, electronic, and structural properties of semiconducting polymers are still not well understood.[18-27]

One way to control the structural changes inherent in the chemical doping process is to use solution sequential processing (SqP), which starts with the deposition of a pure polymer film followed by addition of the dopant using a solvent that swells but does not dissolve the polymer. We have previously shown that with SqP, the polymer crystallinity and domain orientation are largely preserved throughout the doping process, in sharp contrast to doping performed using the traditional co-dissolution method.[6] Doping via SqP also allowed us to study how the optical and electrical properties of F_4TCNQ-doped poly-(3-hexylthiophene-2,5-diyl) (P3HT) films change as the polymer crystallinity was controllably tuned.[20] Using optical spectroscopy, 2-D grazing-incidence wide-angle X-ray scattering (GIWAXS), and theoretical modeling, we argued that the F_4TCNQ anion must lie within the lamellae of the polymer crystallites (i.e., between the side chains and not the π-stacks) or in amorphous regions of the film.20 Hamidi-Sakr et al. also reached the same conclusion by studying sequentially-doped

aligned P3HT films, in which the F_4TCNQ anion absorption transition dipole was orthogonal to that of the polaron on the polymer backbone.[19]

Most research on doped semiconducting polymers has focused on semicrystalline materials such as P3HT or poly(2,5-bis(3-tetradecylthiohen-2-yl)thieno[3,2-*b*]thiophene) (PBTTT).[28-30] But a few recent studies have focused on more amorphous polymer materials, which appear to behave differently from the more crystalline polymers. For example, regiorandom P3HT (RRa-P3HT) has a disordered array of side chains and thus does not readily crystalize in films, even though its backbone to the more heavily investigated regioregular (RR) P3HT. Chew *et al*. have argued that amorphous conjugated polymers like RRa-P3HT become more ordered after doping.[18] Lim *et al*. have studied the electrical properties of blends of regioregular (RR) and regiorandom (RRa) P3HT vapor doped with F_4TCNQ, and found using grazing-incidence wide-angle x-ray scattering (GIWAXS) and resonant soft X-ray scattering (RSoXS)[31] that doping indeed increases order and long-range connectivity in originally disordered regions of the blend.

In this work, we extend our knowledge of the effects of doping on amorphous conjugated polymers by examining the structural effects of two different dopants (F_4TCNQ and $FeCl_3$) as well as a related non-dopant small molecule, tetracyanoquinodimethane (TCNQ), on RRa-P3HT. We choose TCNQ as a non-dopant due to its structural similarity with F_4TCNQ, allowing us to isolate the structural role of space-filling of the added molecule compared to changes induced by charge transfer reactions with oxidizing dopants like F_4TCNQ. We also investigate $FeCl_3$ as an alternate dopant that sits in a different place relative to the polymer to provide information about whether the morphological changes induced upon doping are controlled predominantly by interactions with the dopant or simply by the creation of hole polarons on the polymer backbone.

We show by studying the optical, electrical and structural properties of our doped/infiltrated RRa-P3HT films that the incorporation of either F_4TCNQ or $FeCl_3$ induces an increase in both crystallinity and molecular ordering of the original RRa-P3HT structure. This increased ordering produces a structure that is very similar to that of RR-P3HT upon doping, with the dopant anions sitting in the lamellar regions between the P3HT side chains and the backbone π-stacks reorienting with respect to the unit cell.[22,24,32] However, the incorporation of the non-dopant TCNQ has no effect on the RRa-P3HT crystallinity or molecular ordering, suggesting that the observed structural reorganization is not simply due to a space filling phenomenon. Moreover, the fact that RRa-P3HT doped with either F_4TCNQ or $FeCl_3$ returns to its original, non-ordered structure upon thermal dedoping indicates that the increased order and crystallinity upon doping is due to the presence of polarons on the polymer backbone.

We begin our study by examining the optical spectroscopy of RRa-P3HT films with and without various small molecule additives infiltrated by SqP, shown in Figure 7.1. The details of how we prepared these films are given in the Supporting Information (SI). The pure spin-coated RRa-P3HT film has a broad absorption peak centered at 447 nm or 2.76 eV (dark blue curve) that results from the band gap or exciton transition of the polymer. This absorption spectrum is significantly blue-shifted compared to that of RR-P3HT and similar to what is seen for RRa-P3HT in solution,[33] confirming that RRa-P3HT maintains an amorphous morphology in the solid state due to the steric hindrance of its randomly-oriented side chains.[34]

Upon infiltration of TCNQ into films of RRa-P3HT film, the absorption spectrum (green curve) does not show an obvious changes, but we can confirm the successful incorporation of TCNQ into our by seeing its presence in the solution absorbance after re-dissolving the infiltrated film in dichloromethane (see Fig. S1 in the SI). Upon the SqP addition of either F_4TCNQ (red curve) or $FeCl_3$ (purple curve), we see a decrease in the neutral exciton absorption

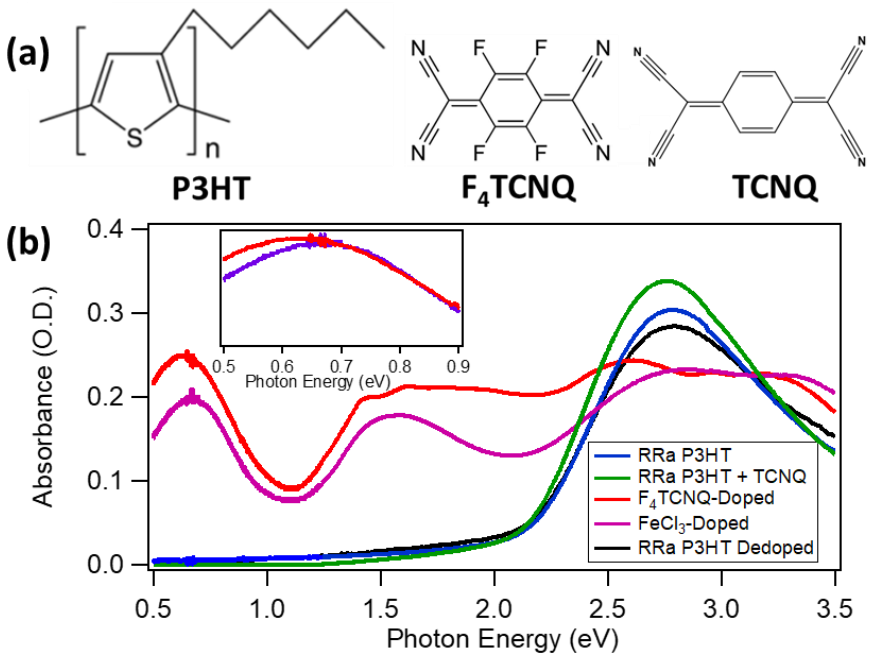

Figure 7.1: (a) Molecular structures of P3HT, F_4TCNQ, and TCNQ and (b) UV-Vis absorbance of a thin film of RRa-P3HT (blue), and similar films infiltrated by SqP with F_4TCNQ (red), $FeCl_3$ (pink), and TCNQ (green), showing successful incorporation of each of the small molecules. The new bands centered near 1.55 eV and 0.65 eV result from the production of polarons, indicating doping has occurred with F_4TCNQ and $FeCl_3$. The thermally dedoped film (black) confirms successful removal of dopant in the films. The inset shows the normalized low-energy P1 absorption for the F_4TCNQ- and $FeCl_3$-doped films; the relative blueshift of the $FeCl_3$-doped P1 absorption is indicative of more trapped charge carriers.

of RRa-P3HT at 2.76 eV and the appearance of two new broad absorptions centered near 1.55 eV and 0.65 eV that have been assigned to the presence of hole polarons on the P3HT backbone.[5,35-37] In addition to this polaronic absorption, we also see optical signatures of the dopant anions for both F_4TCNQ (1.42 eV, 1.61 eV, 1.79 eV, and 2.97 eV)[6,38,39] and $FeCl_3$ (3.47 eV),[5] verifying that charge transfer and thus doping has taken place.

In order to take a closer look at the structural effects upon doping with F_4TCNQ or $FeCl_3$ or infiltrating TCNQ via SqP, we performed a series of 2D-GIWAXS measurements. GIWAXS largely investigates the structural properties of the crystalline portions of the sample, providing information on relative crystallinity, molecular packing distances, and polymer orientation. By

selectively integrating over specific portions of the 2-D diffractogram (details given in the SI), we are able to separate the out-of-plane from the in-plane scattering to glean more information on the effect of polymer domain orientation. Although RRa-P3HT is a much more disordered and amorphous than semicrystalline RR-P3HT, undoped RRa-P3HT films still have enough order to see characteristic lamellar stacking and π-stacking peaks, as can be seen in the raw 2-D GIWAXS diffractograms (Figure S2).

The radially-integrated diffractograms of pure RRa-P3HT (blue curve), RRa-P3HT with TCNQ (green curve), and RRa-P3HT doped with 0.003M F_4TCNQ (red curve) are shown in Figure 7.2a. Pure RRa-P3HT has a lamellar side-chain stacking peak (100) at q = 0.41 $Å^{-1}$ and a broad, disordered π-stacking peak (010) at q = 1.49 $Å^{-1}$. When F_4TCNQ is added to the polymer, the lamellar stacking peak shifts to smaller q (0.36 $Å^{-1}$) and a new π-stacking peak appears at larger q (1.83 $Å^{-1}$), denoted as (010)*. These changes are similar to those previously seen for F_4TCNQ-doped RR-P3HT (see also Fig. S3).[6,20] In addition to these peak shifts, there is a clear change in lamellar crystallinity for the doped RRa-P3HT, as indicated by the increase in height of the (100) peak as well as the appearance of new lamellar overtones in the (200) and (300) peaks seen at q = 0.76 $Å^{-1}$ and q = 1.14 $Å^{-1}$, respectively.

In addition to the appearance of higher-order lamellar peaks upon doping with F_4TCNQ, Figure 7.2b shows that the polymer domain orientation changes and becomes much more highly edge-on oriented. This is evidenced by the dramatic increase of the (100) intensity and decrease in the (010) intensity for the F_4TCNQ-doped sample in the out-of-plane diffraction shown in Figure 7.2b. These changes are non-monotonic with doping concentration, as shown in Fig. S4 and discussed in the SI. As mentioned in the introduction, this F_4TCNQ-induced ordering of the amorphous regions of RRa-P3HT films has recently been demonstrated by Lim *et al.*,[31] who have

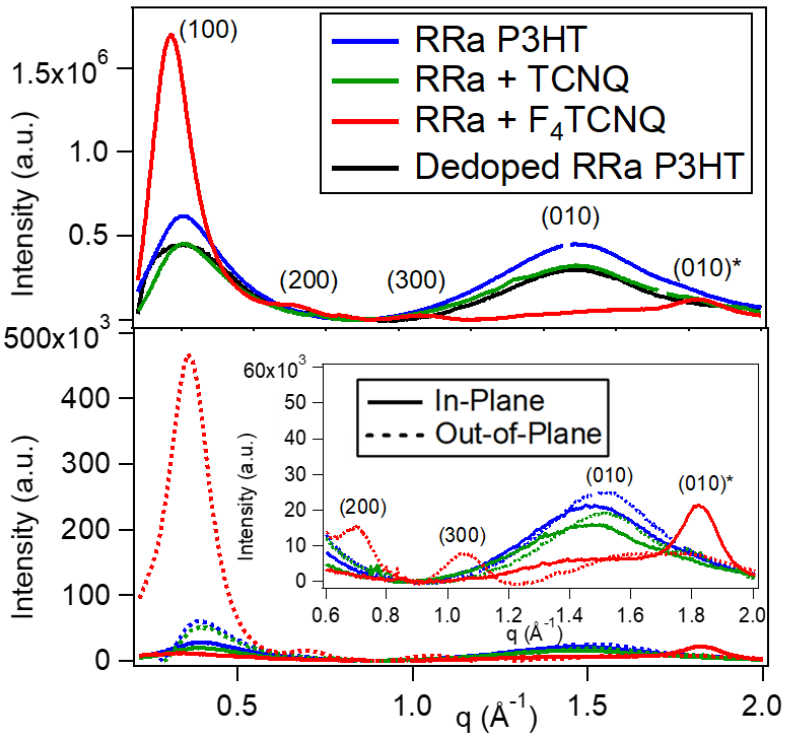

Figure 7.2. (a) Radially-integrated diffraction of undoped RRa-P3HT (blue), 0.003M F_4TCNQ-Doped RRa-P3HT (red), RRa-P3HT with TCNQ (green), and dedoped RRa-P3HT and (b) in-plane (solid) and out-of-plane integrations (dashed) with the inset zoomed in on the lamellar overtones and π-stacking region. Doping with F_4TCNQ shows a clear increase in molecular order/overall crystallinity as well as the introduction of a strong preference for edge-on orientation. In contrast, infiltration with the structurally similar TCNQ has little effect on the RRa-P3HT structure, indicating that simple space filling is not responsible for the increased ordering upon doping.

argued that the stiffening of the P3HT backbone in the amorphous regions leads to longer correlation lengths and thus improvements in charge transport.

Figure 7.2 also shows that upon the addition of TCNQ to the RRa-P3HT films (green curve), there is virtually no structural change in the RRa-P3HT, except perhaps for a small decrease in overall crystallinity. The absence of any orientation change in Figure 7.2b further confirms that the incorporation of TCNQ is not altering the RRa-P3HT structure. If TCNQ were to intercalate into the polymer structure in a manner similar to F_4TNCQ, we would expect some change/shift in the polymer morphology. Instead, the observed lack of any structural change

with TCNQ suggests the F_4TCNQ-doping induced changes is not a neutral π-stacking or space-filling phenomenon, but instead is clearly connected with the doping process.

In order to determine how the doping process drives the induced order seen in doped RRa-P3HT films, we examine the structure of $FeCl_3$-doped RRa-P3HT in Figure 7.3. The radially-integrated diffraction in Figure 7.3a shows that the addition of $FeCl_3$ leads to similar increased (100) as seen with F_4TCNQ (detailed peak locations are given in Table S1), while the in- and out-of-plane scattering shown in Figure 7.3b shows that $FeCl_3$ doping induces a similar increase in edge-on domain orientation as with F_4TNCQ. These results show that the structural changes

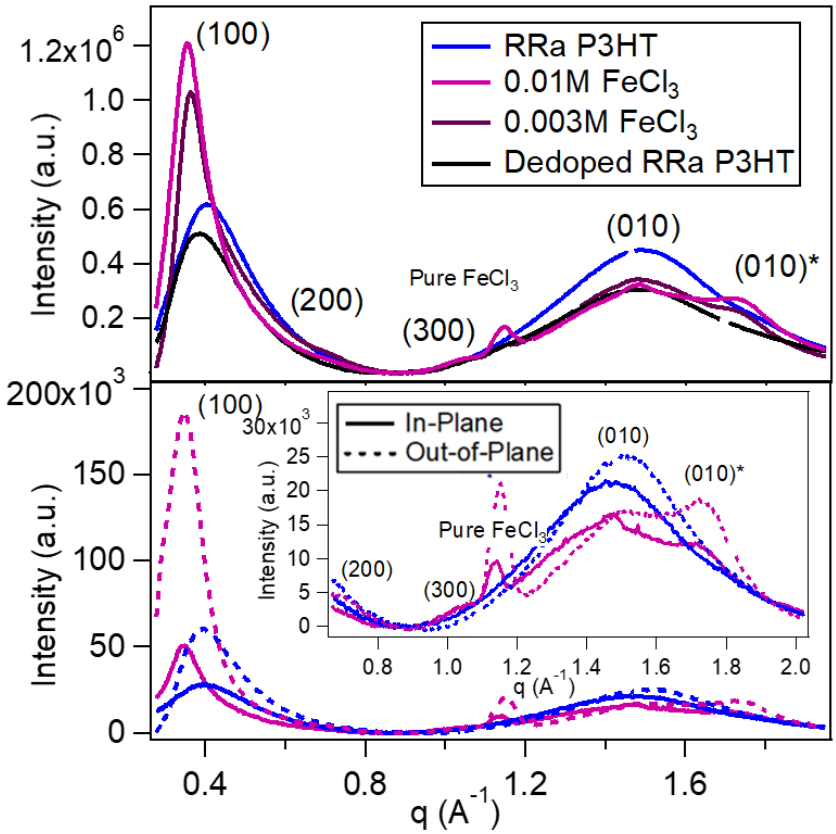

Figure 7.3. (a) Radially-integrated diffraction of undoped RRa-P3HT (blue), 0.01M $FeCl_3$-doped RRa-P3HT (pink), 0.003M-doped RRa-P3HT (purple), and dedoped RRa-P3HT (black) and (b) in-plane (solid) and out-of-plane integrations (dashed) with the inset zoomed in on the lamellar overtones and π-stacking regions. The similar dopant-induced ordering (increase of (100) intensity, appearance of lamellar overtones and increased edge-on orientation) to what is seen with F_4TCNQ indicates that the structural changes are due to primarily to the polarons created by the doping process.

are more related to polaron formation rather than the way the dopants fill space in the crystallites.

We find that by thermal annealing of both the F_4TCNQ-doped and $FeCl_3$-doped RRa-P3HT samples (black curves in Figs. 7.2a and 7.3a, respectively), the structure goes right back to that of undoped RRa-P3HT. This dedoping is also confirmed by the disappearance of the polaronic and anionic absorptions as well as the recovery of the excitonic absorption seen in Figure 7.1 (black curve). This further suggests that the induced ordering and reorganization of the polymer chains upon doping is not induced simply by adding a molecule and space-filling because the altered crystallinity and ordering would largely be maintained. Instead, this structural reorganization upon doping can be attributed to the polymer chains being pulled closer together in order to delocalize the polaron.

Although the structural changes upon doping RRa-P3HT are significant, comparison of the total scattering intensity measure for doped versions of both RR-P3HT and RRa-P3HT (see SI Figure S3) indicate that the overall crystallinity of the doped RRa-P3HT is still significantly lower than doped RR-P3HT. GIWAXS probes only the crystalline domains in films that contains both amorphous and crystalline regions. While this data suggests that we can dramatically increase the crystalline fraction of the film using doping, a much larger fraction of the doped RRa-P3HT films are amorphous, compared to similar doped RR-P3HT. We also find that the F_4TCNQ-doped regiorandom sample is more crystalline than the $FeCl_3$-doped sample (Figure S3). This suggests that packing constraints may play some role in the induced crystallization, as the longer, flat F_4TCNQ molecule is likely to fit better into the lamellar regions than $FeCl_3$. The fact that $FeCl_3$ is still able to increase crystallinity upon doping, however, implies that fundamentally, this structural reorganization can be attributed to packing changes to allow for delocalizing the polaron.

Having examined the structural effects upon incorporating small molecule dopants into RRa films, we now take a more detailed look at the changes in the UV-Vis upon doping. Interestingly, the F_4TCNQ-doped RRa-P3HT sample shows a significant redshift (~150 meV) of the undoped main exciton absorption band, suggesting an increase in crystalline order of the remaining neutral polymer regions upon doping. Indeed, the position of the shifted peak is very similar to that in RR-P3HT. This increase in crystalline order in the undoped component of the doped of RRa-P3HT film suggests that when domain level crystallization occurs, both doped and undoped regions get swept up in the doping-induced structural changes. This increased order of RRa-P3HT upon doping has previously been correlated with the planarization and straightening of the polymer backbone, as observed using Raman spectroscopy.[18,31,40–42] As noted above, TCNQ does not result in any polaron formation, as expected. The fact that the neutral exciton absorption for TCNQ treated films is also unaffected, again rules out simple space filling as the primary source of the increased order.

It is worth noting that the low-energy polaron absorption band (often referred to as the P1 band)[43] we see in our RRa-P3HT samples in Figure 7.1 are quite a bit blue-shifted from that seen in RR-P3HT. If the polaron is at a similar absolute energy in both RR-P3HT and RRa-P3HT, this blue-shit could be attributed to the wider band gap and deeper valence band of RRa-P3HT. Alternatively, modeling the spectra of doped P3HT has shown that as the distance between the dopant anion and polymer backbone directly affects the location of this P1 absorption peak; in particular the closer the anion to the polymer backbone, the more tightly bound and blueshifted the absoption.[18,20,44,45] Using this model, the most blue-shifted species contributing to the P1 absorption would consist of dopant anion and polymer polaron sites that are almost in molecular contact. Such tight polaron/anion pairs would presumably sit in the amorphous regions of the polymer film where there are no packing constraints keeping the anion away from the polymer. The peak is broad and extends significantly to the red, suggesting there are also much larger

dopant anion-polaron distances, presumably in the crystalline domains. Looking at the inset in Figure 7.1, which shows normalized versions of the F_4TCNQ and $FeCl_3$ derived P1 absorption peaks, we see that indeed, the blue edge of the P1 absorption is unaltered when comparing F_4TCNQ- (red) and $FeCl_3$-doped (pink) RRa-P3HT samples, as there is a significant amorphous fraction in both films. There is more intensity at the red edge for the F_4TCNQ-doped sample compared to the $FeCl_3$ doped material, consistent with the observation of a higher crystalline fraction in the F_4TCNQ doped material (Figure S3), as previously discussed.

The conductivities of the F_4TCNQ-doped and $FeCl_3$-doped RRa-P3HT films were measured to be 0.02 S/cm and 0.01 S/cm, respectively, using the van der Pauw method. Even with the improved ordering and similar structural rearrangement observed in the GIWAXS data, we find that the conductivity is still an order of magnitude lower compared to its more crystalline regioregular counterpart. This is in agreement with the idea that a significant fraction of the film is still amorphous, and in those regions, carriers are less mobile due to the close presence of the counterions, as indicated by the P1 peak absorption (inset Figure 7.1). The difference in conductivity can likely be attributed to the difference in crystallinity between materials produced with the different dopants, as characterized by GIWAXS.

The idea that polaron formation during doping drives a structural reorganization helps add to our growing understanding of how anion distance relates to carrier mobility. For our doped RRa-P3HT films, the dopant anions are close to the polaron in the amorphous parts of the film, resulting in low conductivities. The increased crystallinity and order of the F_4TCNQ-doped film relative to the FeCl3-doped film helps further separate the F_4TCNQ anion and polaron, helping increase the conductivity. On this continuum, highly crystalline polymers like 100% RR-P3HT and PBTTT hold dopant counter ions further from the polarons, resulting in yet higher mobilities.[5,16,20,46,47] Liu *et al*. showed that with large dopants like $Mo(tfd)_3$ that cannot

infiltrate RR-P3HT crystallites, there was still a structural reorganization that they attributed to the polaron formation process.[48] We have recently shown that with a similarly large functionalized dodecaborane cluster, the crystallinity of doped RR-P3HT eventually gets destroyed, despite producing record-setting solution-processed P3HT conductivities.[49] This suggests that when small molecule dopants can intercalate into the polymer structure, polymer crystallinity can help to separate the dopant anions from polarons, while for large dopants, polymer crystallinity is less important.

In summary, we have incorporated RRa-P3HT films with a range of small molecules and used thermal dedoping to explore the structural changes induced upon doping. Optical and electrical measurements confirm successful doping with both F_4TCNQ and $FeCl_3$, resulting in low, but measurable conductivities due to the creation of trapped carriers. Upon doping, regardless of dopant we induce a structural reorganization of the doped RRa-P3HT to a more crystalline and more ordered structure, which reverts back to the initial state upon dedoping. The fact that no structural changes occur upon incorporation of TCNQ, which is similar to F_4TCNQ but is not able to dope the films, strongly suggest the increases in crystallinity are due to polaron formation, rather than molecular packing constraints that occur upon the incorporation of the small molecules into the films.

7.1. Experimental Methods

Materials & Film Preparation. RRa P3HT (Sigma Aldrich), F_4TCNQ (TCI Chemicals), $FeCl_3$ (EM Science), and TCNQ (Alfa Aesar) were used as purchased. Glass and silicon substrates were cleaned sequentially by sonicating in soapy water, DI water, acetone, and isopropanol for 10 minutes each, then placed under rough vacuum to remove all traces of residual solvent, and finally transferred into a nitrogen glove box for use.

RRa P3HT films were spin coated at 1000 rpm for 60 seconds and then 3000 rpm for 10 seconds, out of 20 mg/mL solution in *o*-DCB, producing films that were ~80 nm thick. This was followed by a second spin-coating step where the RRa P3HT films were infiltrated by small molecule solutions spin-coated on top of the dried RRa P3HT film at 4000 rpm for 10 seconds. The solutions for this second step were prepared by dissolving each small molecule (F_4TCNQ, $FeCl_3$, and TCNQ) in a blend of 50:50 DCM:Ethanol by volume.

Conductivity Measurements. Conductivity measurements in the Van der Pauw geometry were performed using a custom made apparatus in ambient atmosphere using a Keithley 2400 Sourcemeter where the max current sourced was held to 1 mW total power. The current was swept negative to positive, rotated 90°, and repeated. The slope of the *I-V* curves were then fit to the Van der Pauw equation. Samples were prepared on glass, with silver paste applied at the corners of the film to act as contacts. All reported data was averaged over 10 simultaneous measurements for multiple samples.

Film Characterization. 2-D grazing incidence wide-angle X-ray scattering (GIWAXS) experiments were performed at the Stanford Synchrotron Radiation Lightsource on beamline 11-3 using a wavelength of 0.9742 Å with an incidence angle of 0.12°. Figure S2 shows the full 2-D diffractograms of our RRa P3HT thin film samples. These diffractograms were radially integrated to obtain the diffraction patterns (0-10° for in-plane, 70-80° for near out-of-plane, and 0-180° for full integrations) shown in the main text. The 2-D images were collected on a plate with the detector 250 mm away from the center of the measured sample. The beam spot had a width of ~150 μm and a helium chamber was used to reduce the noise. The software package WxDiff was used to reduce the GIWAXS data and subsequent analysis was performed in IgorPro.

The UV-vis absorption data were acquired from 300-2500 nm using a Shimadzu UV-4191PC UV-VIS-NIR Scanning Spectrophotometer for films prepared on glass substrates.

7.2. Supporting Information

Supporting Information is available in Appendix F.

7.3. References

(1) Sirringhaus, H.; Tessler, N.; Friend, R. H. Integrated Optoelectronic Devices Based on Conjugated Polymers. *Science (80-.).* **1998**, *280* (June), 1741.

(2) Arias, A. C.; MacKenzie, J. D.; McCulloch, I.; Rivnay, J.; Salleo, A. Materials and Applications for Large Area Electronics: Solution-Based Approaches. *Chem. Rev.* **2010**, *110* (1), 3–24.

(3) Yu, G.; Gao, J.; Hummelen, J. C.; Wudl, F.; Heeger, A. J. Polymer Photovoltaic Cells: Enhanced Efficiencies via a Network of Internal Donor-Acceptor Heterojunctions. *Science (80-.).* **1995**, *270* (5243), 1789–1791.

(4) Gao, Z. Q.; Mi, B. X.; Xu, G. Z.; Wan, Y. Q.; Gong, M. L.; Cheah, K. W.; Chen, C. H. An Organic P-Type Dopant with High Thermal Stability for an Organic Semiconductor. *Chem. Commun. (Camb).* **2008**, No. 1, 117–119.

(5) Yamamoto, J.; Furukawa, Y. Electronic and Vibrational Spectra of Positive Polarons and Bipolarons in Regioregular Poly(3-Hexylthiophene) Doped with Ferric Chloride. *J. Phys. Chem. B* **2015**, *119* (13), 4788–4794.

(6) Scholes, D. T.; Hawks, S. A.; Yee, P. Y.; Wu, H.; Lindemuth, J. R.; Tolbert, S. H.; Schwartz, B. J. Overcoming Film Quality Issues for Conjugated Polymers Doped with F4TCNQ by Solution Sequential Processing: Hall Effect, Structural, and Optical Measurements. *J. Phys. Chem. Lett.* **2015**, *6* (23), 4786–4793.

(7) Jacobs, I. E.; Aasen, E. W.; Oliveira, J. L.; Fonseca, T. N.; Roehling, J. D.; Li, J.; Zhang, G.; Augustine, M. P.; Mascal, M.; Moulé, A. J. Comparison of Solution-Mixed and Sequentially Processed P3HT:F4TCNQ Films: Effect of Doping-Induced Aggregation on Film Morphology. *J. Mater. Chem. C* **2016**, *4* (16), 3454–3466.

(8) Méndez, H.; Heimel, G.; Winkler, S.; Frisch, J.; Opitz, A.; Sauer, K.; Wegner, B.; Oehzelt, M.; Röthel, C.; Duhm, S.; et al. Charge-Transfer Crystallites as Molecular Electrical Dopants. *Nat. Commun.* **2015**, *6*, 8560.

(9) Fincher, Jr., C. R.; Ozaki, M.; Tanak, M.; Peebles, D.; Lauchlan, L.; Heeger, A. J. Electronic Structure of Polyacetylene: Optical and Infrared Studies of Undoped Semiconducting (CH)x and Heavily Doped Metallic (CH)X. *Phys. Rev. B* **1979**, *20* (4).

(10) Seeger, K.; Gill, W. D.; Clarke, T. C.; Street, G. B. Conductivity and Hall Effect Measurements in Doped Polyacetylene. *Solid State Commun.* **1978**, *28* (10), 873–878.

(11) Karpov, Y.; Erdmann, T.; Raguzin, I.; Al-Hussein, M.; Binner, M.; Lappan, U.; Stamm, M.; Gerasimov, K. L.; Beryozkina, T.; Bakulev, V.; et al. High Conductivity in Molecularly P-Doped Diketopyrrolopyrrole-Based Polymer: The Impact of a High Dopant Strength and Good Structural Order. *Adv. Mater.* **2016**, 6003–6010.

(12) Gao, J.; Roehling, J. D.; Li, Y.; Guo, H.; Moulé, A. J.; Grey, J. K. The Effect of 2,3,5,6-Tetrafluoro-7,7,8,8-Tetracyanoquinodimethane Charge Transfer Dopants on the Conformation and Aggregation of Poly(3-Hexylthiophene). *J. Mater. Chem. C* **2013**, *1* (36), 5638.

(13) Yu, S.; Frisch, J.; Opitz, A.; Cohen, E.; Bendikov, M.; Koch, N.; Salzmann, I. Effect of Molecular Electrical Doping on Polyfuran Based Photovoltaic Cells. *Appl. Phys. Lett.* **2015**, *106* (20).

(14) Lu, G.; Blakesley, J.; Himmelberger, S.; Pingel, P.; Frisch, J.; Lieberwirth, I.; Salzmann, I.; Oehzelt, M.; Di Pietro, R.; Salleo, A.; et al. Moderate Doping Leads to High Performance of Semiconductor/Insulator Polymer Blend Transistors. *Nat. Commun.* **2013**, *4*, 1588.

(15) Wang, Z.; Zou, Y.; Chen, W.; Huang, Y.; Yao, C.; Zhang, Q. The Role of Weak Molecular Dopants in Enhancing the Performance of Solution-Processed Organic Field-Effect Transistors. *Adv. Electron. Mater.* **2018**, *1800547*, 1800547.

(16) Glaudell, A. M.; Cochran, J. E.; Patel, S. N.; Chabinyc, M. L. Impact of the Doping Method on Conductivity and Thermopower in Semiconducting Polythiophenes. *Adv. Energy Mater.* **2015**, *5* (4).

(17) Lim, E.; Peterson, K. A.; Su, G. M.; Chabinyc, M. L. Thermoelectric Properties of Poly(3-Hexylthiophene) (P3HT) Doped with 2,3,5,6-Tetrafluoro-7,7,8,8-Tetracyanoquinodimethane (F4TCNQ) by Vapor-Phase Infiltration. *Chem. Mater.* **2018**, *30* (3), 998–1010.

(18) Chew, A. R.; Ghosh, R.; Shang, Z.; Spano, F. C.; Salleo, A. Sequential Doping Reveals the Importance of Amorphous Chain Rigidity in Charge Transport of Semi-Crystalline Polymers. *J. Phys. Chem. Lett.* **2017**, 4974–4980.

(19) Hamidi-Sakr, A.; Biniek, L.; Bantignies, J. L.; Maurin, D.; Herrmann, L.; Leclerc, N.; Lévêque, P.; Vijayakumar, V.; Zimmermann, N.; Brinkmann, M. A Versatile Method to Fabricate Highly In-Plane Aligned Conducting Polymer Films with Anisotropic Charge Transport and Thermoelectric Properties: The Key Role of Alkyl Side Chain Layers on the Doping Mechanism. *Adv. Funct. Mater.* **2017**, *27* (25), 1–13.

(20) Scholes, D. T.; Yee, P. Y.; Lindemuth, J. R.; Kang, H.; Onorato, J.; Ghosh, R.; Luscombe, C. K.; Spano, F. C.; Tolbert, S. H.; Schwartz, B. J. The Effects of Crystallinity on Charge Transport and the Structure of Sequentially Processed F4TCNQ-Doped Conjugated Polymer Films. *Adv. Funct. Mater.* **2017**, *27* (44), 1–13.

(21) Jacobs, I. E.; Cendra, C.; Harrelson, T. F.; Bedolla Valdez, Z. I.; Faller, R.; Salleo, A.; Moulé, A. J. Polymorphism Controls the Degree of Charge Transfer in a Molecularly Doped Semiconducting Polymer. *Mater. Horizons* **2018**, 3–6.

(22) Thomas, E. M.; Brady, M. A.; Nakayama, H.; Popere, B. C.; Segalman, R. A.; Chabinyc, M. L. X-Ray Scattering Reveals Ion-Induced Microstructural Changes During

Electrochemical Gating of Poly(3-Hexylthiophene). *Adv. Funct. Mater.* **2018**, *1803687*, 1–8.

(23) Tang, K.; McFarland, F.; Travis, S.; Lim, J.; Azoulay, J. D.; Guo, S. Aggregation of P3HT as a Preferred Pathway for Its Chemical Doping by F4-TCNQ. *Chem. Commun.* **2018**, *1* (c), 11925–11928.

(24) Hase, H.; O'Neill, K.; Frisch, J.; Opitz, A.; Koch, N.; Salzmann, I. Unraveling the Microstructure of Molecularly Doped Poly(3-Hexylthiophene) by Thermally Induced Dedoping. *J. Phys. Chem. C* **2018**, *122*, 25893–25899.

(25) Hynynen, J.; Kiefer, D.; Yu, L.; Kroon, R.; Munir, R.; Amassian, A.; Kemerink, M.; Müller, C. Enhanced Electrical Conductivity of Molecularly P-Doped Poly(3-Hexylthiophene) through Understanding the Correlation with Solid-State Order. *Macromolecules* **2017**, *50* (20), 8140–8148.

(26) Neelamraju, B.; Watts, K. E.; Pemberton, J. E.; Ratcliff, E. L. Correlation of Coexistent Charge Transfer States in F_4TCNQ-Doped P3HT with Microstructure. *J. Phys. Chem. Lett.* **2018**, 6871–6877.

(27) Liu, W.; Müller, L.; Ma, S.; Barlow, S.; Marder, S. R.; Kowalsky, W.; Köhn, A.; Lovrincic, R. The Origin of the π-π Spacing Change upon Doping of Semiconducting Polymers. *J. Phys. Chem. C* **2018**, *122* (49), 27983–27990.

(28) Cochran, J. E.; Junk, M. J. N.; Glaudell, A. M.; Miller, P. L.; Cowart, J. S.; Toney, M. F.; Hawker, C. J.; Chmelka, B. F.; Chabinyc, M. L. Molecular Interactions and Ordering in Electrically Doped Polymers: Blends of PBTTT and F4TCNQ. *Macromolecules* **2014**, *47* (19), 6836–6846.

(29) Patel, S. N.; Glaudell, A. M.; Peterson, K. A.; Thomas, E. M.; O'Hara, K. A.; Lim, E.; Chabinyc, M. L. Morphology Controls the Thermoelectric Power Factor of a Doped Semiconducting Polymer. *Sci. Adv.* **2017**, *3* (6), 24–26.

(30) Jha, A.; Duan, H. G.; Tiwari, V.; Thorwart, M.; Miller, R. J. D. Origin of Poor Doping Efficiency in Solution Processed Organic Semiconductors. *Chem. Sci.* **2018**, *9* (19), 4468–4476.

(31) Lim, E.; Glaudell, A. M.; Miller, R.; Chabinyc, M. L. The Role of Ordering on the Thermoelectric Properties of Blends of Regioregular and Regiorandom Poly(3-Hexylthiophene). *Adv. Electron. Mater.* **2019**, *1800915*, 1–11.

(32) Chew, A. R.; Ghosh, R.; Shang, Z.; Spano, F. C.; Salleo, A. Sequential Doping Reveals the Importance of Amorphous Chain Rigidity in Charge Transport of Semi-Crystalline Polymers. *J. Phys. Chem. Lett.* **2017**, *8* (20), 4974–4980.

(33) Chen, T.-A.; Wu, X.; Rieke, R. D. Regiocontrolled Synthesis of Poly(3-Alkylthiophenes) Mediated by Rieke Zinc: Their Characterization and Solid-State Properties. *J. Am. Chem. Soc.* **1995**, *117* (1), 233–244.

(34) Brown, P. J.; Thomas, D. S.; Köhler, A.; Wilson, J. S.; Kim, J. S.; Ramsdale, C. M.; Sirringhaus, H.; Friend, R. H. Effect of Interchain Interactions on the Absorption and Emission of Poly(3-Hexylthiophene). *Phys. Rev. B - Condens. Matter Mater. Phys.* **2003**, *67* (6), 1–16.

(35) Wang, C.; Duong, D. T.; Vandewal, K.; Rivnay, J.; Salleo, A. Optical Measurement of Doping Efficiency in Poly(3-Hexylthiophene) Solutions and Thin Films. *Phys. Rev. B* **2015**, *91* (8), 085205.

(36) Brown, P. G.; Sirringhaus, H.; Harrison, M.; Shkunov, M.; Friend, R. H. Optical Spectroscopy of Field-Induced Charge in Self-Organized High Mobility Poly(3-Hexylthiophene). *Phys. Rev. B - Condens. Matter Mater. Phys.* **2001**, *63* (12), 1–11.

(37) Pingel, P.; Neher, D. Comprehensive Picture of P-Type Doping of P3HT with the Molecular Acceptor F4TCNQ. *Phys. Rev. B - Condens. Matter Mater. Phys.* **2013**, *87* (11), 1–9.

(38) Pingel, P.; Neher, D. Comprehensive Picture of P-Type Doping of P3HT with the Molecular Acceptor F4TCNQ. *Phys. Rev. B - Condens. Matter Mater. Phys.* **2013**, *87* (11), 1–9.

(39) Le, T. H.; Nafady, A.; Qu, X.; Martin, L. L.; Bond, A. M. Detailed Electrochemical Analysis of the Redox Chemistry of Tetrafluorotetracyanoquinodimethane TCNQF4, the Radical Anion [TCNQF4]??-, And the Dianion [TCNQF 4]2- in the Presence of Trifluoroacetic Acid. *Anal. Chem.* **2011**, *83* (17), 6731–6737.

(40) Hynynen, J.; Kiefer, D.; Müller, C. Influence of Crystallinity on the Thermoelectric Power Factor of P3HT Vapour-Doped with F4TCNQ. *RSC Adv.* **2018**, *8* (3), 1593–1599.

(41) Wood, S.; Hollis, J. R.; Kim, J. S. Raman Spectroscopy as an Advanced Structural Nanoprobe for Conjugated Molecular Semiconductors. *J. Phys. D. Appl. Phys.* **2017**, *50* (7).

(42) Tsoi, W. C.; James, D. T.; Kim, J. S.; Nicholson, P. G.; Murphy, C. E.; Bradley, D. D. C.; Nelson, J.; Kim, J. S. The Nature of In-Plane Skeleton Raman Modes of P3HT and Their Correlation to the Degree of Molecular Order in P3HT:PCBM Blend Thin Films. *J. Am. Chem. Soc.* **2011**, *133* (25), 9834–9843.

(43) Beljonne, D.; Cornil, J.; Sirringhaus, H.; Brown, P. J.; Shkunov, M.; Friend, R. H.; Brédas, J. L. Optical Signature of Delocalized Polarons in Conjugated Polymers. *Adv. Funct. Mater.* **2001**, *11* (3), 229–234.

(44) Ghosh, R.; Chew, A. R.; Onorato, J.; Pakhnyuk, V.; Luscombe, C. K.; Salleo, A.; Spano, F. C. Spectral Signatures and Spatial Coherence of Bound and Unbound Polarons in P3HT Films: Theory Versus Experiment. *J. Phys. Chem. C* **2018**, *122* (31), 18048–18060.

(45) Ghosh, R.; Pochas, C. M.; Spano, F. C. Polaron Delocalization in Conjugated Polymer Films. *J. Phys. Chem. C* **2016**, *120* (21), 11394–11406.

(46) Patel, S. N.; Glaudell, A. M.; Peterson, K. A.; Thomas, E. M.; O'Hara, K. A.; Lim, E.; Chabinyc, M. L. Morphology Controls the Thermoelectric Power Factor of a Doped Semiconducting Polymer. *Sci. Adv.* **2017**, *3* (6), 24–26.

(47) Kang, K.; Watanabe, S.; Broch, K.; Sepe, A.; Brown, A.; Nasrallah, I.; Nikolka, M.; Fei, Z.; Heeney, M.; Matsumoto, D.; et al. 2D Coherent Charge Transport in Highly Ordered Conducting Polymers Doped by Solid State Diffusion. *Nat. Mater.* **2016**, *15* (8), 896–902.

(48) Liang, Z.; Zhang, Y.; Souri, M.; Luo, X.; Boehm, A. M.; Li, R.; Zhang, Y.; Wang, T.; Kim, D. Y.; Mei, J.; et al. Influence of Dopant Size and Electron Affinity on the Electrical Conductivity and Thermoelectric Properties of a Series of Conjugated Polymers. *J. Mater. Chem. A* **2018**, *6* (34), 16495–16505.

(49) Aubry, T. J.; Axtell, J. C.; Basile, V. M.; Winchell, K. J.; Lindemuth, J. R.; Porter, T. M.; Liu, J. Y.; Alexandrova, A. N.; Kubiak, C. P.; Tolbert, S. H.; et al. Dodecaborane-Based Dopants Designed to Shield Anion Electrostatics Lead to Increased Carrier Mobility in a Doped Conjugated Polymer. *Adv. Mater.* **2019**, *31* (11), 1–8.

Chapter 8. Conclusion

The first part of this thesis focused on utilizing self-assembly as a method to controllably improve semiconducting polymer charge transport properties. The electronic tunability and the ability to control the self-assembly provide logical routes to improve device performance in various organic electronics. The inherent disorder of semiconducting polymers, however, results in kinks and bends along the polymer backbone that disrupt the π-conjugation and decrease the overall conductivity. One way to prevent disordered self-assembly and maintain good charge transport properties is to take advantage of self-assembly dynamics to straighten the polymer chains. We predict that using an amphiphilic alternating copolymer, or conjugated polyelectrolyte (CPE), with a rigid hydrophobic backbone and charged hydrophilic side chains all on the same side of the polymer will create a driving force to form a wedge-type structure. Upon self-assembly in water, these wedge structures should self-assemble into rod-like micelles with the hydrophobic backbone on the inside and the charged hydrophilic side chains outside interacting with the water.

Using this design rule, we synthesized poly(cyclopentadithiophene-alt-thiophene) (PCT), an alternating copolymer with cyclopentadithiophene and thiophene monomer units, whose similar bond angles should straighten the polymer backbone relative to previously synthesized CPEs. CryoEM images confirm micelle formation with average an average diameter of 2 nm. Using small-angle X-ray scattering (SAXS) on various concentrations of high- and low-MW fractions of PCT, we provide further confirmation of cylindrical micelle formation. Solution SAXS profiles and the resulting *P(r)* Fourier transformations provide further proof of this cylindrical micelle formation: featureless raw scattering decays and a sharp peak at low distances representative of the cylinder diameter followed by a decay for correlations along the length of the cylinder, respectively. The radially averaged SAXS profiles are fit to the

Guinier/power law to determine the straightness of the cylinders, indicating perfectly straight rod-like structures for low-MW fractions. Final confirmation of the straightened cylindrical micelle structure using this amphiphilic self-assembly design rule is produced with Dammin bead models of the SAXS data. By confirming the expansion this design rule for straightening polymer chain, we open up the possibilities for the incorporation of appropriate acceptors to study charge transfer properties both in solution and solid-state, as well as the synthesis of similarly rigid CPEs.

The second part of this thesis focused on controlling the self-assembly of polymer:fullerene bulk heterojunctions (BHJs) for organic photovoltaic (OPV) devices. The nanoscale morphology of these BHJs is extremely important in determining the OPV device performance and efficiencies, with the polymer and fullerene requiring mixing on length scales of ~20 nm to prevent charge recombination, but also maintain separate conductive domains for efficient charge collection at the electrodes. Using sequential processing (SqP), a technique where the , the polymer is first deposited and out of a semi-orthogonal solvent or solvent blend, as to not dissolve the underlying polymer layer, the fullerene is intercalated into the pre-existing polymer film. The fullerene casting solvent can be further tuned using co-solvent blends such that there are varying ratios of swelling solvent (one that interacts with the polymer film) and non-solvent (one that does not preferentially dissolve the polymer film). We predict that by tuning this fullerene casting solvent up to the point of polymer dissolution, we are able to control the amount of vertical phase mixing between polymer and fullerene, thus improving the device performance.

We show that using SqP and tunable co-solvent blends we can controllably form favorable BHJ nanoscale morphologies with two systems of varying crystallinity in conjunction with $PC_{61}BM$ as the electron acceptor: semi-crystalline poly[(4,8-bis[(ethylhexyl)oxy]benzo[1,2-

b:4,5-*b*']dithiophene-2,6-diyl)(3-fluoro-2-[(2-ethylhexyl)carbonyl]thieno[3,4-*b*]thiophenediyl)] (PTB7) and amorphous poly[(4,8-di(2-butyloctyl)oxybenzo[1,2-*b*:4,5-*b*']dithiophene-2,6-diyl)-alt-(2,5-bis(4,4'-bis(2-octyl)dithieno[3,2-*b*:2'3'-*d*]silole-2,6-diyl)thiazolo[5,4-*d*]thiazole)] (PSDTTT). To probe the morphologies on both the local and global scales, we employ grazing-incidence wide-angle X-ray scattering (GIWAXS) and neutron reflectometry (NR), respectively. The GIWAXS data shows that for both polymers, the polymer orientation is not drastically altered, while the polymer crystallinity decreases and the fullerene crystallinity increases with increasing amount of swelling solvent, suggesting more fullerene intercalation for BHJ formation. The NR and resulting vertical phase profiles confirm our ability to tune ideal BHJ formation as a function of increasing swelling solvent: with more swelling solvent for each polymer system, we find that we are able to increase the amount of mixed polymer:fullerene region to improve the efficiency of charge transfer and thus, overall device efficiency. Interesting to note, for PSDTT (the more amorphous polymer), the fullerene resides near the silicon interface, suggesting that despite the nature of fullerene intercalation with SqP, swelling the polymer layer allows for the thermodynamically favorable state as predicted by each materials' respective surface energies.

In the last part of this thesis, we look to understand and control the morphological effects of molecular doping to improve the polymer conductivity via the introduction of additional charge carriers. For p-type doping, small molecule dopants that have a sufficiently low-lying LUMO to accept an electron from the polymer LUMO introduce positive charge carriers, or holes/polarons, along the polymer backbone. In particular, we will focus on the small molecule F_4TCNQ, which has been widely studied for its ease of solution processing and relative stability compared to halide or acid dopants, and poly(3-hexylthiophene-2,5-diyl) (P3HT). We show that sequential doping (the BHJ equivalent of SqP) preserves the polymer film quality as well as the nanoscale morphology. This allows for more dopant to be incorporated,

and therefore further increase the conductivity relative to the traditional blend-casting methods. In fact, we show that with appropriate swelling solvents, we are able to achieve conductivities as high as 5.5. S/cm.

Next we investigate the effects of crystallinity on the structure-function relationship of doping P3HT with F_4TCNQ. By tuning the processing solvent from fast drying to slow drying, and by incorporating 100% regioregular P3HT, we are able to tune the polymer crystallinity prior to F_4TCNQ doping with sequential doping. Using GIWAXS, we find that F_4TCNQ resides in either the disordered amorphous regions of the polymer or between the P3HT side chains in the crystalline lamellar regions. The optical spectroscopy shows that with increasing crystallinity, the polaron absorption redshifts, suggesting increased polaron delocalization across the polymer backbone. This idea is corroborated with theoretical modeling the of the polaron absorption, confirming that the F_4TCNQ anion is not π-stacking with P3HT to form a cation-anion co-crystal. Instead, this data suggests that the increased crystallinity is attributing to keeping the F_4TCNQ anion further away from the polaron, allowing for more mobile carriers and measured conductivities up to 12 S/cm.

We follow this up by studying the interplay between polymer crystallinity, swellability, and HOMO level using a statistical copolymer of P37S-*stat*P3HT. We show that while the ability for each polymer to be doped is dominated by the HOMO-LUMO offset between polymer and dopant, respectively, the final doped polymer crystallinity best correlated with increased conductivity. Using GIWAXS and differential scanning calorimetry (DSC) in conjunction with ellipsometry porosimetry, we find that the doped-state crystallinity is dependent on the pure copolymer crystallinity and its swellability. This shows that the ability of the copolymer film to restructure morphologically and allow for dopant intercalation is key to producing mobile

charge carriers as opposed to trapped carriers, resulting in 20 S/cm for pure P37S polymer films.

We end our study of the structure-function relationship in doped semiconducting polymer thin films by investigating the effect of doping on the amorphous regions in P3HT. By using regiorandom (RRa) P3HT, we are able to study the amorphous region morphology with GIWAXS. Specifically, we use a variety of small molecules to glean more information about the effect of small molecule intercalation: the non-dopant, π-stackable tetracyanoquinodimethane (TCNQ); the doping, π-stackable F_4TCNQ; and the doping, non-π-stacking $FeCl_3$. Whereas the non-doping TCNQ has no structural effects on the RRa P3HT (via GIWAXS), both F_4TCNQ and $FeCl_3$ have peak shifts characteristic of a reorientation of the P3HT crystal lattice. In fact, both dopants show the appearance of the lamellar overtones and drastic increase in edge-on orientation(from isotropic), signifying that the act of doping is inducing long-range order and crystallization of the amorphous regions in P3HT. Furthermore, upon thermal dedoping of our films, we see the structural changes are reversed, providing confirmation that the structural effects are due to the electrostatic doping process rather than being small molecule specific.

Overall, this thesis focused on understanding and controlling the self-assembly properties of semiconducting polymers. Fundamentally, it took an aim to control polymer chain straightness in an effort to improve charge transport properties by designing and characterizing a new self-assembling amphiphilic CPE that forms straight cylindrical micelles in water via PCT. In an effort to control a more applicable system, we were able to show that by tuning the fullerene casting solvent and fabricating SqP OPV devices, we improved the device performance of our solar cells by improving the global polymer:fullerene mixing. With the investigation of the structural effects of doping on semiconducting polymers, we further the field of polymer

doping by providing insight on how to create highly mobile carriers by distancing the polaron and dopant anion using polymer crystallinity.

APPENDIX A. Supporting Information for Chapter 2

Additional Bead Models

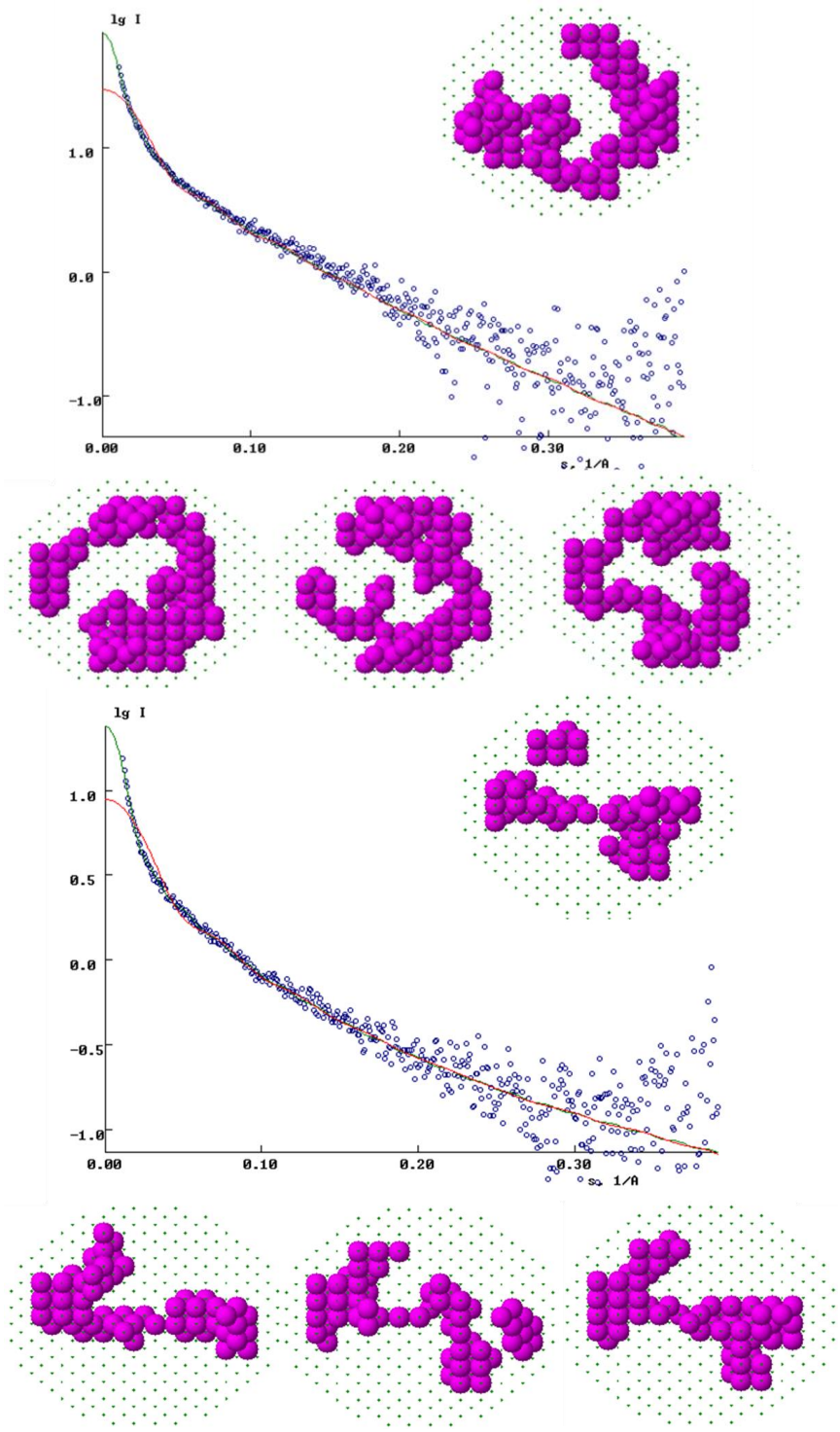

Figure A.2: Additional bead models for High- and Low-MW PCT.

Solution SAXS Analysis

The indirect transform program GNOM was used for the solution SAXS data processing. The 1-D SAXS curves are fit and smoothed and the particle-distance distribution function, *P(r)*, are evaluated. In order to use for DAMMIN bead modeling, GNOM files must be saved as a ".out" file type.

GNOM INPUT PARAMETERS

Angular Scale (1/2/3/4)	1
Kernel already calculated (Y/N)	No
Type of system (0/1/2/3/4/5/6)	0
Zero condition at r=rmin (Y/N)	Yes
Zero condition at r=rmax (Y/N)	No
Rmax for evaluating p(r)	**Varied**
Experimental setup (0/1/2)	0

The best fit is determined from the quality estimate number after each run in addition to a physically correct *P(r)* function.

The corresponding ".out" files that contain the raw SAXS data and the GNOM fits to the data are then input into DAMMIN for bead models representative of our PCT system. All fits were performed using "Expert Mode." Bold values indicate parameters that were input in to the program, whereas the non-bold values were calculated by the program based on the given inputs and data.

DAMMIN INPUT PARAMETERS

Computation mode:	**Expert**
Maximum diameter of the particle :	350.0
Solution at Alpha = 0.221E+01 Rg : 0.105E+03 I(0):	0.175E+05
Radius of gyration read:	105.0
Number of GNOM data points:	343
Maximum s value [1/angstrom]:	0.3235
Number of Shannon channels:	30.89
Number of knots in the curve to fit:	**55**
A constant was subtracted:	9.234
Maximum order of harmonics:	**20**
Point symmetry of the particle:	P1
Sphere diameter [Angstrom]:	**140.0**
Packing radius of dummy atoms:	**5.000**
Radius of the sphere generated:	70.00
Number of dummy atoms:	1985
Number of equivalent positions:	1
Expected particle anisometry:	Unknown
Excluded volume per atom:	707.6
Radius of 1st coordination sphere:	14.10
Minimum number of contacts:	5
Maximum number of contacts:	12
Looseness penalty weight:	**6.000e-3**
No of non-solvent atoms:	1985
Initial DAM looseness:	7.571e-3

Disconnectivity penalty weight:	**6.000e-3**
Initial DAM # of graphs:	1742
Discontiguity value:	0.0
Center of the initial DAM: 0.0000 0.0000 0.0000	
Peripheral penalty weight:	0.3000
Peripheral penalty value:	0.6029
Looseness fixing threshold:	0.0
R-factor fixing threshold:	0.0
***** The structure was randomized *****	
No of non-solvent atoms:	1023
Randomized DAM looseness:	0.1022
Randomized DAM # of graphs:	911
Discontiguity value:	2.258
Randomized peripheral penalty value:	0.6033
Weight: 0=s^2, 1=Emphasis->0, 2=Log:	1
***** Porod weight with emphasis at low s *****	
Initial scale factor:	9.153e-11
Scale factor fixed (Y=Yes, N=No):	N
Initial R^2 factor:	0.8020
Initial R factor:	0.8955
Initial penalty:	0.1952
Initial fVal:	0.9971
Variation of the target function:	1.574e-4
CPU per function call, seconds:	1.297e-4

Initial annealing temperature:	1.000e-3
Annealing schedule factor:	0.9500
# of independent atoms to modify:	1
Max # of iterations at each T:	138950
Max # of successes at each T:	13895
Min # of successes to continue:	46
Max # of annealing steps:	200

APPENDIX B. Supporting Information for Chapter 3

Photovoltaic Device and Active Layer Fabrication Procedures. We fabricated polymer:fullerene BHJ solar cells by starting with cleaning pre-patterned tin-doped indium oxide (ITO; TFD Inc.) coated substrates with four successive sonication steps: detergent solution, deionized water, acetone and isopropanol for approximately 10 min each. The ITO substrates were treated with an air plasma (200 mTorr, 15 min) after drying in vacuum for at least 30 min. We then deposited a thin layer of PEDOT:PSS by spin-coating the solution in air at 5000 rpm for 20 s. The PEDOT:PSS-covered substrates were then baked at 150 ºC for 20 min in air. The J-V measurements were performed in an argon atmosphere using a Keithley 2400 source meter. We used a xenon arc lamp and an AM-1.5 filter as the excitation source, with the intensity calibrated to match 1 sun.

GIWAXS. 2-D GIWAXS experiments were performed at the Stanford Synchrotron Radiation Lightsource on beamline 11-3 using a wavelength of 0.9742 Å. Figure S1 corresponds to the radially integrated pattern of the data from the full 2-D diffractogram. Each data curve in Figure S1 is the average of at least three different samples prepared under the same conditions. The 2-D images were collected on a plate with the detector 400 mm away from the center of the measured sample. The beam spot had a width of ~150 μm. A helium chamber was used to reduce the noise. The software package WxDiff was used to analyze the GIWAXS data.

NR Fits. The neutron reflectivity fits, as seen in Figure S4 were modeled using the Motofit software package in IGOR Pro. This package utilizes a slab-model approach with extensions for surface roughness, thickness, and SLD to perform a non-linear least-squares regression on the experimental reflectivity curves, resulting in vertical phase profiles. The overall thicknesses for each fit were matched with the actual film thicknesses as measured by

profilometry. SLD values for pure domains were taken from the literature or from previous experimental results. In addition to these values, the roughness of each slab was factored in and all three variables were iteratively refined until a quality fit was obtained.

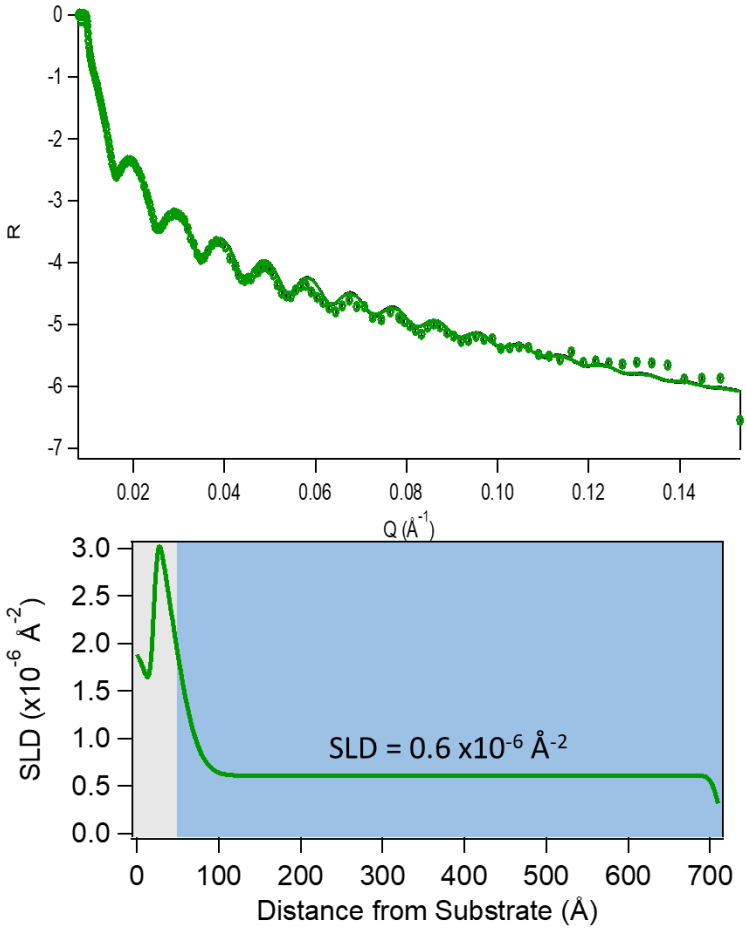

Figure B.2: Raw NR of PTB7 film and fit, along with corresponding SLD profile.

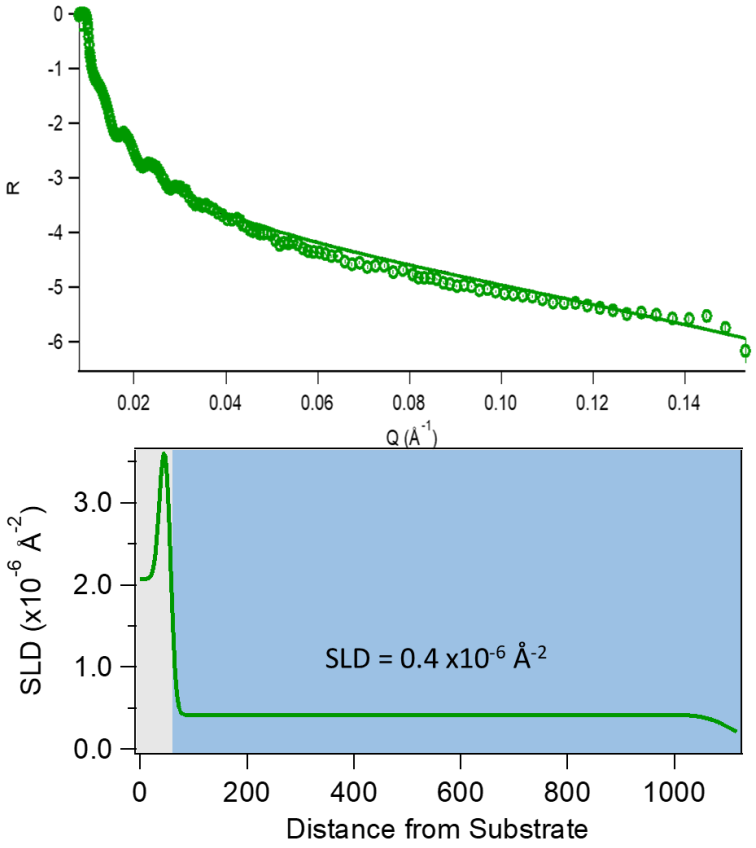

Figure B.3: Raw NR of PSDTTT film and fit, along with corresponding SLD profile.

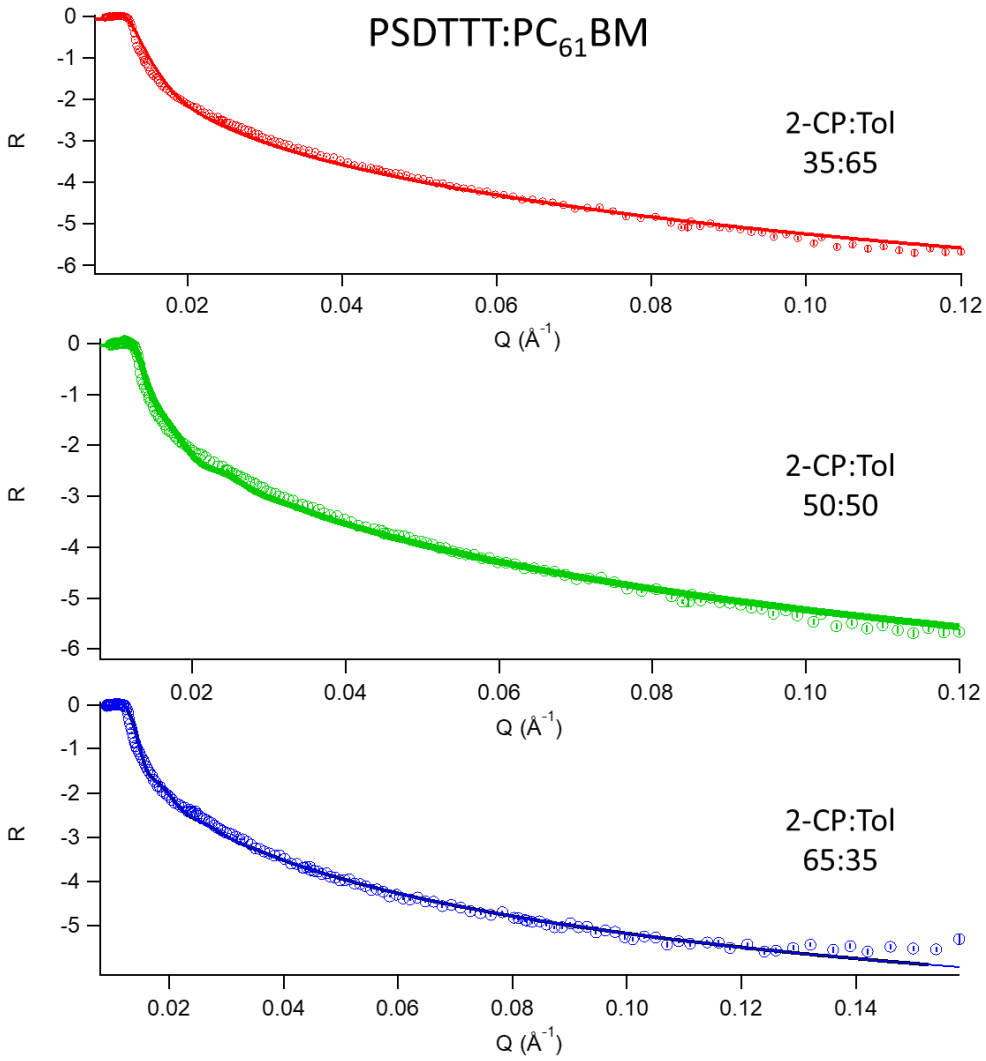

Figure B.4: Raw NR and corresponding fit for PSDTTT:$PC_{61}BM$ system.

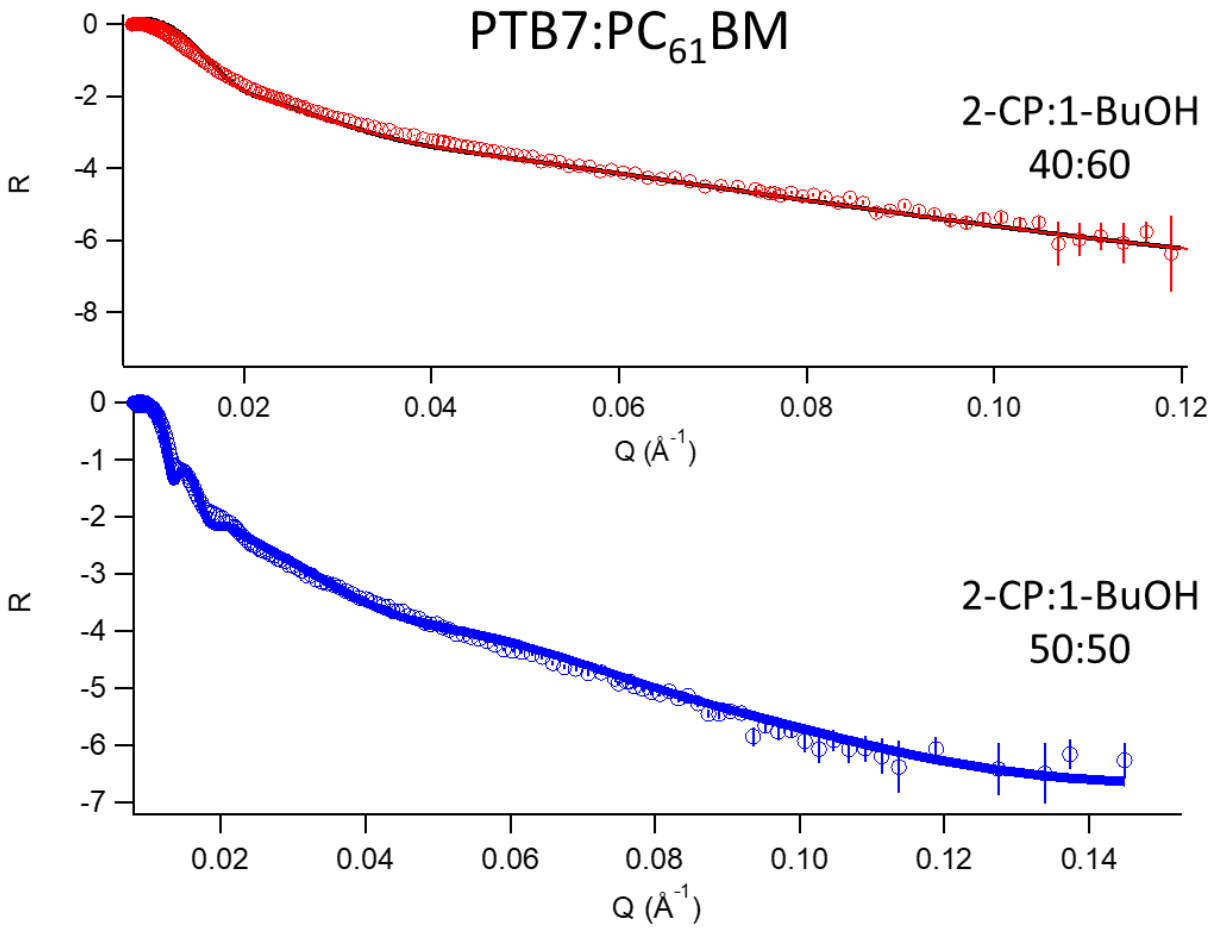

Figure B.5: Raw NR and corresponding fit for PTB7:$PC_{61}BM$ system.

Contact Angle Measurements. To evaluate the surface energies of the polymers and fullerene derivatives used in this study, we performed contact angle measurements on thin films of each pure organic material. We used two different liquids, water and ethylene glycol (EG), to obtain pairs of contact angles for each material, and then calculated the surface energy of each pure material using the Wu model:

$$\gamma_{\text{water}}(1+\cos\theta_{\text{water}}) = \frac{4\gamma^{\text{d}}_{\text{water}}\gamma^{\text{d}}}{\gamma^{\text{d}}_{\text{water}}+\gamma^{\text{d}}} + \frac{4\gamma^{\text{p}}_{\text{water}}\gamma^{\text{p}}}{\gamma^{\text{p}}_{\text{water}}+\gamma^{\text{p}}} \quad (1)$$

$$\gamma_{\text{EG}}(1+\cos\theta_{\text{EG}}) = \frac{4\gamma^{\text{d}}_{\text{EG}}\gamma^{\text{d}}}{\gamma^{\text{d}}_{\text{EG}}+\gamma^{\text{d}}} + \frac{4\gamma^{\text{p}}_{\text{EG}}\gamma^{\text{p}}}{\gamma^{\text{p}}_{\text{EG}}+\gamma^{\text{p}}} \quad (2)$$

$$\gamma^{\text{total}} = \gamma^{\text{d}} + \gamma^{p} \tag{3}$$

where θ is the droplet contact angle on the organic thin film; γ^{total} is the surface energy of the organic material, which is equal to the sum of dispersion (γ^{d}) and polarity (γ^{p}) components; γ_{i} is surface energy of the liquid droplet (water or EG); and $\gamma_{\text{i}}^{\text{d}}$ and $\gamma_{\text{i}}^{\text{p}}$ are the dispersion and polarity components of γ_{i}. The images used to measure the contact angles for both liquids on thin films of PTB7, PSDTTT, and PCBM are shown in Fig. B.7 The surface energies we determined from these angles using Eqs. (2)-(4) and literature values for γ_{water} and γ_{EG} (including their dispersion and polarity components)[61] are summarized in Table B.1.

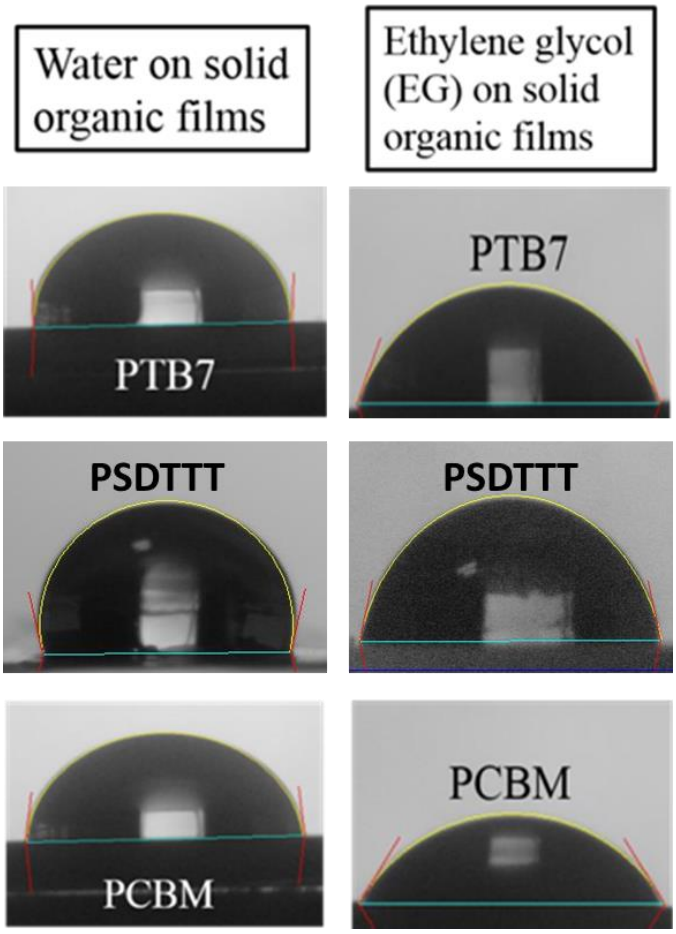

Figure B.6: Contact angle images for organic thin films with water and ethylene glycol.

Organic Layer	Contact Angle Water *(degree)*	Contact Angle EG *(degree)*	Surface Energy *(mJ/m^2)*
PTB7	92.7	66	26.1
PCBM	85.2	56.5	30.4
PSDTTT	102.9	75.6	22.4

Table B.1: Summary of measured contact angles and the calculated surface energies.

APPENDIX C. Supporting Information for Chapter 4

Materials & Sample Preparation

P3HT (Rieke Metals, Inc. Sepiolid P100) and F_4TCNQ (TCI Chemicals) were used as purchased. Glass substrates were cleaned by sequentially sonicating in water, acetone, and isopropanol. For SqP, P3HT films were spin coated at a rate of 1000 rpm for 60 s from a 20 mg/ml solution in ODCB, producing films that were ~110 nm thick. This was followed by a second spin-coating step where the P3HT film was infiltrated by a F_4TCNQ solution spin-coated on top of the dried P3HT film at 4000 rpm for 10 s. The solution for this second step was prepared by dissolving F_4TCNQ in DCM at 1 mg/ml and using the solution as-is or after serial dilution to produce the range of concentrations used. For higher-concentration 5 mg/ml F_4TCNQ solutions, we used a blend of 75:25 THF:DCM by volume as the solvent to increase the solubility of the dopant without dissolving the underlying P3HT film. For doped films prepared by the traditional blend-casting method, appropriate amounts of F_4TCNQ were added to the polymer solution to achieve the desired doping ratios while maintaining the P3HT concentration at 10 mg/ml in ODCB. Blend-cast solutions were also made using chloroform, but the quality of the resultant cast films was inferior to those prepared using ODCB, so details of the properties of these films were not included in the main text. We also attempted to improve the film quality of doped films prepared by the blend-cast method by diluting the doped solutions in excess amounts of solvent to help solubilize the material. However, this resulted in very thin films even at reduced spin speeds that hindered accurate electrical measurements (data not included).

Film thicknesses were measured using a Veeco Dektak 150 Profilometer. Not surprisingly, the measured thicknesses were dependent on the amount of dopant and the method used to dope the films. Surface roughness scans were measured using the profilometer over a lateral distance of 2 mm, leading to the average thickness and RMS roughness values quoted in the text.

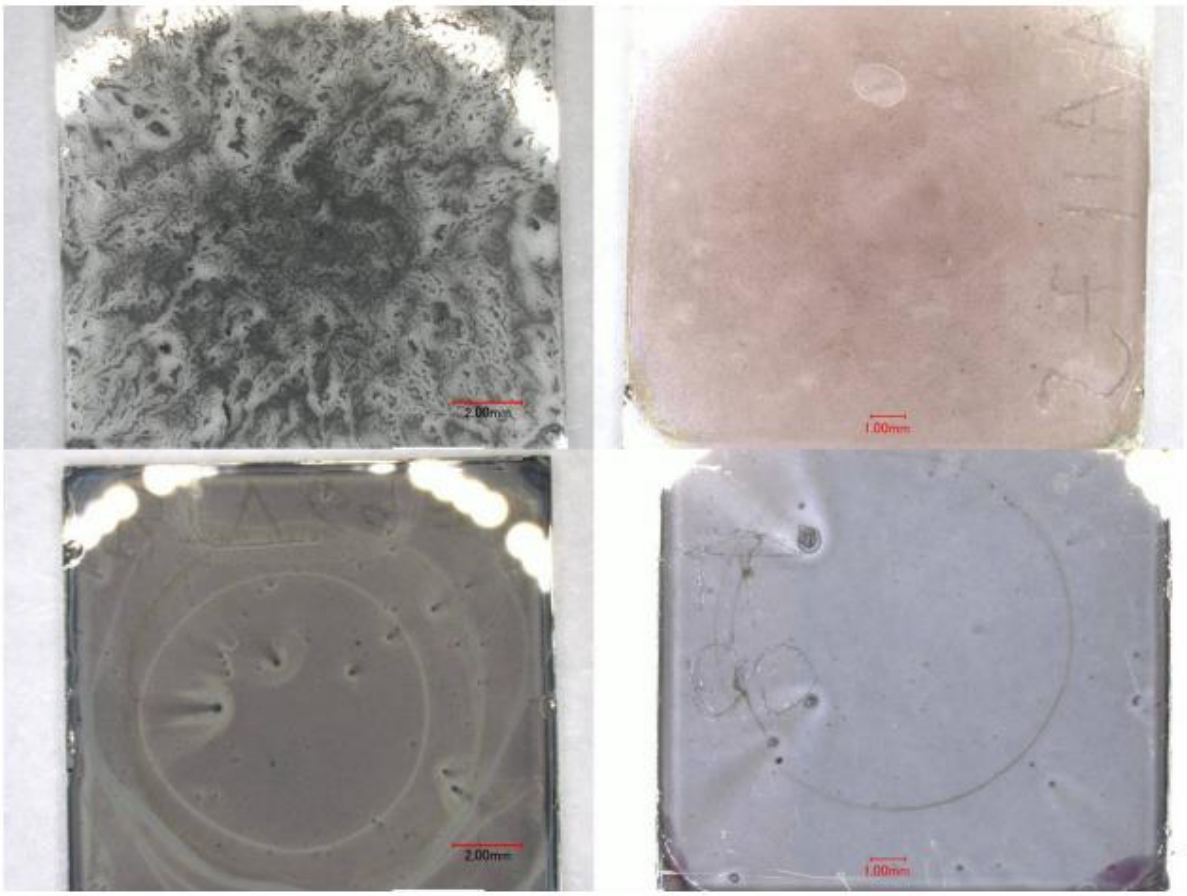

Figure C.1. Optical micrographs of highly-doped blend-cast (top left, scale bar 2 mm), low-doped blend-cast (top right, scale bar 1 mm), 5 mg/ml sequentially-processed doped (bottom left, scale bar 2 mm), and 1 mg/ml sequentially-processed doped (bottom right, scale bar 1 mm) F4TCNQ:P3HT films.

Optical microscopy images were taken using a VHX-1000 microscope, and as seen in Fig. C.1, the appearance of disorder in the blend-cast doped samples is obvious even on length scales visible by the naked eye. The faint appearance of the ring in these images is due to the spin coater chuck leaving a residue on the back side of the glass, and the scratches are labels etched into the back side of the glass substrate in order to identify the samples. The images presented in the main text are zoomed in over the central portion of those shown in Fig. C.1.

GIWAXS

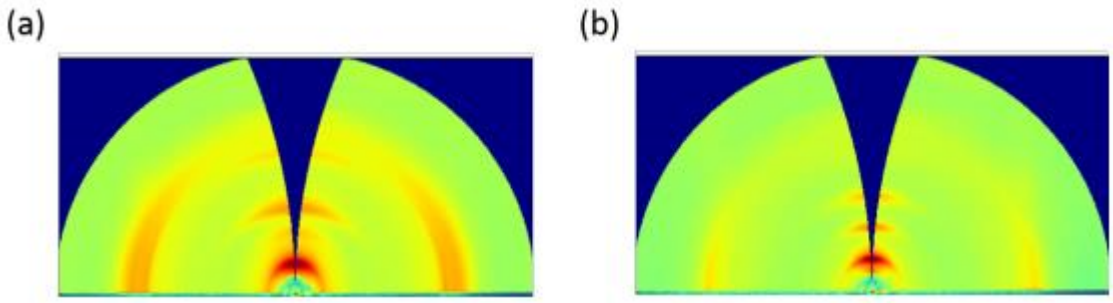

Figure C.2. GIWAXS Diffractograms of the 17 wt% BC doped (a) and 1 mg/ml SqP doped (b) P3HT films used in the main text. The removed wedges are to take into account the grazing incidence geometry. Slices of the true near-out-of-plane scattering and the approximate out-of-plane scattering shown in the main text are essentially identical.

The grazing incidence geometry has been taken into account to reveal the true, near-out-of-plane scattering as seen in Fig. C.2. The near-out-of-plane scattering is essentially identical to the out-of-plane scattering shown in the main text. Fully radially-integrated versions of the diffractograms for a variety of SqP and blend-cast F_4TCNQ P3HT films are shown in Figs. C.3 to C.5.

As seen in Fig. C.4, with increasing concentration of F_4TCNQ, the (100) peak shifts to progressively lower *q*, starting at 0.39 $Å^{-1}$ for pure P3HT (red curve) to 0.32 $Å^{-1}$ for both 17 wt% and 30 wt% blend-cast films (blue and pink curves, respectively). This is indicative of increased incorporation of F_4TCNQ between the P3HT side chains. As the F_4TCNQ concentration increases, new peaks also begin to grow in at 1.38 $Å^{-1}$ and 1.77 $Å^{-1}$, which are in the region of the (010) π-π stacking scattering. At higher concentrations (17 wt% and 30 wt%) a new peak in the π-π stacking region appears around 1.52 $Å^{-1}$, as discussed in the main text.

Fig. C.5 shows that with increasing concentration of F_4TCNQ used in the SqP method (concentrations given in mg/mL), the (100) peak also progressively shifts to lower q from 0.39 $Å^{-1}$ for pure P3HT (red curve) to 0.35 $Å^{-1}$ for the 1 mg/mL (pink curve) sequentially-processed doped film, again indicative of increased incorporation of F_4TCNQ between P3HT side chains. The appearance of the peak at 1.77 $Å^{-1}$ also occurs in the sequentially-processed doped films,

with the ratio of the 1.77 $Å^{-1}$ peak to the 1.67 $Å^{-1}$ peak being greater than seen in the blend-cast doped films.

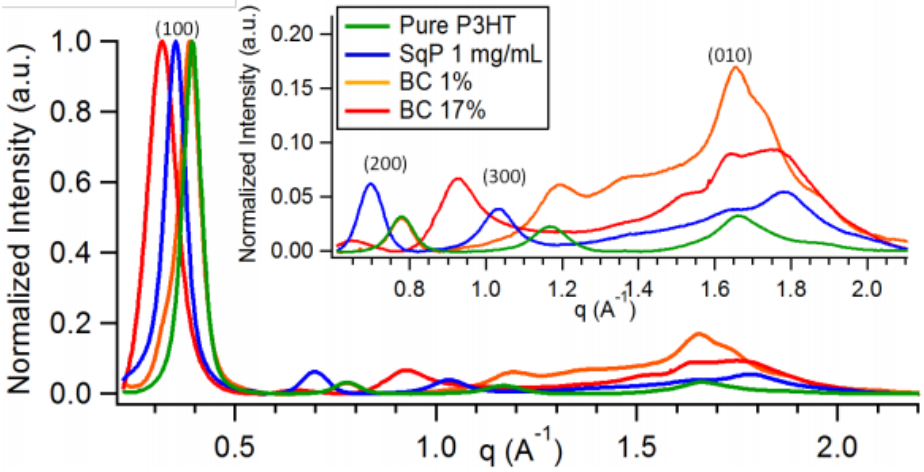

Figure C.3. Full radially-integrated 2-D grazing-incidence wide-angle X-ray scattering (GIWAXS) for films of F_4TCNQ-doped P3HT via the blend-casting method (1 wt% and 17 wt%, orange and red, respectively) and the SqP method (1 mg/mL, blue curves), as well as that for undoped P3HT (110-nm thick, green curves).

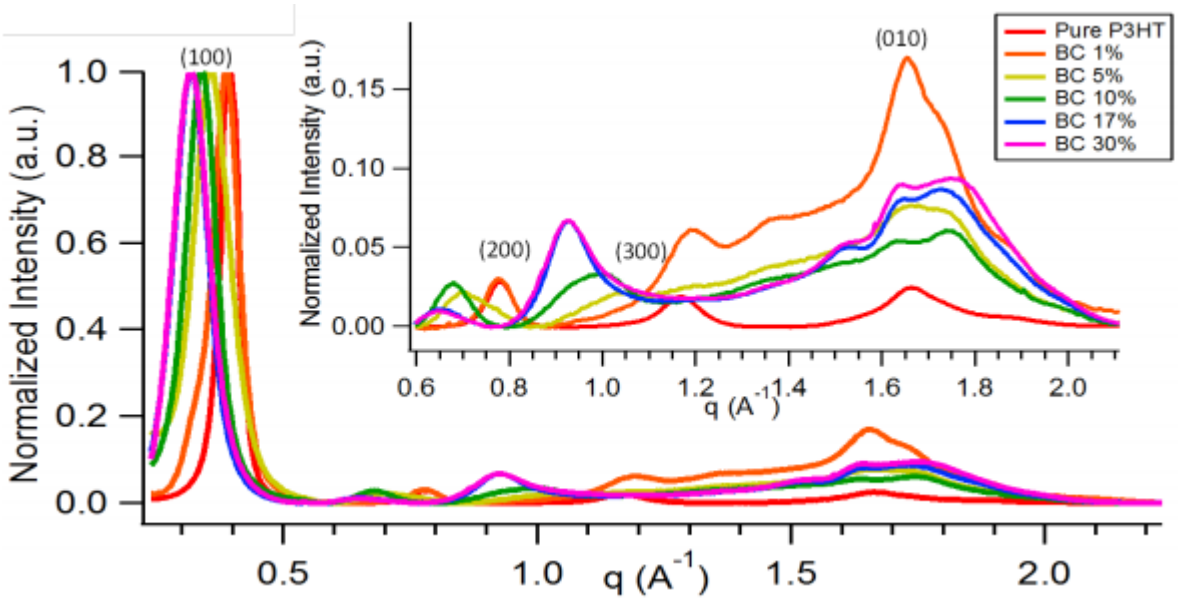

Figure C.4. Full radially integrated 2-D GIWAXS for blend-cast F_4TCNQ-doped P3HT films at varying concentrations of the dopant.

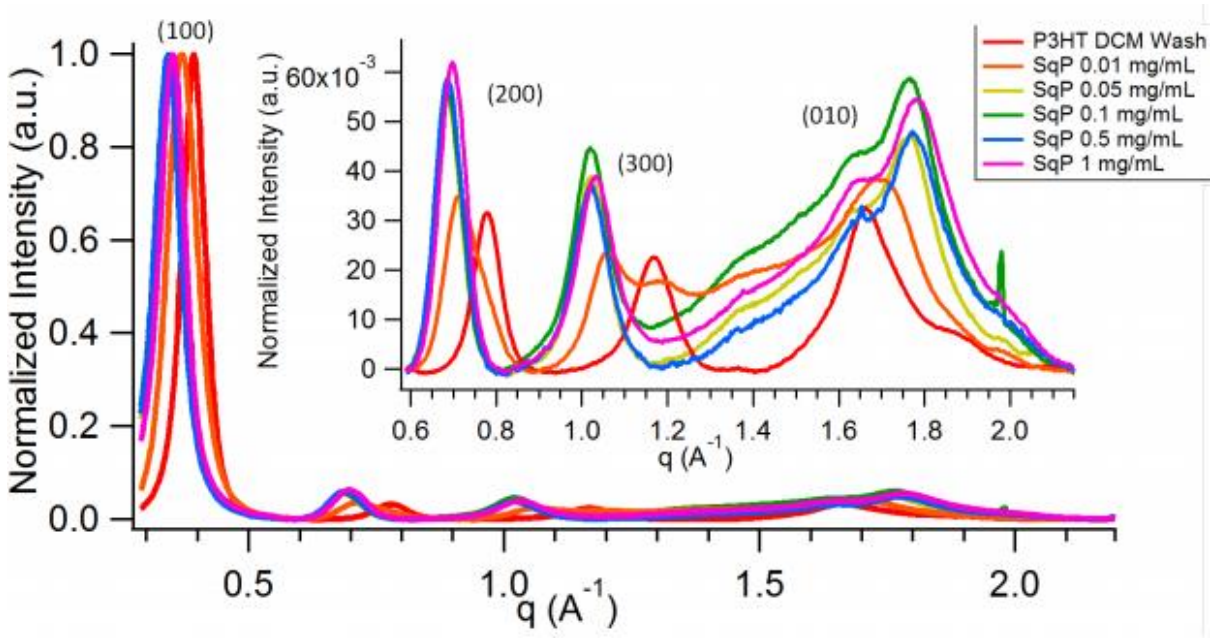

Figure C.5. Full radially integrated 2-D GIWAXS for F_4TCNQ-doped P3HT films prepared via SqP at varying dopant concentrations.

Conductivity Measurements

Collinear four-point probe measurements were performed using a custom made apparatus in ambient atmosphere using a Keithley 2400 Sourcemeter sourcing a DC current of 1-100 μA with a probe spacing of 2.5 mm. Conductivity measurements in the Van der Pauw geometry were also performed using a custom made apparatus in ambient atmosphere using a Keithley 2400 Sourcemeter where the max current sourced was held to 1 mW total power. The current was swept from negative to positive, rotated 90°, and repeated. The slope of the I–V curves were then fit to the Van der Pauw equation. Samples in the Van der Pauw geometry were prepared as described in main text, with silver paste applied at the corners of the film to act as contacts. All reported data was averaged over 10 simultaneous measurements for multiple samples. Due to the roughness and variability of the film thickness for the blend-cast films, we presented the measured sheet resistance values in Table 4.1 of the main text instead of conductivity values.

Analysis of the UV-Vis-NIR Absorption Spectrum

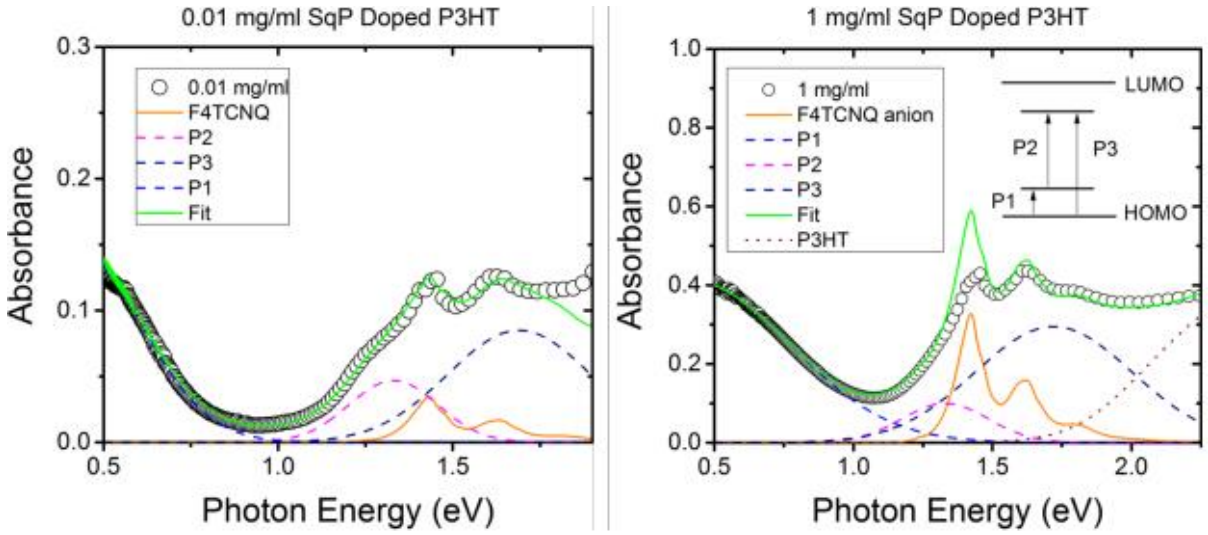

Figure C.6. Absorption fits for P3HT films doped by SqP method with 0.01 mg/ml F_4TCNQ (left) and 1 mg/ml F_4TCNQ (right).

To decompose the 0.01 mg/ml and 1 mg/ml doped spectra in Fig. C.6, we begin by first measuring the references spectrum for both the F_4TCNQ neutral and anion forms at known concentration in ODCB as a solvent as seen in Fig C.7. We were able to isolate the anion by adding in an excess of tetrabutylammonium iodide, molar ratio > 10:1, to reduce the F_4TCNQ. We then normalized the spectra to our film thickness and the concentration measured via the Hall effect, knowing that this is the minimum amount of anions necessary as the Hall effect only measures free carriers and there is a non-insignificant amount of trapped carriers and possibly bipolaronic species that would increase the number of anions present. Then we used previous assignments of the polaron peaks, in the area of interest between 0.5 and 2.25 eV to represent the P1 (blue dashed curve), P2 (pink dashed curve), and P3 (navy dashed curve) polaron absorption bands (see Fig. C.6 inset for origin of these peaks) and scaled accordingly to our higher doping amount. Finally, we used a reasonable sum of Gaussian bands representing the red-edge (aggregate portion) of the neutral, undoped P3HT absorption (dotted maroon curve). The exact peak positions and FWHM we used for the polaron peaks are as follows: 0.4 eV and 0.5 eV for P1, 1.33 eV and 0.22 eV for P2, and 1.72 eV and 0.4 eV for P3 for the 1 mg/ml sample, and 0.42 eV and 0.27 eV for P1, 1.33 eV and 0.18 eV for P2, and 1.69 eV and 0.29 eV

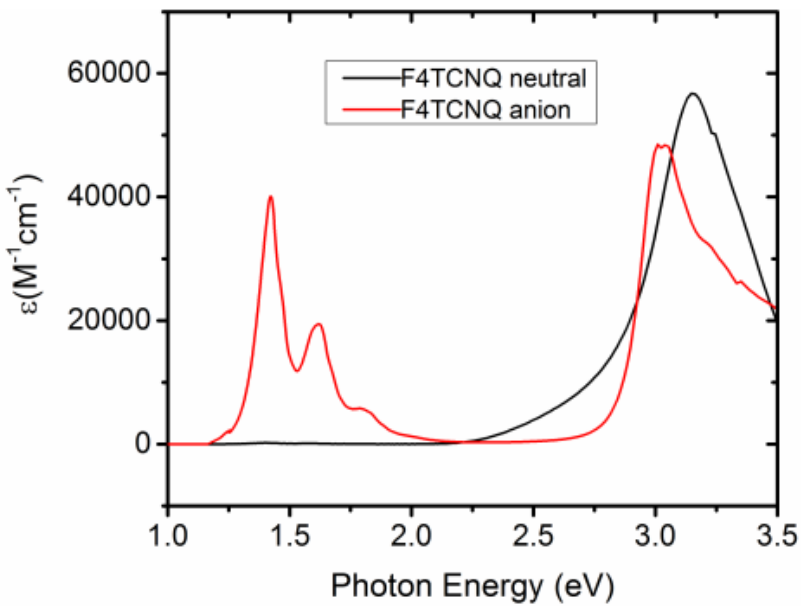

Figure C.7. Reference spectrum of F_4TCNQ neutral (black curve) and anion (red curve) taken in solution state dissolved in ODCB.

for P3 for the 0.01 mg/ml sample. The resulting combination of the polaron, anion, and neutral P3HT curves gives the fit (green solid curve) that is overlayed on top of the 0.01 mg/ml (left panel) and 1 mg/ml (right panel) SqP doped film absorptions (black open circles).

For the high dopant concentration, there is an obvious disagreement in the region of peak absorbance for the F_4TCNQ anion, with the spectral shape being fairly close, but the intensity being much too large to match the experimental spectrum of the doped film. As mentioned previously, since the carrier concentration measured by the Hall effect only takes into account the mobile carriers, the anion concentration would realistically need to be scaled even higher to account for any carriers that absorb but are trapped, or that formed bipolarons. We attribute this mismatch to the fact that the cross-section of the F_4TCNQ anion must be lower in this particular environment, and the solution phase cross-section is not applicable at these high dopant concentrations. To get the fit to reasonable agreement, the extinction coefficient or carrier concentration must be lowered at least by a factor of 2. Without a reasonable cross-section to use, the fit becomes largely invalid for the purposes of extracting extinction

coefficients and comparing the amount of free carriers relative to trapped carriers due to the large error. For the low dopant concentrations, when we scale the anion cross-section by just the free carrier amount the absorption is unidentifiable. For the fit in the left panel of Fig. C.6, the anion concentration used was 3 orders of magnitude higher than the free-carrier concentration, in good agreement with previous work claiming a the majority of carriers are trapped at low doping ratios. While this result is in much better agreement with previous work, the discrepancy in the cross-section between low and high doping amounts discourages any attempt to extract meaningful carrier concentrations from fitting absorption spectra. Based on these findings, we chose not to include any analysis of the total carrier concentrations or absorption cross-sections of the carriers at low or high dopant amounts in the main text. All absorption measurements were performed using a Shimadzu UV-3101PC UV-VIS-NIR Scanning Spectrophotometer and a Perkin Elmer Lambda 25 Spectrometer.

Temperature Dependence of F_4TCNQ doping of P3HT

As shown in Fig. C.8, after heating F_4TCNQ-doped P3HT films to ~90°C, the absorption peaks corresponding to the F_4TCNQ anion and P3HT polaron begin to decrease and eventually disappear. The inset in Fig. C.8 is expanded around the anion absorption region for clarity. The return of the neutral P3HT absorption near 500 nm (and shoulder near 600 nm) upon heating is also readily visible upon heating. There was no return of the anion or polaron peaks even after several hours had passed, suggesting an irreversible de-doping of the films upon heating. As mentioned in the main text, similar de-doping of blend solutions of these materials also has been observed with increased temperature.

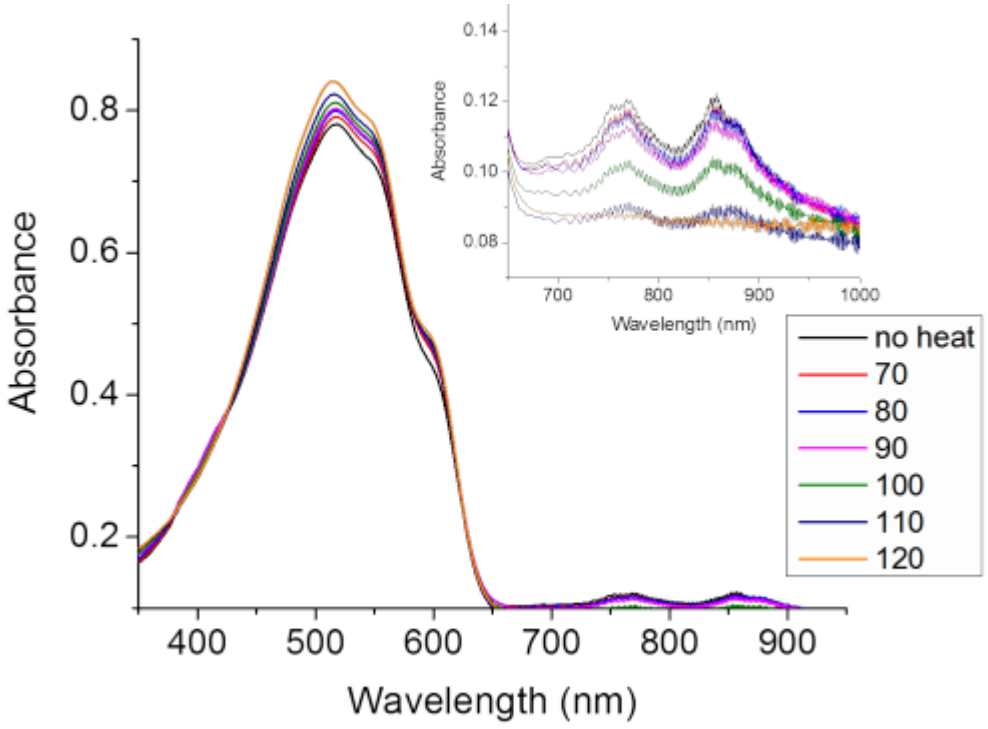

Figure C.8. Temperature dependence of the absorption spectrum of modestly-doped P3HT films after mild heating for 10 min. The samples were packaged in an argon atmosphere and then raised to the appropriate temperature for 10 min, removed, and allowed to cool prior to the measurements.

Hall Effect Measurements

An AC field hall method was used to accurately measure carrier concentration and mobility for these low mobility doped P3HT samples. The AC field technique provides effectual measurements because the method can distinguish the hall voltage signal form unwanted background signal, as the DC field hall effect measurements proved ineffective. The samples were measured using AC field Hall method using the Lake Shore model 8407 system with an AC field amplitude of 1.2T RMS. The 0.01 mg/ml sample used a current of 10 nanoamps, 0.1 mg/ml used 10 μA, and both 1 mg/ml and 5 mg/ml used 100 μA of current. Current reversal was used to remove the thermal electric voltages and the inductive pickup voltages. The 0.01 mg/ml sample was measured 167 times over 24 hours, the 0.1 mg/ml samples was measured 287 times over 36 hours, and the 1 mg/ml and 5 mg/ml samples were measured 81 times each over 10

hours. The data from the AC field hall measurement can be found below in Table C.1. The associated errors for the mean values are ~80% for 0.01 mg/ml, ~20% for 0.1 mg/ml, ~20% for 1 mg/ml, and ~7% for the 5 mg/ml sample. The mean conductivity of the 5 mg/ml sample is significantly lower than what we measured, and we attribute this to a slight sample degradation of the doped films before and during measurement, so the data for this particular concentration is not included in the main text.

	V_H (μV)	R_H (cm^3/C)	n ($1/cm^3$)	ρ (Ωcm)	μ (cm^2/Vs)	Type (P or N)
0.01 mg/ml	2.02	19.3313	4.254E16	5876	0.0033	P
0.1 mg/ml	1.51	0.0135	2.432E20	2.02	0.0067	P
1 mg/ml	15.28	0.0154	4.308E20	0.638	0.0241	P
5 mg/ml	12.31	0.0130	5.971E20	0.5731	0.0226	P

Table C.1. Summary of results of the mean values of the hall voltage (V_H), hall coefficient (R_H), carrier concentration (n), resistivity (ρ), mobility (μ), and carrier type (P for holes, N for electrons) from AC field Hall effect measurements on SqP doped P3HT thin films with various concentrations of F_4TCNQ casting solvent.

APPENDIX D. Supporting Information for Chapter 5

Materials, Synthesis, and Characterization

The poly(3-hexylthiophene-2,5-diyl) (P3HT) material used in preparation of the thin films denoted "CF-cast" and "ODCB-cast" in the main text was purchased from Rieke Metals, and was used without further alterations.

The P3HT material denoted "100% RR P3HT" in the main text was synthesized under inert atmosphere per a literature procedure as follows. To a Schlenk flask, 1,3-bis(diphenylphosphino)propane (6.2 mg, 0.015 mmol) and Chloro(tolyl)(PPh_3)$_2$Nickel(II) (7.5 mg, 0.01 mmol) were added, then dried under high-vacuum for 1 h. Following drying, anhydrous THF (3 mL) was added, allowing for ligand exchange and the formation of the catalyst. Another Schlenk flask was charged with 2-bromo-3-hexyl-5-iodothiophene (0.216 mL, 1 mmol). The starting material was dried under high-vacuum, then anhydrous THF (9.5 mL) was added. The monomer was synthesized by the addition of *i*-PrMgCl (0.45 mL, 0.95 mmol, 2 M in THF) under nitrogen at 0 °C, then stirring at room temperature (RT) for 1 h. The monomer solution was added to the catalyst solution, and allowed to stir for 1 h at RT. The reaction mixture was then quenched with HCl (1 mL, 5 M in H_2O), resulting in a toluene/H-capped P3HT. The resultant polymer was precipitated by the addition of MeOH (50 mL), and the precipitate was collected by vacuum filtration. Soxhlet extractions was performed on the polymer, using MeOH and acetone to remove impurities and P3HT oligomers. A final Soxhlet using $CHCl_3$ was performed to collect the polymer and remove any residual catalyst. The $CHCl_3$ was removed, then the P3HT was dissolved in THF and again precipitated into MeOH, and collected via filtration.

NMR (see Fig. D.1) was used to determine polymer number average molecular weight via end-group analysis, yielding a final degree of polymerization of 105 (Mn = 17.4 kg/mol). Polymer

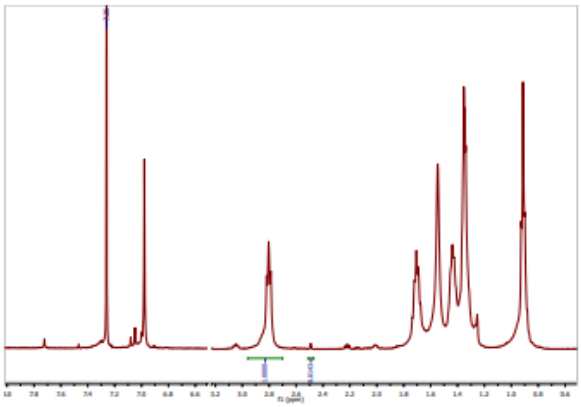

Figure D.1. ^{1}H NMR spectrum of synthesized 100% RR P3HT batch.

regioregularity was determined by analysis of the ratio of integrations comparing head-tail couplings with head-head and tail-tail couplings, showing a 100% RR polymer. ^{1}H NMR Shifts: δ 7.43 (m, 2H), 7.24 (m, 2H), 6.98 (s, 1H), 2.80 (t, 2H (2H between the peaks at 2.8 and 2.61), J = 7.7 Hz), 2.61 (t, 2H (2H between the peaks at 2.8 and 2.61), J = 7.6), 2.49 (s, 3H) 1.71 (quint, 2H, J = 7.6 Hz), 1.48-1.38 (m, 2H), 1.37-1.30 (m, 4H), 0.91 (t, 3H, J = 7.2 Hz).

^{1}H NMR spectra were obtained on a Bruker AV-500 spectrometer using $CDCl_3$ as a solvent. Bis(triphenylphosphine)nickel(II) dichloride, 1,3-bis(diphenylphosphino)propane, and isopropyl magnesium chloride (*i*-PrMgCl) (2 M in tetrahydrofuran (THF)) were purchased from Sigma Aldrich and used without further purification. 2-Bromo-3-hexyl-5-iodothiophene was purchased from Fisher and passed through a short silica column to remove the copper stabilizer before use. THF was dried with a solvent drying system by Innovative Technologies.

Film Preparation

All substrates were cleaned by sequentially sonicating in soapy water, DI water, acetone, and isopropanol for 5-10 minutes each, then placed under rough vacuum to remove all traces of residual solvent, and finally transferred into a nitrogen glove box for use.

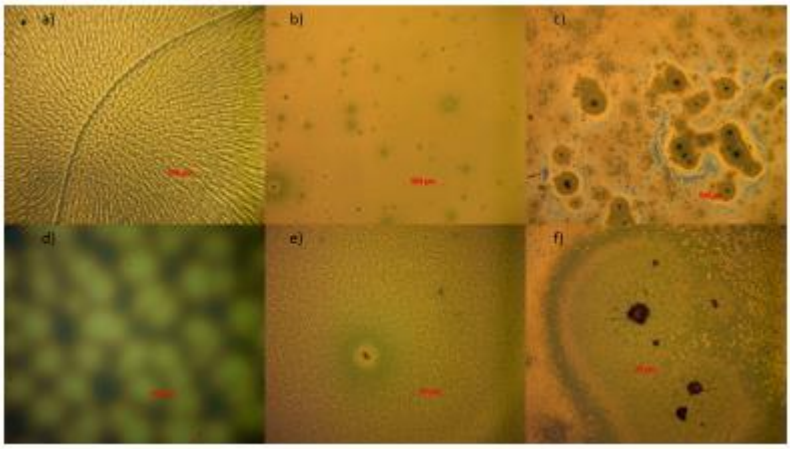

Figure D.2. Optical microscope images of P3HT films prepared as follows: a,d) cast from CF, b,e) cast from ODCB, c,f) 100%-RR P3HT cast from ODCB. Magnifications are 5x for the images in the top row and 50x for those in the bottom row.

The films cast from chloroform were dissolved in chloroform at a concentration of 10 mg/mL and spin cast at 1000 rpm for 60 seconds. These films were dry upon removal from the spin coater. The films cast from ODCB (both the Rieke and the in-house synthesized 100% RR) were dissolved in ODCB at a concentration of 20 mg/mL and spin cast at 1160 rpm for 20 seconds, then 3000 rpm for 1 second. This allowed for even distribution of the polymer on the substrate and removal of excess solution while leaving the film still wet. These films were then removed and placed immediately in a small glass petri dish with a lid placed over the top. This allowed for a solvent saturated environment and slower drying time of the P3HT films. Films prepared in this way were imaged using an optical microscope and the results are shown in Fig. D.2. The films were visibly different by eye, and upon closer inspection we saw what appeared to be crystallites or aggregates in the more crystalline films. The CF-cast film (Fig. D.2 a,d) appeared wavy due to the rapid drying time but devoid of any crystallite-type features. The ODCB-cast film (Fig. D.2 b,e) had crystallite features, but these were smaller and less numerous than those seen in the 100%-RR P3HT films (Fig. D.2c,f).

GIWAXS

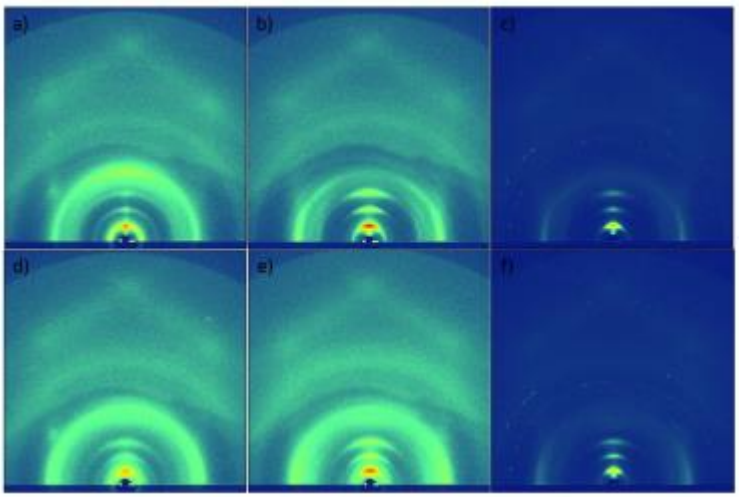

Figure D.3. Intensity color mapped GIWAXS diffractograms for CF-cast P3HT washed with DCM a), ODCB-cast P3HT washed with DCM b), 100%-RR P3HT washed with DCM c), CF-cast P3HT SqP doped with 1 mg/mL F_4TCNQ in DCM d), ODCB-cast P3HT SqP doped with 1 mg/mL F_4TCNQ in DCM e), and 100%-RR P3HT SqP doped with 1 mg/mL F_4TCNQ in DCM f).

2-D grazing incidence wide angle X-ray scattering (GIWAXS) experiments were performed at the Stanford Synchrotron Radiation Lightsource on beamline 11-3 using a wavelength of 0.9742 Å with an incidence angle of 0.12°. Fig. D.3 shows the full 2-D diffractograms of our different polymer systems. These diffractograms were radially integrated to obtain the diffraction patterns (0-10° for in-plane, 70-80° for out-of-plane, and 0-180° for full) shown in the main text. The 2-D images were collected on a plate with the detector 250 mm away from the center of the measured sample. The beam spot had a width of ~150 μm and a helium chamber was used to reduce the noise. The software package WxDiff was used to reduce the GIWAXS data and subsequent analysis was performed in IgorPro.

Ellipsometry

To study polymer swelling, spectroscopic ellipsometry was performed on a PS-1000 instrument from Semilab at room temperature. A UV-visible CCD detector adapted to a grating spectrograph analyzes the signal reflected by the sample. The light source is a 75 W Hamamatsu Xenon lamp. For these measurements only, the various P3HT films were spun onto Si substrates

with a thin (~2 nm) native oxide layer, and the samples were then placed in a glass container custom-designed to contain the vapor of a solvent (i.e., dichloromethane, DCM) around the sample while still allowing unencumbered access and egress of the optical beams. The film thickness is monitored until it reaches steady state while being exposed to DCM vapor in the container. With a series of calibration measurements, we found that the partial pressure of DCM solvent in the container reached 90% of the known room-temperature vapor pressure of DCM. Data analysis was performed using the associated SEA software. The thickness was obtained by fitting only the 600-1000 nm spectral region (to avoid the excitonic P3HT absorption of the films) using the Cauchy model. For quantitative analysis, the Bruggemann effective medium approximation (EMA) was applied to experimentally determine the refractive index of the binary polymer/solvent mixture using the known refractive indices of the pure film and solvent. We measured the refractive index as a function of wavelength for each P3HT film of different crystallinity prior to DCM exposure. When used for the EMA along with the refractive index of DCM, the volume fraction of P3HT and DCM become quantifiable in the swelled P3HT film, yielding the values reported in the main text.

Spectroscopy

The UV-vis absorption data were acquired from 3.5-0.5 eV using a Shimadzu UV3101PC UV-VIS-NIR Scanning Spectrophotometer for films prepared independently on both glass substrates and a KBr plate. FTIR data was acquired for films prepared on KBr plates using a Jasco FT/IR-420 spectrometer from 220-7000 cm^{-1} in transmittance mode, which was subsequently converted to absorbance. Figure D.4 shows the raw FTIR data, including the general lack of absorption for all of the undoped samples. In order to smooth some of the sharp neutral polymer vibrational peaks, we used the difference spectrum of the doped and pure samples for the IR data. Both the UV-Vis-NIR data and the IR data were first normalized to each other at ~0.5 eV to account

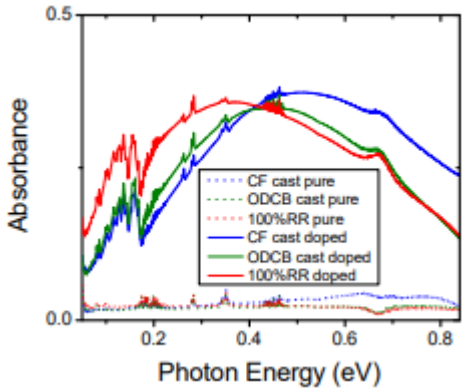

Figure D.4. FTIR absorbance data for P3HT films prepared as follows: undoped films of CF-cast (blue dots), ODCB-cast (green dots), 100%-RR P3HT (red dots), as well as F_4TCNQ-doped films of CF-cast (blue curve), ODCB-cast (red curve), and 100%-RR P3HT (red curve).

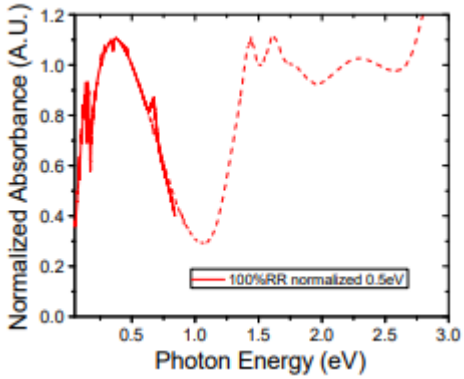

Figure D.5. Combined FTIR and UV-vis-NIR data, normalized at 0.5 eV, for the 100%-RR P3HT SqP-doped with 1 mg/mL F_4TCNQ in DCM. The solid line is the FTIR portion of the data and the dashed line shows the UV-Vis-NIR portion of the data.

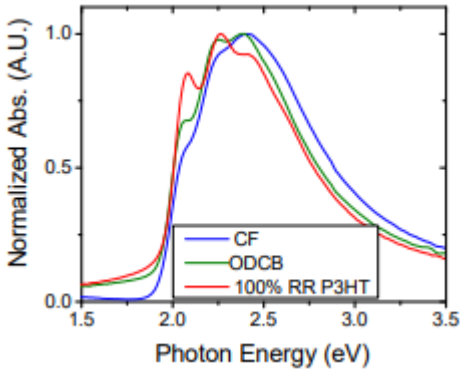

Figure D.6. Normalized absorbance of neutral P3HT cast from chloroform (red) and ODCB (black), and 100% regioregular P3HT cast from ODCB (blue).

for a slightly decreased intensity of the signal of the IR measurement at the high energy edge

of the detector, as seen in Fig. D.5 for the 100% RR P3HT sample. The resulting curves were then renormalized to the P1 polaron peak intensity to allow for easier comparison of spectral shifts, resulting in the figure in the main text.

Aggregation Model Fits for Neutral P3HT Films with Different Crystallinity

It is well known that the optical absorption of P3HT films is highly sensitive to the degree of crystallinity. Figure D.6 shows that the absorption spectrum of the pristine ODCB-cast commercial P3HT film (black curve) is red-shifted relative to the CF-cast film (red curve) and also shows an increase in the amplitude of the vibronic feature located near 2.0 eV; these features are associated with a higher degree of molecular ordering in the ODCB-cast film. These features are even further enhanced in the pristine 100%-RR P3HT film (blue curve), indicating an even higher degree of order. We can quantify the degree of order in our pristine P3HT films using the ratio of the amplitudes of low-energy 0-0 to higher-energy 0-1 vibronic features using the model developed by Spano. With this ratio, Spano's model gives the bandwidth W of the P3HT exciton by:

$$\frac{A_{0-0}}{A_{0-1}} = \left(\frac{1 - 0.24W/\omega_0}{1 + 0.073W/\omega_0} \right)^2 \qquad \text{(D.1)}$$

where ω_0 = 1400 cm^{-1} = 0.174 eV is the frequency of the P3HT C=C stretch that is displaced upon excitation. In this model, an increase in the 0-0 to 0-1 ratio corresponds to an increase in J-aggregate-like character with a more planarized backbone and increased conjugation length, resulting in a decreased exciton bandwidth. For our three pristine P3HT films, *W* changes from 0.135 eV for the CF-cast and 0.11 eV for the ODCB-cast commercial material to 0.044 eV for the 100% RR P3HT film.

With the fitted values of W in hand, we can then model the ordered portion of the full absorption spectrum, A, by:

$$A \propto \sum_{m=0} \left(\frac{e^{-\lambda}\lambda^{m}}{m!} \right) \left(1 - \frac{We^{-\lambda}}{2\omega_{\circ}} \sum_{n \neq m} \frac{\lambda^{n}}{n!\,(n-m)} \right)^{2} e^{-\left(\frac{(\hbar\omega - E_{0\text{-}0} - m\hbar\omega_{\circ})^{2}}{2\sigma^{2}} \right)} \tag{D.2}$$

where λ is the Huang-Rhys factor, which as is conventional with P3HT we set equal to 1.0, ω_0 is the same intramolecular vibration energy used in Eq. (D.1), E0-0 is the 0–0 transition energy, σ is the width of the vibronic transition, and n and m are the vibrational level quantum numbers. Eq. (D.2) was used to fit the aggregate portion of the experimental absorption spectrum. The amorphous contribution was simply the difference between the total film absorption and the aggregate contribution. The total absorbance of the films as well as the fits are included in Fig. D.7 a-c). In order to account for differences in oscillator strength, we then weighted the aggregate and amorphous contributions to absorbance by multiplying the intensity at each energy by the corresponding photon energy used to excite and the results are in Fig. D.7 d-f). Once properly weighted, the aggregate and amorphous contributions were independently integrated from 1.75 eV to 3.5 eV. The ratio of these two numbers relative to the total contribution gives the % aggregates and % amorphous content reported in the main text in good agreement with previous results on similar films.

Model Fits for Doped P3HT with Anions

In our analysis of the mid-IR polaron absorption spectrum of doped P3HT π-stacks in the presence of F_4TCNQ dopants, we utilize the Holstein molecular crystal Hamiltonian. Here, each thiophene HOMO is coupled to neighboring thiophene HOMO's within a given polymer chain through the hole transfer integral t_{intra}. Interchain coupling between nearest neighbors across adjacent chains is dictated by t_{inter}. The Hamiltonian includes spatially uncorrelated ("short-

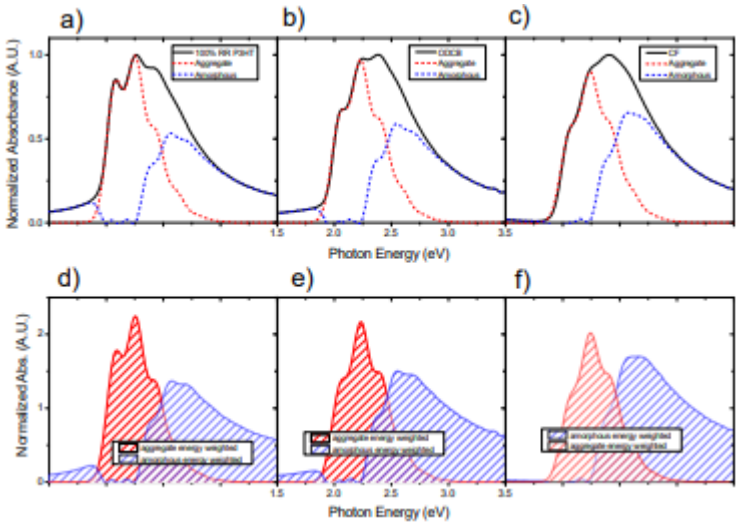

Figure D.7. Normalized experimental absorption data (black curves) and aggregate (red dashed curves) and amorphous (blue dashed curves) contributions for 100%-RR P3HT a), ODCB-cast P3HT b), and CF-cast P3HT c). The fits were then weighted by the photon energy to account for differences in oscillator strength, as replotted in panels d-f).

range") site-energy deviations due to structural/torsional disorder, chemical defects, inhomogenous electric fields, and the presence of dopants. The F_4TCNQ^- anion is considered to be a point change ($-e$) displaced at a distance danion from the center of the first 10mer polythiophene chain within a π-stack. (see Fig. 4.4(c) in the main text). The point charge interacts Coulombically with the hole, partially localizing it over several nearby thiophene units. The Hamiltonian for a disordered π-stack containing M N-mer chains is given by,

$$H = H_\circ + H_{\text{dis}} + H_{\text{dopant}} \tag{D.3}$$

where H_0 is given by,

$$H_\circ = \sum_{m=1}^{N-1}\sum_{n=1}^{M} t_{\text{intra}}\{d^\dagger_{m+1,n}d_{m,n} + h.c.\} + \sum_{m=1}^{N}\sum_{n=1}^{M-1} t_{\text{inter}}\{d^\dagger_{m,n+1}d_{m,n} + h.c.\}$$
$$+ \hbar\omega_{\text{vib}}\sum_{m=1}^{N}\sum_{n=1}^{M} b^\dagger_{m,n}b_{m,n} + \hbar\omega_{\text{vib}}\sum_{m=1}^{N}\sum_{n=1}^{M}\{\lambda(b^\dagger_{m,n} + b_{m,n}) + \lambda^2\}d^\dagger_{m,n}d_{m,n} \tag{D.4}$$

Here, h.c. refers to Hermitian conjugate. The operators $d^{\dagger}_{m,n}(d_{m,n})$ create (annihilate) a hole on the *m*th thiophene unit of the $_n$th chain. The first two terms represent electronic energy with t_{intra} and t_{inter} taken to be −0.40 eV and −0.15 eV, respectively, consistent with DFT calculations. The last term accounts for the local vibronic coupling involving the symmetric aromatic/quinoidal vibrational stretching mode with energy ($\hbar\omega_{vib}$) equal to 0.17 eV. The Huang-Rhys factor, which is a measure of the vibronic coupling, is set to λ^2= 1. The operators $b^{\dagger}_{m,n}$ ($b_{m,n}$) create (annihilate) a vibrational quanta on the *m*th thiophene unit of the *n*th chain. The disorder (H_{dis}) and dopant (H_{dopant}) terms in Eq. (D.3) are respectively given by:

$$H_{\text{dis}} = \sum_{m=1}^{N}\sum_{n=1}^{M} \Delta E_{m,n} d^{\dagger}_{m,n} d_{m,n} \tag{D.5}$$

and

$$H_{\text{dopant}} = \sum_{m=1}^{N}\sum_{n=1}^{M} \frac{-e^2}{4\pi\varepsilon_{\circ}\varepsilon|\mathbf{r}_{m,n} - \mathbf{r}_{\text{anion}}|} d^{\dagger}_{m,n} d_{m,n} \tag{D.6}$$

$\Delta E_{m,n}$ in Eq. (D.5) refers to random fluctuations in the energy of a hole located at (m,n). $\Delta E_{m,n}$ is selected randomly from a Gaussian distribution with a standard deviation σ:

$$P(\Delta E_{m,n}) = (2\pi\sigma^2)^{-\frac{1}{2}} exp(-\frac{\Delta E^2_{m,n}}{2\sigma^2}) \tag{D.7}$$

with no spatial correlation. In previous simulations for undoped P3HT aggregates, a value of σ = 0.3 eV reproduced the measured line width of the mid-IR spectrum. In Eq. (D.6), the distance of the dopant anion from the *m*th thiophene unit of the *n*th chain is given by $|r_{m,n}-r_{anion}|$. Here, $r_{m,n}$ is the position vector for the *m*th thiophene ring on the *n*th chain, assuming a nearest neighbor separation of 0.40 nm between thiophene rings along a chain, and a separation

between adjacent chains within a π-stack of 0.40 nm. r_{anion} is the position vector of the dopant anion. In Eq. (D.6), ε_0 is the vacuum permittivity and ε is (unit-less) relative permittivity. In all calculations to follow we use a relative permittivity of ε = 1, 2, or 3 as well as a distance-dependent dielectric constant given by,

$$\varepsilon(r_{ij}) = \varepsilon_r - (\varepsilon_r - 1)exp^{-sr_{ij}}(1 + sr_{ij} + (sr_{ij})^2/2) \tag{D.8}$$

where r_{ij} is the distance between the positive and negative charges in Å and the bulk dielectric constant ε_r and the parameter s are set to 3.0 and 0.3 $Å^{-1}$ respectively. The distance dependence accounts for the reduced dielectric screening for cation/anion separations less than approximately 1 nm (i.e., distances where the molecular nature of the medium is important and the continuum approximation breaks down).

Analogous to neutral excitons, the single hole basis set used to represent the Hamiltonian in Eq. (D.3) is truncated to include all one- and two-particle excitations. Such a basis set has been very successful in reproducing the mid-IR line shapes measured by Chang *et al*. The polarized absorption spectrum is evaluated using the following expression:

$$A_j(\omega) = \left\langle \sum_{ex} f_j^{ex} W_{LS}[\hbar\omega - (E_{ex} - E_G)] \right\rangle_c \tag{D.9}$$

where, the index j (= x,y) indicates the polarization, with x lying along a polymer chain and y lying along the aggregate (interchain) axis. The sum in Eq. (D.9) is over all the polaron excited states and $\langle \ldots \rangle_c$ represents an average over many site-energy disorder configurations (typically several thousand). W_{LS} is the homogenous line shape function taken to be a narrow Gaussian with a standard deviation of 0.045 eV (much less than σ = 0.3 eV). The oscillator strength, f_j^{ex} in Eq. (D.9), which involves the j-polarized transition from the polaron ground state, ψG to the higher excited state, ψex, is given by:

$$f_j^{ex} = \frac{2m_e}{3e^2\hbar^2}(E_{ex} - E_G)|\langle \psi_G|\hat{\mu}_j|\psi_{ex}\rangle|^2, \tag{D.10}$$

where

$$\hat{\mu} = e\sum_{m,n} \mathbf{r}_{m,n} d^{\dagger}_{m,n} d_{m,n} \tag{D.11}$$

is the dipole moment vector.

The calculated mid-IR absorption spectrum as a function of anion distance in the π-stacking direction from an oxidized P3HT dimer containing two 10-mer chains is shown in Fig. 5.4 of the main text. The stack was parameterized as follows: t_{intra} = −0.4 eV, t_{inter} = −0.15 eV, ε = ε(r_{ij}), $\hbar\omega_{vib}$ = 0.17 eV, and λ^2 = 1. Disorder along and across chains is uncorrelated – the SS model– and distributed according to a Gaussian of width 0.3 eV. We have determined (not shown) that the presence of a third chain leads to only small changes in the absorption spectra.

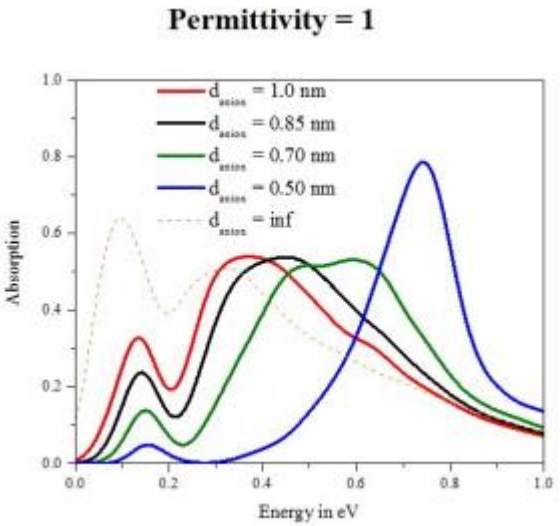

Figure D.8. The calculated absorption spectrum of a P3HT hole within a chain containing 10 thiophene rings with an anion placed next to a π-stack at various distances, d_{anion}, from the chain center. The Hamiltonian in Eq. (D.3) was parameterized in a manner similar to the figure in the main text, with the only difference being ε = 1.(t_{intra} = −0.4 eV, t_{inter} = −0.15 eV, ε = ε(r_{ij}), $\hbar\omega_{vib}$ = 0.17 eV, and λ^2 = 1)

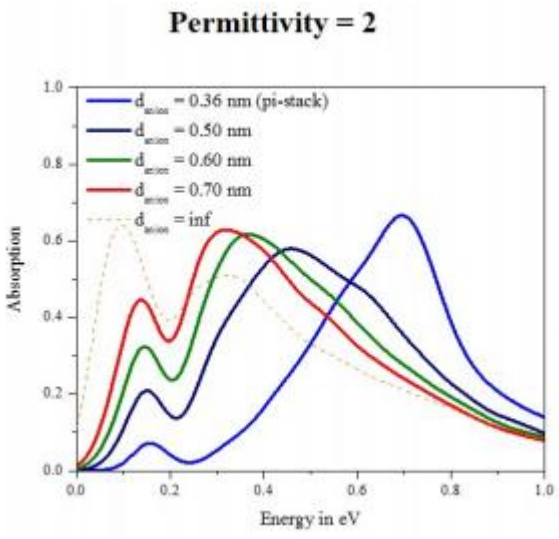

Figure D.9. The calculated absorption spectrum of a P3HT hole within a chain containing 10 thiophene rings with an anion placed next to a π-stack at various distances, d_{anion}, from the chain center. The Hamiltonian in Eq. (D.3) was parameterized in a manner similar to the figure in the main text, with the only difference being ε = 2.(t_{intra} = −0.4 eV, t_{inter} = −0.15 eV, ε = ε(r_{ij}), $\hbar\omega_{vib}$ = 0.17 eV, and λ^2 = 1)

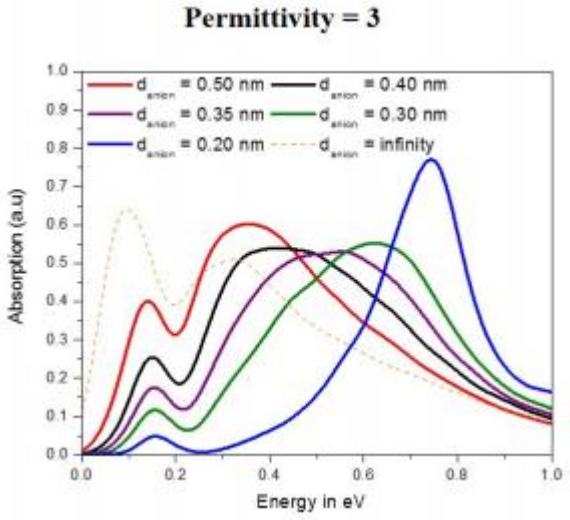

Figure D.10. The calculated absorption spectrum of a P3HT hole within a chain containing 10 thiophene rings with an anion placed next to a π-stack at various distances, d_{anion}, from the chain center. The Hamiltonian in Eq. (D.3) was parameterized in a manner similar to the figure in the main text, with the only difference being ε = 2.(t_{intra} = −0.4 eV, t_{inter} = −0.15 eV, ε = ε(r_{ij}), $\hbar\omega_{vib}$ = 0.17 eV, and λ^2 = 1)

Similarly parameterized simulations were performed with different values of ε, shown here in Figs. D.8-D.10. As ε approaches 3, the continuum value for bulk P3HT, the distance at which the polaron localizes (represented by a blue shift and narrowing of the peak in the mid-IR)

becomes smaller. If one could extend the bulk dielectric constant down to molecular distances, this could be indicative of greater amounts of anions in the crystallite π-stacks. However, we believe that use of the bulk value of ε is not physical at such short distances and therefore we chose to use the distance-dependent ε, described above, instead.

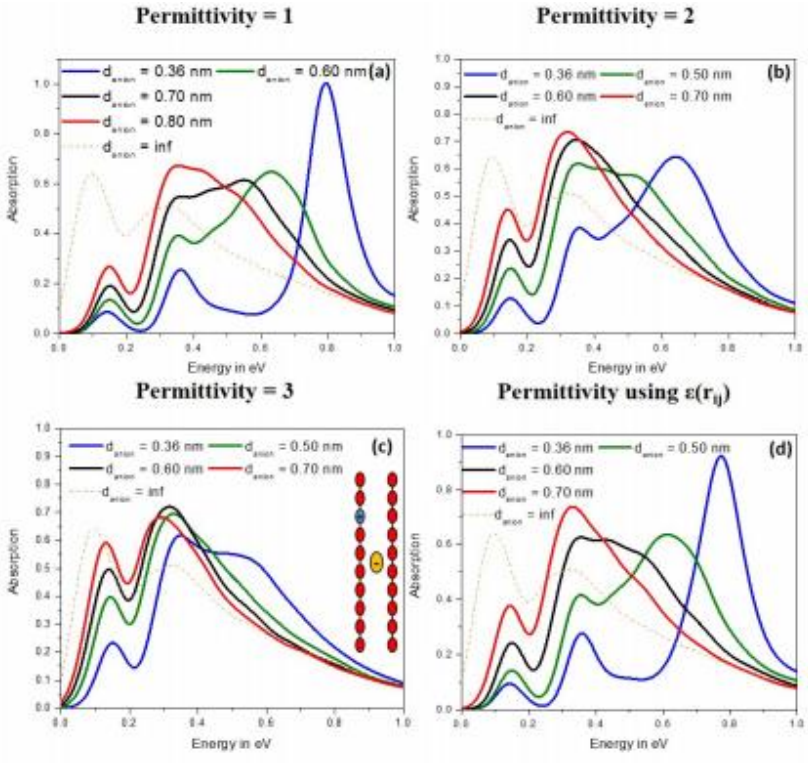

Figure D.11. The calculated absorption spectra of a P3HT hole within a chain containing 10 thiophene rings with an anion placed above a π-stack at various distances, d_{anion}, from the chain center (cartoon picture inset in figure). The Hamiltonian in Eq. (D.3) was parameterized similar to the figure in the main text, with the values for ε being (a) ε = 1, (b) ε = 2, (c) ε = 3, and (d) ε = ε(r_{ij}). (t_{intra} = −0.4 eV, t_{inter} = −0.15 eV, ε = ε(r_{ij}), $\hbar\omega_{vib}$ = 0.17 eV, and λ^2 = 1)

Similar to the calculated mid-IR spectrum discussed above, we also calculated the mid-IR absorption spectrum as a function of anion distance above a π-stack in the lamellar direction from an oxidized P3HT dimer containing two 10-mer chains (see Fig. D.11(c)). The conclusions for these calculated spectra also depend on the value of ε chosen, and we argue that the distance-dependent ε(r_{ij}) makes the most physical sense for the same reasons discussed above.

To understand the implications of this assumptions, we again repeated the calculation with multiple values of ε, all of which are plotted in Fig. D.11.

Conductivity

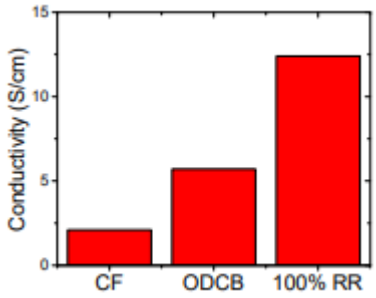

Figure D.12. Conductivity of P3HT films SqP doped with 1 mg/mL F_4TCNQ in DCM measured by the Van der Pauw method.

In-plane conductivity was measured for all doped samples using both collinear 4-point probe and the Van der Pauw method. As we previously reported, these measurement methods gave good agreement with each other. The room-temperature values in Fig. D.12 were measured in-house at UCLA by the Van der Pauw method, and the values reported in Table 5.2 of the main text were also measured independently in the Van der Pauw geometry at Lake Shore Cryotronics. The temperature-dependent conductivity values reported in the main text, whose raw values are shown in Fig. D.13, were measured using a Lake Shore model 8404 series AC/DC Hall Measurement System at Lake Shore. Figure D.14 plots the conductivity versus the temperature raised to various fractional powers, allowing us to easily visualize power laws as straight lines to investigate the agreement with various hopping charge transport models. The SqP-doped CF-cast P3HT film's conductivity was linear over the entire $T^{-1/3}$ range, but the more crystalline samples saw conductivity with two different regions of linearity at low and high temperatures. At low T's, the ODCB-cast and 100%-RR P3HT samples conductivities both fit well to a $T^{-1/2}$ temperature dependence, corresponding to the Efros-Shklovskii VRH model. At higher T's, the 100%-RR P3HT film's conductivity fits better to a $T^{-1/4}$ temperature dependence,

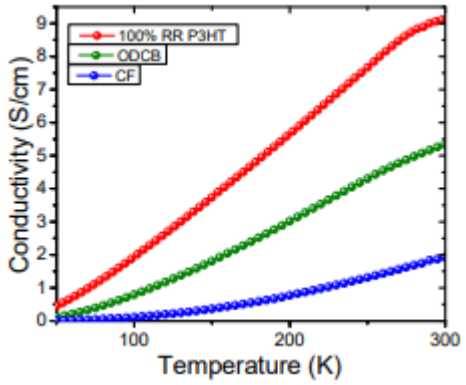

Figure D.13. Temperature-dependent conductivity for P3HT films SqP-doped with 1 mg/mL F_4TCNQ prepared with 100%-RR P3HT (red spheres), ODCB-cast P3HT (green spheres), and CF-cast P3HT (blue spheres).

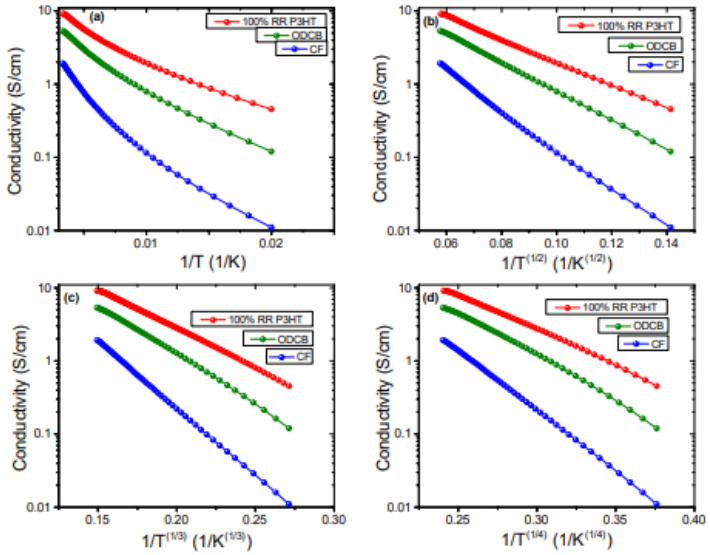

Figure D.14. Temperature dependent conductivity of 100% RR P3HT (red spheres), ODCB cast P3HT (green spheres), and CF cast P3HT (blue spheres) SqP doped with 1 mg/mL F_4TCNQ in DCM plotted as a function of inverse temperature raised to various powers corresponding to different transport models a-d).

corresponding to traditional Mott VRH. Since the highest temperature we measure is room temperature, we neglect any dedoping, which is known to occur when doped P3HT is exposed to higher temperatures.

AC Magnetic Field Hall Effect

As mentioned in the main text, we used the Hall effect to quantify the number of carriers as well as the carrier mobility within our doped polymer samples. Our previous efforts to utilize traditional DC Hall effect techniques gave unreliable experimental data, where the noise was larger than the signal of the measurement. This was a result of both poor electrode alignment, which in the Van der Pauw configuration gives offset voltages larger than the signals, and the fact that the mobility is intrinsically low for our materials. Thus, we turned to a more sensitive technique using AC magnetic field Hall measurements with a Lake Shore model 8400 series AC Hall probe system. In this technique, the magnetic field is oscillated at a particular frequency to make the voltage that is a result of the Lorentz force become time dependent, allowing it to be distinguished from the static misalignment offset voltage. More information concerning this technique is given in the references included in the main text. Even using this technique, there was still a slight error due to degradation of the doped films during the long measuring times. This error could be largely eliminated simply by flowing nitrogen continuously over the samples while the measurements were being performed, leading to very reproducible results with low systematic errors. Even though our AC Hall data is quantitatively robust, the interpretation of that data is much more complicated because the Hall effect relies on the interaction between the charge carriers and the magnetic field, and it is not completely understood how trapped charges in disordered systems respond to magnetic fields, as discussed in the main text.

APPENDIX E. Supporting Information for Chapter 6

Synthesis and Characterization of P37S-*stat*-P3HT Copolymers

Synthesis of statistical copolymers is carried out according to the procedure referenced in the main text.

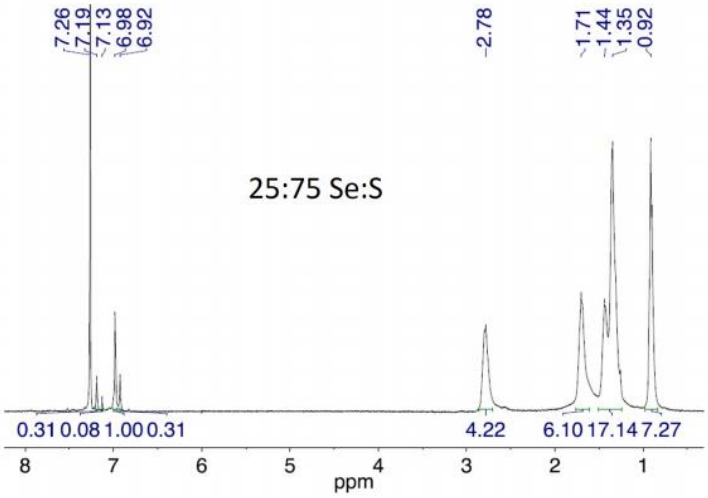

Figure E.1. ^{1}H NMR spectrum of the 25:75 Se:S copolymer.

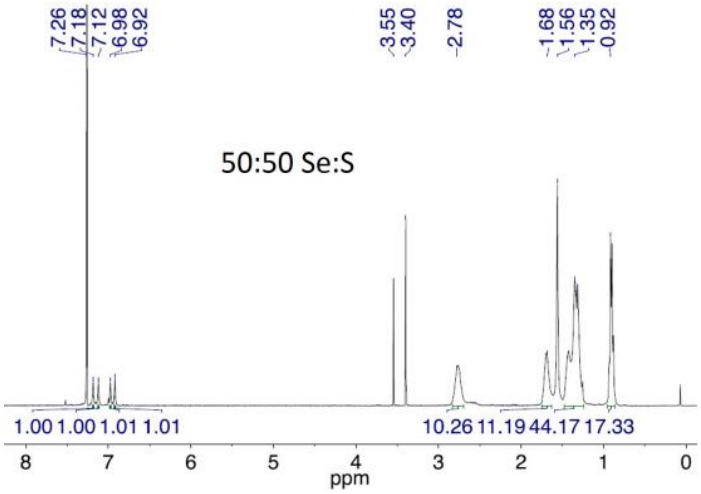

Figure E.2. ^{1}H NMR spectrum of the 50:50 Se:S copolymer.

NMR spectra were recorded on a Varian Mercury 400 spectrometer (400 MHz). Polymer molecular weights were determined using a Viscotek HT-SEC module 350A (1,2,4-

trichlorobenzene stabilized with butylated hydroxytoluene, 140 °C, 1 mL/min) with narrow weight distribution polystyrene standards.

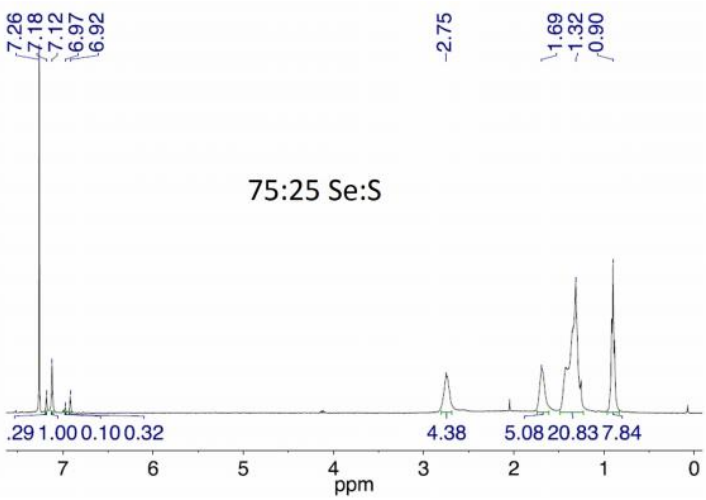

Figure E.3. ^{1}H NMR spectrum of the 75:25 Se:S copolymer.

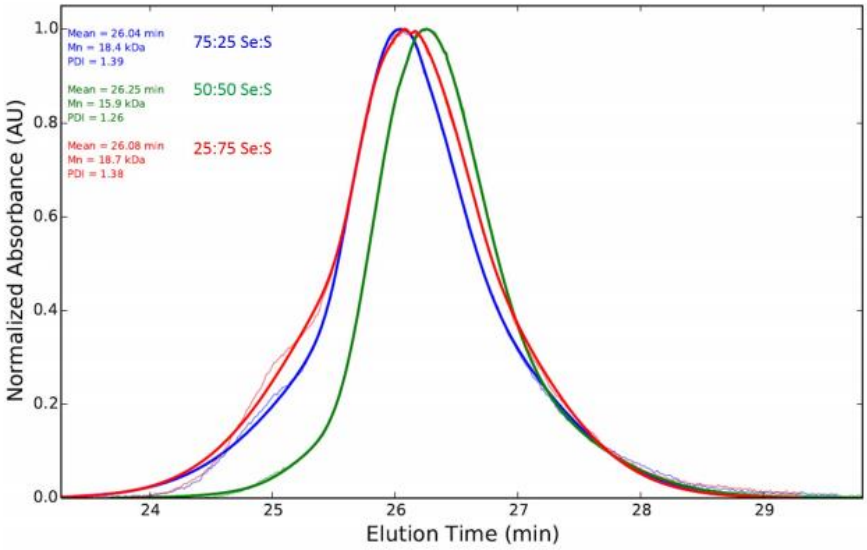

Figure E.4. GPC curves for different statistical copolymers.

Spectroscopy

In order to better understand the relationship between bandgap and crystallinity in the copolymer series, we utilized UV-vis and FTIR spectroscopy. The UV-vis-NIR region from 3.5−0.5 eV was measured using a Shimadzu UV-3101PC UV-VIS-NIR Scanning Spectrophotometer for films

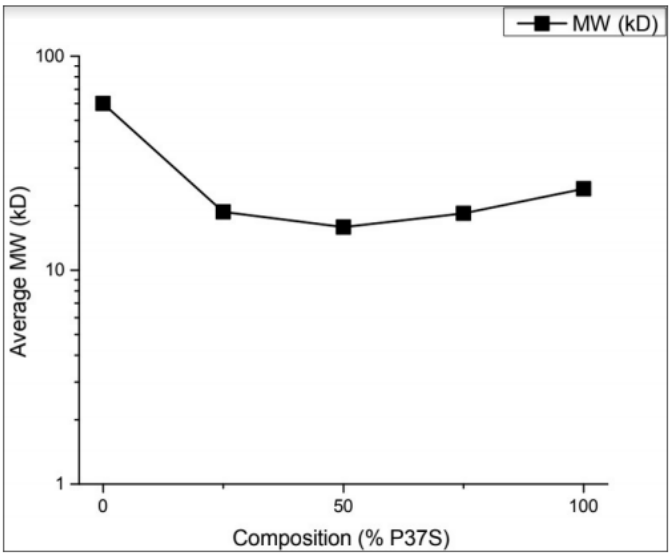

Figure E.5. Average molecular weight of the different statistical copolymers. The trend in MW data across the copolymer series presented in this figure does not match any observed trend in the main text, and is not believed to be a contributing factor in the study presented.

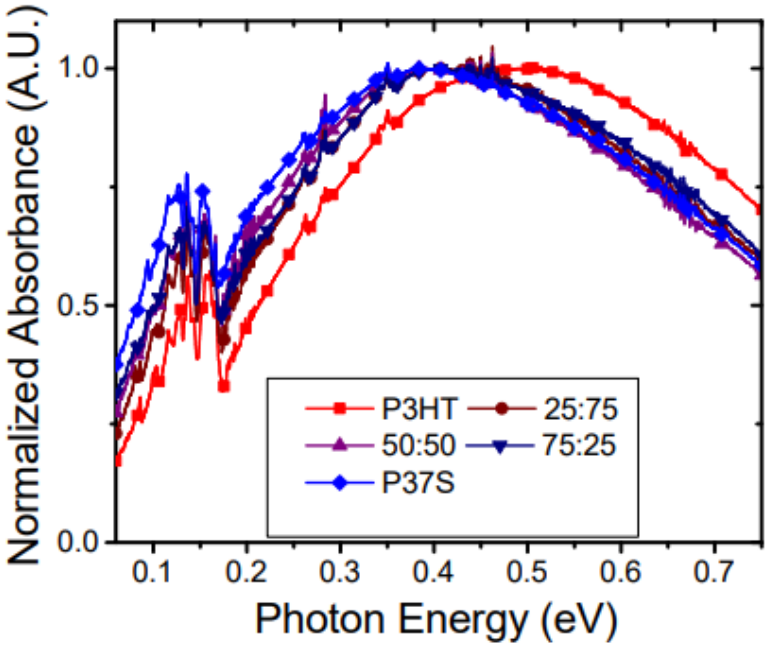

Figure E.6. Combined normalized UV-VIS-NIR and FTIR absorption data for the copolymer series sequentially doped with 1 mg/mL F_4TCNQ in DCM from 0.05–0.75eV.

prepared on KBr plates. The IR region from 220-7000 cm^{-1} was measured using a Jasco FT/IR-420 Spectrometer in transmittance mode on the same films prepared on KBr plates. The FTIR data was converted to absorbance and then combined with the UV-VIS-NIR data and normalized

to peak height as seen in Fig. E.6. The peaks include many vibrational features overlayed onto the broad Gaussian peak representing the low energy polaron. Although these individual vibrational modes have been used to extract information related to the extent of doping, we were only interested in looking at the polaron peak location and intensity in this study in order to compare relative trends in polaron delocalization and environment within the series.

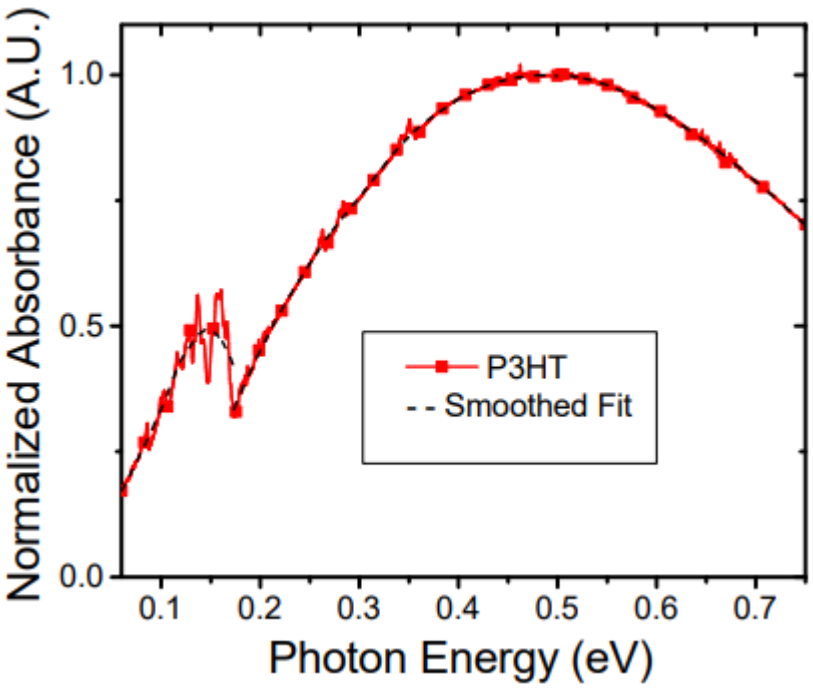

Figure E.7. Combined and normalized UV-VIS-NIR and FTIR absorption data for 100% P3HT sequentially doped with 1 mg/mL F_4TCNQ in DCM (red squares) with a Loess smoothing procedure (black dashes) overlayed to show agreement.

The peak below ~0.17 eV is related to the interchain polaron transition and contains many IR-active vibrational modes that account for the fine structure that is superimposed. The ratio of this low-energy interchain absorption compared to the higher-energy intrachain absorption between 0.35–0.5 eV has been shown to be a good indication of the relative level of delocalization of the polaron, both within the crystallite and spatially separated from the anion. In order to better distinguish the general peak locations and intensities within the fine structure, we used separate Loess smoothing functions for the ranges 0.05–0.17 and 0.17–0.75 eV in order to maintain the 'dip' at 0.17 eV. The results of this smoothing procedure (black

dashes) for the doped 100% P3HT film is overlayed on the original data (red curve), showing excellent agreement. The compilation of all of smoothed curves resulted in Fig. 6.2(a) in the main text. It is worth mentioning that the smoothing procedure averages the intensity of the interchain component of the absorption below 0.17 eV, likely underestimating the actual value. However, we used the same smoothing process for all samples in our series, ensuring that relative trends are accurate.

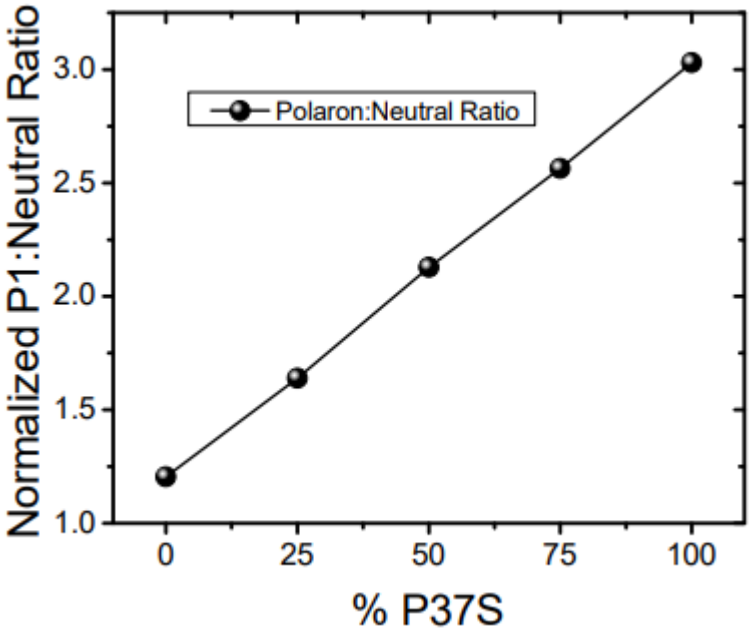

Figure E.8. Plot showing the relative intensity of the P1 polaron peak compared to the amount of remaining neutral absorbance for the entire doped copolymer series.

The percent of neutral absorption intensity quenched shown in Fig. 6.2b of the main text was generated by taking the ratio of the intensity of the neutral absorption peak in the doped state to that of the undoped state to get the remaining fraction of undoped absorbance. Subtracting this quantity from unity gave the fraction of neutral absorption that was quenched by doping. If the data are instead pre-normalized to the low-energy polaron peak, as was done in main text Fig. 6.2a, one can obtain a rough estimate of the polaron absorption relative to the amount of remaining neutral absorption. Figure E.8 shows this comparison, which is linear with copolymer composition as expected given how the HOMO level of the polymers vary across the

series. When normalized this way, this data also indicated that either the carriers generated from the higher-Se content materials have lower cross-sections, resulting in more quenching of the neutral to produce the same effective polaron peak absorbance, and/or that a significant fraction of the carriers generated are trapped, giving rise to a different polaron absorption with a different spectrum and cross-section. Since the polaron absorption intensities do not agree with the free carrier concentrations determined by our AC Hall effect measurements (reported in Fig. 6.5 of the main text), we can conclude that, regardless of the cause, optical measurements are not a reliable method for determining mobile carrier concentrations that are important for the electrical properties of this class of materials.

GIWAXS

2-D grazing incidence wide angle X-ray scattering (GIWAXS) experiments were performed at the Stanford Synchrotron Radiation Lightsource on beamline 11-3 using a wavelength of 0.9742Å with an incident angle of 0.12°. Figure E.9 shows the full 2-D diffractograms of our different polymer systems. These diffractograms were radially integrated to obtain the diffraction patterns (0-10° for in-plane, 70–80° for out-of-plane, and 0-180° for full). The 2-D images were collected with a Rayonix model MX225 X-ray CCD 250 mm away from the center of the measured sample. The beam spot had a width of ~150 μm and a helium chamber was used to reduce the noise. The software package WxDiff was used to reduce the GIWAXS data and subsequent analysis was performed in IgorPro.

As seen in Fig. E.10(a), with increasing selenophene content, the (010) peak shifts to progressively lower *q*, starting at 1.64 $Å^{-1}$ for pure P3HT (red curve) to 1.59 $Å^{-1}$ for pure P37S (blue curve). This is indicative of the larger selenium atom relative to sulfur, increasing the π-stacking distance. The low relative ratios of the (100) peak intensity to the (010) peak intensity

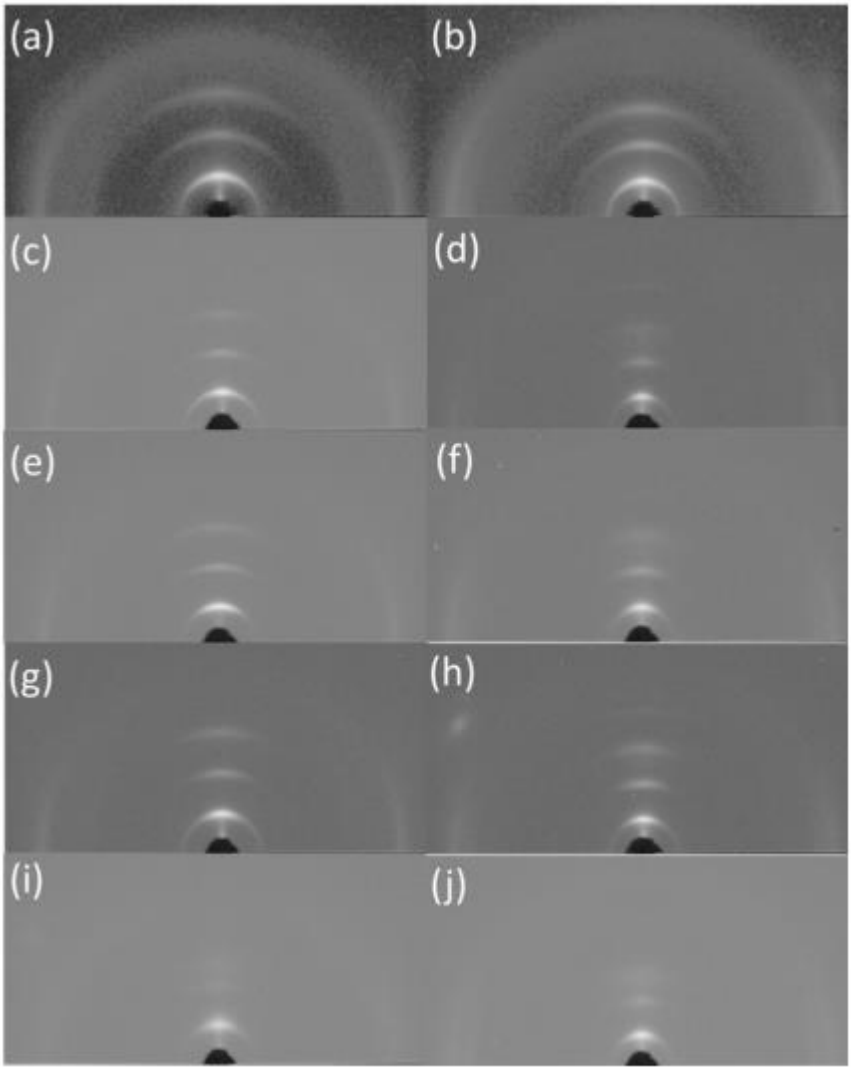

Figure E.9. 2-D diffractogram images of (a) P3HT, (b) P3HT doped, (c) P3HT:P37S 25:75, (d) P3HT:P37S 25:75 doped, (e) P3HT:P37S 50:50, (f) P3HT:P37S 50:50 doped, (g) P3HT:P37S 75:25, (h) P3HT:P37S 75:25 doped, (i) P37S, and (j) P37S doped.

for each polymer curve is indicative of an edge-on orientation, regardless of selenophene content.

Upon doping, as seen in Figure E.10(b), a new peak begins to grow in at 1.76 $Å^{-1}$ for P3HT (red curve). This smaller π-stacking peak appears for each polymer sample, with a similar trend to lower q with more selenophene content as the undoped samples. Also similar to the undoped

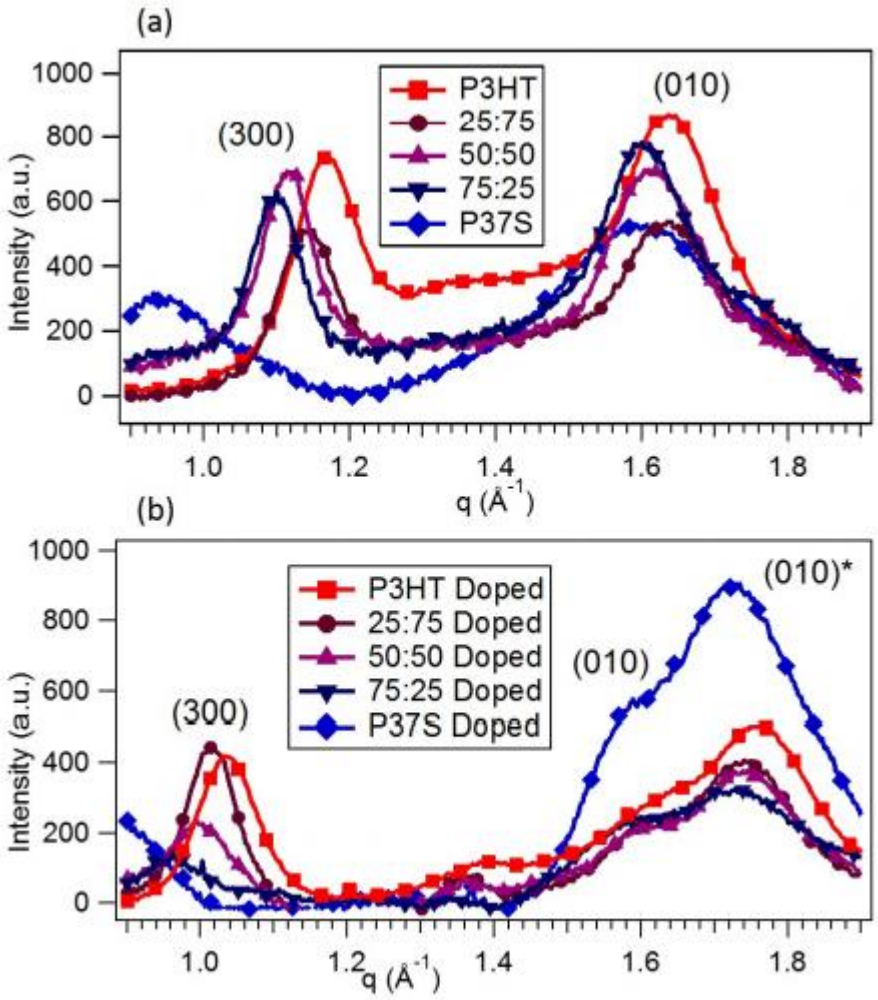

Figure E.10. Radially integrated diffraction of π-stacking region for (a) pure polymer films and (b) F4TCNQ doped polymer films.

samples, the doped polymers are edge-on oriented, with low relative ratios of (100) to (010) peak intensities.

Taking a closer look at the π-stacking trends, we see that for the pure films, there is a trend towards lower q with increasing selenophene content. After doping, this π-stacking region results in two different peaks, denoted as undoped (010) and doped (010)*. The general trend for both the undoped (010) and doped (010)* shows a shift to lower q with selenophene content, similar to the pure polymer films. The 75:25 material with the least-shifted doped π-stacking peak matches perfectly with the Hall measurements that show it is the least doped, which also

	Peak Locations q (Å^{-1})		
	Before Doping (010)	After Doping (010)	After Doping (010)*
P3HT	1.635	1.589	1.758
25:75	1.631	1.603	1.741
50:50	1.618	1.592	1.742
75:25	1.614	1.580	1.728
P37S	1.599	1.564	1.729

Table E.1. π-stacking (010) peak locations in q (Å^{-1}) for radial integrations of both pure and doped films.

follows the trend of having the least swellability as discussed in the main text. Therefore, the excess F_4TCNQ that does not participate in the doping process and corresponding decrease in π-stack spacing, could be frustrating the polymer stacking and decreasing the crystallinity for the doped 75:25 sample.

Differential Scanning Calorimetry

To corroborate the GIWAXS crystallinity trends, differential scanning calorimetry (DSC) was performed on as-synthesized copolymer powders. The DSC curves are shown in Figure E.11(a) for the first and (b) for the second cycles. The DSC change in enthalpy of melting and crystallization were obtained using a Perkin Elmer® DSC 8000, a dual furnace instrument equipped with an IntraCooler. The samples were measured in vented Al pans in an inert N_2 atmosphere. The heat flow from 30 °C to 300 °C at a rate of 10 °C/min was recorded then the area under the peaks was used to determine the change in enthalpy. The variation in shape/background slope we observed between samples is attributed to differences in heat flow between the reference and baseline pans. The calculated change in enthalpy energies are plotted in Figure E.12, confirming minimal variation between the 1st and 2nd cycle melt and freezing energies.

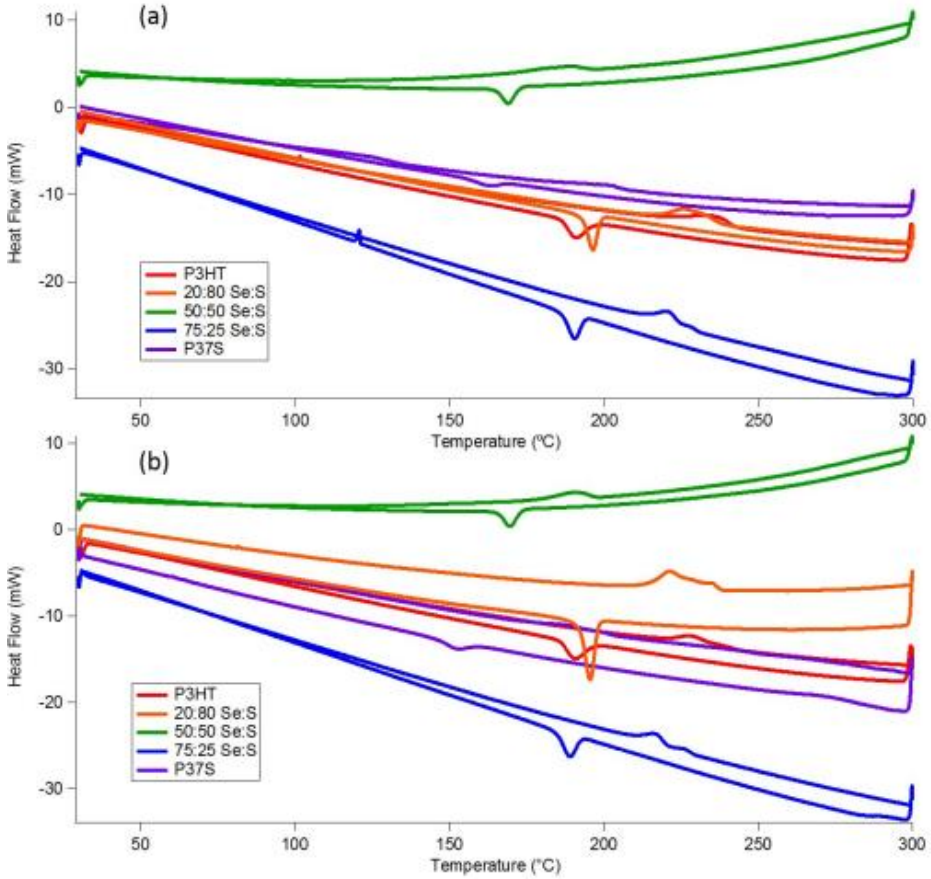

Figure E.11. DSC curves for statistical copolymers with increasing amount of Se for (a) the 1st cycle and (b) the second cycle measurements.

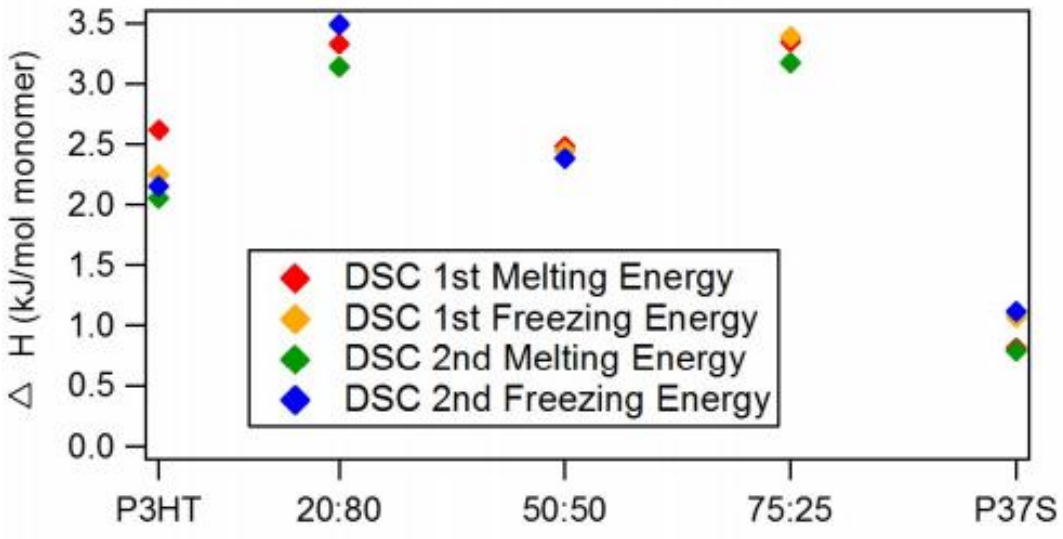

Figure E.12. Calculated change in enthalpy energies for statistical copolymers with increasing amount of Se.

Cyclic Voltammetry

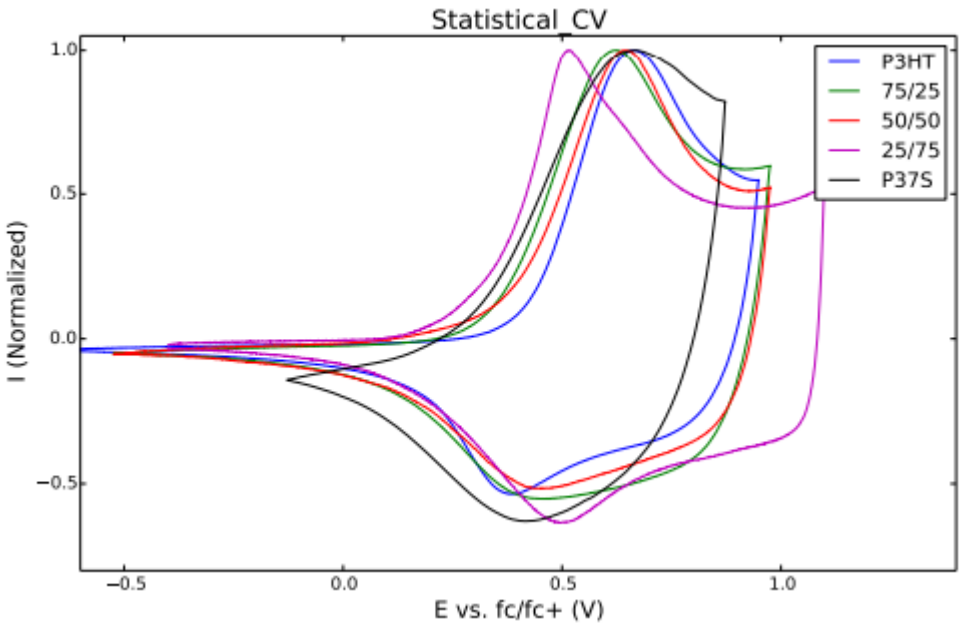

Figure E.13. Cyclic voltammetry curves for statistical copolymers with increasing amount of Se.

P3HT %	100	75	50	25	0
Ox onset 1	1.08	0.85	0.83	0.76	0.44
Ox onset 2	1.08	0.85	0.83	0.75	0.44
Ox onset 3	1.06	0.89	0.91	0.75	0.44
Ox onset 4		0.88	0.91	0.74	
Ox onset avg	1.07	0.87	0.87	0.75	0.44
fc/fc+	0.61	0.52	0.52	0.48	0.13
E vs fc	0.46	0.34	0.35	0.27	0.31
homo	-5.26	-5.14	-5.15	-5.07	-5.11

Table E.2. Cyclic voltammetry values (in V relative to Fc/Fc+) for the oxidation onset and calculated HOMO energy levels (in V relative to vacuum) for the statistical copolymer series.

Cyclic voltammetry scans for our copolymer series are shown in Figure E.13. Electrochemical measurements were recorded on films drop-cast on a Pt working electrode in MeCN/NBu_4PF_6 (0.1 M) versus Ag/AgCl (scan rate 100 $mV \cdot s^{-1}$) with Fc/Fc^+ as an internal standard, using a BASi Epsilon potentiostat. The HOMO levels have been calculated from the oxidation onset values, which are listed in Table E.2. We note that within the ~50 mV error of cyclic voltammetry

measurements, the reported HOMO levels are in general agreement with our conclusions in the main text.

Ellipsometry/Porosimetry

	Fit Range (nm)	Fit (R^2)	Thickness Change (%)
P3HT	860-1000	0.86	14
25:75	860-1000	0.96	21
50:50	860-1000	0.92	25
75:25	860-1000	0.96	16
P37S	860-1000	0.85	22

Table E.3. Fitting data for ellipsometry measurements performed on films before and after swelling with DCM in order to calculate the change in thickness.

To study polymer swelling, spectroscopic ellipsometry was performed on a PS-1000 instrument from Semilab at room temperature. A UV-visible CCD detector adapted to a grating spectrograph analyzed the signal reflected by the sample. The light source was a 75-W Hamamatsu Xenon lamp. For these measurements, the various polymer films were spun onto Si substrates with a thin (~2 nm) native oxide layer, and the samples were placed in a glass container custom-designed to contain the vapor of a solvent (i.e., dichloromethane, DCM) around the sample while still allowing unencumbered access and egress of the optical beams. The film thickness was monitored until it reached steady state while being exposed to DCM vapor in the container. With a series of calibration measurements, we found that the partial pressure of DCM solvent in the container reached 90% of the known room-temperature vapor pressure of DCM. Data analysis was performed using the associated SEA software. The thickness was obtained by fitting only the 860−1000 nm spectral region (to avoid the excitonic absorption of the various copolymer films) using the Cauchy model. By fitting the thickness prior to swelling and during swelling we can extract the percent change in film thickness caused by swelling, which are the values reported in the main text.

Electrical Measurements

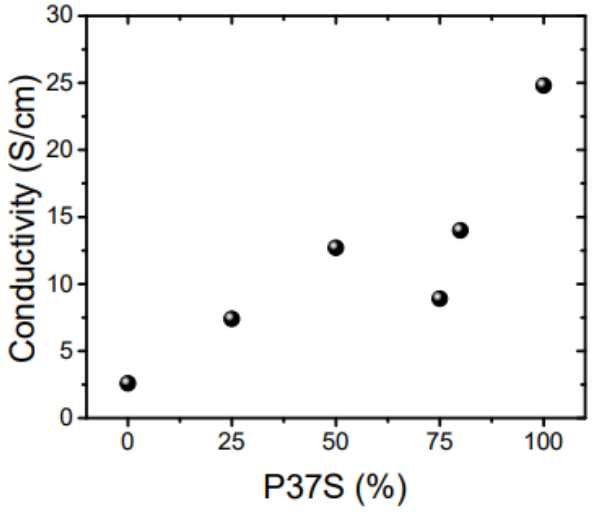

Figure E.14. Conductivity measurements for statistical copolymers with increasing amounts of P37S.

In-house conductivity measurements were performed on samples prepared as described in the main text on glass substrates with dimensions of 1.5×1.5 cm. We performed both collinear 4-point probe measurements with a probes spacing of 1.5 mm and Van der Pauw measurements with silver paste electrodes on the corners of the substrates. The results of our conductivity measurements are shown in Fig. E.14. Because of the large deviation from the linearity in conductivity at the 75:25 Se:S copolymer ratio, we also measured the conductivity of a similar ratio material (80:20) to verify that the lower value was real; the results of this measurement are also shown in Fig. E.14. That fact that two different materials in this composition range show values that fall below the trend of the rest of the series verifies that there is a morphological reason (higher crystallinity) why samples with this particular monomer ratio have decreased conductivities.

AC magnetic field Hall measurements were performed with a LakeShore model 8400 series AC/DC Hall Measurement System. This technique is described in the references in the main text, and the procedure was similar to our previously published work. The samples were

measured with N_2 gas flowing through the sample chamber to reduce degradation. This limited the change in conductivity over time to < 5% of the total during the 15-hour time span of data collection. The slightly lower conductivity values for our AC-Hall samples compared to what we measured in-house was due to the several-day time delay between fabrication and completion of the AC Hall measurements (whereas the in-house measurements were also performed on the same day the samples were fabricated). The average data from the AC Hall measurements as well as the error is included for all samples is presented in the following tables:

	Hall Voltage	R_H	n	Conductivity	μ	Carrier Type
Unit	μV	cm^3/C	$1/cm^3$	S/cm	$cm^2/(Vs)$	
Mean value	1.3	0.015	4.6E20	2.66	0.041	P
Error of the mean	0.1	0.001	3E19		0.001	92/100

Table E.4. AC Hall data for 100% P3HT.

	Hall Voltage	R_H	n	Conductivity	μ	Carrier Type
Unit	μV	cm^3/C	$1/cm^3$	S/cm	$cm^2/(Vs)$	
Mean value	2070	0.0176	3.59E20	5.0	0.086	P
Error of the mean	30	0.0002	4E18		0.001	100/100

Table E.5. AC Hall data for 25:75 Se:S.

	Hall Voltage	R_H	n	Conductivity	μ	Carrier Type
Unit	μV	cm^3/C	$1/cm^3$	S/cm	$cm^2/(Vs)$	
Mean value	16.0	0.0128	5.9E20	5.38	0.0688	P
Error of the mean	0.6	0.0005	4E19		0.0005	99/100

Table E.6. AC Hall data for 50:50 Se:S.

	Hall Voltage	R_H	n	Conductivity	μ	Carrier Type
Unit	μV	cm^3/C	$1/cm^3$	S/cm	$cm^2/(Vs)$	
Mean value	2100	0.026	2.2E20	3.23	0.083	P
Error of the mean	200	0.002	4E19		0.007	89/100

Table E.7. AC Hall data for 75:25 Se:S.

	Hall Voltage	R_H	n	Conductivity	μ	Carrier Type
Unit	μV	cm^3/C	$1/cm^3$	S/cm	$cm^2/(Vs)$	
Mean value	14.3	0.0109	6.0E20	16.0	0.1742	P
Error of the mean	0.3	0.0002	1E19		0.0002	100/100

Table E.8. AC Hall data for 100% P37S.

APPENDIX F. Supporting Information for Chapter 7

Materials and Film Preparation

RRa P3HT (Sigma Aldrich), F_4TCNQ (TCI Chemicals), $FeCl_3$ (EM Science), and TCNQ (Alfa Aesar) were used as purchased. Glass and silicon substrates were cleaned sequentially by sonicating in soapy water, DI water, acetone, and isopropanol for 10 minutes each, then placed under rough vacuum to remove all traces of residual solvent, and finally transferred into a nitrogen glove box for use.

RRa P3HT films were spin coated at 1000 rpm for 60 seconds and then 3000 rpm for 10 seconds, out of 20 mg/mL solution in *o*-DCB, producing films that were ~80 nm thick. This was followed by a second spin-coating step where the RRa P3HT films were infiltrated by small molecule solutions spin-coated on top of the dried RRa P3HT film at 4000 rpm for 10 seconds. The solutions for this second step were prepared by dissolving each small molecule (F_4TCNQ, $FeCl_3$, and TCNQ) in a blend of 50:50 DCM:Ethanol by volume.

Conductivity Measurements

Conductivity measurements in the Van der Pauw geometry were performed using a custom made apparatus in ambient atmosphere using a Keithley 2400 Sourcemeter where the max current sourced was held to 1 mW total power. The current was swept negative to positive, rotated 90°, and repeated. The slope of the *I-V* curves were then fit to the Van der Pauw equation. Samples were prepared on glass, with silver paste applied at the corners of the film to act as contacts. All reported data was averaged over 10 simultaneous measurements for multiple samples.

UV-Vis Absorption

The UV-vis absorption data were acquired from 300-2500 nm using a Shimadzu UV-4191PC UV-VIS-NIR Scanning Spectrophotometer for films prepared on glass substrates.

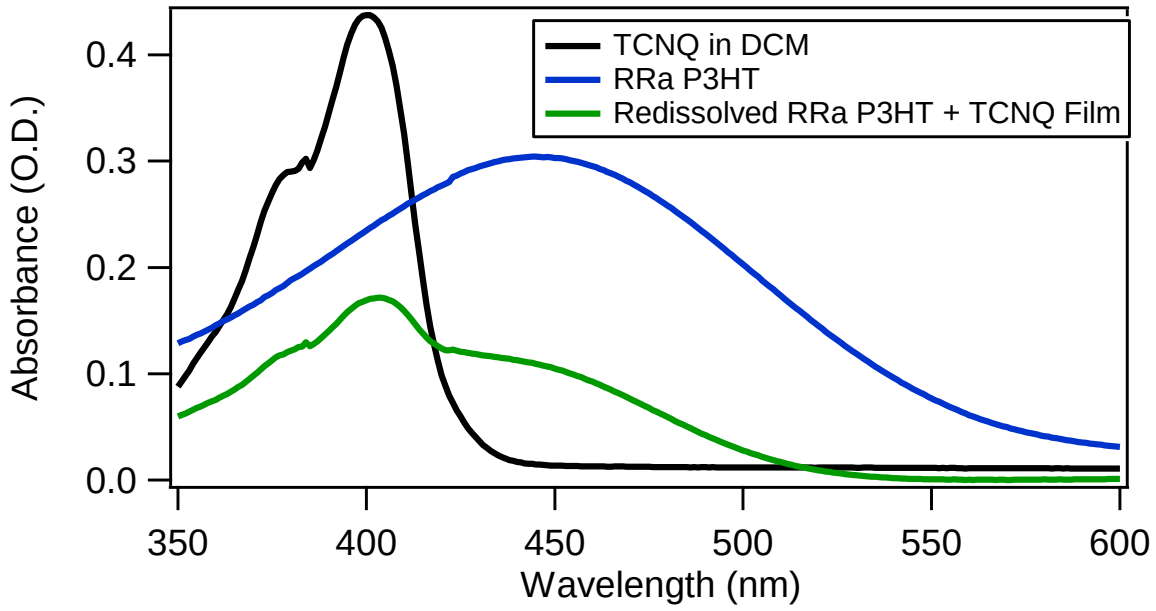

Figure F1: UV-vis absorbance of TCNQ dissolved in DCM (black), RRa P3HT film (blue), and a RRa P3HT + TCNQ film redissolved in DCM (green), confirming the presence of TCNQ in the film.

Figure F1 shows the UV-vis absorbance of TCNQ dissolved in DCM (black), pure RRa-P3HT film (blue), and a RRa-P3HT incorporated with TCNQ film that was redissolved in DCM (green). The redissolved film shows the spectral signature of TCNQ as seen in the pure TCNQ dissolved in DCM (black) in addition to the spectral signature of a RRa-P3HT film (blue).

GIWAXS

2-D grazing incidence wide-angle X-ray scattering (GIWAXS) experiments were performed at the Stanford Synchrotron Radiation Lightsource on beamline 11-3 using a wavelength of 0.9742 Å with an incidence angle of 0.12°. Figure F2 shows the full 2-D diffractograms of our RRa P3HT thin film samples. These diffractograms were radially integrated to obtain the diffraction patterns (0-10° for in-plane, 70-80° for near out-of-plane, and 0-180° for full integrations)

shown in the main text. The 2-D images were collected on a plate with the detector 250 mm away from the center of the measured sample. The beam spot had a width of ~150 μm and a helium chamber was used to reduce the noise. The software package WxDiff was used to reduce

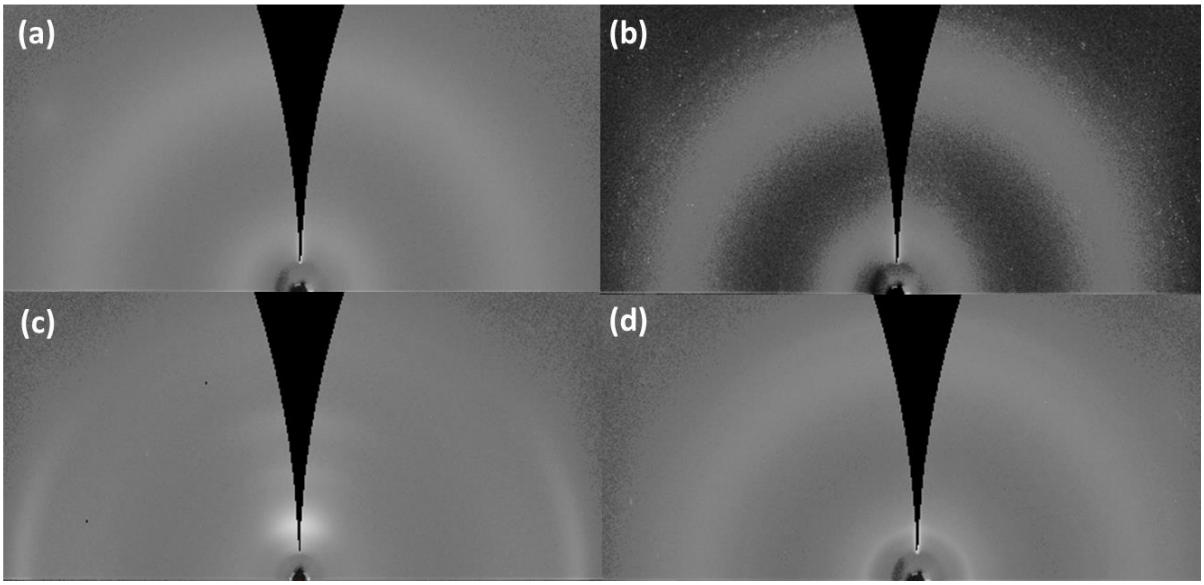

Figure F2: Raw diffractograms of (a) Pure RRa-P3HT, (b) RRa-P3HT + TCNQ, (c) RRa-P3HT F_4TCNQ Doped, and (d) RRa-P3HT $FeCl_3$-Doped

the GIWAXS data and subsequent analysis was performed in IgorPro.

Figure S2 shows the raw diffractograms after having been corrected for the grazing-incidence geometry. The broad amorphous quality for both the lamellar and π-stack spacing is indicative of the amorphous RRa-P3HT scattering. This amorphous signature is not disrupted upon the addition of TCNQ. However upon the addition of dopants (both F_4TCNQ and $FeCl_3$) results in more defined lamellar and π-stacking peaks as discussed in the main text.

Figure F3 shows full radial integrations for pure RRa-P3HT (blue), RRa-P3HT doped with F_4TCNQ (green), and RR-P3HT doped with F_4TCNQ (black). The diffraction data shows that upon doping the RRa-P3HT film shows a structural change similar to that of doped RR-P3HT films, with a shift in lamellar overtones to lower *q* (suggestive of dopant intercalating into the lamellar regions) and an appearance of π-stacking peak at higher *q* that has been reported to be due to

the π-stacks reorienting with respect to the unit cell. The increased crystallinity and appearance of lamellar overtones are discussed heavily in the main text.

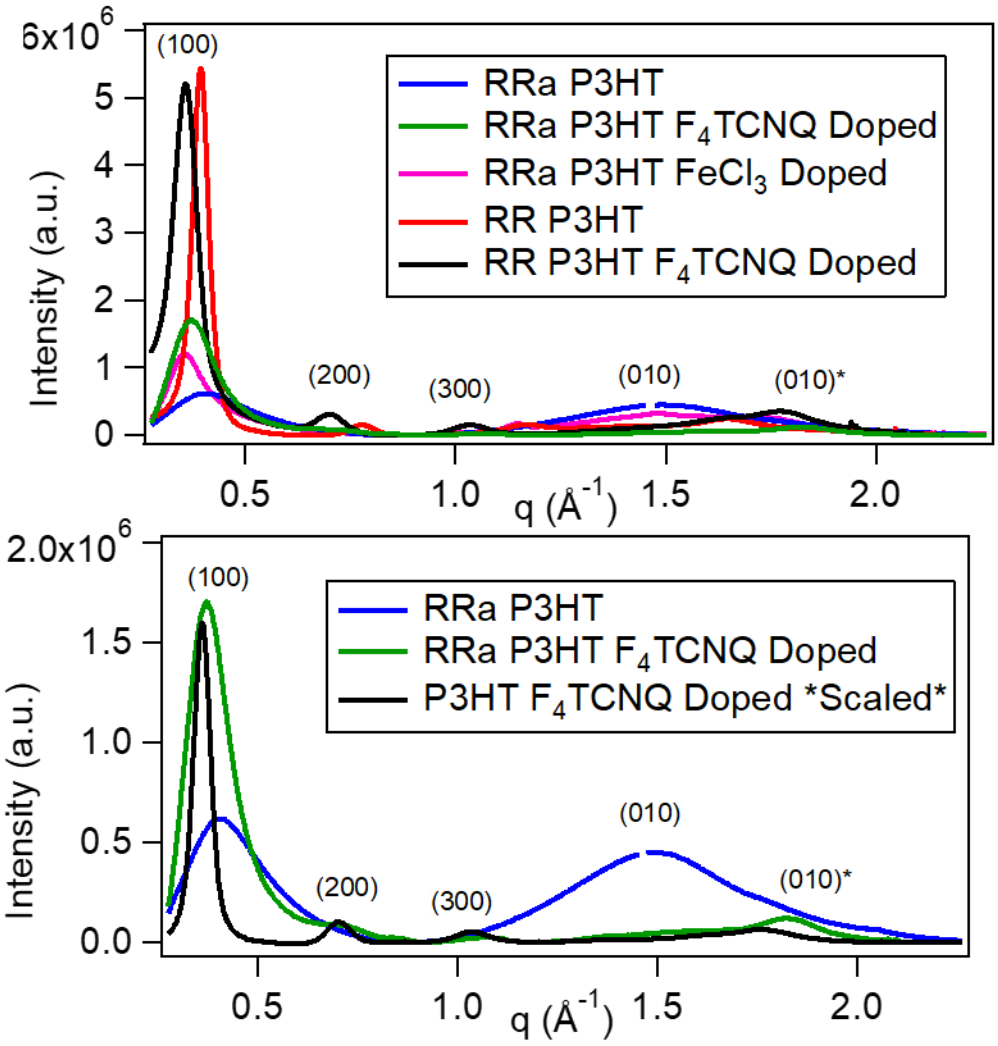

Figure F3: Full radial integrations of pure RRa P3HT (blue), F_4TCNQ doped RRa P3HT (green), $FeCl_3$ doped RRa P3HT (pink), RR P3HT (red) and F_4TCNQ doped RR P3HT (black), confirming a change in morphology of the RRa P3HT to a similar crystal structure of RR P3HT.

The orientation change and ordering is also apparent in samples doped with less F_4TCNQ, although to a lesser extent, as seen in Figure F4.The 0.05 mg/mL doped F_4TCNQ sample actually has a decrease in lamellar crystallinity, but still there is a structural rearrangement and ordering occurring with the appearance of the lamellar overtones and new π-stacking peak. As

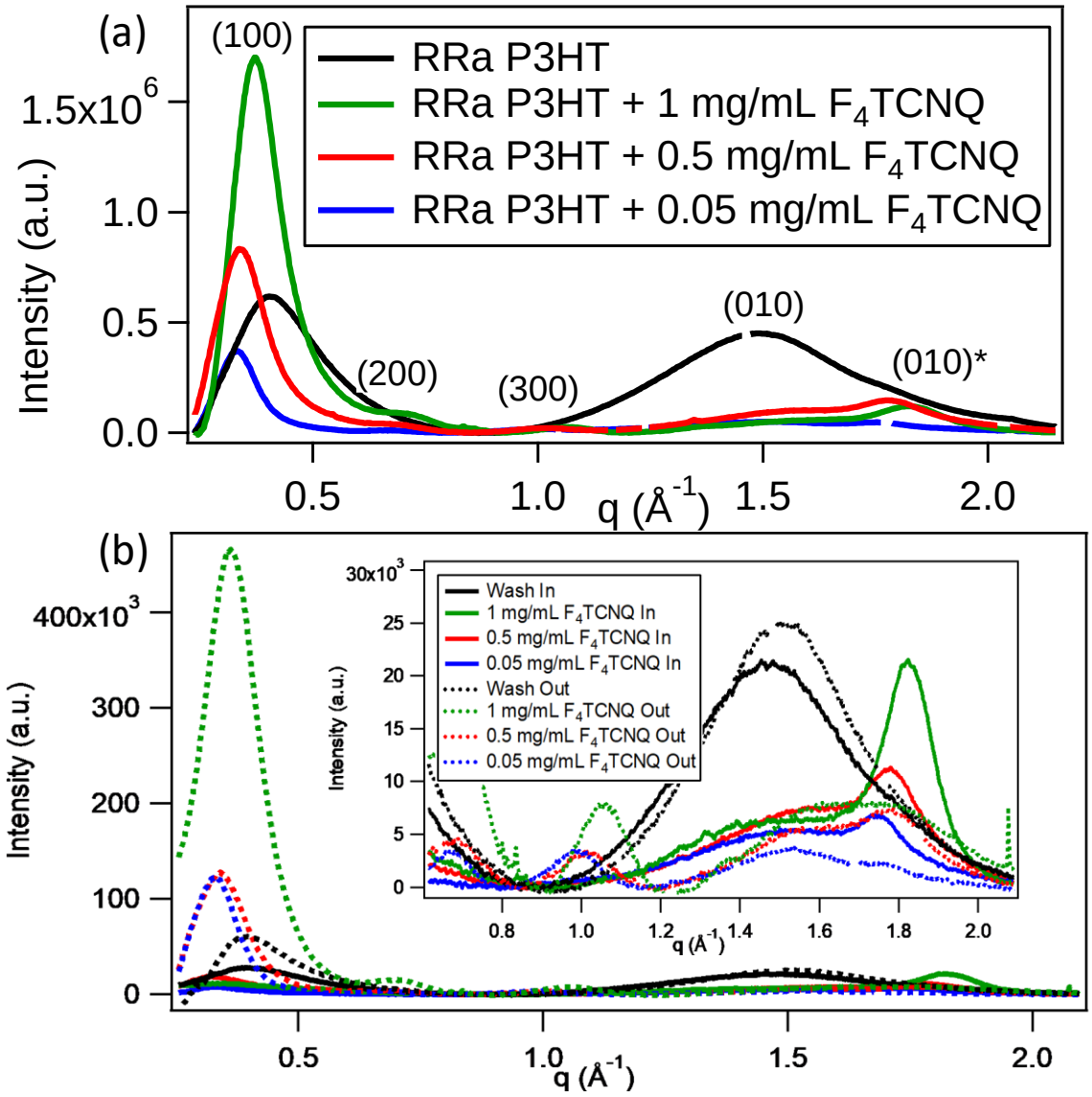

Figure F4: (a) Full radial integrations of pure RRa P3HT (black), 1 mg/mL F_4TCNQ doped RRa P3HT (green), 0.5 mg/mL F_4TCNQ doped RRa P3HT (red), and 0.05 mg/mL F_4TCNQ doped RRa P3HT (blue) and (b) In-plane (solid line) vs. out-of-plane (dashed line) integrations showing the morphological effects of F_4TCNQ doping occur even at lower F_4TCNQ doping levels.

the doping concentration increases, we see a further increase in lamellar crystallinity and long range order, as well as more edge-on orientation character. This suggests that the dopant is doping the crystalline regions first, followed by the amorphous regions, as mentioned in the main text.

Thermal Annealing/Dedoping

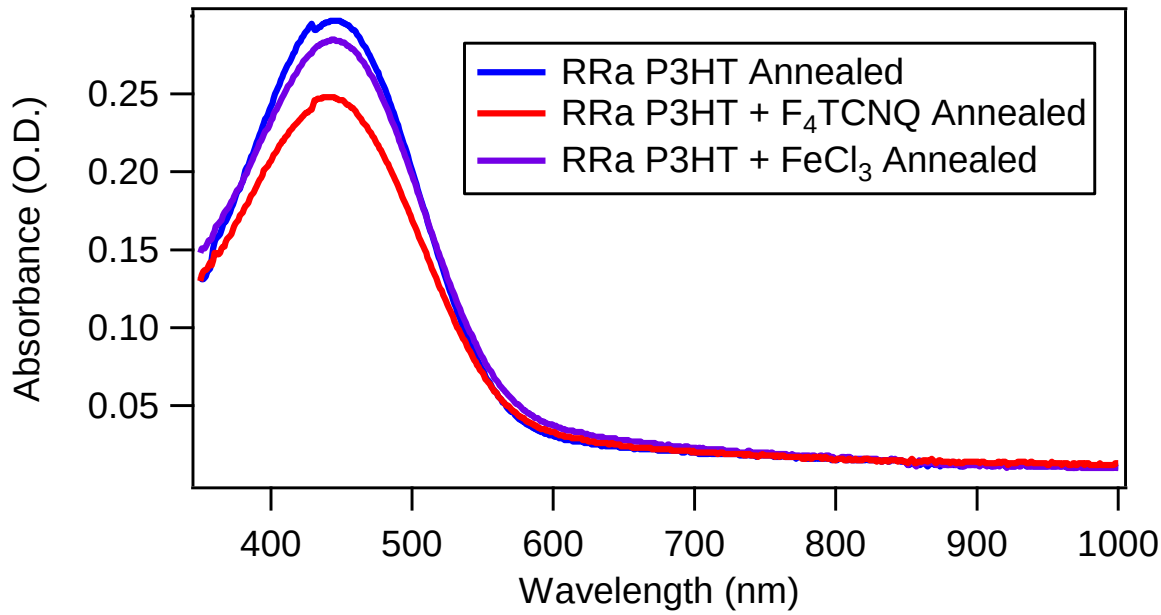

Figure F5: Absorbance of thermally dedoped RRa-P3HT films of pure RRa-P3HT (blue), F_4TCNQ-doped RRa P3HT (red), and $FeCl_3$-doped RRa-P3HT (purple) showing the successful dedoping of RRa-P3HT with the disappearance and P2 and dopant anion peaks as well as the reappearance of the neutral exciton absorption.

In addition to using $FeCl_3$ as our non-π-stacking dopant and TCNQ as our non-dopant control, we can use thermal annealing to dedope the doped RRa P3HT films and look at the structural effect upon removing the polaron from the system. Thermal dedoping provides another opportunity to further understand the polymer-dopant interaction and its reversibility. Each sample was annealed at 110°C in air for 20 minutes in order to dedope our samples. The UV-Vis of dedoped samples (via thermal annealing) can be seen in Figure F5, showing loss of the dopant anion peaks and P2 peak as well as a full recovery of the main absorption band. Additionally, we see neutral F_4TCNQ and $FeCl_3$ absorption peaks at 359 nm and 357 nm, respectively, further confirming the removal of polarons from the previously doped films.

The structural effect of dopants on the amorphous RRa-P3HT is further investigated by looking at the polymer structure of our dedoped (via thermal annealing) samples. For simplicity, we

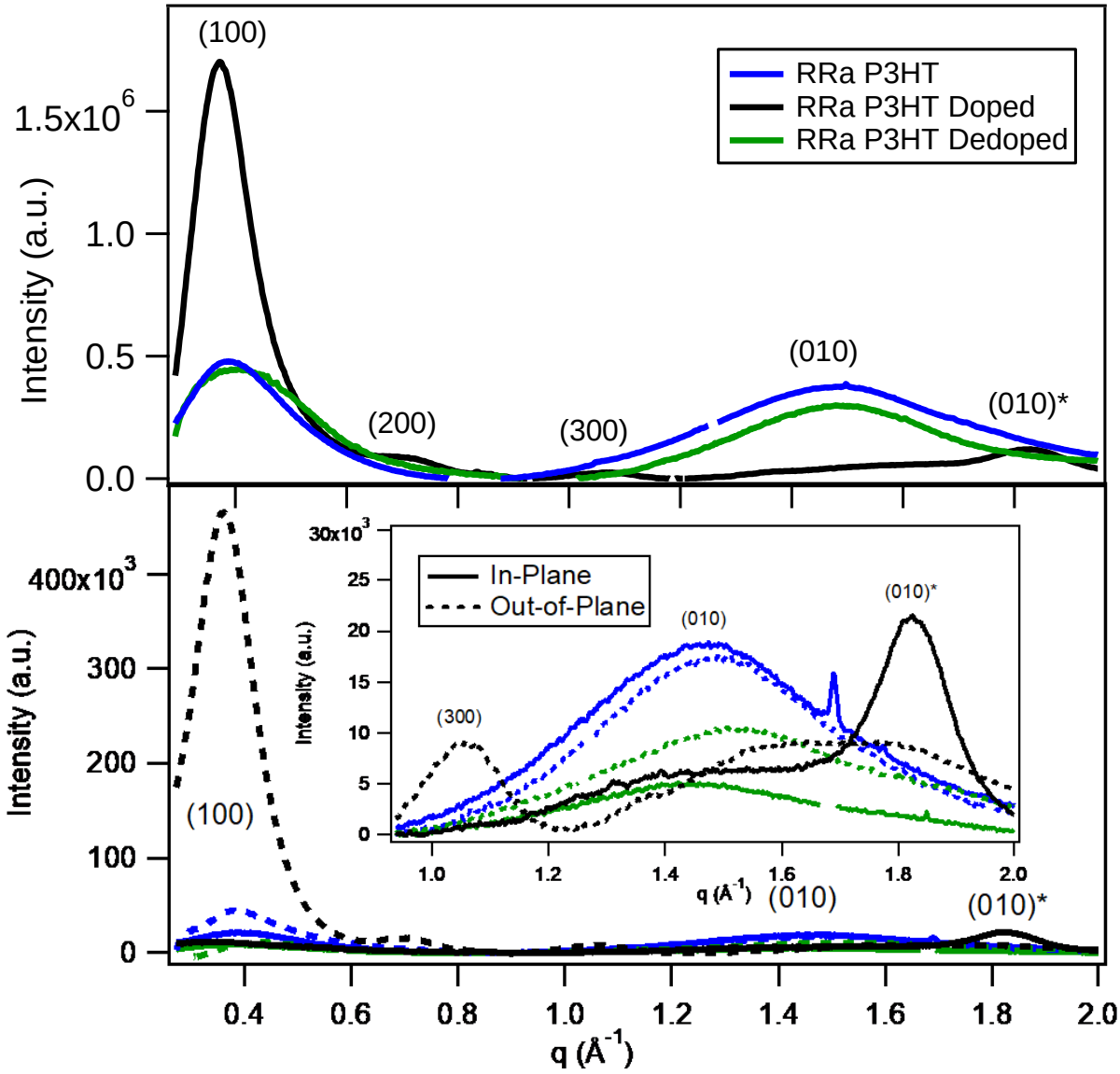

Figure F6. (a) Radially integrated diffraction for pure RRa P3HT (blue), doped RRa P3HT (black), and thermally dedoped RRa P3HT (green) and (b) in-plane (solid) and out-of-plane integrations (dashed) of the same samples.

only show the 0.003M F_4TCNQ doped (black) and dedoped (green) RRa P3HT samples. The radially integrated diffraction of the annealed samples can be seen in Figure F6a. In stark contrast to increased order of the doped structures, the annealed samples show no new structural features and have broad lamellar and π-stacking peaks just like the undoped amorphous RRa P3HT, with slight decreases in crystallinity across all samples. These shifts back from the larger, more ordered lamellar spacing and tighter packed π-spacing in the doped state

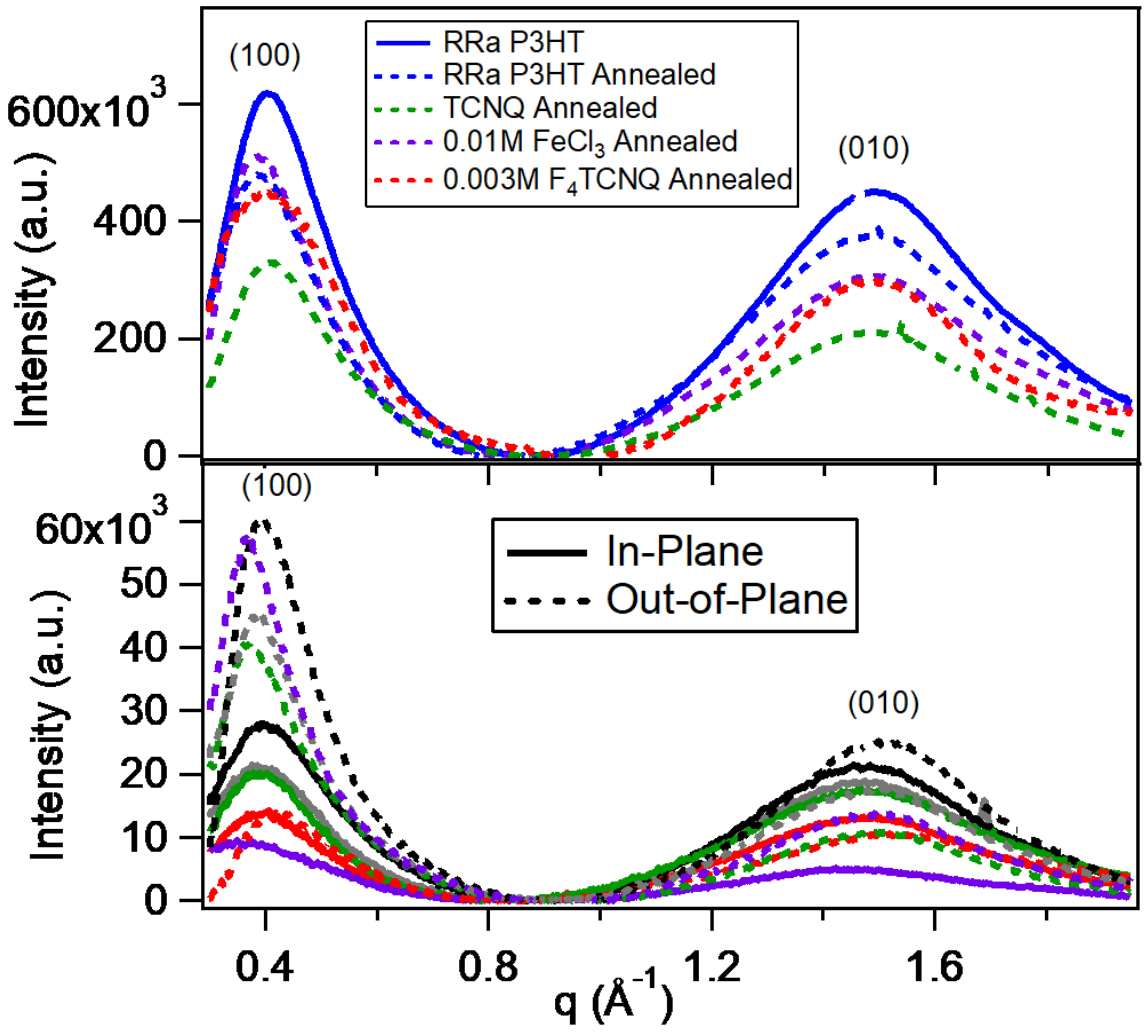

Figure F7: (a) Full radial integrations of pure RRa P3HT (blue) compared to annealed RRa P3HT (dashed blue), annealed RRa P3HT +TCNQ (dashed green), annealed 0.01M $FeCl_3$ doped RRa P3HT (dashed purple), and annealed 0.003M F_4TCNQ doped RRa P3HT (dashed red) and (b) in-plane vs. out-of-plane data, showing the reversion of the RRa P3HT morphology upon annealing/dedoping.

confirm that the dopants (or at least the charges introduced by them) are no longer in the polymer matrix. Furthermore, the in-plane vs. out-of-plane data in Figure F6b show that upon thermal annealing, the polymer orientation also reverts to the undoped isotropic state. Again, TCNQ has no structural effect on the RRa P3HT film upon thermal annealing and we see a similar trend when thermally annealing the $FeCl_3$-doped RRa films (refer to Figure F7). These structural

changes back to the initial amorphous state, as well as the loss of anion and polaron absorbance peaks in the UV-Vis data, confirm the importance of the polaron formation during the doping process.

	(100) Peak Location ($Å^{-1}$)	(010) Peak Location ($Å^{-1}$)
RRa-P3HT	0.41	1.49
RRa-P3HT + TCNQ	0.41	1.49
RRa-P3HT + F4TCNQ	0.36	1.51
RRa-P3HT + FeCl3	0.38	1.48

	(200) Peak Location ($Å^{-1}$)	(300) Peak Location ($Å^{-1}$)	(010)* Peak Location ($Å^{-1}$)
RRa-P3HT	N/A	N/A	N/A
RRa-P3HT + TCNQ	N/A	N/A	N/A
RRa-P3HT + F4TCNQ	0.72	1.06	1.83
RRa-P3HT + FeCl3	0.76	1.05	1.72

Table F1: Peak locations of for the lamellar and pi-stacking peaks for RRa-P3HT Films and lamellar overtones and new pi-stacking peak locations for small molecule incorporated films.